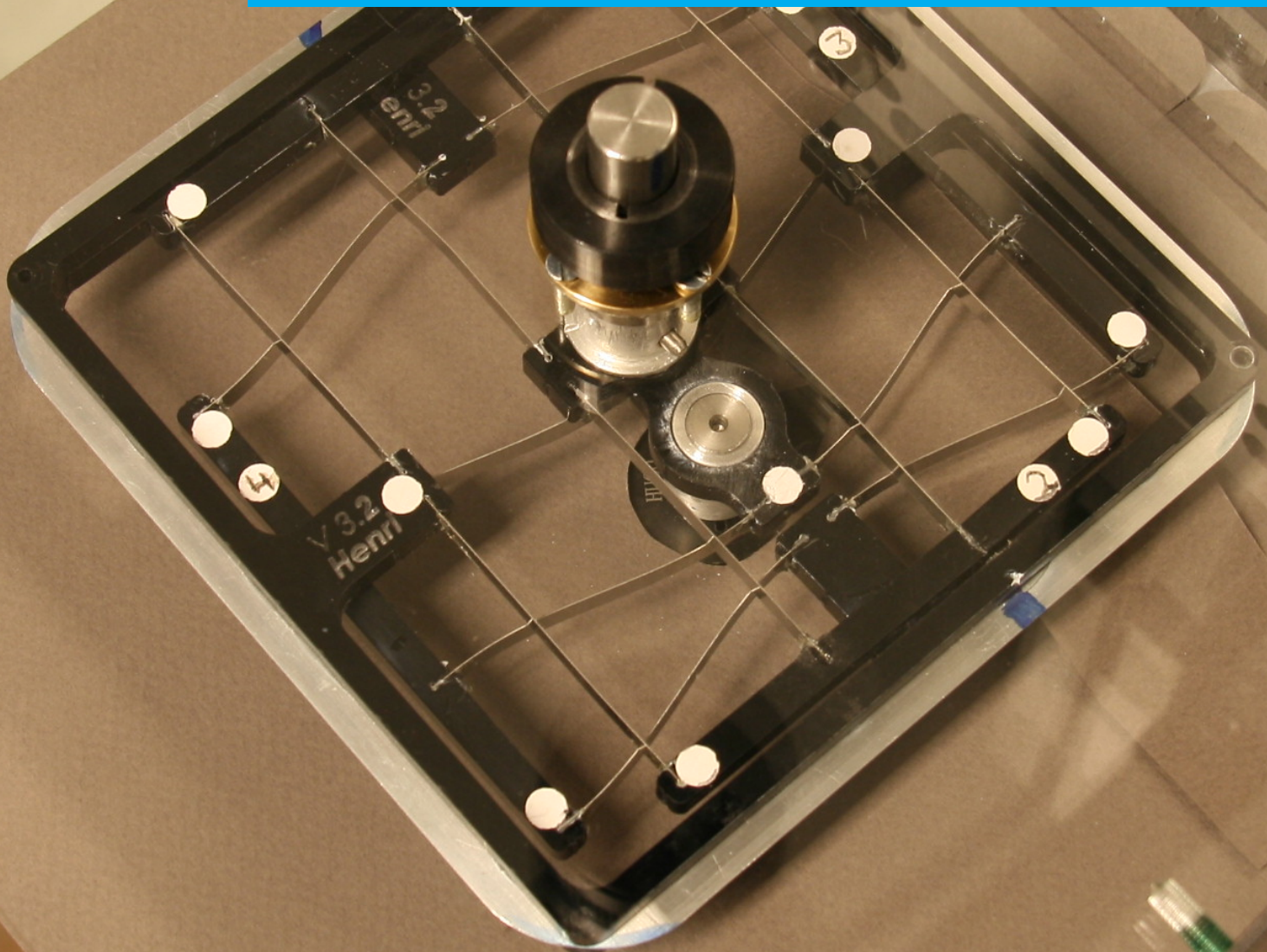


Department of Precision and Microsystems Engineering

The Dynamics of Compliant Rotational Power Transmissions

H.W. van der Deijl

Report no : 2018.010
Coach : Ir. D. Farhadi Machekposhti
Professor : Prof. dr. ir. J.L. Herder
Specialisation : Mechatronic System Design
Type of report : Master Thesis
Date : 25 May 2018



The Dynamics of Compliant Rotational Power Transmissions

by

H.W. van der Deijl

to obtain the degree of Master of Science
at the Delft University of Technology,
to be defended publicly on Friday May 25, 2018 at 11:00 AM.

Student number:	4163915	
Project duration:	December 1, 2016 – May 25, 2018	
Thesis committee:	Prof. dr. ir. J.L. Herder,	TU Delft, Chair
	Ir. D. Farhadi Machekposhti,	TU Delft, Supervisor
	Dr. ir. D. de Klerk,	TU Delft
	Dr. ir. A.L. Schwab,	TU Delft

An electronic version of this thesis is available at <http://repository.tudelft.nl/>.

Preface

The past seven years I have been working towards my degree in Engineering. I always knew that I wanted a career in engineering. Luckily, I did not regret my choice for a Bachelor and Master in Mechanical Engineering a single time. The combination of theory and practice is what I love about this study, and what I sought and found in my final thesis project. Hopefully, this thesis will be the successful closing of the past seven years.

Many people have supported me during my thesis project. First of all, I would like to thank my daily supervisor Davood, for all his support, feedback and enthusiasm. He has been a source of inspiration during the whole project. I would like to thank Just for his feedback and his fresh mind during the periodic meetings. I would like to thank Dennis for his great help with the experimental part of this project, as well as his overall support. Also, I would like to thank Arend Schwab and Paul van Woerkom for their advice on the dynamic modelling. Special thanks to Arend for joining the committee as the external member.

Furthermore, I would like to thank all the support staff. First of all thanks to Patrick, Harry, Rob and Spiridon, who were always available for lab support. Secondly, Wim, Gerard and René from the workshops, for their great advice and help during the manufacturing of the experimental setup and the prototypes. Furthermore, Rijk van Manen, with whom I took the first steps in designing and building the experimental setup.

Moreover, I would like to thank all fellow students from the office, who were a daily support for the past year. Special thanks to Martijn, not only for claiming half of my desk, but even more for being my graduation soul mate. And off course, thanks to my girlfriend and family, who had to cope with me during the whole project, and have been a great support. Finally, thanks to all others not mentioned who I have bothered during this project.

*Henri van der Deijl
Delft, May 2018*

Contents

1	Introduction	1
2	Paper: Dynamics of a Compliant Parallel Rotational Power Transmission	3
3	Discussion	21
4	Conclusion	23
A	Literature review towards the dynamic analysis of compliant rotational couplings	25
A.1	Introduction	25
A.2	Literature review	26
A.2.1	Kinematics of (conventional) rotational couplings.	26
A.2.2	Dynamics of conventional rotational couplings	30
A.2.3	Dynamics of compliant rotational couplings.	31
A.3	Results: potential failure chart	31
A.4	Conclusion	32
B	Finite Element Modal Analysis	35
B.1	Description of the model	35
B.1.1	Build up of the model	35
B.2	Ansys Mechanical APDL Code	37
B.3	Mode shapes	43
B.3.1	Zero axle misalignment - zero angle	44
B.3.2	20mm axle misalignment - zero angle	48
B.3.3	20mm axle misalignment - 45° angle.	51
B.3.4	20mm axle misalignment - 90° angle.	55
B.3.5	Check of multibody models - rigid support bodies.	58
C	Theoretical model	61
C.1	Description of the Oldham coupling	61
C.1.1	Conversion to a compliant design	62
C.1.2	Specific design used in the case study	62
C.2	Finding the equations of motion	64
C.2.1	Elastic deformations	64
C.2.2	Kinetic and potential energy	65
C.2.3	Lagrange.	66
C.2.4	Choice of generalised coordinates	66
C.3	Analysis of the equations of motion.	68
C.3.1	Radial balance	69
C.4	Modal analysis	69
C.4.1	Description of the results	71
C.4.2	Results	73
C.5	Time integration	80
C.5.1	Method	80
C.6	Time integration results.	82
C.6.1	5DOF model	82
C.6.2	17DOF model	88
C.6.3	Suggested improvements	94
C.7	Matlab code.	95

D	Experimental setup	111
D.1	Description of mechanical setup	111
D.2	Measurement of torsional vibration.	115
D.3	Measurement of planar motion	118
E	Orientation into Redesign	119
E.1	Introduction	119
E.2	Design requirements	119
E.3	Transmission between parallel axis: functional analysis.	119
E.4	Stiffness: prismatic compliant joints	120
E.4.1	Beam flexures	120
E.4.2	Flexure modules	120
E.4.3	Planar prismatic compliant joints using beam flexures	121
F	Reflection	127
	Bibliography	129

Introduction

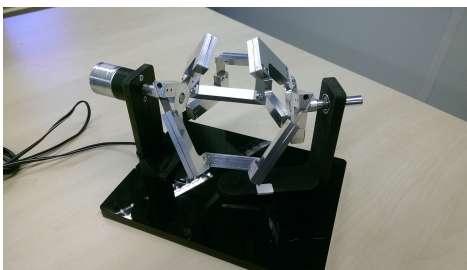
Compliant mechanisms transfer motion, force or energy by using elastic deformation of its flexure joints [3]. In conventional rigid-body mechanisms, motion is accomplished by rolling or sliding contacts between different rigid bodies. Compliant mechanisms have many advantages over conventional rigid-body mechanisms, such as the lack of friction, backlash, wear, need for lubrication and assembly. These benefits make them especially attractive for applications where precision and accuracy is needed.

Compliant mechanisms are primarily implemented for quasi-static applications. However, above benefits make them also attractive for applications where besides precision and accuracy, speed is desired. A specific example is a high-speed positioning stage in a cleanroom environment, or a pick-and-place robot in food industry. In these environments lubrication is undesired, and the monolithic nature of compliant mechanisms make them more suitable for cleaning with fluids.

However, the implementation of compliant mechanisms in dynamic applications is not always straightforward. Where conventional mechanisms have near zero on-axis and near infinite off-axis stiffness, compliant transmissions have nonzero on-axis stiffness and finite or even low off-axis stiffness. Often, this introduces lower resonance frequencies. Furthermore, the kinematics are less defined due to the off-axis compliance.

Despite their attractiveness, still little research has been done into the dynamics of compliant mechanisms. Only a view straightforward but unsophisticated analysis methods exist to analyse their dynamic behaviour. Common numerical methods such as finite element analysis can be used, but these are cumbersome and do not directly give the designer a clear insight in influential parameters. Furthermore, as a designer often desires certain kinematics, this wish is harder to fulfil when kinematics are ill defined. This all hinders the implementation of compliant mechanisms in dynamic applications.

A field of mechanisms in which dynamics cannot be neglected is that of rotational couplings. Here, a rotational coupling is defined as a mechanism which transfers rotational motion and power from one rotating body or shaft to another. The axis of rotation of both bodies are not collinear. Their misalignment can be



(a) Design of a compliant universal coupling for large misalignments from within the PME department [1]



(b) An industrial compliant coupling for small misalignments [2]

Figure 1.1: Examples of compliant rotational couplings

parallel as well as angular. The presence of inertial forces on the rotating bodies, even at steady motion, make this a specific dynamic application.

A branch of couplings in which compliance can be especially beneficial due to its lack of friction and backlash, is that of the constant velocity (CV) coupling. The goal of a CV coupling is to transfer the rotational motion one-to-one between the axis, without introducing a velocity error. Emergence of such an error can introduce vibrations and high stress levels, and is thus undesired. Common examples of CV couplings are the double Hooke coupling for angular misalignments, or the Oldham coupling for parallel misalignments.

At the department of Precision and Microsystem Engineering compliant versions of both examples given above were already designed. However, it was observed that these couplings do not perform well in a dynamic environment. Only low velocities can be achieved before yield or fracture would occur in internal members. Also, velocity error was expected due to internal resonances. To the authors knowledge, no compliant CV couplings for large misalignments, suitable for dynamic applications, yet exist.

As indicated earlier, little research has been done into the dynamics of compliant mechanisms. To the authors knowledge, no work at all exists about the dynamics of large misalignment compliant CV couplings.

The goal of this work is to fill in this knowledge gap. This is the first step towards the design of compliant rotational couplings for dynamic applications. The scope is narrowed down to the family of couplings with Oldham kinematics, suitable for parallel misalignment only. The movement of its centre of mass during operation makes it particularly interesting for dynamic analysis. Furthermore, a compliant Oldham design is available within the department already on which can be elaborated. Moreover, the planar design facilitates 2D analysis. In this work, its dynamic performance will be analysed, predicted, evaluated and optimized.

The to be found knowledge will improve the designer's understanding of the coupling's dynamics. Methods to predict and optimize the coupling's performance will be presented. This will ease the design process and make implementation more attractive. Moreover, this work can serve as a stepping stone for analysis of other compliant rotational couplings as well as an inspiration for the analysis of compliant mechanisms in general.

The main body of this thesis consists of the paper 'The Dynamics of a compliant parallel rotational power transmission'. This paper is to be submitted to Elsevier's journal of Mechanisms and Machine Theory. In this paper, the dynamics of the Oldham family of couplings is analysed and predicted. Also, a case study is executed for a specific design, for which performance is evaluated and optimized. This case study serves as a validation of the proposed analysis and prediction methods. Then, a discussion and conclusion for the whole thesis project will be given.

More detailed work can be found in the appendices. In appendix A, the above indicated knowledge gap was first indicated in a brief literature review, and potential dynamic problems within a compliant coupling where indicated. In appendix B the used ANSYS finite element model and its results are given. Then, in appendix C the proposed analysis method based on multibody dynamics is discussed elaborately. Some more detailed modelling results are given here as well. Furthermore, in appendix D the used experimental evaluation method is discussed. During this project a experimental testing setup was designed and built to evaluate the dynamic performance of any (compliant) rotational coupling. Moreover, in appendix E a first orientation into the redesign of a compliant Oldham coupling is given. Finally, a short reflection on the thesis project can be found in appendix F.

2

Paper: Dynamics of a Compliant Parallel Rotational Power Transmission

Dynamics of a compliant parallel rotational power transmission

Henri van der Deijl

H.W.vanderdeijl@planet.nl

Davood Farhadi Machekposhti

D.FarhadiMachekposhti@tudelft.nl

Dennis de Klerk

D.deKlerk@tudelft.nl

Just Herder

J.L.Herder@tudelft.nl

Precision and Microsystems Engineering
Delft University of Technology
Mekelweg 2
Delft, 2628 CD, The Netherlands

In this work, a first step is taken in the dynamic analysis of large misalignment compliant rotational couplings. For this, the dynamic performance of the family of compliant Oldham couplings is analysed and predicted. A straightforward generic analysis method for this family of couplings is proposed, based on multibody dynamics. Predictions can now be given of 1) the maximum attainable velocity before instability due to centrifugal forces occurs, 2) the lower resonance modes originating from the used flexure mechanisms, and 3) the characteristics of the resulting velocity error.

A case study is performed on an existing design within this family, validating the proposed modelling techniques. Its dynamic performance is evaluated experimentally and its failure mechanisms are indicated. Based on the gained knowledge, the design was optimized, expecting a 198% increase of its maximum velocity. This work facilitates the design and implementation of compliant Oldham couplings in dynamic applications.

1 Introduction

Compliant mechanisms have many advantages over conventional rigid-body mechanisms, such as the lack of friction, backlash, wear, need for lubrication and assembly. These benefits make them especially attractive for applications where precision and accuracy is needed, such as po-

sitional stages [1] or motion transmission. Several compliant universal joints already exist in the state of the art [2]. Machekposhti et al. proposed designs for compliant transmission mechanism between parallel [3], as shown in figure 1, and angular [4] axis, for applications where a precise rotational constant velocity (CV) transmission is needed.

However, the compliant nature of these transmissions often leads to dynamic problems, due to which most of these mechanisms are not yet applicable for dynamic applications in which considerable rotational speed is needed. Where conventional mechanisms have near zero on-axis and near infinite off-axis stiffness, compliant transmissions have nonzero on-axis stiffness and finite or even low off-axis stiffness. This can introduce dynamic problems and makes analysis more complicated. In the whole field of compliant mechanisms (with large deformation), little research has been done into their dynamic behaviour and overcoming dynamic problems.

Often, common finite element analysis (FEA) techniques are used for modelling, of which some examples are [5]. These methods are well understood and offer the use of many standard methods. However, modelling is cumbersome and does not lead to quick insight in influential design parameters.

Other work is based on the pseudo-rigid-body model (PRBM), in which flexures are represented as binary rigid links with torsional springs at the joints. Examples for four

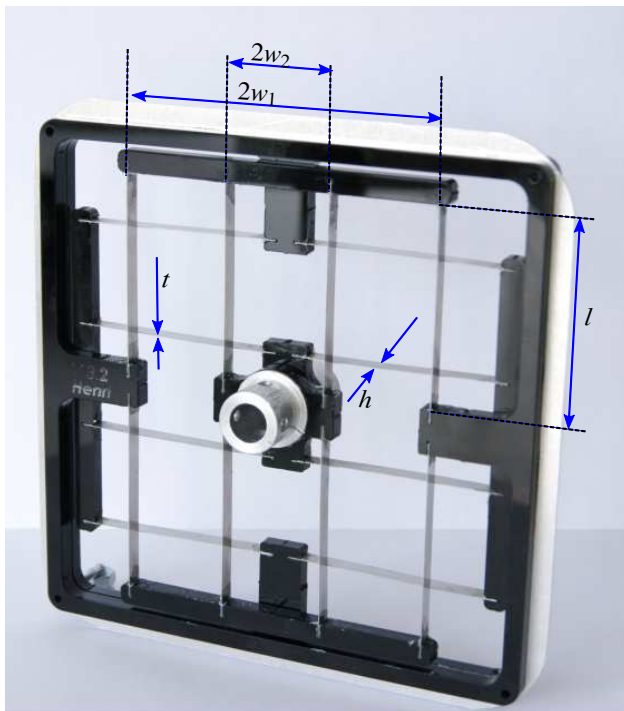


Fig. 1. Prototype of a compliant Oldham coupling as designed by Mashekpshiti, using two perpendicular DP-DP flexures.

bar linkages are [6] in which the PRBM is used directly, or [7] in which dynamic equivalents of flexure stiffness and inertia are implemented. This method is very straightforward, but as the rigid model still has only one degree of freedom (DOF), much of the dynamics is neglected and only one eigenfrequency can be predicted.

In the field of compliant rotational transmissions with large deformations particularly little research has been done. Flexible couplings for small angular or parallel misalignment such as bellow or flexible beam couplings [8] are already frequently used in industry, and some works are available about their dynamic performance and effect on connected rotor systems [9, 10, 11, 12, 13, 14].

However, the dynamics of flexure based CV couplings accommodating large misalignments is different due to among others significantly larger displacements, low off-axis stiffness and internal bodies suspended compliantly. To the authors knowledge, this family of couplings has not been studied yet. The lack of understanding of the dynamics hinders their implementation, despite the potential benefits mentioned. In this work a start is made in filling in this knowledge gap.

In this work, the dynamic performance of the family of Oldham-based constant velocity compliant transmissions between parallel rotational axis is analysed, predicted, evaluated and optimized in a generic way. For this first step in filling in the knowledge gap, this family is chosen as analysis can be done in the planar domain. Emphasis will lie on the motion transmission and the dynamic aspects of varying output loads is not studied. With the gained knowledge,

design and implementation will be facilitated. Furthermore, this work can be a starting point in the dynamic analysis of other families of rotational compliant couplings.

First, a generic modelling method is proposed to gain insight in the dynamics of an Oldham coupling using any type of internal compliant prismatic joints. Then, a case study of a specific design as suggested by Mashekpshiti [3] is given in which the results of the generic model will be compared with FEA and experimental results. In the discussion section design improvements for dynamic application are suggested.

2 Background

In figure 2 a kinematic representation of a rigid-body conventional Oldham coupling [15] can be seen (from here on 'coupling'). It has three movable bodies being the input axis with crank (2), the output axis with crank (4) and the coupler body (3). The coupler connects to both input and output via two perpendicular prismatic joints. Two fixed and fully rotating revolute joints connect the input and output axis to the ground (1) with a mutual distance of l_1 which is the parallel axle offset.

If the input (2) rotates through some angle, then both coupler (3) and output shaft (4) rotate through the same angle, making it a constant velocity coupling.

For a full cycle motion of the input link, the centre of the coupler (3) moves along the dotted circular path twice, with diameter l_1 and centre of rotation midway between input and output axis, at $l_1/2$.

Prismatic joints A conventional prismatic joint has one degree of freedom (1DOF) being linear translation. Neglecting friction, this translation motion direction is normally modelled as having zero stiffness. All other five directions form the degrees of constraint (5DOC). Assuming the two bodies are rigid, the 5DOC, also known as the bearing directions, can be seen as infinitely stiff.

In the case of the compliant Oldham coupling which uses compliant prismatic joints, these assumptions are no longer valid. Compliant mechanisms transfer motion, force or energy by using elastic deformation of its flexure joints [2]. Such a joint can thus be described by a stiffness in each direction, having a motion stiffness which should be orders of magnitude lower than the bearing stiffnesses. Especially for flexure based joints, non-constant and non-linear bearing stiffness are common which can be highly dependent on the motion direction displacement [16, 17].

3 Method

In this section, first dynamic performance criteria are defined. Then, the proposed analysis method is given. Based on this method, the performance prediction methodology is explained.

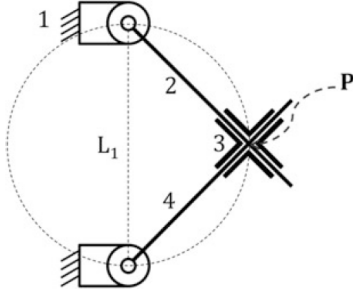


Fig. 2. Conventional rigid-body kinematics of an Oldham coupling [3].

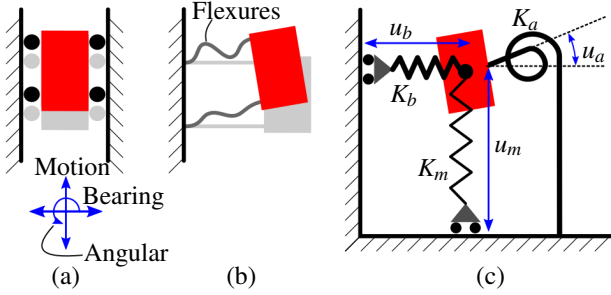


Fig. 3. Planar schematic of (a) a conventional rigid-body prismatic joint, (b) its compliant counterpart, (c) a PRBM of a compliant prismatic joint, indicating the decoupled stiffnesses K and displacements u in motion, bearing and angular direction, indexed with m , b and a respectively.

3.1 Dynamic performance criteria

To assess the performance of the coupling, two criteria are defined. As the objective of the coupling is to transfer motion between input and output one-to-one, the first criterion is the dimensionless velocity transfer error as defined by equation 1 ('velocity error'). The second criterion is the maximum operational velocity without permanently damaging the coupling ('operational limit').

$$\varepsilon_{\text{velocity}} = \frac{\omega_{\text{in}} - \omega_{\text{out}}}{\omega_{\text{in}}} \quad (1)$$

3.2 5DOF generic multibody model

Analysis in this work will be done in the planar domain, reducing a prismatic joint to one DOF in motion direction and two DOF in translational bearing and angular bearing directions. In figure 3 a planar schematic of both a conventional and compliant prismatic joint is given, together with a pseudo-rigid-body model.

Two of these joints in series and perpendicular form the Oldham coupling as will be studied in this work. The full cycle revolute joints of the input and output axles remain as conventional rigid-body revolute joints. In figure 4 a schematic representation of the coupling is given, which is the compliant counterpart of figure 2. The same three mov-

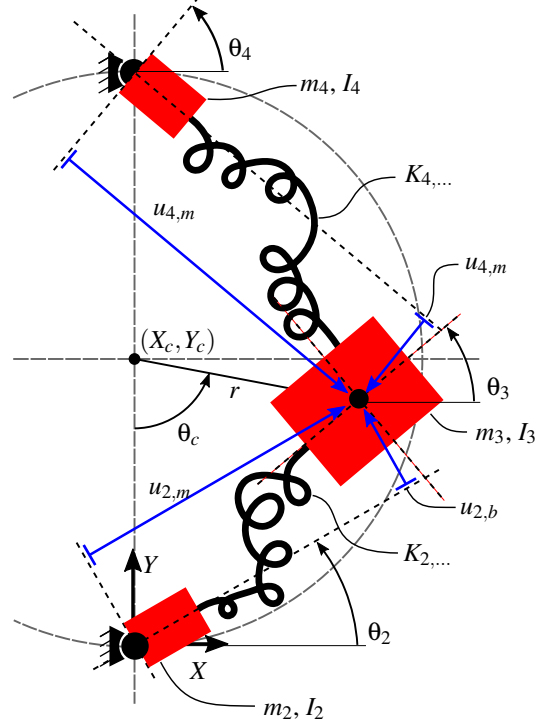


Fig. 4. Dynamic multibody model of a compliant Oldham coupling. The stiffnesses of both prismatic joints are symbolised by two randomly formed coil springs. Each of these consist of three decoupled stiffness directions as depicted in figure 3c. Translational deformations of these stiffnesses are depicted in blue. Rotational deformations are not depicted, but are simply the difference in body rotation. The three rigid bodies are depicted in red, with their centre of mass (COM) represented as a black dot. The dashed circle represents the path a rigid-body Oldham coupling will describe.

ing rigid bodies discussed earlier can be recognised, but are now connected elastically.

Based on figure 4 a planar parametric dynamic multibody model is built which is applicable to the whole family of compliant Oldham couplings.

The input axis is chosen as the origin of the inertial reference frame (X, Y) , with angles Θ measured counterclockwise from the positive X -axis. In this frame, the 3 · 3 body coordinates \mathbf{X} and their inertias \mathbf{M} are defined.

$$\mathbf{X} = [X_2, Y_2, \Theta_2, X_3, Y_3, \Theta_3, X_4, Y_4, \Theta_4]^T \quad (2)$$

$$\mathbf{M} = \text{diag}[m_2, m_2, I_2, m_3, m_3, I_3, m_4, m_4, I_4] \quad (3)$$

The two revolute joints (axle bearings) constrain the axles to $X_2 = Y_2 = X_4 = 0$ and $Y_4 = l_1$. Five DOF remain, being $[\Theta_2, X_3, Y_3, \Theta_3, \Theta_4]^T$. (X_c, Y_c) is the centre point of the circular path described by the coupler in the case of a rigid-body Oldham coupling. Due to the now finite stiffness in bearing directions, the coupler does not describe a perfect circle anymore.

To both axles, a reference frame (x_n, y_n) is connected, rotated with Θ_n , which defines the 'ground' of the two prismatic stages. The coupler link is the 'motion stage' for both. The two sets of three decoupled stiffnesses \mathbf{K} are deformed by elastic deformations \mathbf{u} . The subscripts give the corresponding 'ground' axle number followed by 'm' for motion direction, 'b' for translational bearing direction and 'a' for angular bearing direction, similar to figure 3. The deformations can be seen as projections of the coupler body coordinates on the two moving reference frames, resulting in the following (see also figure 4):

$$\mathbf{u} = [u_{2,m}, u_{2,b}, u_{2,a}, u_{4,b}, u_{4,m}, u_{4,a}]^T \quad (4)$$

$$= \begin{bmatrix} (X_3 - X_2) \cos \Theta_2 + (Y_3 - Y_2) \sin \Theta_2 \\ -(X_3 - X_2) \sin \Theta_2 + (Y_3 - Y_2) \cos \Theta_2 \\ \Theta_3 - \Theta_2 \\ -(X_4 - X_3) \cos(\Theta_4) - (Y_4 - Y_3) \sin(\Theta_4) \\ (X_4 - X_3) \sin(\Theta_4) - (Y_4 - Y_3) \cos(\Theta_4) \\ \Theta_4 - \Theta_3 \end{bmatrix} \quad (5)$$

$$\mathbf{K} = \text{diag}[K_{2,m}, K_{2,b}, K_{2,a}, K_{4,b}, K_{4,m}, K_{4,a}] \quad (6)$$

To describe the dynamic behaviour of the coupling, a set of generalised coordinates \mathbf{q} is chosen, in which the quasi-circular path of the coupler is described more naturally using polar coordinates r and θ_c .

$$\mathbf{q} = [\theta_2, \theta_c, r, \theta_3, \theta_4]^T \quad \text{with:} \quad (7)$$

$$\Theta_2 = \theta_2 \quad (8)$$

$$X_3 = X_c + r \sin(\theta_c) \quad (9)$$

$$Y_3 = Y_c - r \cos(\theta_c) \quad (10)$$

$$\Theta_3 = \theta_3 \quad (11)$$

$$\Theta_4 = \theta_4 \quad (12)$$

Forming the equations of motion Using the body coordinates \mathbf{X} and inertias \mathbf{M} the system's kinetic energy \mathcal{T} can be computed, as well as the potential energy \mathcal{V} using deformations \mathbf{u} and stiffnesses \mathbf{K} . The conservative equations of motion (EoM) are formed using the Lagrange equations as given below:

$$\frac{d}{dt} \left(\frac{\partial \mathcal{T}}{\partial \dot{\mathbf{q}}} \right) - \frac{\partial \mathcal{T}}{\partial \mathbf{q}} + \frac{\partial \mathcal{V}}{\partial \mathbf{q}} - \mathbf{Q}_s = \mathbf{0} \quad (13)$$

The first and last element of the forcing vector \mathbf{Q}_s represent the external torque at input and output axle respectively:

$$\mathbf{Q}_s = [T_{\text{in}}, 0, 0, 0, T_{\text{out}}]^T \quad (14)$$

Resulting in the five individual EoM:

$$I_2 \ddot{\theta}_2 + \frac{\partial V}{\partial \theta_2} - T_{\text{in}} = 0 \quad (15)$$

$$m_3 r^2 \ddot{\theta}_c + 2m_3 r \dot{r} \dot{\theta}_c + \frac{\partial V}{\partial \theta_c} = 0 \quad (16)$$

$$m_3 \ddot{r} - m_3 \dot{\theta}_c^2 r + \frac{\partial V}{\partial r} = 0 \quad (17)$$

$$I_3 \ddot{\theta}_3 + \frac{\partial V}{\partial \theta_3} = 0 \quad (18)$$

$$I_4 \ddot{\theta}_4 + \frac{\partial V}{\partial \theta_4} - T_{\text{out}} = 0 \quad (19)$$

In all equations, the first term represents an inertial force opposing acceleration in the specific direction. The partial derivatives of potential energy represent the elastic forces, as the stiffness profiles are still general. Equation 15, 18 and 19 describe the three body rotations, also showing an external torque in case of the axles. Equation 16 (unit torque) and 17 (unit force) describe the translation of the coupler. Due to the polar coordinate system, two more inertial forces arise as the second term, being the Coriolis and centrifugal force respectively for both equations.

3.3 Performance predictions

Based on the EoM, the effect of different parameters on the dynamic behaviour can already be observed. In specific, effective radial stiffness and velocity error content will be discussed.

Effective radial stiffness The effective stiffness in radial direction r of the coupler body during rotation equals the partial derivative of EoM 17 at steady motion when $\dot{r} = 0$. It consists of a positive elastic and negative inertial part resulting from centrifugal force and can be expressed as:

$$K_{\text{radial}} = K_{\text{radial,el}} - K_{\text{radial,cent}} \quad (20)$$

$$= \underbrace{\frac{\partial^2 \mathcal{V}}{\partial r^2}}_{\text{elastic}} - \underbrace{m_3 \dot{\theta}_c^2}_{\text{centrifugal}} \quad (21)$$

When the effective stiffness approaches zero or even becomes negative, r will grow boundlessly and instability will occur. In practice, significant increase of r can lead to internal parts of the prismatic joints interfering with each other or with the surrounding (support) structure, or flexure yield, ultimately leading to failure. Thus, for proper working of the coupling, $K_{\text{radial}} \gg 0$. Notice that the stiffness decreases with $\dot{\theta}_c^2$ (polar angle of path velocity) which is equal to $(2\dot{\theta}_2)^2$ (input axis velocity) during steady motion.

Constant elastic stiffness In the case of constant stiffness values and if $T_{\text{in}} + T_{\text{out}} = 0$ (constant system energy), steady

motion rotation can exist in the form of:

$$\dot{\mathbf{q}} = [\dot{\theta}_2, 2\dot{\theta}_2, 0, \dot{\theta}_2, \dot{\theta}_2]^T \quad (22)$$

Then, all inertial forces vanish except for the centrifugal force. For the input and output axle, the elastic components equilibrate the external torque. For the coupler body rotation and polar angle the net elastic force is zero. In radial direction, the centrifugal force equilibrates the elastic force. If both compliant prismatic joints have an equal set of stiffness profiles, K_{radial} simplifies as given below, with which also the constant radius r for steady motion as function of velocity can be formulated:

$$K_{\text{radial,constant}} = K_m + K_b - m_3 \dot{\theta}_c^2 \quad (23)$$

$$r = \frac{(K_m + K_b)r_0}{(K_m + K_b) - m_3 \dot{\theta}_c^2} \quad (24)$$

In this again $\dot{\theta}_c^2 = (2\dot{\theta}_2)^2$, and r_0 is the radius at static equilibrium. In the last equation, it can be clearly seen that r goes to infinity when the denominator (radial stiffness) goes to zero.

Non-constant elastic stiffness When the stiffness profiles are non-constant and state dependent, steady motion rotation does not always exist. When K_{radial} is not constant, this results in a oscillating radius during rotation. This also makes the point of zero stiffness dependent on the state (system angles for example), and it will first occur at the minimum of $K_{\text{radial,el}}$.

Radius change \dot{r} will result in a Coriolis force in θ_c -direction (equation 16), which in turn, together with possible changes in the tangential elastic component $\partial \mathcal{V} / \partial \theta_c$, leads to a non-constant tangential velocity $\dot{\theta}_c$. Peaks in $\dot{\theta}_c$ can lead to peaks in centrifugal force and zero radial stiffness at an input axle velocity lower than expected based on the equations for steady motion.

Velocity error frequency content Resonance modes containing rotation of the output axle θ_4 can, if excited, contribute to the velocity error (equation 1). Two rotational resonance modes can be estimated using the rotational stiffness of each compliant prismatic joint, being the one at input side combined with inertias I_3 and I_4 (equation 25) and the one at output side with inertia I_4 (equation 26). For this, the input axle is seen as the fixed world. When the angular stiffness $K_{n,a}$ is non-constant, these frequencies can also be dependent on the state of the system. Note that output inertia I_4 not only consists of the output link and axle, but also of the inertia load of the coupling in application, which thus influences these frequencies.

$$f_{\text{rot, input side}} = \frac{1}{2\pi} \sqrt{\frac{K_{2,a}}{I_3 + I_4}} \quad (25)$$

$$f_{\text{rot, output side}} = \frac{1}{2\pi} \sqrt{\frac{K_{4,a}}{I_4}} \quad (26)$$

3.4 Modal analysis

In order to gain insight in the resonance frequencies and stability of the system at certain rotational velocities, a modal analysis can be done at several steady motion equilibrium configurations. The input axis angle θ_2 and velocity $\dot{\theta}_2$ are prescribed resulting in a 4DOF system, in order to remove the else arising rigid body mode. For simplicity, the external forcing \mathbf{Q}_s is neglected, no damping is applied. At the prescribed conditions for θ_2 and $\dot{\theta}_2$, a numerical approximation of the equilibrium configuration is found using a Newton-Raphson scheme starting from an initial guess and iterating to a steady motion point for which $\ddot{\mathbf{q}} = \mathbf{0}$, $\dot{\mathbf{q}} = \dot{\mathbf{q}}_{\text{eq}}$, $\mathbf{q} = \mathbf{q}_{\text{eq}}$. Notice that in the case of non-constant stiffness this equilibrium is only valid at this specific point, and will change with changing stiffness.

Around the equilibrium configuration, the linearised system matrices can be built:

$$\mathbf{K} = \left. \frac{\partial(\mathbf{f}_\mathcal{V} + \mathbf{f}_\mathcal{T})}{\partial \mathbf{q}} \right|_{\substack{\mathbf{q}=\mathbf{q}_{\text{eq}} \\ \dot{\mathbf{q}}=\dot{\mathbf{q}}_{\text{eq}} \\ \ddot{\mathbf{q}}=\mathbf{0}}} \quad (27)$$

$$\mathbf{C} = \left. \frac{\partial \mathbf{f}_\mathcal{T}}{\partial \dot{\mathbf{q}}} \right|_{\substack{\mathbf{q}=\mathbf{q}_{\text{eq}} \\ \dot{\mathbf{q}}=\dot{\mathbf{q}}_{\text{eq}} \\ \ddot{\mathbf{q}}=\mathbf{0}}} \quad (28)$$

$$\mathbf{M} = \left. \frac{\partial \mathbf{f}_\mathcal{T}}{\partial \ddot{\mathbf{q}}} \right|_{\substack{\mathbf{q}=\mathbf{q}_{\text{eq}} \\ \dot{\mathbf{q}}=\dot{\mathbf{q}}_{\text{eq}} \\ \ddot{\mathbf{q}}=\mathbf{0}}} \quad (29)$$

resulting in the linearised EoM with respect to the linearisation point:

$$\mathbf{M}\ddot{\mathbf{q}} + \mathbf{C}\dot{\mathbf{q}} + \mathbf{K}\mathbf{q} = \mathbf{0} \quad (30)$$

$$\mathbf{q} = \mathbf{q}_{\text{eq}} + \tilde{\mathbf{q}}, \quad \dot{\mathbf{q}} = \dot{\mathbf{q}}_{\text{eq}} + \dot{\tilde{\mathbf{q}}} \quad (31)$$

The four second order differential equations of equation 30 can be written as a set of eight first order equations 32 as given by [18], using state vector \mathbf{z} and system matrices \mathbf{A} and \mathbf{B} .

$$\tilde{\mathbf{A}}\dot{\mathbf{z}} + \tilde{\mathbf{B}}\mathbf{z} = \mathbf{0} \quad \text{with:} \quad (32)$$

$$\tilde{\mathbf{A}} = \begin{bmatrix} \mathbf{M} & \mathbf{0} \\ \mathbf{0} & \mathbf{K} \end{bmatrix}, \quad \tilde{\mathbf{B}} = \begin{bmatrix} \mathbf{C} & \mathbf{K} \\ -\mathbf{K} & \mathbf{0} \end{bmatrix} \quad (33)$$

The eigenvalue problem 34 can then be formed with $\boldsymbol{\lambda}$ being the roots and \mathbf{V} the matrix of eigenvectors, which could be solved numerically:

$$\boldsymbol{\lambda} \tilde{\mathbf{A}} \mathbf{V} = -\tilde{\mathbf{B}} \mathbf{V} \quad (34)$$

The mode shapes can then be represented in the original generalised coordinates \mathbf{q} , being the sum of the found modes and

the linearisation point:

$$\mathbf{z} = \begin{bmatrix} \Delta \dot{\mathbf{q}} \\ \Delta \mathbf{q} \end{bmatrix} = \mathbf{V} e^{\lambda t} = \mathbf{V} \left(e^{\Re(\lambda)t} \cdot e^{\Im(\lambda) i t} \right) \quad (35)$$

$$= \mathbf{V} \left(e^{\Re(\lambda)t} (\cos \Im(\lambda)t + i \sin \Im(\lambda)t) \right) \quad (36)$$

$$\begin{bmatrix} \dot{\mathbf{q}} \\ \mathbf{q} \end{bmatrix} = \begin{bmatrix} \Delta \dot{\mathbf{q}} \\ \Delta \mathbf{q} \end{bmatrix} + \begin{bmatrix} \dot{\mathbf{q}}_{\text{eq}} \\ \mathbf{q}_{\text{eq}} \end{bmatrix} \quad (37)$$

For the conservative system without damping, the imaginary part of a λ at a certain linearisation point gives the resonance frequencies of the system. A positive real part of λ indicates instability of the coupling and results in an exponentially growing (unbounded) motion, as for example at the point of zero effective radial stiffness.

3.5 Time integration

The found EoM can be integrated in time to get insight in the motion of the different bodies during rotation. With this, also the velocity error can be computed. Explicit numerical ordinary differential equation solvers can be used, for which the EoM often need to be written as two sets of first order equations. As a time step a value smaller than the period time of the highest eigenfrequency should be used. Integration can become unstable due to build-up of numerical errors or approach of instability points such as the zero radial stiffness point at higher velocities. Some damping can be added to the system to overcome this. A straightforward damping model is proportional or Rayleigh damping where the damping matrix is a function of stiffness and mass, in which α and β are scalar constants of proportionality:

$$\mathbf{C}_{\text{int}} = \alpha \mathbf{M} + \beta \mathbf{K} \quad (38)$$

This can be further simplified by only taking the diagonal terms of \mathbf{M} and \mathbf{K} , which eliminates coupling between the coordinates via the damping matrix. The proportionality constants are often determined empirically [19] or just tuned until integration is stable. The resulting damping ratio can be evaluated as a function of resonance frequencies using:

$$\zeta = \frac{1}{2} \left(\frac{\alpha}{\omega_n} + \beta \omega_n \right) \quad (39)$$

As a comparison, empirical damping ratios for flexure mechanisms can be found in for example [6].

As initial conditions for integration, static of steady motion equilibria can be used, which can be found using a Newton-Raphson iteration scheme.

4 Results: case study of the DP-DP design

In this section, a case study is shown of a specific compliant Oldham coupling design based on [3] as an example of

the suggested modelling method. The goal is firstly to validate the proposed analysis and prediction method and secondly to evaluate the dynamic performance of this specific design. In this section, only results will be given; further interpretation can be found in the discussion section.

First, the used compliant prismatic joints and overall design implementation are described. Then, an extension of the proposed modelling method is given for this specific design. Moreover, the used experimental setup is described. Furthermore, results from the multibody model, FEA and experiment are given and compared. The results are firstly categorised by the scenarios of zero and maximum axle misalignment, and secondly by the dynamic performance criteria.

4.1 Compliant design

The design is based on [3] as depicted in figure 1 which uses two DP-DP compliant prismatic joints [17,16] and is designed for a maximum parallel axle misalignment of 20 mm.

In one DP-DP layer, flexures connect the axle bodies, via two intermediate bodies (from here on 'shuttles'), to the coupler body. All bodies are made from PMMA and are seen as rigid in the multibody model. Design parameters are depicted in figure 1 and scalar values are given in table 1. The degree of compliance distribution $a_0 = 1/2$ is considered for the flexures (distributed compliance). AISI316L stainless steel is used as flexure material with Young's modulus $E = 193$ GPa, glued into slits in the PMMA bodies. An aluminum sheet metal ring is glued between the two DP-DP layers to increase resonance frequencies within/stiffness of the coupler body, as we are interested in the dynamics of the flexure mechanism only, not in the dynamics of the supporting bodies.

In equation 41, 40 and 42 the stiffness formulation of the DP-DP prismatic joints is given in motion, bearing and angular direction respectively [17]. As can be seen, the bearing and angular stiffness depend on motion deformation u_m squared. For zero misalignment no motion direction deformation is present and as a result all stiffness values are constant, if deformation due to dynamics is neglected.

Table 1. Design parameters.

l [mm]	h [mm]	t [mm]	w_1 [mm]	w_2 [mm]
50	5	0.2	14	28

$$K_m = \frac{2EI}{l^3} k_{11}^0 \quad (40)$$

$$K_b = \frac{2EI}{l^3} \frac{k_{33}}{\left(1 + k_{33} \left(g_{11}^{(1)} + \frac{(k_{11}^{(1)})^2}{k_{11}^{(0)}}\right) \left(\frac{u_m}{2l}\right)^2\right)} \quad (41)$$

$$K_\theta = \frac{2EI}{l^3} \frac{4w_1^2 w_2^2}{(w_1^2 + w_2^2)} \frac{k_{33}}{\left(1 + k_{33} g_{11}^{(1)} \left(\frac{u_m}{2l}\right)^2\right)} \quad (42)$$

where:

$$k_{11}^{(0)} = \frac{6}{(3 - 6a_0 + 4a_0^2)a_0} \quad (43)$$

$$k_{11}^{(1)} = \frac{3(15 - 50a_0 + 60a_0^2 - 24a_0^3)}{(3 - 6a_0 + 4a_0^2)a_0} \quad (44)$$

$$g_{11}^{(1)} = \frac{2a_0^3(105 - 630a_0 + 1440a_0^2 - 1480a_0^3 + 576a_0^4)}{175(3 - 6a_0 + 4a_0^2)} \quad (45)$$

$$k_{33} = \frac{6l^2}{a_0 t^2} \quad (46)$$

$$I = \frac{ht^3}{12} \quad (47)$$

4.2 Evaluation method

Below, parameters are given for the suggested 5DOF model, and an extension to a 17DOF model is given for this specific compliant design.

4.2.1 Multibody model

The above discussed stiffness formulation of the DP-DP prismatic joint can be used directly in the proposed 5DOF model. In table 2 the used inertia values are given, which match input and output axle inertia of the experimental setup. Furthermore, the shuttle and flexure inertia is distributed over the coupler and axis bodies equally, as the shuttle bodies are not modelled.

Extension to 17DOF model Especially for zero deformation in motion direction, the four shuttles are underconstraint and encounter low stiffness in plane, perpendicular to the flexures. As for ease of implementation of any prismatic joint, the generic 5DOF model only uses the stiffness profiles of the entire joints. The dynamics of internal masses such as the shuttles are neglected however. As an comparison, an extended model is proposed incorporating the dynamics of these shuttles. For this all four shuttles s_i ($i = 1 \dots 4$) are modelled as a rigid body with planar freedoms $X_{s,i}, Y_{s,i}, \Theta_{s,i}$, adding $4 \cdot 3 = 12$ freedoms, resulting in a 17DOF model.

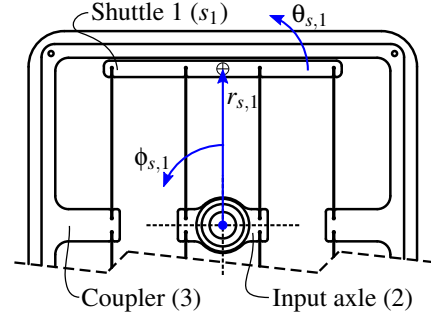


Fig. 5. Generalised coordinates of a shuttle body as used in the 17DOF model, for one shuttle of one DP-DP layer.

Similar to the coupler body, the shuttle centres of mass can also be described in polar coordinates $\phi_{s,i}, r_{s,i}$, with as the origin the axle connected to that specific layer. In figure 5 one shuttle and its generalised coordinates is depicted.

As can be seen in figure 5, four beam flexures are connected to each shuttle; two towards the axle and two towards the coupler body. Each pair can be modelled as a parallelogram flexure system (P-flexure). The stiffness profiles of such a P-flexure as given by [17] are used. Stiffnesses in motion, bearing and angular direction are given in equation 48, 48 and 50 respectively.

$$K_m = \frac{2EI}{l^3} k_{11}^0 \quad (48)$$

$$K_b = \frac{2EI}{l^3} \frac{k_{33}}{\left(1 + k_{33} g_{11}^{(1)} \left(\frac{u_m}{2l}\right)^2\right)} \quad (49)$$

$$K_\theta = \frac{2EI}{l^3} w^2 \frac{k_{33}}{\left(1 + k_{33} g_{11}^{(1)} \left(\frac{u_m}{2l}\right)^2\right)} \quad (50)$$

Parameters $E, I, l, k_{11}^{(0)}, k_{11}^{(1)}, k_{33}$ and $g_{11}^{(1)}$ remain as stated before. The parameter w is the distance between the two flexures of each P-flexure. For the inner pair $w = w_1$, for the outer $w = w_2$, as given in table 1. In total, the four shuttles with each two P-flexures results in $4 \cdot 2 \cdot 3 = 24$ stiffness and deformation terms. Inertia values for each body are given in table 2, for which shuttle inertia obviously is no longer distributed over the coupler and axle bodies.

Using the P-flexure stiffness formulation, a problem arises as due to the decoupling of the three stiffness direction in one parallelogram flexure, displacement in motion direction will not lead to displacement in bearing direction. Flexure arclength then is not conserved. A modelling improvement can be made by enforcing the pseudo-rigid-body kinematics of a fixed-guided beam as given by Howell [20]. Then, the bearing direction displacement is a function of the motion direction displacement (equation 51 and figure 6), using $\gamma = 0.8517$.

Table 2. Body inertias.

	$I_2[\text{kgm}^2]$	$m_3[\text{kg}]$	$I_3[\text{kgm}^2]$	$I_4[\text{kgm}^2]$	$m_{s,i}[\text{kg}]$	$I_{s,i}[\text{kgm}^2]$
5DOF	1.6032×10^{-3}	5.4047×10^{-2}	2.7358×10^{-4}	5.4502×10^{-6}	-	-
17DOF	1.6032×10^{-3}	4.5992×10^{-2}	2.3677×10^{-4}	5.4502×10^{-6}	4.0273×10^{-3}	1.2925×10^{-5}

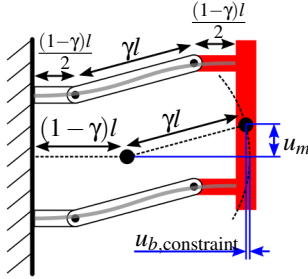


Fig. 6. PRBM of two fixed-guided beams as given by [20] forming a prismatic joint, showing the kinematics leading to the bearing direction displacement for motion direction displacement.

$$u_{b,\text{constraint}} = \gamma l - \sqrt{(\gamma l)^2 - u_m^2} \quad (51)$$

This constraint can be enforced via the deformation expression \mathbf{u} by adding the relative bearing displacement from the constraint $u_{b,\text{constraint}}$ to the original bearing displacement u_b :

$$u_b^* = u_b + u_{b,\text{constraint}} \quad (52)$$

This way, bearing direction stiffness is felt when deviating from the PRBM kinematics, but deviation still is possible.

Matching the experimental setup To be able to compare the multibody model results with the experiments, the bearing frictions on both input and output axles are modelled as linear increasing with velocity. Two constant friction torques are added to the forcing vector \mathbf{Q}_s . Two velocity depended torques are implemented via a second damping matrix \mathbf{C}_{ext} with only two non-zero terms, on the diagonal, for $\dot{\theta}_2$ and $\dot{\theta}_4$. Those four parameters are then estimated by calculating the motor torque using its motor constants and the measured current for two reference measurement. The first is done by accelerating the input axle only, disconnected from coupling and output axle, giving the input side parameters. In the second, the coupling is reconnected and the whole system is accelerated. Subtracting the first friction torques from the latter gives the output parameters.

4.2.2 Finite element analysis

The described multibody modal analysis does not contain elastic deformation of the coupling's bodies. To assess the multibody models and to find potential elastic body

modes, a finite element analysis is executed using ANSYS APDL. All bodies and flexures are modelled using BEAM188 elements and the two DP-DP layers are connected together using MPC184 constraint elements. The output axle inertia is added matching the setup using MASS21. All beam flexures are divided in 50 elements, the bodies are modelled with an element length of 2 mm. A perturbed modal analysis is done for multiple coupling angles and axle misalignments. Only relevant results will be discussed.

4.2.3 Experimental setup

An experimental setup is built to study the dynamic behaviour of the coupling during rotation, as depicted in figure 7. The input and output axles are guided by conventional bearings. The upper (output) bearing and support structure can be translated horizontally to apply axle misalignment.

To study the velocity error, Baumer EIL580P incremental optical encoders are connected to both axles giving 2048 pulses as well as a single reference pulse per rotation. Furthermore, motor current and voltage is measured with which motor torque can be estimated.

To get insight in the planar motion during rotation, an IDT NX4S1 high speed camera system is used. White marker points on the bodies of the coupling (figure 7) are tracked during motion using IDT Motion Studio.

Reference measurement To identify possible setup resonances, a reference measurement is done using a Huco stainless steel 34 mm OD bellow coupling instead of the compliant coupling, at zero axle misalignment. The frequency content of the velocity error is shown in a Campbell diagram in figure 8. The diagonal lines of increased amplitude starting from the origin represent excitations being the n th multiple of the rotational frequency (n th order). Dominant orders 1 (unbalance), 2 (misalignment), and multiples of 8 (8-pole DC motor) can be indicated. Resonance frequencies will appear as vertical lines, of which one can be seen around 980 Hz. Hand calculation of the output axle inertia oscillating in the angular stiffness of the bellow coupling yields a frequency of circa 2100 Hz. Coupling and output axle inertia oscillating in the angular stiffness of the whole input axle yields a frequency of circa 1110 Hz. It is expected that the experimentally found frequency is a combination of bellow coupling and axle stiffness and inertias. All other resonances found in the next measurements can be allocated to the coupling prototype or its effect on the setup.

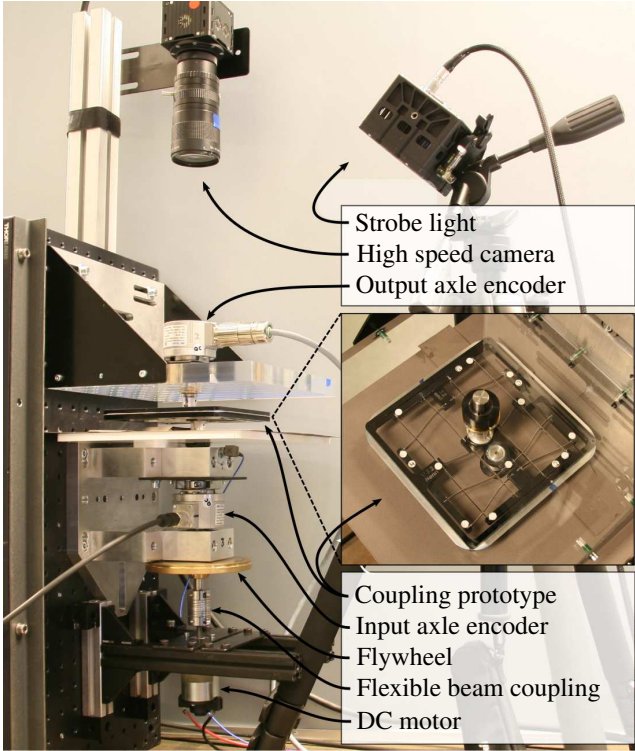


Fig. 7. Measurement setup used for the experimental evaluation. The input axle is driven by a Crozet 82 800 0 brushed DC motor, coupled by an aluminum flexible beam coupling. To the input axle a flywheel is fixed to smoothen the input velocity. For sensor data acquisition and analysis a Müller-BBM PAK system is used. The camera has a perpendicular view on the coupling, through the transparent upper axle support structure. A resolution of 1024×1024 of a 300mm area yields a measuring resolution of circa 0.3mm, at 1000 frames per second.

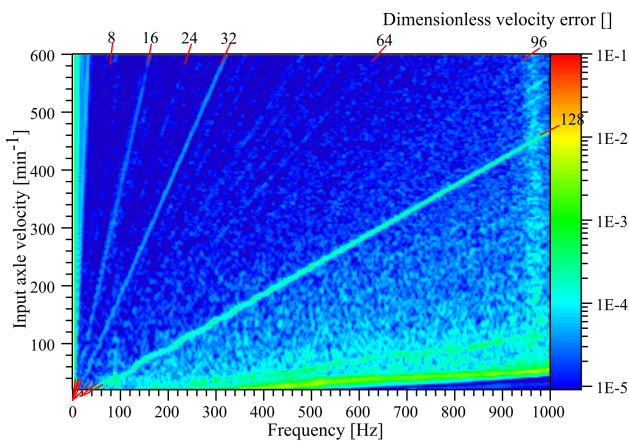


Fig. 8. Campbell diagram of the velocity error frequency content for a ramp up in rotational velocity of the industrial bellow coupling, with zero axle misalignment. The colour indicates the velocity error amplitude.

4.3 Evaluation results

In this section, evaluation results are given, divided in two operational scenarios; at zero and at maximum (20 mm) axle misalignment. For both scenarios, the coupling's resonance modes are discussed first, which characterise its behaviour. Then, results for the two performance criteria being velocity error $\epsilon_{\text{velocity}}$ and the operational limit velocity, are given for the multibody model, FEA and experiment.

4.3.1 Zero axle misalignment

As with zero axle misalignment the compliant prismatic joints remain undeformed during rotation, the stiffness and thus resonance frequencies do not depend on the input axle angle.

Mode shapes In this section, the first eight resonance modes resulting from the 17DOF multibody model are discussed. These are compared with the 5DOF model and FEA. In table 3 the frequencies resulting from each are given.

In the 17DOF model, the first four modes originate from the low stiffness of the shuttles along their length axis. The mode shape does not contain output axle rotation, and are thus not expected to have a significant contribution to the velocity error. The FEA yields a similar result. In the 5DOF model the intermediate shuttles are not modelled individually.

Around 490 Hz a rotational mode of the coupler body and output axle is found, in which both oscillate in the angular stiffness of the input side DP-DP layer. The 5DOF model yields similar results, as does equation 25. However, the FEA gives a mode shape containing similar input layer angular deflection at 89 Hz already. Here, significant deformation of the intermediate shuttles is present as well, resulting in a much lower frequency. It is expected that this mode contributes significantly to the velocity error, as the output axle rotation is significant in this shape.

Translational oscillation of the coupler body in two directions occurs around 2000 Hz in the 17DOF model. The 5DOF model yields somewhat lower frequencies. These modes contain the radial motion of the coupler body, which becomes unbounded at zero effective radial stiffness. In the FEA only the first 50 modes reaching to circa 1 kHz are analysed. Several (translational) modes at lower frequencies are present resulting from body deformations.

The 17DOF model gives oscillation of the output axle in the angular stiffness of the output DP-DP layer at 4460 Hz, being significantly higher than the first rotational mode as $I_4 \ll I_3$ for this setup. Again, the 5DOF model yields a somewhat lower frequency, as well as Equation 26.

These higher frequency flexure modes are not expected to contribute significantly to the velocity error due to internal damping and bearing friction. Furthermore, the FEA yields many resonance modes below 1 kHz already, which thus also contain body deformations. Two of those are expected to contribute to the velocity error due to a significant output axle rotation, and are given in the last two rows of table 3.

Table 3. Resonance frequencies of the coupling for zero axle misalignment at standstill, as computed with different models. The mode number of the specific model is indicated with a '#'. Furthermore, in the last column resonance frequencies as found in the experiment are given together with an error relative to the FEA results.

Mode description and frequency [Hz]	Multibody model		Eq. 25, 26	FEA	Experimental
	17DOF	5DOF			
Modes originating from flexure deformation					
Shuttle translation	39 (#1-4)	-	-	39.7-40.7 (#1-4)	39 (-3%)
Output and coupler rotation (I_3 and I_4)	494 (#5)	496 (#5)	488	89 (#7)	92 (+3%)
Coupler translation	2011 (#6-7)	1897 (#2-3)	-	-	-
Output rotation (I_4)	4460 (#8)	3584 (#4)	4240	-	-
Modes originating from deformation of both flexure and supporting bodies					
Output rotation due to coupler, intermediate shuttle and flexure bending	Elastic body deformation is not incorporated in the multibody models.			356 (#18)	327 (-9%), 365 (+3%)
Output rotation due to output layer intermediate shuttles and flexure bending (I_4 ?)				751 (#45)	832 (+11%)

Velocity error In figure 9 the experimental frequency content of the velocity error is given for a ramp up of the compliant joint from standstill to 600 min^{-1} . Apart from the engine orders, five resonance frequencies can be distinguished as vertical bands at a constant frequency, with different amplitudes. Frequency values are given in table 3 including the relative difference with respect to adjacent FEA results.

The first resonance at 39 Hz matches with the translational shuttle modes from table 3, which was not expected to introduce a significant velocity error however. The second resonance matches the 7th FEA mode, which was indeed expected to be dominant in the velocity error. The third and fourth resonance are close to FEA mode 18, the fifth resonance is closest to FEA mode 45, but all three with a significant difference.

Operational limit For zero axle misalignment, a velocity of circa 800 min^{-1} is reached in the experiments without failure. The operational limit thus is not identified, but exceeds this value.

Without axle misalignment, in theory the COM of the coupler body remains in line with both input and output axle during rotation. There thus is no nett centrifugal force which can give a negative contribution to the radial stiffness. However, due to manufacturing tolerances the coupler body COM can be slightly off-centre. The bearing stiffness of the DP-DP flexures in undeformed case is more than three orders of magnitude larger than at its maximum deflection of 20 mm. Even if the coupler COM will be off centre due to manufacturing tolerances, it is not likely that the decrease in radial

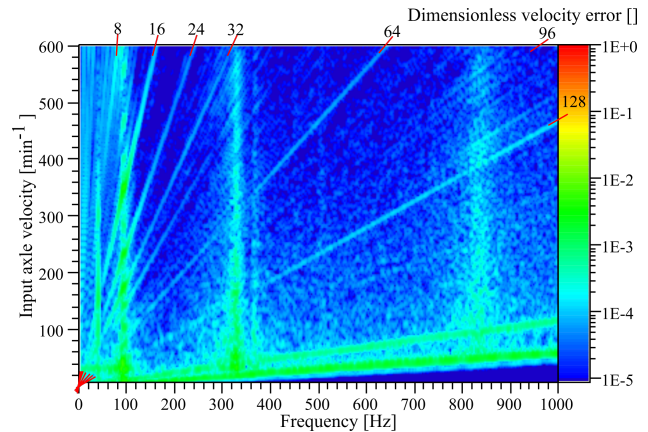


Fig. 9. Campbell diagram of the velocity error frequency content for a ramp up in rotational velocity of the compliant coupling, with zero axle misalignment. The color indicates the velocity error amplitude.

stiffness will determine the operational limit.

Looking at the mode shapes, the first resonance occurs at circa 40 Hz. It was observed that this frequency increased in amplitude at intersection with the 8th order excitation coming from the DC motor. It is expected that at intersection with the stronger second order at around 1200 min^{-1} this resonance can lead to failure.

4.3.2 Maximum axle misalignment

For the case of $l_1 = 20 \text{ mm}$ axle misalignment, the deformation in motion direction u_m of each prismatic joint varies

sinusoidally every rotation with an amplitude of l_1 and a phase difference of 90° between the two joints. Bearing and angular stiffness depend on motion deformation u_m squared, and thus vary with an periodicity of half a revolution of the coupling. As a result, resonance frequencies now change dramatically with the input axle angle.

Mode shapes First, resonance modes at standstill will be discussed (solid lines in figure 10), after which modes which significantly change with velocity are given (dashed lines in figure 10). In the upper graph of figure 10 the first five resonance frequencies resulting from the 17DOF modal analysis are given for varying input axle angles at standstill. This frequency path is passed through twice per rotation. At zero input angle, the first four resonance shapes are again originating from the low stiffness of the intermediate shuttles along their length axis. At that point, one DP-DP layer is undeformed resulting in two shuttle modes at 39 Hz similar to the zero axle misalignment case. The other layer however is deformed by the maximum 20 mm, resulting in two modes; the shuttles moving in opposite direction at 360 Hz and in equal direction at 25 Hz. The latter also contains motion direction deformation of the other DP-DP layer, resulting in a tangential motion of the coupler body with respect to its circular path. From zero up to 90 degrees input angle, the deformation is gradually transferred from one to the other DP-DP layer interchanging the frequencies.

A static FEA modal analysis is done at 0° , 45° and 90° , of which the results are given in the upper graph of figure 10 as marker points. For the first two modes, results are close to the 17DOF model. The third and fourth mode are close as well at their minima, at their maxima similar mode shapes cannot be found unambiguously however.

In the lower graph the first three modes of the 5DOF model are shown. The lowest frequency represents the same tangential coupler motion as that of the 17DOF model. The second mode represents radial coupler body motion, and the third rotational motion as discussed in the next alinea.

The rotational mode of I_3 and I_4 oscillating in the angular stiffness of the input side DP-DP layer is found at 488 Hz for zero input angle for the 17DOF model. As this angular stiffness decreases with motion direction deformation, the frequency drops to 75 Hz at 90 degrees when the first layer is totally deflected. The 5DOF yields a similar frequency, being the third frequency line at zero angle. The extrema of this resonance frequency also result from equation 25 for the extreme stiffness values: $75 \text{ Hz} \leq f_{\text{rot, input side}} \leq 494 \text{ Hz}$. The FEA however gives significantly lower values ($62 \text{ Hz} \leq f_{\text{rot, FEA}} \leq 87 \text{ Hz}$) for this mode as was already observed in the zero misalignment scenario, as body deformations also contribute to this mode. However, the FEA frequency also shows a minimum at 90° .

Similar to the zero misalignment scenario, two other modes with a significant output axle rotation contribution are found in the FEA; 330 Hz and 470 Hz at zero angle, 304 Hz and 741 Hz at 90° .

Some modes furthermore depend on the rotational ve-

locity significantly. As described in the method section, the effective radial stiffness consists of an elastic part and a part originating from the centrifugal forces. The elastic part has its minimum at 45° when both DP-DP layers are equally deflected and both bearing stiffnesses $K_{2,b}$ and $K_{4,b}$ are relatively low. The centrifugal forces rise with the rotational velocity squared, resulting in a decrease of effective radial stiffness. In the upper graph of figure 10 the first two modes at 650 min^{-1} are given as dashed lines, in which the first clearly approaches zero every $45 + n \cdot 90^\circ$. This mode shape is motion in radial direction of the coupler body, in combination with motion of all four intermediate shuttles, and is expected to determine the operational limit of this design.

This first mode resulting from the 5DOF model is shown in the lower graph as well, having a similar course. However, for this model the point of zero stiffness occurs at 620 min^{-1} already.

Due to the shown significant shifts in frequencies for both angle and velocity, it is expected that the frequency content of the velocity error no longer consist of clear individual resonance frequencies, but of broader frequency regions of increased amplitude.

Velocity error In figure 11 the experimental frequency content of the velocity error is given for this scenario. It is clear that velocity error amplitude is significantly higher over the whole spectrum than for the zero misalignment case. As expected, less clear resonance lines are visible, as frequency now varies with angle and velocity. Especially from 0 up to circa 500 Hz error amplitudes are increased. Some specific increases in amplitude can be seen at 20-40Hz, 60-100Hz, 170 Hz, 285 Hz and 350 Hz. At low velocity, vaguely a zigzag pattern can be seen in the first two regions showing the varying frequencies. This will be discussed in more detail later. At higher velocities this representation only gives the average frequency over multiple rotations, and the zigzag is not observable anymore.

The first band of increased amplitude at 20-40Hz matches the range of frequencies expected for the first two shuttle modes as in figure 10. The 60-100Hz range matches the FEA results for the first rotational mode. The three other peaks cannot be matched unambiguously to the modelling results, yet the second rotational FEA mode at 304-330 Hz is in the vicinity of the peaks at 285 and 350 Hz.

At velocities where an engine order intersects a resonance frequency, further increase in amplitude is visible. For example the second order is clearly visible for $500\text{-}600 \text{ min}^{-1}$ at which it produces an excitation of around 17-20Hz which excites the first mode. A second example is the eighth order, which crosses the 60 to 100 Hz region at around 550 min^{-1} .

Angle dependency of velocity error In figure 12 a waterfall diagram of the velocity error is given for rotation at a constant velocity of circa 50 min^{-1} . Here, the zigzagging frequencies during a revolution are more clear. In the diagram, red lines indicate whole revolutions, at 0° input axle rotation. It is observed that indeed the shift in frequencies

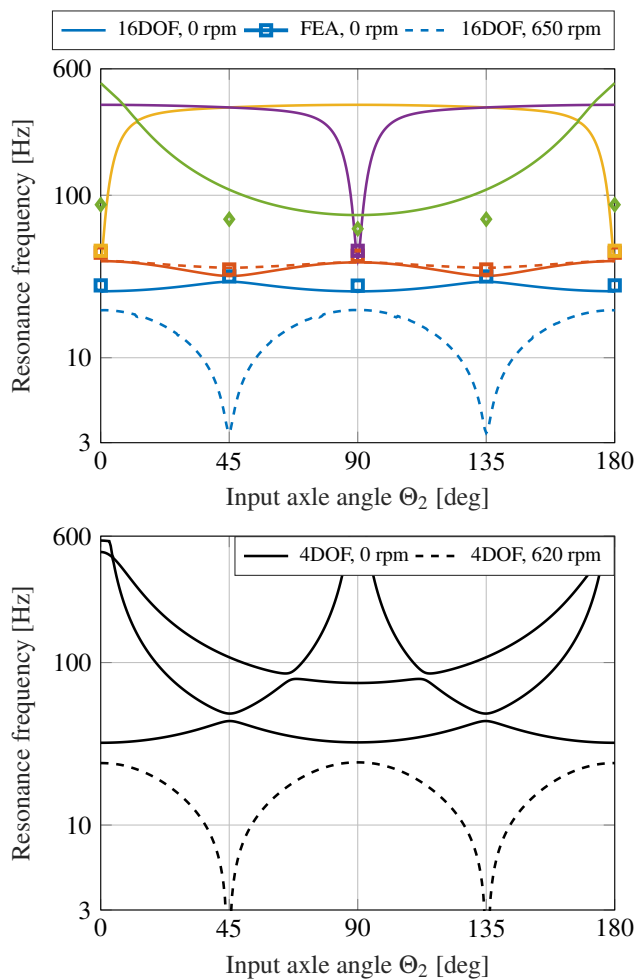


Fig. 10. Resonance frequencies of the coupling at an maximum axle misalignment of 20 mm, on a logarithmic scale, as a function of the input axle angle. This behaviour repeats every 180° . Upper graph: 17DOF model results, first six static resonance frequencies and first two at maximum velocity, as well as static FEA results at several points. Lower graph: 5DOF model results, first three static resonance frequencies and the first at maximum velocity.

is periodic with half a rotation, as expected, most clear in the 60-100 Hz region. At the start of a revolution amplitude is high around 89 Hz, and then shifts in time to 62 Hz at a quarter rotation after which it starts increasing again. Furthermore, a similar but more vague behaviour is seen at 290-310 Hz in the vicinity of the second rotational FEA mode at 304-330 Hz. The intermediate shuttle resonances in the 20-40 Hz as seen at higher velocities in figure 11 are not substantial here.

Changes in the velocity error as a function of the input angle are even more clear in figure 13, where the error amplitude is shown for a ramp up in velocity (vertical), with on the horizontal axis input axle angle. Again a pattern repeating every 180° is visible. For higher velocities, amplitudes increase and the pattern shifts to the right (occurs at larger angle).

In figure 14 the characteristics of the absolute time do-

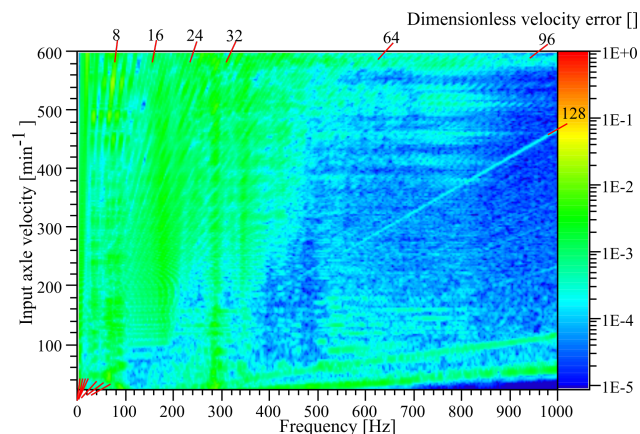


Fig. 11. Campbell diagram of the velocity error frequency content for a ramp up in rotational velocity of the compliant coupling, with 20 mm axle misalignment. On the horizontal axis frequency and on the vertical axis rising rotational velocity. The color indicates the velocity error amplitude.

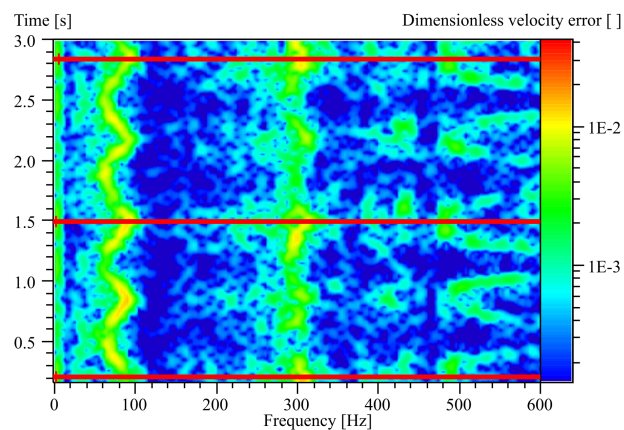


Fig. 12. Waterfall diagram of the velocity error frequency content at a constant rotational velocity of circa 50 rpm of the compliant coupling, with 20 mm axle misalignment. On the horizontal axis frequency and on the vertical axis time. The color indicates the velocity error amplitude. The beginning of each revolution (zero input angle) are given as red lines.

main error signal are given for both experiment and time integration results of the multibody models. This for three constant velocities. It is expected that time integration results give a poor representation of the error. It was observed that friction and damping parameters are highly influential on the results, yet cannot be determined with high accuracy from the experimental setup.

Operational limit In the method section it is predicted that instability and unbounded motion in radial direction will occur when the effective radial stiffness approaches zero. The mode shape containing this radial motion of the coupler body is already discussed above. The velocity at which zero stiffness occurs can be predicted using this modal analysis and

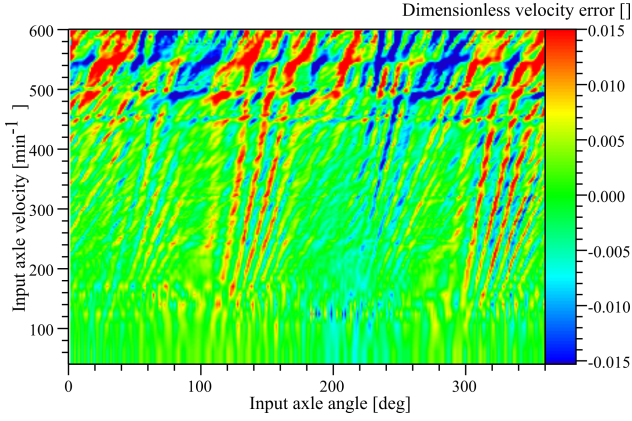


Fig. 13. Velocity error ε , with on the horizontal axis the input axle angle and on the vertical axis rotational velocity. The error color scale is saturated to make the behaviour more clear, so the maximum values are not correct.

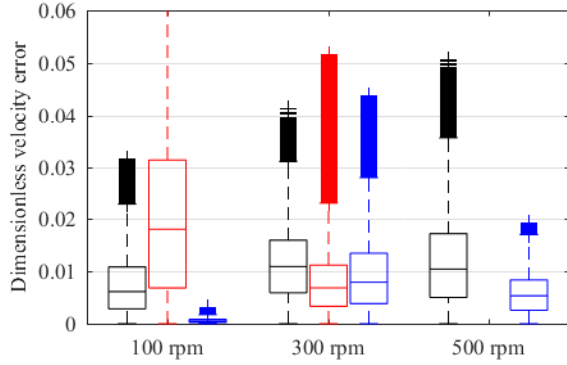


Fig. 14. Absolute value of the dimensionless velocity error ε at three constant rotational velocities, resulting from experiment (black), 5DOF (red) and 17DOF (blue) model. For the 5DOF model, at 100 and 300 RPM no proportional damping was needed for integration stability. However, at 500 RPM no trustworthy integration results were obtained at all. For the 17DOF model, stiffness proportional damping with $\beta = 6.5 \cdot 10^{-7}$ was applied. On each box, the centre mark indicates the median, and the bottom and top edges of the box indicate the 25th and 75th percentiles, respectively. The whiskers extend to the most extreme data points not considered outliers, and the outliers are plotted individually using the '+' symbol.

occurs at the emergence of a positive real root. For this, multiple linearisation points are formed for incremental increasing velocity $\dot{\theta}_2$. Input angle θ_2 is set at $\pi/4$, the point of minimum elastic radial stiffness. Velocity $\dot{\theta}_2$ and radius r at first occurrence of a positive real root are shown in table 4, for both 5 and 17DOF model.

The zero stiffness point can also be predicted using the radial stiffness expressions given in the method section. As bearing direction stiffness is state dependent, r and therefore $\dot{\theta}_c$ (due to Coriolis force) are non-constant. Equation 23 thus does not hold. However, an estimation can be made by pretending that steady motion for the 5DOF model does exist at:

$$\mathbf{q} = [\pi/4, \pi/2, r, \pi/4, \pi/4]^T \quad (53)$$

$$\dot{\mathbf{q}} = [\dot{\theta}_2, 2\dot{\theta}_2, 0, \dot{\theta}_2, \dot{\theta}_2]^T \quad (54)$$

Two free coordinates remain: r and $\dot{\theta}_c$. Equation 17 then simplifies to equation 55, which partial derivative to r gives the effective radial stiffness. Solving this set of two equations (equation 55 and 56) gives an estimation of the input axle velocity and radius at the point of zero radial stiffness, which is given in table 4:

$$\frac{\partial V}{\partial r} - 4m_3\dot{\theta}_2^2 r = 0 \quad (55)$$

$$K_{\text{radial}} = \frac{\partial}{\partial r} \left(\frac{\partial V}{\partial r} - 4m_3\dot{\theta}_2^2 r \right) = 0 \quad (56)$$

The behaviour at decreasing radial stiffness is studied experimentally using the motion tracking. In figure 15 the path of the coupler body (showing radius r) is given for experiments at several velocities $\dot{\theta}_2$. In the same graph, similar paths resulting from time integration of the 17DOF model are shown. Markers indicate the coupler body location at $\theta_2 = n \cdot 90^\circ$ for counterclockwise rotation. For the two lower velocities the time integration and experimental data lie close together. At the highest velocity however, the deviation is larger. Furthermore, a discrepancy can be seen in the coupler body location markers. In the experimental data the coupler body has a larger 'path lag', θ_c lags its quasi-static location of $\theta_c = 2\theta_2$.

Experimentally, the failure point is hard to define. At a certain velocity it can be heard that the shuttles hit the coupler body, but failure does not occur immediately. At that point impulses can be seen in the velocity error frequency data, and the velocity error increases significantly. In most cases, shuttle breakage only occurred when velocity is increased even further. In table 4 the experimentally found velocities are given for the point that collision is heard first and the point fracture occurred.

5 Discussion

5.1 Proposed modelling method

The proposed 5DOF model is able to predict the first static resonance frequency within 14% with respect to the FEA. For maximum misalignment, the found frequency range matches the increased amplitudes found in the experiment. Furthermore, the operational limit is predicted as 6% lower than the experimental fracture velocity.

The extended 17DOF furthermore reflects the dynamics of the four internal shuttles of the specific case study design.

¹The collision velocity is an average of four measurements, the fracture velocity results from a single measurement with rapid acceleration until fracture occurred.

Table 4. Velocities and radii at the operational limit. For the models, the given point is at zero radial stiffness. For the experiment, two velocities are given: at first notice of internal collision and at fracture of one of the intermediate shuttles.

	Eq. 55, 56	Multibody model		Experiment ¹	
		5DOF	17DOF	Collision	Fracture
$\dot{\theta}_{2,\text{lim}}$ [rpm]	624	621	652	580	660
r_{lim} [mm]	15.2	15.1	14.1		

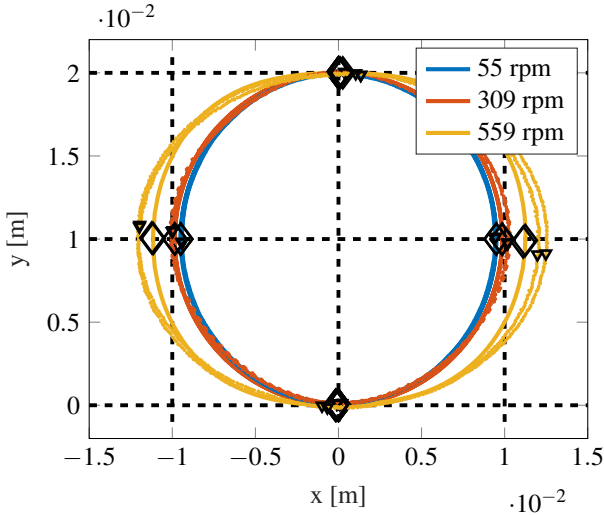


Fig. 15. Path of the coupler body during rotation at different velocities. The dotted lines represent the experimental data, the dashed lines the 17DOF EoM time integration.

For zero axle misalignment, the first four resonance frequencies originating from those shuttles are predicted within 4% error of the FEA, and 1% error of the experiment. For maximum axle misalignment, the first two resonances match the FEA results at standstill within 9%, for higher velocities the predicted range of frequencies is reflected by the experiment. The operational limit is predicted at an 2% lower velocity than the experimental fracture velocity.

As shown in the result section, the first rotational mode of the coupling, which as expected is dominant in the velocity error, is not predicted correctly by both multibody models. Shuttle and coupler body deformation plays a significant role in this mode, which was not expected at first. It can be seen that at 90° input axle angle, when angular stiffness of the input side DP-DP layer is minimal, the model results are within 20% of the FEA and 21% of the experiment. However, away from this angle the stiffness of the DP-DP rises, and shuttle and coupler body becomes dominant, which is not represented by the multibody models. When the proposed modelling method is used, care thus has to be taken that results only are accurate when the deformation of the modelled flexure is dominant.

Looking at the modal analysis, used for resonance mode and operational limit prediction, several remarks can be made. Firstly, no damping or load is implemented, where the

damped natural frequencies are lower for an underdamped system. Secondly, the steady motion equilibria used for linearisation are only valid for the specific stiffness values at that point (which vary significantly), and are likely to be never reached during higher velocity rotation due to the inertia. This explains the too large radii predicted at the operational limit. Thirdly, as seen in the experiments, collision of the shuttles occurs at a velocity well before the radial stiffness becomes zero, as the decrease of radial stiffness already introduces too large radial and shuttle displacements.

Furthermore, prediction of the velocity error via time integration turned out inaccurate. Several potential causes can be indicated. Firstly, some bearing, encoder and air friction is inherent to the model. Estimating these effects via the motor current and voltage is inaccurate, and are furthermore depended on bearing alignment, axial play and lubrication. Secondly, the explicit integration method is sensitive for error accumulation, and for some higher velocity implementation of stiffness proportional damping was needed to remain integration stability. Thirdly, the internal damping in the coupling, for example in the glued connections, is hard to determine and is not modelled.

The effect of a high torque load on the coupling is not studied in this work. However, the proposed modelling method does incorporate the transmission torque. Furthermore, using two perpendicular compliant prismatic joints in the Oldham kinematics yields a statically balanced mechanism [3], so that the use of high stiffness prismatic joints does not affect the actuation torque.

5.2 Experimental

A few flaws in the experimental evaluation can be indicated. Firstly, no proper way to measure the bearing friction of the setup was found. The used method via the motor current is inaccurate as exact motor efficiency is not known, and is impractical for measuring individual bearing. Furthermore, at the output axle a journal bearing is used for which friction can be altered by changing the axial play. This to be able to apply some output load to the coupling. However, adjusting this play is cumbersome and badly repeatable, as again friction can not be measured accurately. The use of a precise torque sensor would be preferable, which are expensive however.

Secondly, not all resonance frequencies found in the experiments can be matched with modelling results unambiguously. As only rotational sensor data is available, the modal displacement in other directions is not known and the exact

mode shape cannot be determined. Use of accelerometers placed on different bodies can give more insight. However, especially for the smaller bodies, a significant mass will be added, and data transfer from the rotating structure to the fixed world is cumbersome. Another option is to attempt to extract frequency data from the motion tracking. However, only frequencies up to circa 250 Hz can be observed due to the frame rate, and only large amplitudes are visible due to the resolution.

Finally, a higher input axle stiffness is preferred. Although 12 mm stainless steel is used, its relative long length results in a reasonably low stiffness of 714 Nm rad^{-1} , where the minimum angular stiffness of one DP-DP layer is 62 Nm rad^{-1} . A shorter or thicker axle will result in higher stiffness. Implementing the axle elasticity in the FEA can give insight in its effect.

5.3 Suggested optimization

Within the current design using the DP-DP flexure mechanism, some design improvement suggestions will be proposed categorised by inertia and stiffness changes, showing the effect on the performance criteria.

Inertia By looking at the relation for the effective radial stiffness (55 and 56), the parameters to increase the velocity at zero stiffness can be indicated directly. Decreasing m_3 can be done by choosing other materials or shape for the coupler body. More beneficial however is to invert the DP-DP design, connecting the outer ring to the axle resulting in the middle body being the coupler body, significantly lowering mass m_3 and inertia I_3 , with only a marginal increase of I_2 and I_4 . The 5DOF modal analysis yield a improved operational limit at a rotational speed of $19.9 \text{ Hz} = 1193 \text{ min}^{-1}$, the 17DOF gives $34.5 \text{ Hz} = 2069 \text{ min}^{-1}$; a minimal improvement of 198 %. As in the 5DOF model the internal inertia of the DP-DP flexure is distributed over the three bodies as an approximation, this model gives a significantly lower and less realistic value.

The inverted design furthermore gives an increase in some of the eigenfrequencies. The first eigenfrequency resulting from the 17DOF model is slightly increased from 25 Hz to 33 Hz. The first rotational mode with its original minimum at 75 Hz is increased to 174 Hz (232 % increase).

Stiffness Obviously, the stiffness characteristics of the compliant prismatic joints, in the current design the DP-DP flexure, are highly influential on the performance criteria. Within this design, parameters can be optimized for specific objectives. Material and geometric beam parameters as E , I and l have effect on all stiffness directions, as does the compliance distribution parameter a_0 . The effect of a_0 on the bearing/motion stiffness ratio is further analysed in [17], indicating that the decrease of a_0 only gives a significant increase of this ratio for small motion direction displacement values.

Two characteristic stiffness values of the coupling, being actuation and rotational stiffness, have to be looked at before

changing parameters.

The actuation stiffness of the transmission is the stiffness felt changing the axle misalignment. The energy needed is stored in the coupling, during rotation no actuation energy is needed as the coupling is statically balanced. However, the bearing forces and thus bearing frictions at both axles also increase with this stiffness. The actuation stiffness depends on motion and bearing stiffness of the two DP-DP flexure mechanisms in series, and as the motion stiffness is orders of magnitude lower this one is dominant.

The rotational stiffness of the coupling indicating its static load bearing capabilities is formed by the angular stiffness of both DP-DP layers in series.

Without increasing the actuation stiffness the rotational stiffness can be increased by increasing parameters w_1 and w_2 . However, the footprint will increase with it. The difference between w_1 and w_2 gives a maximum for the stroke in motion direction and thus the maximum axle misalignment, which is furthermore limited by the flexure stress.

More improvement can be gained by choosing different prismatic compliant joints than the DP-DP. The underconstraint of the shuttles in the DP-DP flexure contributes to the low bearing to motion stiffness ratio and low internal resonance frequencies. Several strategies to decrease or eliminate this underconstraint are given in literature [21], resulting in improved prismatic joints. Most improvements however limit the motion range to a certain extent.

6 Conclusion

In this work, a straightforward generic analysis method for the family of compliant Oldham couplings is proposed, based on multibody dynamics. Predictions can now be given of 1) the maximum attainable velocity before instability due to centrifugal forces occurs, 2) the lower resonance modes originating from the used flexure mechanisms, and 3) the characteristics of the resulting velocity error.

The analysis and prediction method is validated with a case study for a specific coupling design. For this design, the operational limit and the velocity error are evaluated. Within this design, performance is optimized. For this, a 198% maximum velocity increase and a 232% first rotational frequency increase are expected.

For this family of couplings in general, three important characteristics are indicated which need attention during design. Firstly, as the coupler body COM will always describe a circular path, resulting in centrifugal forces, sufficient radial stiffness is needed for stability. Secondly, the first rotational resonance mode originating from the used flexure mechanism needs to be sufficiently high and is likely to be dominant in the velocity error. Thirdly, the use of underconstraint internal bodies must be prevented, as it is demonstrated that their vibration can contribute to the velocity error. Low resonances, both rotational and internal, can, if excited by dominant engine orders, potentially lead to failure.

References

- [1] X. Herpe, R. Walker, X. Kong, and M. Dunnigan, "Analysis and characterisation of a kinematically decoupled compliant XY stage," *2015 21st International Conference on Automation and Computing: Automation, Computing and Manufacturing for New Economic Growth, ICAC 2015*, no. June, 2015.
- [2] D. Farhadi Macheuposhti, N. Tolou, and J. L. Herder, "A Review on Compliant Joints and Rigid-Body Constant Velocity Universal Joints Toward the Design of Compliant Homokinetic Couplings," *Journal of Mechanical Design*, vol. 137, no. 3, p. 032301, 2015.
- [3] D. Farhadi Macheuposhti, N. Tolou, and J. L. Herder, "A statically balanced fully compliant power transmission mechanism between parallel rotational axes," *Mechanism and Machine Theory*, vol. 119, pp. 51–60, jan 2018.
- [4] D. Farhadi Macheuposhti, N. Tolou, and J. Herder, "A Fully Compliant Homokinetic Coupling," *Journal of Mechanical Design, Transactions of the ASME*, vol. 140, p. 012301, nov 2018.
- [5] Z. Li and S. Kota, "Dynamic Analysis of Compliant Mechanisms," in *Volume 5: 27th Biennial Mechanisms and Robotics Conference*, pp. 43–50, ASME, 2002.
- [6] S. M. Lyon, P. A. Erickson, M. S. Evans, and L. L. Howell, "Prediction of the First Modal Frequency of Compliant Mechanisms Using the Pseudo-Rigid-Body Model," *Journal of Mechanical Design*, vol. 121, no. 2, p. 309, 1999.
- [7] Y.-Q. Yu, L. L. Howell, C. Lusk, Y. Yue, and M.-G. He, "Dynamic Modeling of Compliant Mechanisms Based on the Pseudo-Rigid-Body Model," *Journal of Mechanical Design*, vol. 127, no. 4, p. 760, 2005.
- [8] "Couplings - Flexible Couplings, Bellows, Helical, Junior Flex, Oldham and Multijawed from SDP-SI." Available at <http://www.sdp-si.com/products/Couplings/index.php>.
- [9] M. Xu and R. D. Marangoni, "Vibration Analysis of a Motor-Flexible Coupling-Rotor System Subject To Misalignment and Unbalance, Part I: Theoretical Model and Analysis," *Journal of Sound and Vibration*, vol. 176, no. 5, pp. 681–691, 1994.
- [10] M. Xu and R. Marangoni, "Vibration analysis of a motor-flexible couplingrotor system subjected to misalignment and unbalance Part II: Experimental validation," *Journal of Sound and Vibration 176 681-691.*, 1994.
- [11] I. Redmond and K. Al-Hussain, "Misalignment as a source of vibration in rotating shaft systems," *Proceedings of IMAC-XIX: A Conference on Structural Dynamics, Feb 5-8 2001*, vol. 1, pp. 116–123, 2001.
- [12] S. Prabhakar, A. S. Sekhar, and A. R. Mohanty, "Vibration analysis of a misaligned rotor-coupling-bearing system passing through the critical speed," *Proceedings of the Institution of Mechanical Engineers, Part C: Journal of Mechanical Engineering Science*, vol. 215, pp. 1417–1428, dec 2001.
- [13] a. T. Tadeo and K. L. Cavalca, "A comparison of flexible coupling models for updating in rotating machinery response," *Journal of the Brazilian Society of Mechanical Sciences and Engineering*, vol. 25, no. 3, pp. 235–246, 2003.
- [14] S. Pathan and P. Khaire, "Experimental study to identify the effect of type of coupling on unbalance using frequency spectrum analysis," *IOSR Journal of Mechanical and Civil Engineering Ver. I*, vol. 11, no. 3, pp. 13–16, 2014.
- [15] F. Freudenstein, L. W. Tsai, and E. R. Maki, "The Generalized Oldham Coupling," *Journal of Mechanisms Transmissions and Automation in Design*, vol. 106, no. 4, p. 475, 1984.
- [16] S. Awatar, A. H. Slocum, and E. Sevincer, "Characteristics of Beam-Based Flexure Modules," *Journal of Mechanical Design*, vol. 129, p. 625, jun 2007.
- [17] M. Olfatnia, S. Sood, J. J. Gorman, and S. Awatar, "Large stroke electrostatic comb-drive actuators enabled by a novel flexure mechanism," *Journal of Microelectromechanical Systems*, vol. 22, no. 2, pp. 483–494, 2013.
- [18] M. Géradin and D. J. Rixen, *Mechanical Vibrations: Theory and Application to Structural Dynamics*. John Wiley, 2015.
- [19] J. He and Z.-F. Fu, *Modal analysis*. Butterworth-Heinemann, 2001.
- [20] L. L. Howell, *Compliant mechanisms*. Wiley, 2001.
- [21] R. M. Panas and J. B. Hopkins, "Eliminating Underconstraint in Double Parallelogram Flexure Mechanisms," *Journal of Mechanical Design*, vol. 137, p. 092301, sep 2015.

3

Discussion

In this section, discussion will be given about the complete project. Shortcomings and remarks within fulfilling the four sub-objectives will be given. Then, some general comments about the complete project are stated. Finally, possible future work is suggested. A reflection on the process of this project is given in appendix F. In this discussion, there will be some overlap with the paper presented earlier.

Within this project To analyse and predict the performance of the Oldham coupling, use of a multibody model is proposed. In the resulting models, some shortcomings are indicated. First of all, the numerical time integration of the equations of motion, which can give insight in the coupling's motion in time, is problematic. Without implementation of damping, integration often becomes unstable, primarily for higher rotational velocities. Furthermore, results sometimes appear to be heavily dependent on small changes in the initial conditions. In future work, implementation of an implicit solver could overcome this problem. More information can be found in appendix C.

Secondly, matching the multibody models with the experimental setup is ambiguous. For this, values for the friction torque arising from the bearings and encoders are needed, which vary with velocity. In the experimental setup, all friction is estimated by measuring the DC-motor current. Using the motor parameters, the torque can then be calculated. In future work, use of a dynamic torque sensor can be considered, with which ideally torque variations within a revolution can be measured as well.

As for the time integration implementation of damping is needed in some cases, it would be interesting to know the actual damping within the coupling. More time could be invested to experimentally determine the damping characteristics. Damping is now assumed to be stiffness proportional, which then also can be validated.

Furthermore, a modal analysis was done to find the resonance frequencies with respect to the coupling's angle and velocity. A clear limitation of the multibody model is that all bodies are rigid. Only mechanisms for which the flexure deformations are dominant can be studied properly. For many flexure based compliant mechanisms this is the case however, certainly for the lower and most interesting eigenfrequencies. Nevertheless, body deformation had a significant influence on the first rotational resonance of the case study's design.

It was shown that the results of the finite element analysis (FEA) were in good accordance with the experimental results. For further use of the multibody models, a possible procedure can be to first perform a relatively straightforward static modal analysis with FEA software to determine the contribution of elastic body deformations. Then, if the flexure deformations prove to be dominant, further dynamic analysis can be done using the proposed multibody modelling.

Despite the straightforwardness of the proposed multibody technique, it would be interesting to compare it with other methods. Both accuracy and easy of modelling can be compared. Where FEA is more complex, it is not limited to available stiffness profiles for flexure mechanisms. Another more easy option is multibody dynamics simulation software such as Adams. However, the manual implementation in Matlab or any other programming language gives the designer direct insight in the underlying physics and mathematics.

Some further remarks can be made with respect to the experimental setup and the chosen evaluation method. Several are already given in the paper. One shortcoming being the non-observability of certain mode shapes will be discussed more elaborate next. More detailed information about the setup and experimental method can be found in appendix D.

The primary goal of the setup is to determine the velocity error caused by a coupling, which is done using two optical encoders on both input and output axes. Secondly, using high speed footage, the motion during rotating can be studied. With this, low frequency high amplitude mode shapes in the planar domain can be indicated. However, other mode shapes cannot be determined, as was already discussed in the paper. In future work, other techniques to determine these mode shapes during rotation should be explored. A shaker measurement determining the modes at standstill can furthermore be a good validation of both the multi-body models and the FEA, and might also give insight in the damping characteristics of the coupling.

Optimization of the coupling's dynamic performance forms one of the sub-objectives. In the paper, several properties influencing its performance are indicated, and several design improvements are suggested. An orientation into the redesign of the coupling is furthermore given in appendix E.

In the paper it was already indicated that besides improving the effective radial stiffness, more improvement can probably be gained by optimizing the compliant prismatic joints used. Future work can focus on the design of a more suitable flexure mechanism, without internal underconstraints as with the current intermediate shuttles. Several alternatives are already found in literature (see appendix E), but there still is a challenge in maintaining the needed large range of motion within these more properly constrained designs.

Furthermore, dynamically balancing the design could be explored, eliminating the effects of the constantly moving centre of mass of the coupler body. Also, the use of other kinematics besides the current Oldham kinematics can be investigated, which might benefit the dynamic performance.

Beyond this project Beyond the scope of this project, some future challenges or recommendations can be indicated.

In this work, the effect of the loading on the compliant coupling is not analysed. For most applications, the transmissions of some amount of rotational power is desired. In future works the effect of loading should be investigated. For the experimental evaluation, a method to apply a specified and controlled amount of torque should be developed. Use of a second electric motor in combination with a dynamic torque sensor is a possibility.

During this project, the scope was narrowed down to the family of compliant Oldham couplings. In the literature review, a first orientation of potential dynamic problems in any kind of compliant couplings was performed. It would be interesting to validate these findings and extend the found methods into other compliant couplings or mechanisms. The compliant universal coupling as designed by Farhadi Machekposhti [1] would be a challenging candidate, as it cannot be analysed in the planer domain any more.

The research into compliant rotational couplings would be more valuable if a specific application would be chosen. Potential benefits of the compliant designs over conventional couplings can then be quantified. Furthermore, the designs can then be further optimized for that specific application, which might bring along new challenges.

Moreover, for practical implementation in any kind of application the manufacturing process has to be improved. For complicated designs, additive manufacturing can be attractive, for which attaining suitable material properties might still be a challenge. For the planar designs, more conventional techniques such as wire EDM, water jet or laser cutting are available.

A potential field of application is that of Microelectromechanical systems (MEMS). Here, the planar designs consisting of a minimum amount of layers are most attractive from a production point of view. At this scale, the dynamics will behave differently than on the studied macro scale. Investigating the specific dynamics of compliant rotational couplings at this scale might be very interesting for future work. Multiple challenges such as the experimental validation can be indicated.

4

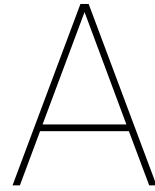
Conclusion

In this thesis, a straightforward generic analysis method for the family of compliant Oldham couplings is proposed, based on multibody dynamics. Stiffness is implemented using already available stiffness characteristics of flexure building blocks. Using this method, predictions can now be given of 1) the maximum attainable velocity before instability due to centrifugal forces occurs, 2) the lower resonance modes originating from the used flexure mechanisms and 3) the characteristics of the resulting velocity error. Key dynamic bottlenecks being zero effective radial stiffness and internal underconstraints are indicated.

The analysis and prediction method is validated with a case study for a specific coupling design. For this design, the operational limit and the velocity error are evaluated. For this, a universal test setup suitable for parallel as well as angular misalignment couplings was designed and fabricated. Within the case study design, improvements are suggested which are expected to significantly increase the dynamic performance. Furthermore, an orientation towards a complete redesign of a compliant Oldham coupling for dynamic applications is executed.

Using the proposed methods, a designer can now analyse, understand and predict the dynamic performance of a compliant Oldham coupling in a straightforward manner. Furthermore, key performance bottlenecks are indicated as well as the handles to elevate those. This all makes implementation of a compliant Oldham coupling in a dynamic application more feasible and attractive. Within this field, the benefits of compliant mechanisms no longer have to be abolished by dynamic problems.

This work is a first step in filling the knowledge gap of the dynamics of compliant rotational couplings. It paves the road for dynamic analysis of other compliant rotational couplings. The proposed modelling techniques can be adapted to other flexure based couplings as well as other flexure based mechanisms. Indicated (potential) dynamic problems can inspire and aid future research.



Literature review towards the dynamic analysis of compliant rotational couplings

A.1. Introduction

Mechanical rotation power couplings are used to transmit a rotational motion from one direction to another. More concrete a coupling is made between two misaligned axles, in which the misalignment can be parallel, angular or both. Many designs exist, of which the Hooke's universal or cardanic coupling for angular misalignments is the most well-known. However, this coupling does not transmit the velocity between the two axles constantly. The introduced error increases with misalignment angle, and can cause dynamic problems and increased stresses in the couplings bodies.

A constant velocity (CV) or homo-kinetic coupling however transmits this motion with a 1:1 ratio during the whole cycle of rotation: the velocity transfer is constant. Also, many of these designs exist. Common examples are the ball-and-groove homo-kinetic couplings used in cars. Also other types based on linkages exist. However, these are all conventional rigid-body mechanisms, with mutual sliding or rolling contacts. Disadvantages such as backlash, friction, wear and need for assembly, maintenance and lubrication are inherent to these mechanisms [4].

Compliant mechanisms in which motion originates from elastic deformation of a monolithic body only do not possess these disadvantages. Already, quite some compliant designs for rotational couplings exist [3]. In industry, compliant couplings for small misalignments are already frequently implemented [5]. However, when large misalignments are needed, the use of compliant couplings still is less common.

Masheposhti designed two compliant rotational couplings for respectively large parallel and angular misalignments, which both offer a CV transfer [1, 6]. A true constant velocity coupling with the advantages of a compliant mechanisms can be attractive for high precision applications due to their lack of backlash and wear, or for application in a clean or vacuum environment as no maintenance or lubrication is needed. Masheposhti however indicated that the dynamic performance of these mechanisms is poor, which is the direct motive for this work. A first observation was that the lack of stiffness in certain directions, inherent to a compliant design, lead to problems at higher velocities. For example, in testing on the Monocup compliant universal joint [1] done by a group of bachelor students, flexure yield occurred at around 400 min^{-1} already. Furthermore, the constant velocity transfer is questionable at higher velocities, as vibrations or distorted kinematics are expected.

Compliant couplings behave differently from conventional rigid body couplings. A rigid body revolute joint for example has very low on-axis stiffness and high off-axis stiffness. A leaf spring used as a compliant revolute joint does have on-axis stiffness and a relative low off-axis stiffness. Especially this different stiffness characteristic gives rise to problems when compliant couplings are used in a dynamic environment. As in rotational transmissions operating at some speed dynamic forces always are present, the dynamics of such a transmission can not be ignored. Large deformations and vibrations caused by dynamic forces can lead to distortion in the coupling's kinematics and ultimately in plastic deformation.

This leads to the goal of this literature review, which is firstly to identify dynamic phenomena potentially deteriorating the performance of compliant rotational couplings, and secondly to review existing methods to model the dynamic behaviour of these couplings. This towards dynamic analysis of the existing compliant

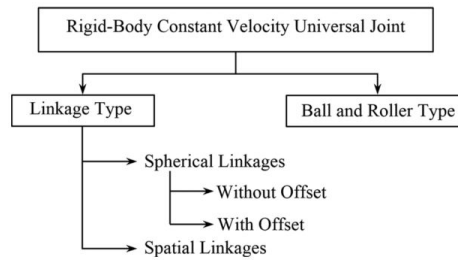


Figure A.1: Schematic classification of CV universal joint kinematics [3]

couplings, and moreover towards the (re)design of compliant rotational couplings, suitable for large misalignments and dynamic applications (significant rotational velocities and accelerations). The performance is defined twofold, firstly being the velocity error generated by the coupling and secondly the maximum operational conditions in terms of angular velocity and acceleration before permanent damage is done to the coupling.

In the first section, the kinematic requirements for a CV joint are discussed, as well as the kinematics used for the compliant designs at hand. In the next section, relevant common dynamic knowledge is summarised. Then, the state of the art in the dynamic analysis of conventional rigid-body couplings and rotor systems is discussed. Finally, already available work in the field of the dynamics of compliant couplings is reviewed, followed by dynamic modelling methods used in the whole field of compliant mechanisms. At the end, a schematic overview of potential dynamic problems for compliant rotational couplings is given in the form of a flowchart.

A.2. Literature review

A.2.1. Kinematics of (conventional) rotational couplings

In this section, the kinematics needed for a constant velocity transfer coupling are discussed. Furthermore the kinematics of a cardan and Oldham coupling will be discussed in more detail, as the compliant designs at hand possess their kinematics.

Hunt constructed a general theory for the kinematic design of a CV coupling, both for angular or parallel misalignments [7]. He concluded that a symmetric configuration with respect to the so called homo-kinetic plane is essential for CV transfer. This plane intersects both axle perpendicularly. In case of a coupling between parallel axles, this plane thus lies at infinity and one must ensure that the design is non symmetric near the coupling.

An overview of rigid-body CV universal joints using different kinematics is given in [3], as a review towards the design of a compliant universal joint. A division is made between different strategies as depicted in figure A.1. As the ball and roller type has several shortcomings among others being difficult to convert to a compliant design due to the rolling contacts, the linkage class is seen as being more suitable. This class can further be divided in spherical and spatial linkages. In the first any point is limited to move in within a set of concentric spherical surfaces. The kinematics of different linkage type joints is analysed, and schematically organised based on the internal kinematic pairs. Strategies for conversion to a compliant design are discussed. This overview finally led to the design of a compliant CV rotational coupling for large misalignments, based on the double Hooke kinematics [1].

A common design of a CV coupling between parallel axles is the Oldham coupling, names to the Irish engineer John Oldham who invented it in 1821. This coupling is a RPPR mechanism which; two revolute joints at supporting each axle and two prismatic joints in between transferring the rotation. Conventionally, the prismatic joints are formed by grooves in the two axle members, and an intermediate body or coupler having matching projections. Sliding contact occurs between grooves and projections. The two grooves are perpendicular, resulting in a CV coupling.

During rotation, the intermediate member describes a circular path in the plane perpendicular to both axles, crossing the centres of the axles. The centre of this path is midpoint between the two axles. This path is passed through twice per rotation, and the angular velocity of the coupler around the centre of the path is twice the input axle velocity. The circular motion of the centre of mass of the coupler body creates a dynamic

imbalance.

The imbalance can also be used as an advantages. Tsai proposes a second-harmonic balancer which by properly arranging two Oldham couplings can eliminate second-harmonic shaking forces, moments of a combination of both [8]. As the angular velocities of all bodies within the system, besides the friction torque no input torque is required. Due to the circular motion of the coupler body, a rotating nett centrifugal force is present, which is used for the balancing purposes. By varying the rotation direction and phase of the two couplings, a nett force or moment can be created with a frequency of twice the input axle frequency.

A generalised design of the Oldham coupling is given and discussed by Freudenstein [9]. He proposes a more general design in which the phase transmission can be altered by changing the straight grooves of the prismatic joints into groves with a certain radius. By altering these radii a desired phase change per rotation can be obtained.

General dynamics In this section, different dynamic phenomena are described. First, all inertia forces acting on a rotating system are given, which is based on Hibbeler [10]. Then, the effect of resonance frequencies and their excitation is investigated. Finally, some instability phenomena are introduced.

Inertia Inertia is the resistance of a mass against its change of motion. In an inertial frame of reference, inertia can be described by Newton's second law of motion: "the vector sum of the forces F on an object is equal to the mass m of that object multiplied by the acceleration a of the object".

$$\mathbf{F} = m\mathbf{a} \quad (\text{A.1})$$

When looking into rotating systems, it is more convenient however to use a rotating (non-inertial) reference frame, which is accelerating with respect to the inertial frame. To explain the motion of a mass in such a reference frame, fictitious or inertial forces must be introduced to account for the observed motion.

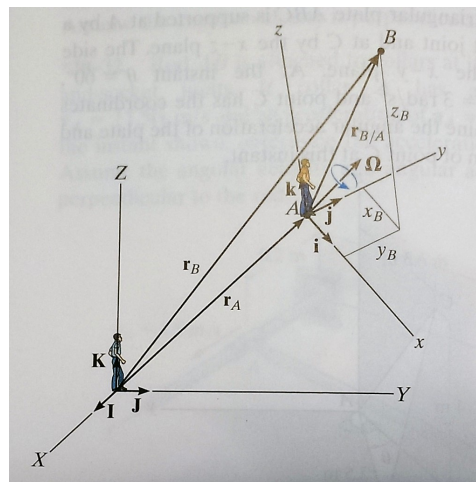


Figure A.2: Translating and rotating non-inertial reference frame ijk

In figure A.2 a general non-inertial reference frame ijk is shown, which can both translate and rotate from the inertial frame IJK . The acceleration of point B can be expressed in the inertial reference frame as:

$$\begin{aligned} \mathbf{a}_B = & \mathbf{a}_A + \dot{\boldsymbol{\Omega}} \times \mathbf{r}_{B/A} + \boldsymbol{\Omega} \times (\boldsymbol{\Omega} \times \mathbf{r}_{B/A}) \\ & + 2\boldsymbol{\Omega} \times (\mathbf{v}_{B/A})_{xyz} + (\mathbf{a}_{B/A})_{xyz} \end{aligned} \quad (\text{A.2})$$

Seen from the moving reference frame, the forces upon the body are $\sum \mathbf{F} = m(\mathbf{a}_{B/A})_{xyz}$. Here, the sum of the forces consists of the external forces on the body and the fictitious forces due to the acceleration of the reference frame.

$$m(\mathbf{a}_{B/A})_{xyz} = \sum \mathbf{F}_{ext} - m[\mathbf{a}_A + \dot{\boldsymbol{\Omega}} \times \mathbf{r}_{B/A} + \boldsymbol{\Omega} \times (\boldsymbol{\Omega} \times \mathbf{r}_{B/A}) + 2\boldsymbol{\Omega} \times (\mathbf{v}_{B/A})_{xyz}] \quad (\text{A.3})$$

On the right hand side, the sum of the external forces and the four inertial forces are seen. From left to right: the force caused by the rectilinear acceleration, the Euler force, the centrifugal force and the Coriolis force. These forces and their impact on rotational joints will now be discussed shortly. For this, the origin of the moving reference frame (A) will be chosen on the axis of rotation of the joint, which is assumed to be fixed to the inertial frame. The joint and thus the reference frame rotates with angular velocity $\boldsymbol{\Omega}$ and angular acceleration $\dot{\boldsymbol{\Omega}}$.

As the axis of rotation is assumed fixed, the moving reference frame has no rectilinear acceleration, $\mathbf{a}_A = 0$.

The Euler force is the cross product of angular acceleration $\dot{\boldsymbol{\Omega}}$ and position vector (radius) $\mathbf{r}_{B/A}$. It is thus perpendicular to both. Due to the minus sign in front of all inertial forces, the Euler force acts in the opposite direction of the transverse acceleration of point B. The force counteracts the angular acceleration.

The centrifugal force is dependent on the angular velocity squared and the radius of point B. Its direction is determined by the double cross product, which always makes it pointing radially outward. If $\boldsymbol{\Omega}$ and $\dot{\boldsymbol{\Omega}}$ are co-linear, which is the case for a rotational joint, this force is perpendicular to the Euler force. It counteracts the acceleration in normal direction caused by the angular velocity.

The Coriolis force is non-zero when point B has a non-zero velocity $(\mathbf{v}_{B/A})_{xyz}$ in the moving frame. It then acts in a direction perpendicular to $\boldsymbol{\Omega}$ and $(\mathbf{v}_{B/A})_{xyz}$. If point B for example has a velocity radially outward from A, the Coriolis force acts in the transverse direction. In a compliant coupling, this force could come into play when a flexible part moves radially outward due to the earlier described centrifugal force.

The inertial forces can have a periodic nature due to the rotation, which will cause vibrations.

Resonance frequencies and mode shapes If the frequency of an applied force is close to a natural frequency of a undamped system, resonance occurs and the amplitude of vibration and stress levels can increase considerable. In compliant mechanisms, the resonance frequencies are often reasonably lower than in rigid body mechanisms (except from the rigid body modes with $\omega_n = 0$) and thus more likely to be excited. First, the determination of the resonance frequencies will be described. Secondly the possible excitations are investigated.

In an undamped one degree of freedom (DOF) system with stiffness k and mass m the first natural frequency can be written as:

$$\omega_n = \sqrt{\frac{k}{m}} \quad (\text{A.4})$$

An example of a 1-DOF system is a revolute joint, which has one DOF being a single axis rotation. Rigid body versions typically have neglectable stiffness in this DOF (on-axis) and high stiffness in other directions (off-axis). If as a replacement a rectangular compliant revolute joint is used (essentially a cantilever beam), this joint has some on-axis stiffness, being the bending of the beam along its length. This stiffness is typically desired as low as possible. The lowest resonance mode then is this bending and thus acts in the DOF of the joint. At higher frequencies, higher order bending modes can also occur. Although these modes are in the desired on-axis direction, excitation can still lead to unwanted (excessive) vibration in the joint.

Where in the rigid joint the off-axis directions are very stiff, this is typically not the case for the compliant beam. Due to this lack in stiffness, off-axis resonance modes will occur at lower frequency. Examples are bending modes in other planes, twisting modes or stretching modes (figure A.3).

When more complex compliant transmission mechanisms are designed using the Rigid-Body Replacement method, compliant revolute joints, modelled as torsion springs, are used to replace the rigid body revolute joints. A mechanism built up from the above described compliant revolute joints has on-axis stiffness and on-axis resonances, but also off-axis stiffnesses and resonances. Both can distort the transmission's behaviour. Determination of the resonance frequencies of such composed mechanisms is less straightforward.

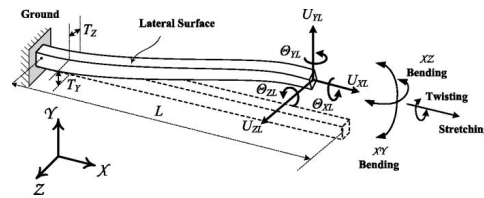


Figure A.3: Different mode types of a fixed-free beam

Several methods will be given in the next sections.

Excitation of natural frequencies Due to the lower natural frequencies of compliant mechanisms, it is likely that these are excited in the working range of the mechanism. Several excitation causes are described now. Most of the excitations are related to the rotational velocity ω of the transmission (not to be confused with the natural frequency ω_n). The most obvious one is an unbalance in one of the bodies of the rotating system. Then there are multiple possible excitations coming from the mechanical setup the coupling is attached to. Furthermore, shock can excite resonances. Finally, some less obvious phenomena leading to excitation are given at the end of the next section.

Unbalance When the COM of a body of the transmission system lays not on the axis of rotation, vibrations can occur with a frequency of an integer multiple of the angular velocity. A simple unbalanced rotating body will generate an excitation with a frequency equal to the rotational velocity of that body, so a first order excitation. These excitations with a frequency proportional to the rotational velocity are called (engine) orders. Compliant transmissions often have multiple parallel linkage chains, and each chain typically has an off-centred COM. Below, several of these excitations are described.

Periodic centrifugal force, whirling When the COM of a body in the transmission lays outside in the axis of rotation, the resultant centrifugal force causes a vibration with ω . This vibration can excite a resonance mode when the frequency ratio $r = \frac{\omega}{\omega_n} \rightarrow 1$. The rotational speed at which this happens is also called the critical speed [11].

Take for example a shaft with some bending stiffness k and a bending mode natural frequency $\omega_n = \sqrt{\frac{k}{m}}$. Near critical speed, the shaft's bending mode is excited. Deflection increases the distance to the axis of rotation which increases the centrifugal forces. The shaft undergoes large deflections and bearing failures can occur due to the large forces transmitted. This phenomena is called whirling [11]. The bending mode 'rotates' with the axle, not necessarily at the same ω , phase lag can occur.

Periodic centrifugal force can also used as an opportunity. Tsai describes an second-harmonic balancer using the 2ω vibration caused by the coupler link in an Oldham coupling [8].

Periodic torque of gravity If an axis of rotation of a transmission system is horizontal, gravity can cause vibrations on the system. The gravitational acceleration g exerts a force on an excentred mass m . As this mass is placed at a radius r from the axis of rotation this force will exert a torque on the rotational system, periodic with the angular rotation θ . This torque thus induces a vibration with frequency ω .

$$\boldsymbol{\tau} = \mathbf{r}_{B/A} \times m \mathbf{g} \quad (\text{A.5})$$

$$\tau = r_{B/A} m g \sin \theta \quad (\text{A.6})$$

Higher order excitations Multiple excitations can originate from the setup to which the coupling is attached. Unbalance is already discussed as a first order excitation. Looking at the mechanical setup, bearing can potentially cause an excitation. Roller bearings can give excitations with a frequency matching the rotational path velocity of the roller elements, which normally is no integer order. Furthermore, all sorts of excitations can come from the driving of the coupling. Examples are the number of motor poles of an electric motor, the number of teeth of a geared transmission within the drive, or combustion in case of an engine. Integer multiples of these orders can sometimes also cause excitations.

Shock A shock is a sudden acceleration, for example caused by a hammer impact. A shock has a broad frequency range, and thus can excite many natural frequencies.

A.2.2. Dynamics of conventional rotational couplings

Numerous studies into the dynamics of conventional rotational couplings and their effect on rotor systems have been done. In the following, only some work regarding linkage type couplings is discussed. As mentioned earlier, the linkage type couplings are more attractive to convert to compliant. Analysis of conventional couplings can serve as an inspiration for the future analysis of compliant versions, and potential problems can be indicated.

The dynamics of the Cardan joint (also universal or Hooke joint) is a frequent topic of analysis, as it is a commonly implemented coupling and as it gives rise to velocity difference increasing with misalignment angle. Placing two couplings with equal angle and 90 deg phase difference in series cancels out this error. However, the intermediate shaft still has an oscillating velocity and loads are non-constant.

An elaborate work into the dynamics of the universal joint is done by Chen [12], in which the dynamic (reaction) forces are expressed. To also incorporate manufacturing tolerances, the revolute joints are modelled as cylindrical joints, changing the mechanism from RRRR to RCCC. Results are applicable for both steady-state as transient case. Acceleration in floating and output link due to the non-constant velocity transfer at misalignment results in significant radial forces in output link, which also give rise to axial torque on output joint.

Ota and Kato studied the dynamics of rotor systems driven by a universal joint [13–15]. Several domains of unstable vibration are indicated. A coupling between the torsional and lateral vibrations is indicated, caused by the universal joint. The angular velocity fluctuations in the rotor system are governed by the misalignment angle. When the shaft vibrates laterally at a critical velocity, this joint angle changes due to this bending and rotating speed deviates, coupling the lateral to the torsional vibrations. The vibrations become unstable at 'nearly half the sum of the natural angular frequency for the lateral vibration and the one for the torsional vibration'. A summed parametric vibration occurs, consisting of both the lateral and torsional frequency.

Instability in rotor systems driven by a universal joint is further analysed by Mazzei [16], indicating instabilities such as flutter, parametric and forced. Very light damping moves flutter instabilities outside the working range of the coupling. Parametric and forced instabilities however were found to occur within the working range. For the first, an increase in bearing damping will stabilize the system and move the zones of parametric instability out of the working range. Forced instability occurred when rotational velocity reaches a systems natural frequency divided by two.

Liu describes an overconstrained Hooke type joint with flexible parts [17], which sort of forms the boundary between a conventional and a compliant coupling. The moving revolute joints in a normal universal joint are replaced by cylindrical joints (RCCR), and the intermediate body (the middle cross in a normal universal joint) is replaced by a flexible plastic part. The flexibility of this part permits the overconstrained coupling to work. The overconstraint turns out to be beneficial, compensating dynamic effects and reducing force magnitudes.

Summary of found phenomena Two instability phenomena found in the above literature are explained in a general sense in this section.

Parametric instability Oscillations can be driven by a varying system parameter in time. This is called parametric oscillation. A common example of this behaviour is the child standing on a swing, standing and squatting periodically [18]. By doing this, he changes the moment of inertia of the swing and thus its resonance frequency. This then drives the oscillation. An initial amplitude is needed to start this phenomena. If the parameters vary with twice the natural frequency of the swing, the amplitude of oscillation can grow exponentially if no energy dissipation mechanism is present. The phase between parameter change and oscillation is constant then.

Parametric excitation is different from the case of a forced or driven oscillator, is then amplitude grows linearly, and no initial amplitude is needed.

Flutter An interpretation of flutter is the energy transfer between adjacent mode shapes, and can thus only occur at coinciding mode frequencies and shapes [19]. One mode absorbs energy and feeds it to the other. This phenomena is mainly known as the interaction between an elastic structure and a fluid flow, such as on an air plane wing. Here, the elastic structure undergoes a harmonic motion at a point of zero nett damping. The nett damping is the sum of the damping in the elastic structure itself and the negative effect of the fluid forces. Negative nett damping will further excite the mode.

In the case of a shaft driven by an universal joint, similar self excited vibrations can thus occur when the fluctuating torque is in phase with the (lateral) velocity of the shaft. Lateral mode shapes can then be excited.

A.2.3. Dynamics of compliant rotational couplings

In this section, first already existing literature about the dynamics of compliant couplings is given. Then, dynamic analysis methods used on other types of compliant mechanisms are discussed.

In the work of Xu [20, 21] the dynamic effect of shaft misalignment and rotor unbalance of a motor-flexible coupling-rotor system is studied and modelled. The model is validated with experimental results.

As perfect alignment between driving and driven machine is almost impossible to achieve and maintain during operation, often flexible couplings are used to accommodate for small misalignments.

Results show that rotor unbalance generates vibrations of the first order, while shaft misalignment generates second order content. Misalignment effects may not be apparent if the second order is not close to one of the systems natural frequencies. The use of flexible couplings can change these natural frequencies.

In the study of Al-Hussain [22], the effect of angular misalignment of two rigid rotors connected through a flexible mechanical coupling is analysed. Dimensionless stability criteria as function of misalignment, coupling and bearing properties are given. It is shown that as the angular misalignment or coupling stiffness terms increase, the stability regions increase accordingly.

Other compliant fields Lyon et al. used the same PRBM used for design and displacement analysis to predict the first resonance frequency of several parallel-guiding and straight-line flexure mechanisms [23]. The flexures are thus modelled as rigid links, with torsional springs at each end. Experimental testing on those was done as a verification. The modelled resonance frequencies match the experimental results for each mechanism with an error less than 9 percent.

Boyle et al. also used the PRBM to study the dynamic response of compliant constant-force compression mechanisms [24]. The results in these studies show the possibility of using the pseudo-rigid-body model in the dynamics of compliant mechanisms.

In the work of Yu a dynamic model of compliant (flexure) mechanisms is proposed, based on the pseudo-rigid-body model and dynamic equivalence [25]. The dynamic equivalent rotational stiffness is given for different loading scenarios. Flexure inertia is modelled as dynamic equivalent lumped mass at the connection points to the motion stage. This results pseudo-rigid-body dynamic model (PRBDM). Using the equivalent stiffness and inertia, potential and kinetic energy is formulated. Substituting these in the Lagrange equation yield the equation of motion, with which the first natural frequency of the system can be calculated. Results are within a few percent accuracy compared to FEA for different case studies.

The methods based on the pseudo-rigid-body models have only one degree of freedom and therefore only one, normally the first, frequency can be predicted.

Li and Kota used existing finite element modelling techniques to study the dynamic behaviour of compliant mechanisms [26]. Planar frame elements are used to model the flexures. Basic formulations are given for building the equations of motion, time integration and damping implementation, frequency spectrum analysis and sensitivities are given. The sensitivity analysis form the basis for dynamic synthesis for compliant mechanisms. As a case study, a stroke amplification mechanism is analysed, in which the benefit of sensitivity analysis is made clear.

As in the finite element approach flexures are modelled using many DOF, the dynamic behaviour can be analysed more in depth than using the often 1DOF PRBM methods. However, building a FE model is more cumbersome, and needs the design to be more established already. Using the PRBM method, the resulting equation of motion is easily understandable and the influence of different parameters is directly clear.

A.3. Results: potential failure chart

The found potential dynamic problems are summarized in the form of a flowchart, in figure A.4. On the left side, the key properties of a coupling are stated. Certain properties then can lead to certain phenomena, which are all given in the middle section. These problems can be the cause of a failure, of which the failure modes and their effect are given on the right side.

In the grey boxes, questions about certain properties are given. If this property holds for the design at hand, then the following (white) boxes indicate potential problems. It however is no guarantee that this problem will indeed occur.

It is not claimed that this flowchart is complete and contains all possible dynamic problems. It is however an schematic overview of the problems found and deduced in this work.

A.4. Conclusion

In this work potential dynamic problems for compliant rotational couplings were indicated. General dynamics of rotational bodies were summed up. It is expected that (inertial) centrifugal and Coriolis forces are potentially harmful when compliance is high in those directions. Furthermore, the origin of resonance and their possible excitations are discussed. In compliant couplings, motion directions will likely have a non-zero resonance frequency, and bearing direction a far from infinite frequency, as opposed to conventional mechanisms. The lower frequencies are more likely to be excited during operation.

In the work about the dynamics of conventional couplings, several instability phenomena were indicated. Parametric instability can occur when system parameters are periodically changing with a frequency matching integers (sub)multiples of a resonance frequency of the system. Flutter instability is a phenomena in which one mode absorbs energy and feeds it to a mode with coinciding mode shape and frequency.

For the case of the dynamics of compliant couplings, work was found concerning the dynamics of rotor systems driven by small misalignment industrial flexible couplings. It was indicated that the flexible couplings can change the natural frequencies of the rotor system. Furthermore, coupling stiffness can increase stability.

A flowchart indicating different potential dynamic phenomena deteriorating the performance of a compliant coupling was build, in which a first relation is given between the couplings characteristics and its performance. It is based on the found phenomena in literature as well as common dynamics knowledge.

Secondly, to the writers knowledge the dynamics of large misalignment compliant rotational couplings has not been studied yet. Research has been done in the field of small misalignment flexible couplings frequently used in industry. This work is not applicable to large misalignment couplings as among others stiffness values are significantly higher. For compliant mechanisms in general, dynamics have primarily been studied using PRBM methods and FEA. The former is straightforward but only gives little insight, while the latter gives more insight but is labour-intensive. Furthermore, in FEA it is less straightforward to gain insight in influential design parameters.

It can thus be concluded that there exists a knowledge gap for the dynamics of (flexure based) large misalignment compliant rotational couplings. This gap hinders design and implementation, despite the potential benefits of a compliant mechanism.

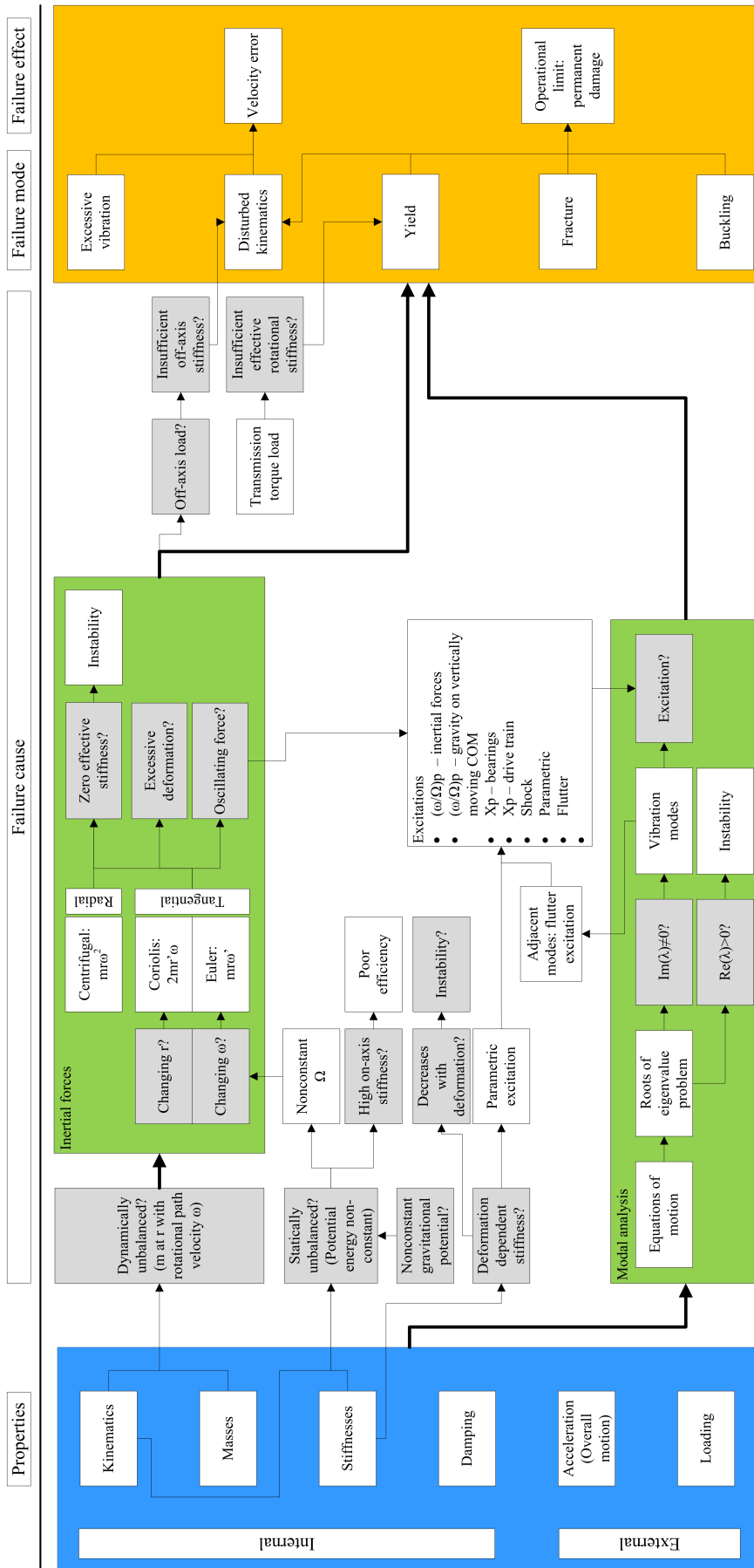


Figure A.4: 'Flow chart' of potential dynamic problems in compliant rotational transmissions, with input angular velocity Ω .

B

Finite Element Modal Analysis

B.1. Description of the model

In this appendix, the Ansys finite element analysis (FEA) model used to find the static resonance frequencies and mode shapes of the compliant Oldham coupling as proposed in [6] is described. A modal analysis is conducted for the undeformed coupling and for some characteristic deformed cases is done.

The goal of this model is twofold. In the first place the goal is to find the resonance frequencies and mode shapes of this coupling under several conditions. These give insight in the stiffness of the whole coupling, and weak points leading to low resonances can be improved. Furthermore the results can be compared with the results from the experiments.

In the second place it is used to compare with the results from the multibody models. Both resonance frequencies and mode shapes can be compared. As the multibody models only incorporate the dynamics of the flexure mechanism, and not of its supported bodies, comparison gives an indication of the applicability of the multibody models. If deformation of the plastic structure is dominant, the multibody models do not give an complete representation of the dynamics of the coupling. In that case, FEA is more suitable, or dominant support body stiffnesses should be incorporated in the multibody model, or the design should be altered in such a way that the support bodies deformations are no longer dominant.

Furthermore, to determine if the multibody models give a correct representation of the flexure dynamics, an altered FEA is done. In that analysis the plastic (PMMA) and aluminium bodies of the flexure mechanisms are given a stiffness many orders higher than their physical values and of the flexure mechanism. This results in the lower mode shapes only originating from the flexure mechanism, which than is a good comparison to the multibody model.

The build Ansys model can also be a starting point for further FEA of the Oldham coupling. From the current model already stress and strain values for certain prescribed deformations or forces can be determined. Furthermore, the model can be a basis for dynamic analysis, such as a transient dynamic analysis.

B.1.1. Build up of the model

The model of the Oldham coupling mostly consists of BEAM188 (Timoshenko) beam elements, in which shear deflections are included. The cross sections of different elements are defined using the SECTYPE command. The 16 AISI316L stainless steel 16 beam flexures are modelled with a Young's modulus $E = 193$ GPa, and a density of $\rho = 7557$ kg/m³. The PMMA bodies with $E = 3.3$ GPa, and a density of $\rho = 1023$ kg/m³, the aluminium reinforcement ring between the two outer PMMA bodies with $E = 70$ GPa, and a density of $\rho = 2476$ kg/m³. The densities of the bodies are tuned such that they match the weight of the separate bodies of the prototype. For all materials a Poisson ratio $\nu = 0.3$ is used.

The model is build parametrically so that different design parameter can be changed easily. At the beginning of the code, also the angle (over the Z-axis) of the coupling can be chosen, as the stiffness depends on this angle when axle misalignment is present. The key points and lines are then constructed automatically in different loops. As the design consists of two DP-DP flexure mechanism layers placed perpendicular onto each other, these loops are executed twice in two different perpendicular coordinate systems. Then, lines representing different elements with different cross sections are categorised, after which the mesh is generated over these different categories (LMESH). For the beam flexures a fixed number of 50 elements per beam is

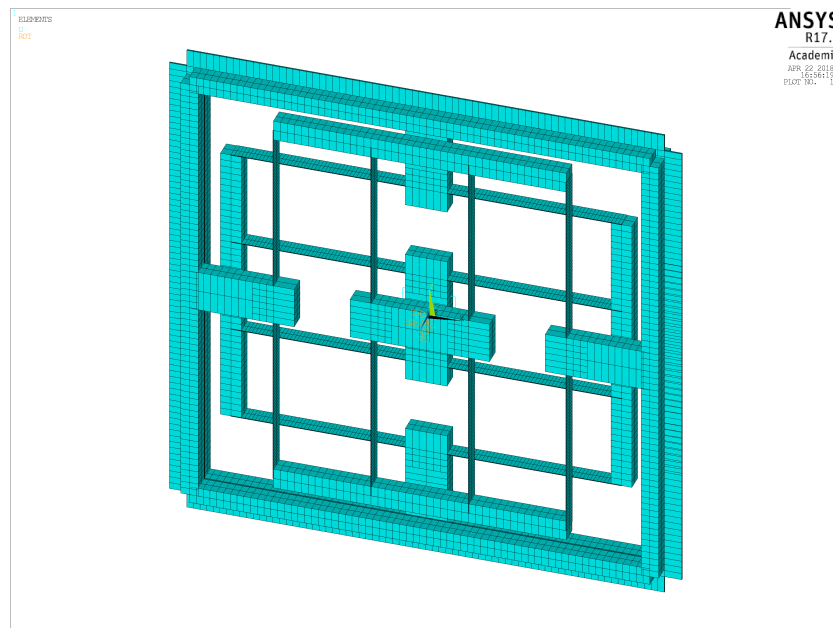


Figure B.1: Mesh of the Oldham coupling

chosen. For the PMMA and aluminum bodies, an fixed element size of 2 mm. Effect of element size is checked by both increasing and decreasing the element sizes, which did not cause significant changes in the results.

In the prototype, the PMMA outer (coupler) body is glued to the aluminium reinforcement ring. This is modelled using 2×16 MPC184 (multi point constraint) elements (this number can easily be enlarged in the code, the constraints are built in a loop). These elements constrain different nodes at different locations rigidly to each other. By doing so, the two PMMA layers and the intermediate aluminium are connected rigidly to each other, and the glue connection is thus modelled as being rigid.

In figure B.1 the mesh before analysis is shown. The input and output axle will be along the Z-axis, but are not modelled in the mesh. The XY-plane is the plane of the DP-DP flexure mechanisms. For the goal of the modal analysis, the input axle connection point (middle body on the foreground) is fixed to the world and thus constrained in all 6 DOF. In case of axle misalignment, the input axle is constraint to a chosen negative Y value. The output axle connection point (middle body in the background) lies at the origin of the coordinate system and is free to rotate along its axis (Z-axis) and constrained in all other directions. The output axle inertia has a significant effect on the couplings rotational mode shapes, and thus is incorporated in the model via a MASS21 element. As only the rotation around the Z-axis is free, only the mass moment of inertia along this axis has to be incorporated.

The analysis itself consists of two parts. In the first part, which is a static analysis, the chosen axle misalignment is applied and static equilibrium is found for this scenario. The second part, the actual modal analysis can then be done of the deformed (prestressed) coupling, a so called 'linear perturbation modal analysis'. 'The purpose of the first phase is to re-establish a snapshot of the stiffness matrices at the specified restart point. The second phase, ending with the second SOLVE command, is for the actual linear perturbation analysis.' (Ansys Manual).

The actual used code is given in the next section.

B.2. Ansys Mechanical APDL Code

Main code:

```

! Finite Element Model Of The COMPLIANT OLDHAM COUPLING As Designed By Davood Farhadi Macheuposhti
! Based on static analysis written by Davood Farhadi Macheuposhti, 2016
! Rewritten for perturbed modal analysis and altered to coupling design as used for experiments by Henri van der Deijl,
  2017

FINISH
/CLEAR
/OUTPUT

pi = 3.14159265359

!!!!!!!!!!!!!!!!!!!!!!!!!!!!!!!!!!!!!!!!!!!!!!!!!!!!!!!!!!!!!!!!!!!!!!!!!!!!

System_RotZ = 0           ! rotation of whole system, default 90, 45=135
Axle_Offset_X = 0        ! output axis offset (misalignment)
Axle_Offset_Y = 0        ! output axis offset (misalignment)
Axle_Offset_RotZ = 270   ! relative rotation between two layers

!!!!!!!!!!!!!!!!!!!!!!!!!!!!!!!!!!!!!!!!!!!!!!!!!!!!!!!!!!!!!!!!!!!!!!!!!!!!

x1 = 0
y1 = 0
x2 = 0
y2 = 0
RotZ2 = Axle_Offset_RotZ
LOCAL, 11, 0, x1, y1, 0, RotZ2 + System_RotZ, 0, 0      ! build coord sys 11, at input axle
LOCAL, 12, 0, x2, y2, 0, System_RotZ, 0, 0             ! build coord sys 12, at output axle

!!!!!!!!!!!!!!!!!!!!!!!!!!!!!!!!!!!! FEA Parameters !!!!!!!!!!!!!!!!!!!!!!!!!!!!!

n_elements = 50           ! number of elements per flexure
frame_el_size = 2e-3      ! element size for PMMA and Alu parts
substeps = 10            ! Substeps for static analysis
nModes = 50              ! Number of mode shapes to compute

!!!!!!!!!!!!!!!!!!!!!!!!!!!!!!!!!!!! Geometry !!!!!!!!!!!!!!!!!!!!!!!!!!!!!

! Cross sections
Flexure_t = .2e-3         ! flexure thickness
Frame_t = 5e-3
Fixture_t = 12e-3
Shuttle_t = 6e-3
Axle_t = 12e-3
Spacer_t = 10e-3

! Geometry
length = 50e-3 ! flexure length
stroke = 28e-3
layerThickness = 5e-3
spacerThickness = .5e-3
nMPC = 1

a = 6e-3           ! x distance from center to begin flexure
b = a + length    ! x distance from center to end flexure
c = 66e-3         ! x distance from center to center of outer ring

d = stroke / 2    ! y distance from center to first flexure
e = d + stroke    ! y distance from center to second flexure

f = c + (Spacer_t-Frame_t)/2 ! center 'radius' of spacer sheet

t = layerThickness
u = spacerThickness

! Output axle
Iaxle = 5.4502e-6 ! inertia of short IDT camera setup output axle

!!!!!!!!!!!!!!!!!!!!!!!!!!!!!!!!!!!! Constants !!!!!!!!!!!!!!!!!!!!!!!!!!!!!

! density with correction factor to match measured mass
E1 = 193e9        ! RVS
v1 = 0.3
rho1 = 7930*.953 ! 7990 = stainless steel, originally 2320
Mul = 0.14

!E2 = 3300e6      ! PMMA
E2 = 100e12       ! assume rigid
v2 = 0.3
rho2 = 1180*.867 ! PMMA

```

```

Mu2 = 0.14

!E3 = 70e9                ! ALU
E3 = 100e12              ! assume rigid
v3 = 0.3
rho3 = 2700*.917
Mu3 = 0.14

!!!!!!!!!!!!!!!!!!!!!!!!!!!! Element types and cross sections !!!!!!!!!!!!!!!!!!!!!!!!!!!!!

/PREP7
ET,1, BEAM188
ET,4, MPC184,1           ! rigid beam
ET,5, MASS21

/ESHAPE,1                ! SCALE=1 (use real constants and section defenitions)

SECTYPE,1,beam,RECT      ! (flexure) SECID, Type, Subtype, Name, REFINKEY
SECDATA ,Flexure_t , t   ! B, H, Nb, Nh (N = number of cells)

SECTYPE,2,beam,RECT      ! (frame) SECID, Type, Subtype, Name, REFINKEY
SECDATA ,Frame_t , t     ! B, H, Nb, Nh (N = number of cells)

SECTYPE,3,beam,RECT      ! (fixture , flexure support) SECID, Type, Subtype, Name, REFINKEY
SECDATA ,Fixture_t , t   ! B, H, Nb, Nh (N = number of cells)

SECTYPE,4,beam,RECT      ! (shuttle) SECID, Type, Subtype, Name, REFINKEY
SECDATA ,Shuttle_t , t   ! B, H, Nb, Nh (N = number of cells)

SECTYPE,5,beam,RECT      ! (axle) SECID, Type, Subtype, Name, REFINKEY
SECDATA ,Axle_t , t      ! B, H, Nb, Nh (N = number of cells)

SECTYPE,6,beam,RECT      ! (axle) SECID, Type, Subtype, Name, REFINKEY
SECDATA ,Spacer_t , u    ! B, H, Nb, Nh (N = number of cells)

!!!!!!!!!!!!!!!!!!!!!!!!!!!! Material property defenition !!!!!!!!!!!!!!!!!!!!!!!!!!!!!

! Material properties 1
MP,EX,1,E1               ! Young's modulus
MP,PRXY,1,v1             ! Poisson's ratio
MP,DENS,1,rho1           ! Density
!MP,Mu,1,Mu1

! Material properties 2
MP,EX,2,E2               ! Young's modulus
MP,PRXY,2,v2             ! Poisson's ratio
MP,DENS,2,rho2           ! Density
!MP,Mu,2,Mu2

! Material properties 3
MP,EX,3,E3               ! Young's modulus
MP,PRXY,3,v3             ! Poisson's ratio
MP,DENS,3,rho3           ! Density
!MP,Mu,3,Mu3

! Material properties 4 (MPC)
MP,DENS,4,0               ! Density

! Added inertia
R,5,0,0,0,0,0,Iaxle

!!!!!!!!!!!!!!!!!!!!!!!!!!!! Keypoints !!!!!!!!!!!!!!!!!!!!!!!!!!!!!

kp = 100                  ! 100 keypoints reserved per layer

!! Two layers
*DO,I,0,2,2
CSYS,11+I/2              ! chose coord sys
n=I*100                  ! layer number range
z = I*(t+u)/2            ! z value for current layer

K,1+n,0,0,z              ! X+
K,20+n,c,c,z             ! Y+
K,30+n,c,-c,z            ! X-
K,40+n,-c,-c,z          ! Y-
K,50+n,-c,c,z

K,25+n,c,0,z             ! X+
K,35+n,0,-c,z            ! Y+
K,45+n,-c,0,z           ! X-
K,55+n,0,c,z             ! Y-

*DO,J,1,nMPC              ! intermediate constrain keypoints
K,20+J+n,c,J*(c/(nMPC+1)),z

```



```

*DO, J, 0, 1
nn = 60+J*30+n
L, nn+1, nn+2
L, nn+2, nn+3
*ENDDO
L, 62+n, 45+n
L, 92+n, 25+n
*ENDDO
*GET, Line_fixture, LINE, 0, NUM, MAXD

!! SHUTTLE
*DO, I, 0, 2, 2
CSYS, 11+I/2          ! chose coord sys
n=I*100              ! layer number range
*DO, J, 0, 2
nn = 60+J*10+n
L, nn, nn+10
L, nn+4, nn+4+10
*ENDDO
*ENDDO
*GET, Line_shuttle, LINE, 0, NUM, MAXD

!! AXLE
*DO, I, 0, 2, 2
CSYS, 11+I/2          ! chose coord sys
n=I*100              ! layer number range
*DO, J, 0, 1
nn = 70+J*10+n
L, nn+1, nn+2
L, nn+2, nn+3
*ENDDO
L, 72+n, 1+n
L, 82+n, 1+n
*ENDDO
*GET, Line_axle, LINE, 0, NUM, MAXD

!! Intermediate sheet
CSYS, 11              ! chose coord sys
n=100                 ! layer number range
*DO, J, 0, 7
nn=20+J*5+n
*DO, JJ, 1, nMPC
L, nn+JJ-1, nn+JJ
*ENDDO
*ENDDO
*DO, J, 0, 6
nn=20+J*5+n
L, nn+nMPC, nn+5
*ENDDO
L, nn+nMPC, 20+n
*GET, Line_spacer, LINE, 0, NUM, MAXD

!! MPC between sheets
! first layer
n = 100

*DO, I, 0, 1
L, 20+n, 20+I*210           ! corner/middle constraint lines
L, 30+n, 30+I*210
L, 40+n, 40+I*210
L, 50+n, 50+I*170
L, 25+n, 25+I*210
L, 35+n, 35+I*210
L, 45+n, 45+I*210
L, 55+n, 55+I*170

*DO, J, 1, nMPC             ! intermediate constraint lines
L, 20+J+n, 20+J+I*210
L, 25+J+n, 25+J+I*210
L, 30+J+n, 30+J+I*210
L, 35+J+n, 35+J+I*210
L, 40+J+n, 40+J+I*210
L, 45+J+n, 45+J+I*210
L, 50+J+n, 50+J+I*170
L, 55+J+n, 55+J+I*170
*ENDDO
*ENDDO
*GET, Line_MPC, LINE, 0, NUM, MAXD

!!!!!!!!!!!!!!!!!!!!!!!!!!!!!!!!!!!!!!!!!!!!!!!!!!!!!!!!!!!!!!!!!!!!!!!!!!!!!!!!!!!!!!!!!!!!!!!!!!!!!!!!!!!!!!!!!!!!!!!!
!!!!!!!!!!!!!!!!!!!!!!!!!!!!!!!!!!!!!!!!!!!!!!!!!!!!!!!!!!!!!!!!!!!!!!!!!!!!!!!!!!!!!!!!!!!!!!!!!!!!!!!!!!!!!!!!!!!!!!!!
! FLEXURE
TYPE, 1                       ! element type beams (flexures)
SECNUM, 1                     ! Sets the element section attribute pointer

```



```

MAT,1
LSEL,S,LINE,,Line_0+1,Line_flexure ! select lines by number, between Line_ID1+1 and Line_ID2
LESIZE,ALL,, ,n_elements ! Define number of elements per line
IMESH,ALL
*GET,ELEM_FLEXURE,ELEM,0,NUM,MAXD

! FRAME
TYPE,1 ! element type frame
SECNUM,2
MAT,2
LSEL,S,LINE,,Line_flexure+1,Line_frame
LESIZE,ALL,frame_el_size,, ! element size
IMESH,ALL
*GET,ELEM_FRAME,ELEM,0,NUM,MAXD

! FIXTURE
TYPE,1 ! element type frame
SECNUM,3
MAT,2
LSEL,S,LINE,,Line_frame+1,Line_fixture
LESIZE,ALL,frame_el_size,, ! element size
IMESH,ALL
*GET,ELEM_FIXTURE,ELEM,0,NUM,MAXD

! SHUTTLE
TYPE,1 ! element type frame
SECNUM,4
MAT,2
LSEL,S,LINE,,Line_fixture+1,Line_shuttle
LESIZE,ALL,frame_el_size,, ! element size
IMESH,ALL
*GET,ELEM_SHUTTLE,ELEM,0,NUM,MAXD

! AXLE
TYPE,1 ! element type frame
SECNUM,5
MAT,2
LSEL,S,LINE,,Line_shuttle+1,Line_axle
LESIZE,ALL,frame_el_size,, ! element size
IMESH,ALL
*GET,ELEM_AXLE,ELEM,0,NUM,MAXD

! SPACER
TYPE,1 ! element type frame
SECNUM,6
MAT,3
LSEL,S,LINE,,Line_axle+1,Line_spacer
LESIZE,ALL,frame_el_size,, ! element size
IMESH,ALL
*GET,ELEM_SPACER,ELEM,0,NUM,MAXD

! MPC
TYPE,4 ! element type MPC
MAT,4
LSEL,S,LINE,,Line_spacer+1,Line_MPC
LESIZE,ALL,, ,1 ! Define number of elements per line
IMESH,ALL

! Input inertia
TYPE,5
REAL,5
KMESH,1,1

! Mass output per component
!esel,s,elem,,1,10
!/SOLU
!irlf,-1
!antype,static
!solve
!eresx,-1
!FINISH
!*get,massele,elem,S,mtot,x

!!!!!!!!!!!!!!!!!!!!!!!!!!!!!!!!!!!!!!!! Constraints !!!!!!!!!!!!!!!!!!!!!!!!!!!!!!!!!!!!!

DK,1,ALL ! output axle constraint in all DOF
DK,1+2*kp,ALL ! input axle constraint in all DOF

DK,1+2*kp,ux,Axle_Offset_X ! misalignment of input with 20mm in y
DK,1+2*kp,uy,Axle_Offset_Y ! -20e-3

!DK,1+2*kp,ux,0.01414 ! misalignment of input with 20mm in x and y
!DK,1+2*kp,uy,0.01414

```

```

DKDELE,1,RotZ      ! freeing the rotational DOF of the output axle

/solu              ! Output mass properties in txt file
/output,mass_output.txt
psolve,elform
/output
finish

/SOL
/ESHAPE,1
OUTRES,ALL,ALL
SOLCONTROL,ON,ON
AUTOTS,ON

!!!!!!!!!!!! Step 1: static analysis: prestress !!!!!!!!!!!!!

/solu              ! enter solution module
antype,0           ! specify static analysis type
nlgeom,1           ! turn on large deflection effects (nonlinear)
pstres,on          ! turn on prestress effects for subsequent modal
nsub,substeps,substeps,substeps ! specify substep range
save               ! save the database
solve              ! solve the nonlinear static prestress case
finish            ! leave the solu
tion module

!!!!!!!!!!!! Step 2: modal analysis !!!!!!!!!!!!!

/solu              ! re-enter solution so we can do a new analysis
antype,,restart,1,substeps,perturb ! specify restart option for linear perturbation
! from last substep in this case
perturb,modal      ! specify modal as next analysis
solve,elform        ! calculate element formulation with solve command
modopt,subsp,nModes ! specify modal options for solution
mexpand,nModes,,YES ! specify number of modes for results calc
solve

!!!!!!!!!!!! Postprocessing

/post1             ! enter general postprocessor
INRES,ALL          ! make sure we read in all results from file
FILE,'PerturbedModal','rstp' ! specify special results file for modal results
! rsts file: modal analysis with sets being modes
! rst file: the static prestress results with sets being substeps
SET,LIST          ! List solutions

!!!!!!!!!!!! Plot mode shapes

/RGB,INDEX,100,100,100,0
/RGB,INDEX,80,80,80,13
/RGB,INDEX,60,60,60,14
/RGB,INDEX,0,0,0,0.15

SET,,, , , , ,20
!PLDISP,0          ! 0 only deformed, 1 def + undeformed
PLNS,EPTO,EQV     ! nodal Von Misses strain

/ESHAPE,1         ! SCALE=1 (use real constants and section defenitions)

!/VIEW,1,1,1,1,3,3 ! Window number, XV, YV, ZV
!/VIEW,1,0,0,1     ! Window number, XV, YV, ZV
!/VIEW,1,1,2,3     ! Window number, XV, YV, ZV

!/REP,FAST
/REPLOT

ANMODE,10,0.10, ,0 ! Animate mode shape, ANMODE, NFRAM, DELAY, NCYCL, KACCEL
!ANMODE,50,0.05, ,1 ! Animate mode shape, ANMODE, NFRAM, DELAY, NCYCL, KACCEL

!/ANFILE,SAVE,'20mm_0deg_Model17',' ',' ' ! save mode shape animation in avi file

```

Code to animate selected mode shapes and to save images of multiple mode shapes:

```

!!!!!!!!!!!! Plot mode shapes
/RGB,INDEX,100,100,100,0
/RGB,INDEX,80,80,80,13
/RGB,INDEX,60,60,60,14
/RGB,INDEX,0,0,0,0.15

SET,,, , , , ,1
!PLDISP,0          ! 0 only deformed, 1 def + undeformed
PLNS,EPTO,EQV     ! nodal Von Misses strain

/ESHAPE,1         ! SCALE=1 (use real constants and section defenitions)

```

```

/VIEW,1,1,1,3,3          ! 3D view      (Window number, XV, YV, ZV)
!/VIEW,1,0,0,1          ! Perpendicular view
!/VIEW,1,1,2,3          ! 3D view      Window number, XV, YV, ZV

/REPLOT

ANMODE,10,0,10, ,0      ! Animate mode shape, ANMODE, NFRAM, DELAY, NCYCL, KACCEL

!/ANFILE,SAVE,'20mm_0deg_Mode17',' ',' ' ! save mode shape animation in avi file

!!!!!!!!!! Save PNG of multiple mode shapes
i_=1
*do,i_,1,50,1           ! loop for i from 1 to 50 per 1

SET,,, , , ,i_         ! Select nth mode shape (set)

!PLDISP,0               ! 0 only deformed, 1 def + undeformed
PLNS,EPTO,EQV          ! nodal Von Misses strain

/ESHAPE,1              ! SCALE=1 (use real constants and section defenitions)
/GFILE, 2400
/SHOW,PNG

/VIEW,1,1,1,3,3          ! 3D view      (Window number, XV, YV, ZV)
!/VIEW,1,0,0,1          ! Perpendicular view
!/VIEW,1,1,2,3          ! 3D view      Window number, XV, YV, ZV
/REPLOT

i_=i_+1
/SHOW,CLOSE
*ENDDO

```

B.3. Mode shapes

In this section the results of the modal analysis for multiple axle misalignments and angles is given. Per scenario, first images of the first 20 mode shapes will be given, after which a description of these mode shapes is given in a table. Thereafter, specific modes of interest are then discussed in more detail. Mode shapes shown have an arbitrary amplitude. For some figure this results in bodies hitting each other, this has no influence on the model, contact is not modelled.

B.3.1. Zero axle misalignment - zero angle

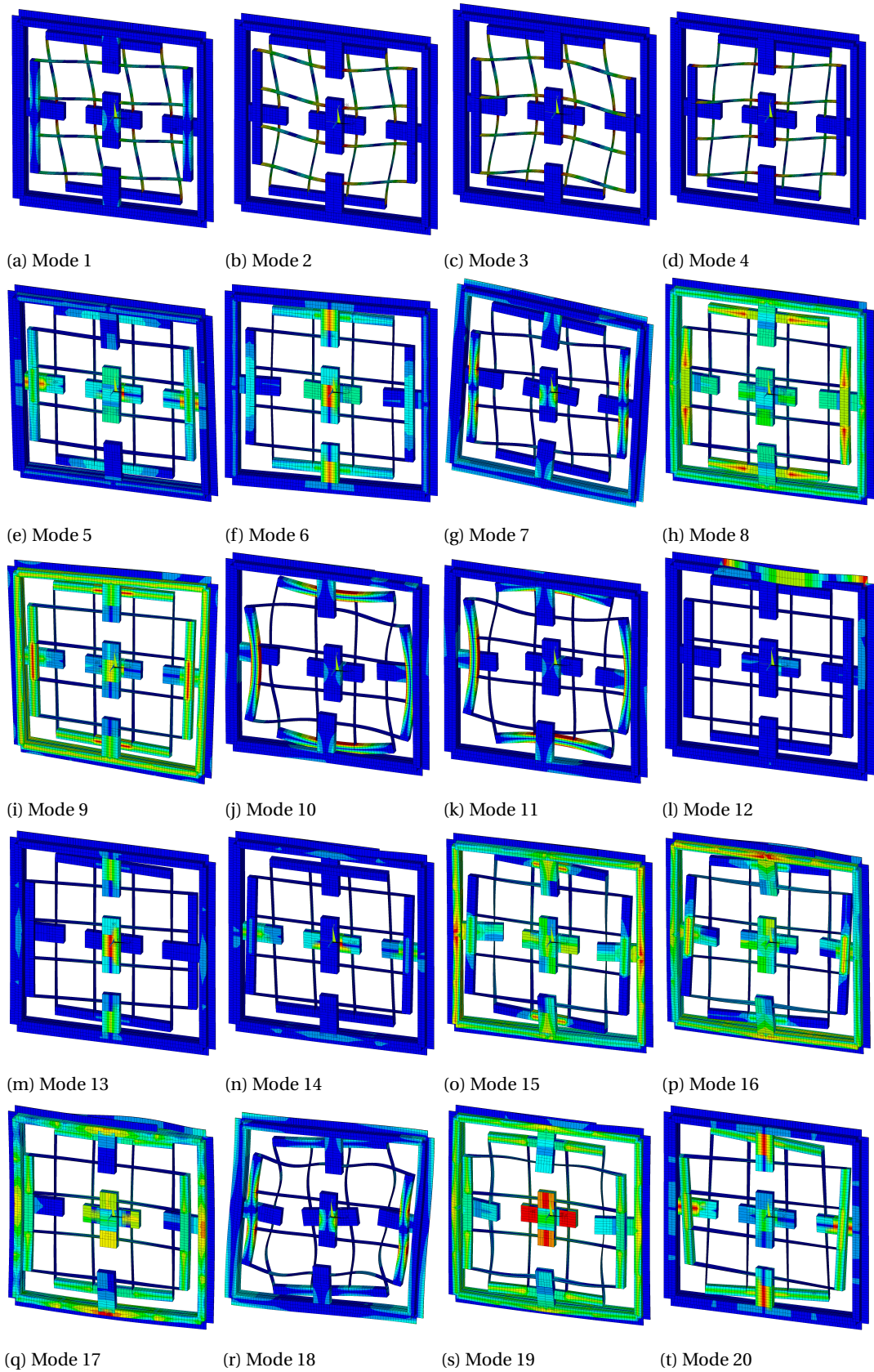
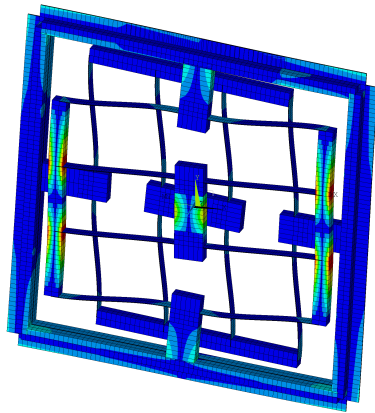


Figure B.2: Mode shapes for zero axle misalignment - zero angle

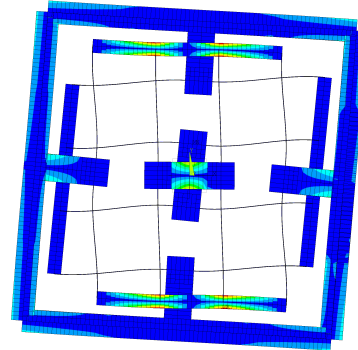
Table B.1: Description of mode shapes for zero axle misalignment - zero angle

#	Freq [Hz]	Dominant motion	Direction of motion	Origin of deformation
1	43.47	shuttles	translation	flexures, first bending mode
2	44.53	shuttles	translation	flexures, first bending mode
3	44.53	shuttles	translation	flexures, first bending mode
4	44.56	shuttles	translation	flexures, first bending mode
5	66.35	coupler	X rotation	flexure connection points of output and coupler body
6	67.49	coupler	Y rotation	flexure connection points of input and coupler body
7	88.54	coupler and output	Z rotation	input and input layer shuttles bending, flexure bending
8	101.86	coupler	Z translation	flexure connection points of coupler
9	147.49	coupler		coupler, torsion in X and Y
10	172.75	coupler	XY translation	shuttle (and flexure) bending
11	173.44	coupler	XY translation	shuttle (and flexure) bending
12	262.94	coupler, reinforcement ring	Z translation	coupler reinforcement ring bending
13	285.64	input layer shuttles	Z translation	flexure connection points of input and coupler body
14	286.03	output layer shuttles	Z translation	flexure connection points of output and coupler body
15	326.46	coupler, flexure connection points	Z translation	(flexure connection points of) coupler body
16	327.46	coupler, flexure connection points	Z translation	(flexure connection points of) coupler body
17	342.53	coupler, flexure connection points	Z translation	(flexure connection points of) coupler body, shuttles
18	355.85	output, coupler	Z rotation	input and shuttles bending, coupler body shear, flexure bending
19	366.49	shuttles, coupler	Z translation	flexure connection points of input, output and coupler body, flexure bending
20	398.05	shuttles	X and Y rotation	flexure connection points of coupler body

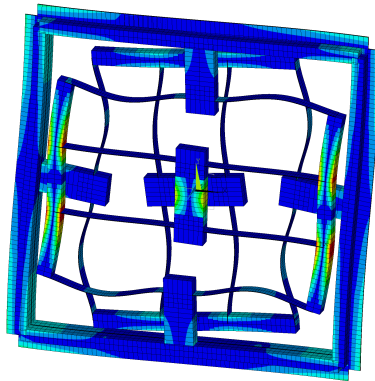
Three modes are specially interesting, as their mode shape possesses a large amount of output axle rotation, and are thus likely to cause significant velocity error between input and output axle when excited. This is mode 7 at 88.54 Hz, mode 18 at 355.85 Hz and mode 45 at 751.34 Hz. Detailed figures of these mode shapes are given below.



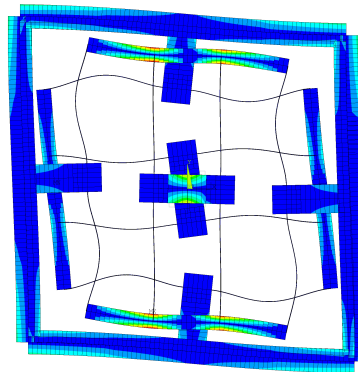
(a) Mode 7



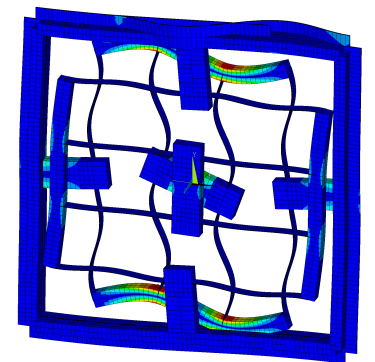
(b) Mode 7 - perpendicular view



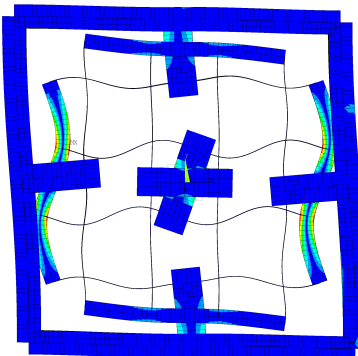
(c) Mode 18



(d) Mode 18 - perpendicular view



(e) Mode 45



(f) Mode 45 - perpendicular view

Figure B.3: Mode shapes with a potentially large effect on the velocity error

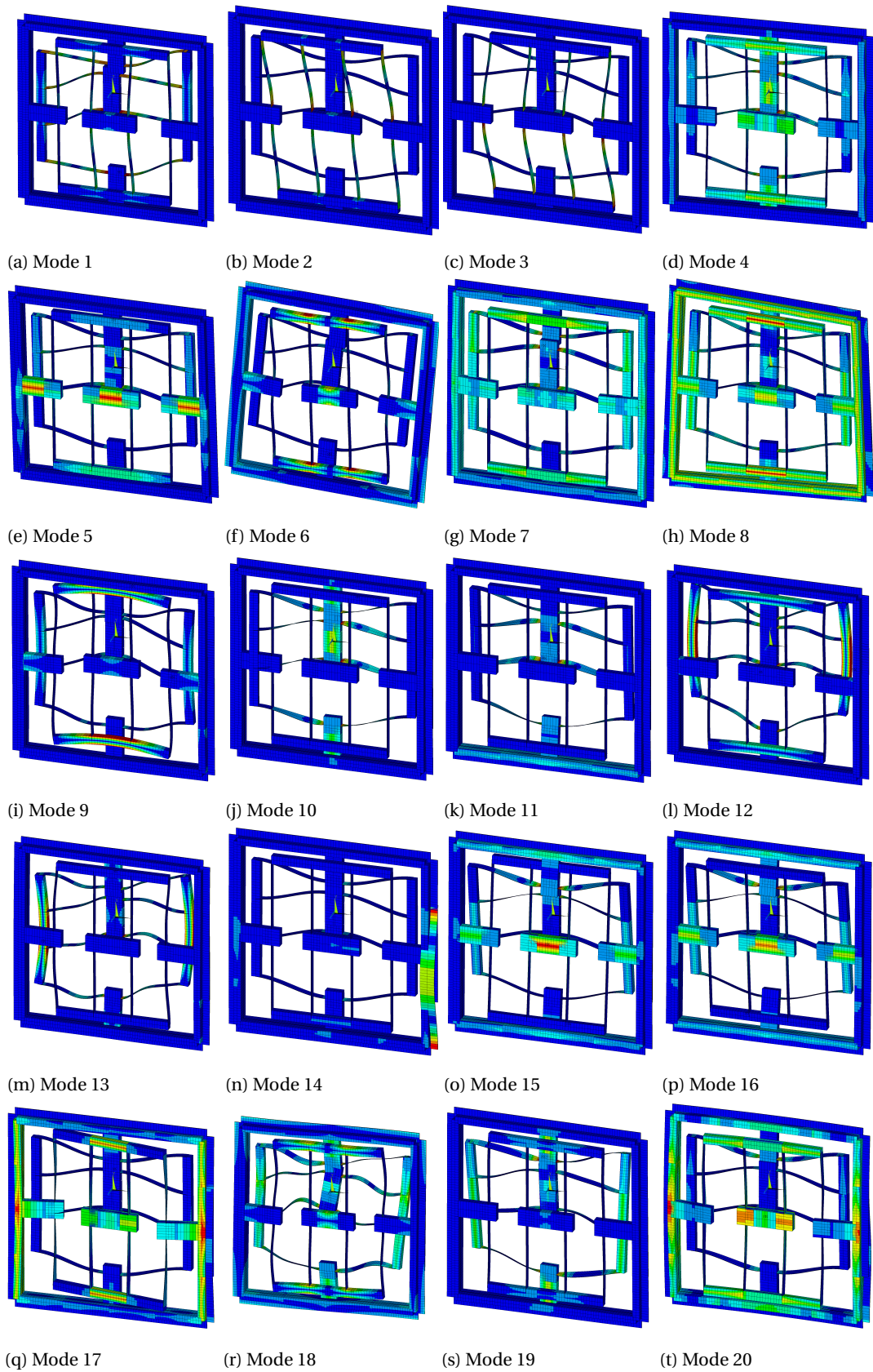
B.3.2. 20mm axle misalignment - zero angle

Figure B.4: Mode shapes for 20 mm axle misalignment - 0° angle

Table B.2: Description of mode shapes for 20 mm axle misalignment - 0° angle

#	Freq [Hz]	Dominant motion	Direction of motion	Origin of deformation
1	27.88	coupler (and output layer shuttles)	X translation (tangential)	flexures
2	44.30	input layer shuttles	X translation (tangential)	flexures, first bending mode
3	45.54	input layer shuttles	X translation (tangential)	flexures, first bending mode
4	55.03	coupler	Y rotation	flexure connection points of input, output and coupler body
5	59.24	coupler	X rotation	flexure connection points of input and coupler body
6	87.51	coupler and output	Z rotation	input and input layer shuttles bending, flexure bending
7	89.77	coupler	Z translation	flexure connection points of coupler, flexures
8	141.88	coupler		coupler, torsion in X and Y
9	164.09	coupler	Y translation	shuttle (and flexure) bending
10	203.13	output layer shuttles	Z translation	flexure connection points of output and coupler body, flexure torsion
11	216.97	output layer shuttles	Z translation, X rotation	lower connection point of coupler body, flexure torsion
12	226.21	output layer shuttles	Y translation	output layer flexures, shuttles
13	250.19	output layer shuttles	Y translation	output layer flexures, shuttles
14	266.26	coupler, reinforcement ring	Z translation	coupler reinforcement ring bending
15	278.80	output layer shuttles	Z translation, X rotation	flexure connection points of input and coupler body
16	299.16	output layer shuttles	Z translation, X rotation	flexure connection points of output and coupler body
17	323.65	input layer shuttles, coupler connection points	Y rotation	flexure connection points of coupler, input, flexure torsion
18	330.46	output	Z rotation	output layer flexures, shuttles
19	332.26	output layer shuttles	Z translation, X rotation	flexure connection points of output and coupler body
20	349.16	input layer shuttles	Z translation	coupler body, input, flexures over stiff side

Again, a few modes which possess a large amount of output axle rotation, and are thus likely to cause significant velocity error between input and output axle when excited.

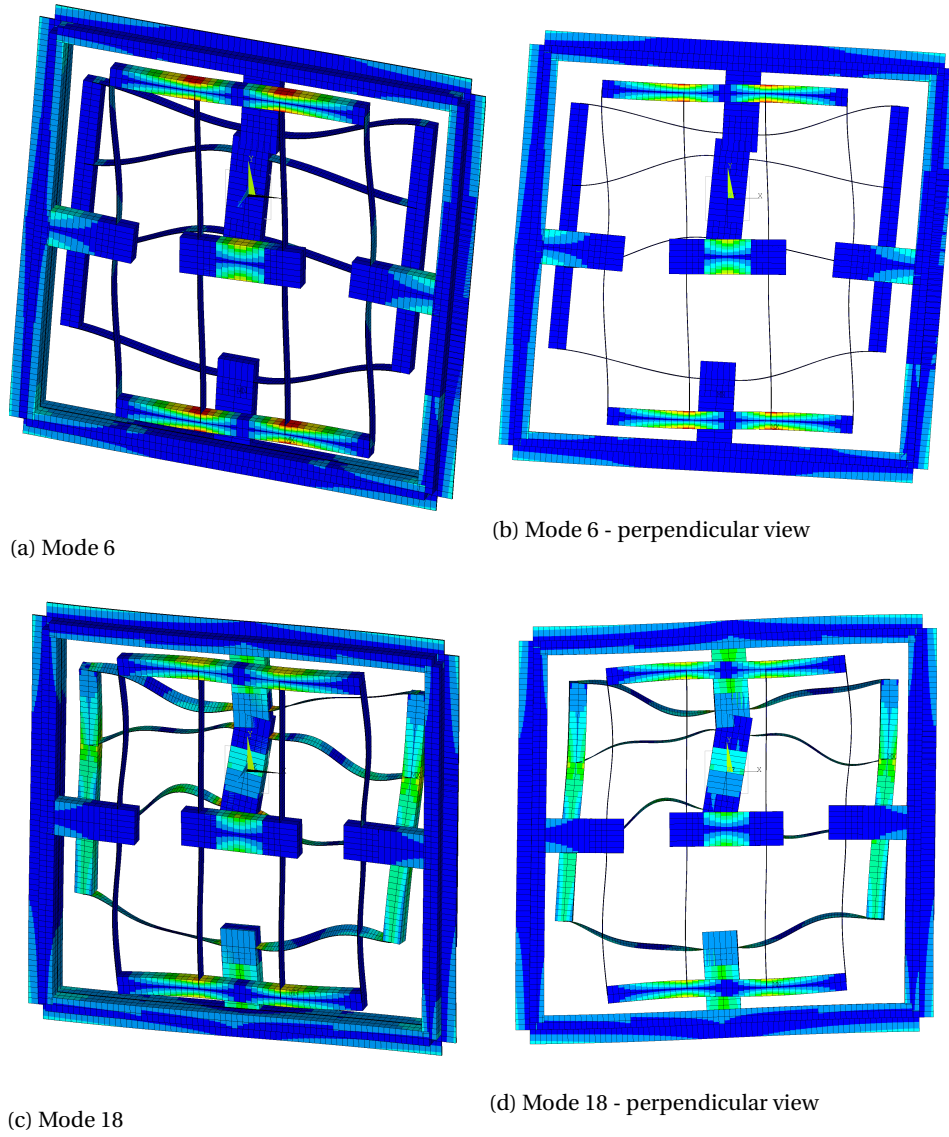


Figure B.5: Mode shapes with a potentially large effect on the velocity error

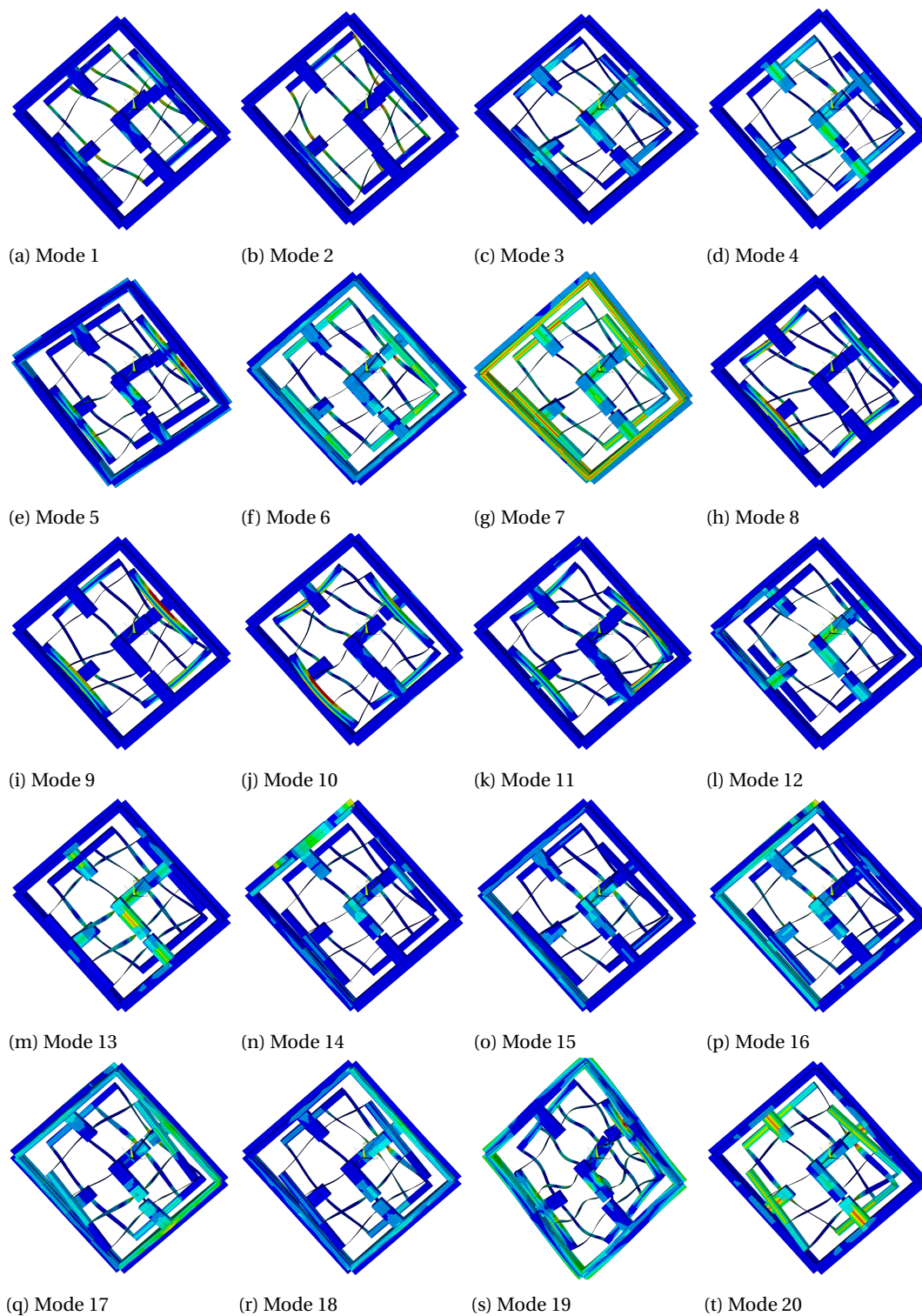
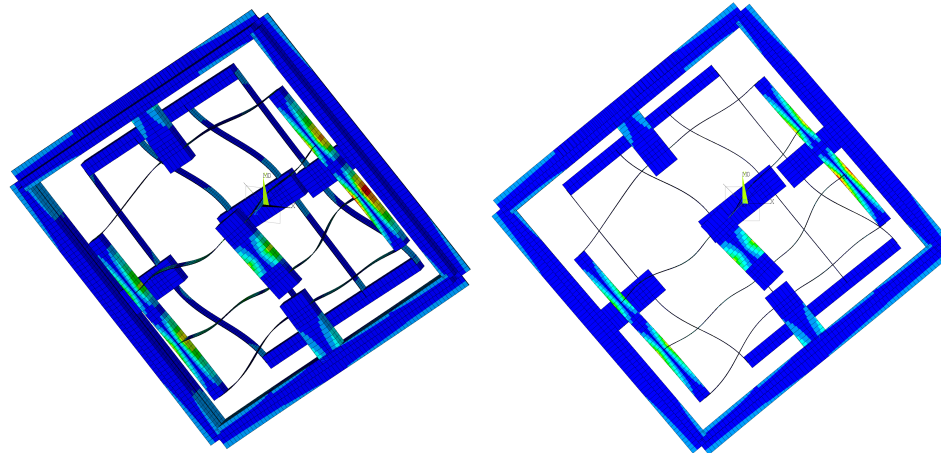
B.3.3. 20mm axle misalignment - 45° angle

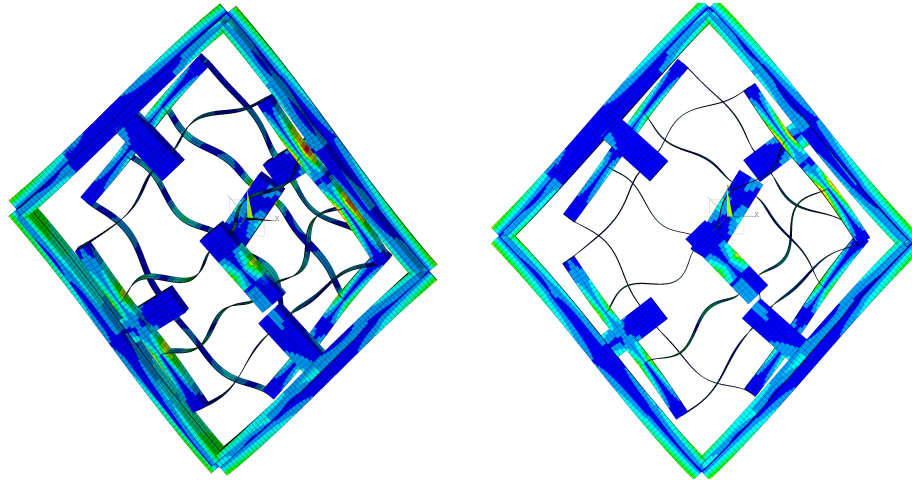
Figure B.6: Mode shapes for 20 mm axle misalignment - 135° angle

Again, a few modes which possess a large amount of output axle rotation, and are thus likely to cause significant velocity error between input and output axle when excited.



(a) Mode 5

(b) Mode 5 - perpendicular view



(c) Mode 19

(d) Mode 19 - perpendicular view

Figure B.7: Mode shapes with a potentially large effect on the velocity error

Table B.3: Description of mode shapes for 20 mm axle misalignment - 135° angle

#	Freq [Hz]	Dominant motion	Direction of motion	Origin of deformation
1	31.65	coupler (Y (tangential)) and shuttles (all in same rotational direction)	flexures, some shuttle deformation as well	
2	34.94	coupler (X (radial)) and shuttle (in opposite rotational direction)	flexures, some shuttle deformation as well	
3	52.14	coupler	X/Y rotation	flexure connection points of output and coupler body, flexures
4	53.78	coupler	X/Y rotation	flexure connection points of input and coupler body, flexures
5	71.22	coupler and output	Z rotation	input and input layer shuttles bending, flexure bending
6	87.28	coupler	Z translation	flexure connection points of coupler, shuttles, flexures
7	140.42	coupler		coupler, torsion in X and Y
8	160.75	shuttles	in shuttle motion direction (in opposite rotational direction per layer)	shuttles, flexures
9	160.97	shuttles	in shuttle motion direction (in opposite rotational direction per layer)	shuttles, flexures
10	218.89	shuttles (in opposite rotational direction per layer), coupler (Y (tangential))	in shuttle motion direction (in opposite rotational direction per layer)	shuttles, flexures
11	223.97	coupler (X (radial)) and shuttles	shuttles, flexures	
12	233.13	shuttles	Z translation	flexure connection points of coupler, input, output, flexure torsion
13	235.76	shuttles	Z translation	flexure connection points of coupler, input, output, flexure torsion
14	257.60	coupler, reinforcement ring	Z translation	coupler reinforcement ring bending
15	261.57	shuttles	Z translation	flexure connection points of coupler, input, output, flexure torsion
16	269.95	coupler (reinforcement ring), shuttles	Z translation	coupler reinforcement ring bending, flexure connection points of coupler, input, output, flexure torsion
17	309.69	coupler, flexure connection points, shuttles	Z translation	(flexure connection points of) coupler body
18	311.98	coupler, flexure connection points, shuttles	Z translation	(flexure connection points of) coupler body
19	313.40	coupler and output	Z rotation	flexure (buckling), coupler body shear
20	355.48	shuttles	X/Y rotation	flexure connection points coupler body, shuttles, flexure torsion

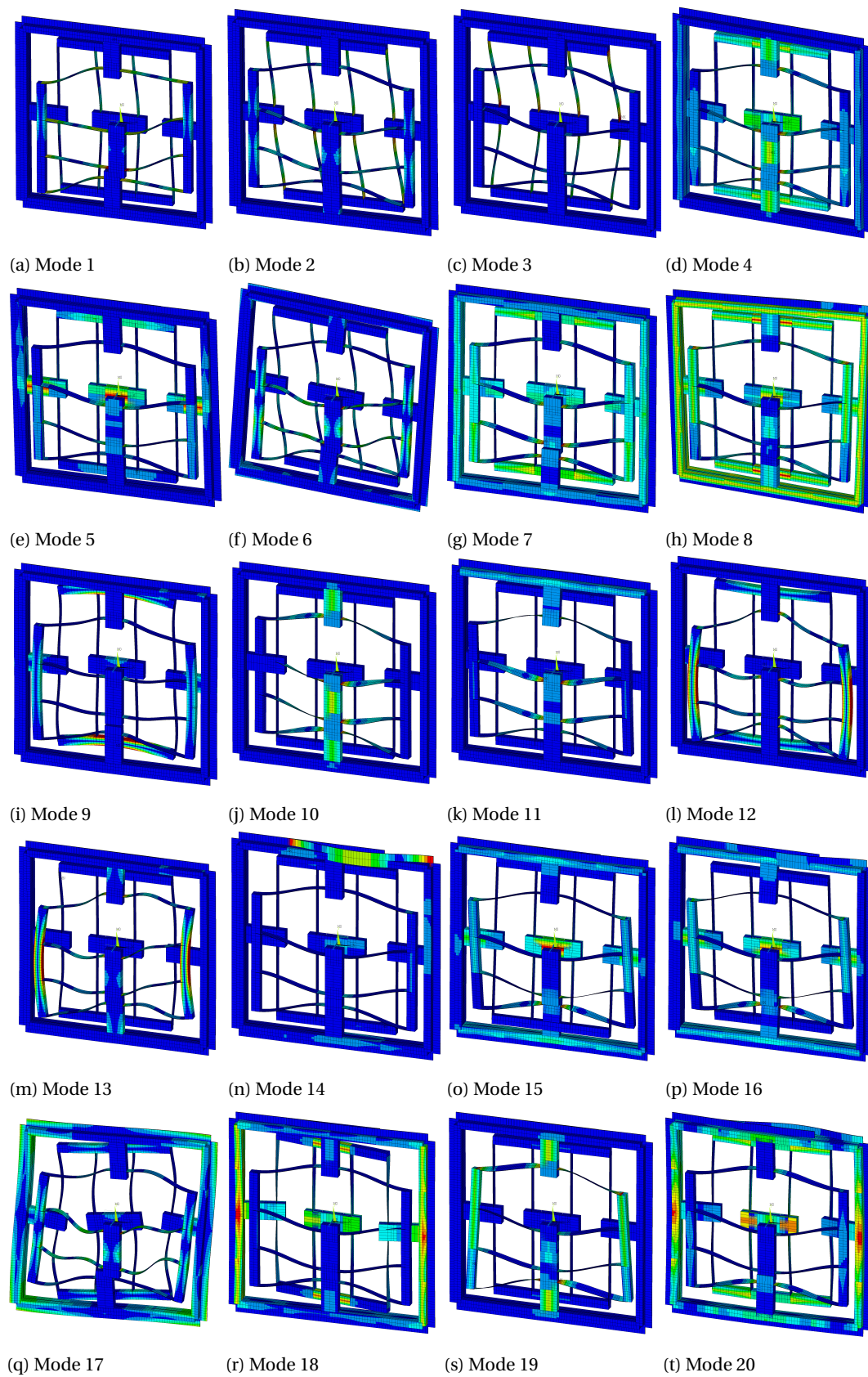
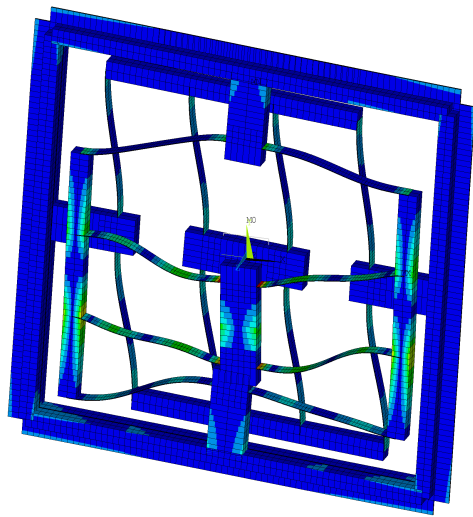
B.3.4. 20mm axle misalignment - 90° angle

Figure B.8: Mode shapes for 20 mm axle misalignment - 90° angle

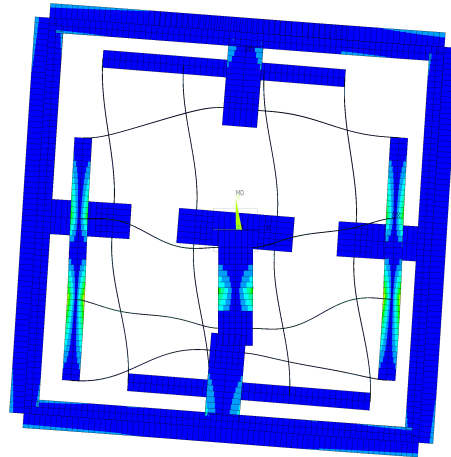
Table B.4: Description of mode shapes for 20 mm axle misalignment - 90° angle

#	Freq [Hz]	Dominant motion	Direction of motion	Origin of deformation
1	27.80	coupler (and input layer shuttles)	X translation (tangential)	flexures
2	42.43	output layer shuttles	X translation (tangential)	flexures, first bending mode
3	45.54	output layer shuttles	X translation (tangential)	flexures, first bending mode
4	55.94	coupler	Y rotation	flexure connection points of input and coupler body
5	58.02	coupler	X rotation	flexure connection points of output and coupler body
6	62.19	coupler and output	Z rotation	input and input layer shuttles bending, flexure bending
7	90.15	coupler	Z translation	flexure connection points of coupler, flexures
8	141.61	coupler		coupler, torsion in X and Y
9	164.11	coupler	Y translation	shuttle (and flexure) bending
10	203.45	input layer shuttles	Z translation	flexure connection points of input and coupler body, flexure torsion
11	216.99	input layer shuttles	Z translation, X rotation	upper connection point of coupler body, flexure torsion
12	226.28	input layer shuttles	Y translation	input layer shuttle (and flexure) bending
13	250.08	coupler body (X (tangential)) and input layer shuttles (Y)	input layer shuttle (and flexure) bending	
14	261.23	coupler, reinforcement ring	Z translation	coupler reinforcement ring bending
15	278.84	shuttles	Z translation, X rotation	flexure connection points of output and coupler body
16	301.17	shuttles	Z translation, X rotation	flexure connection points of output and coupler body
17	304.25	coupler and output	Z rotation	flexure (buckling), coupler body shear
18	323.40	coupler, flexure connection points, shuttles	Z translation	(flexure connection points of) coupler body
19	331.99	shuttles	X rotation	flexure connection points coupler body (input layer), shuttles, flexure torsion
20	350.42	output layer shuttles	Z translation	coupler body at output side, output

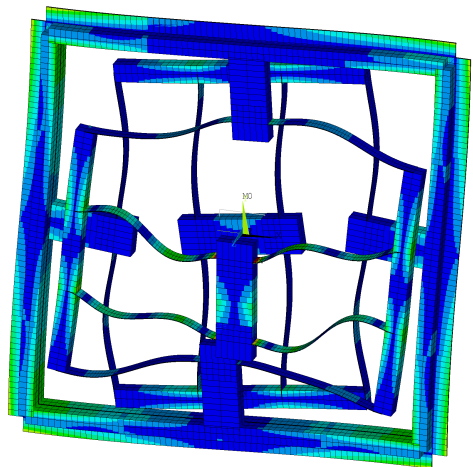
Again, a few modes which possess a large amount of output axle rotation, and are thus likely to cause significant velocity error between input and output axle when excited.



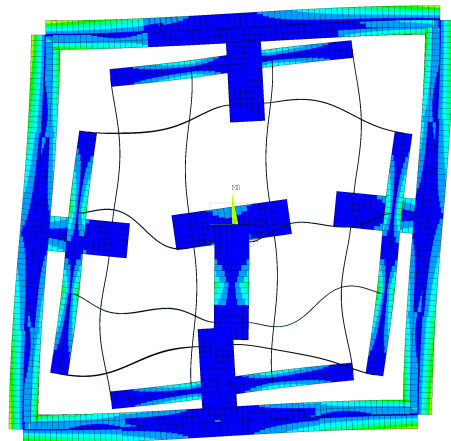
(a) Mode 6



(b) Mode 6 - perpendicular view



(c) Mode 17



(d) Mode 17 - perpendicular view

Figure B.9: Mode shapes with a potentially large effect on the velocity error

B.3.5. Check of multibody models - rigid support bodies

A modal analysis is done using 'near infinite' values for the E-modulus of the PMMA and aluminium support bodies making them rigid, in order to easily check the results of the Matlab multibody models. Of course, these results are less realistic. In the previous sections it can clearly be seen that, also for some lower modes, the elasticity of the PMMA and aluminium parts can be dominant. Below, the FEA equals of the first five modes of the 16DOF Matlab multibody model are given. The first four modes represent the motion of the shuttles in their underconstraint direction. In fifth multibody mode which is the rotational mode shape of the coupler body and output axle, is actually the 24th mode in the FEA. All modes between the fourth and 24th consist of higher order flexure bending modes.

Table B.5: Description of mode shapes for zero axle misalignment - zero angle - with rigid support bodies

#	Freq [Hz]	Dominant motion	Direction of motion	Origin of deformation
1	44.61	flexures and shuttles	underconstraint direction of shuttles	flexures first bending mode
2	44.63	flexures and shuttles	underconstraint direction of shuttles	flexures first bending mode
3	44.63	flexures and shuttles	underconstraint direction of shuttles	flexures first bending mode
4	44.63	flexures and shuttles	underconstraint direction of shuttles	flexures first bending mode
24	531.33	coupler and output	Z rotation	(buckling of) input layer flexures

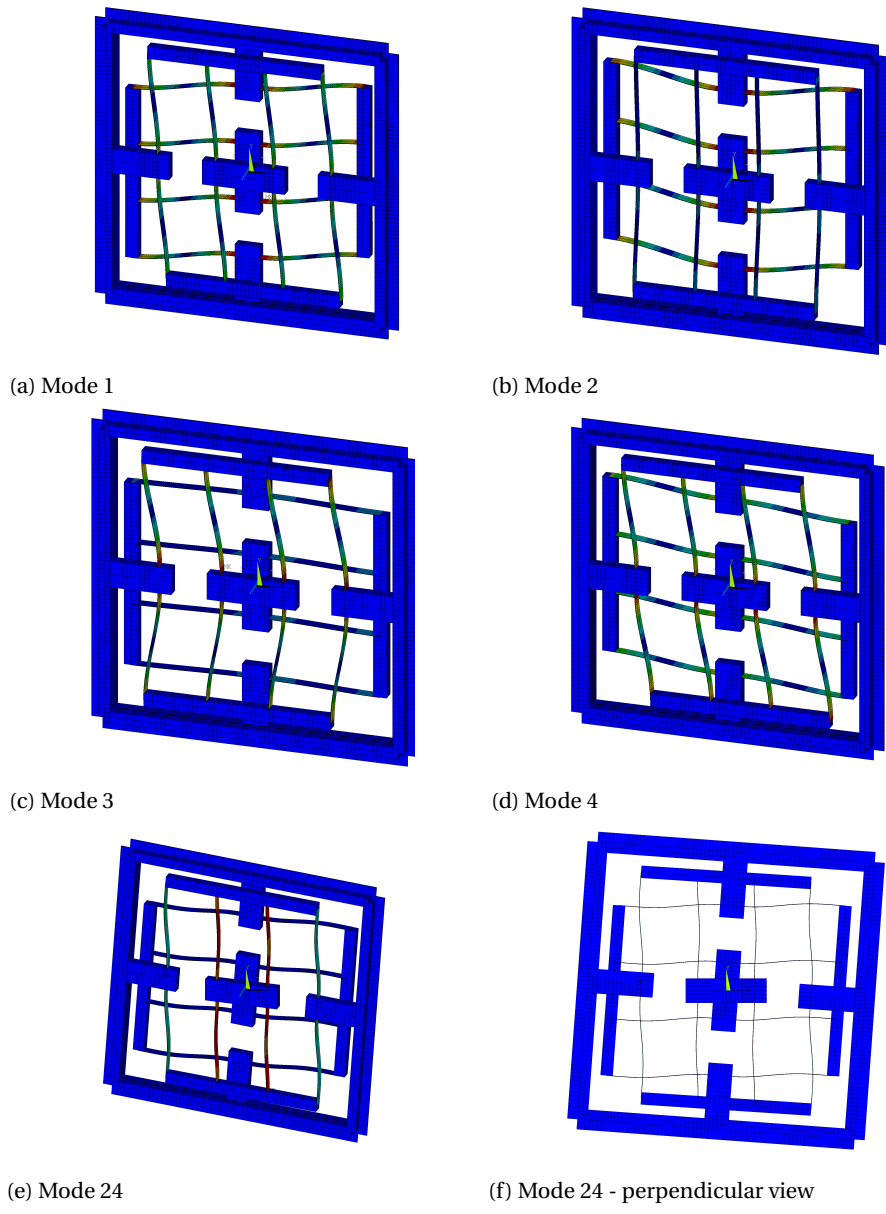
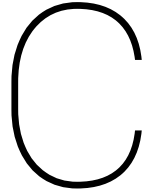


Figure B.10: Interesting mode shapes for zero axle misalignment - zero angle - with rigid support bodies



Theoretical model

C.1. Description of the Oldham coupling

In this section the working of the conventional Oldham coupling is explained. From there on, the conversion to the compliant counterpart is illustrated. The following is based on [6].

In figure C.1b a conventional Oldham coupling can be seen. The rigid-body Oldham coupling is a specific type of four-bar linkage [9]. It has three movable bodies, one coupled to the input shaft, one coupled to the output shaft, and a middle component which is connected to the first two parts by two prismatic joints. In the design analysed in this research, the two prismatic joints are perpendicular to each other. A kinematic representation of the mechanism is shown in figure C.1a. It has two fixed and fully rotating frame joints which act as bearings for two parallel axes. Crank 2 and 4 are rigidly connected to these axis. If the input link, 2, rotates through some angle, then the coupler link, 3, rotates through the same angle. This in turn rotates the output shaft, 4, through the same angle. Therefore, the two links, 2 and 4, rotate together and the velocity ratio remains constant at 1:1 throughout the rotation. Link 1 is the ground link with length L_1 which actually is the offset between input link 2 and output link 4. The two prismatic joints intersect each other perpendicular at point P, the centre of coupler link 3. For a full cycle motion of the input link, the point P moves along a circular path with the diameter L_1 twice. Therefore, the range of motion of each prismatic joint in both directions in each cycle is exactly the distance between the two parallel axes or the offset. The centre of this circular path lies in between the input and output axis, at $L_1/2$.

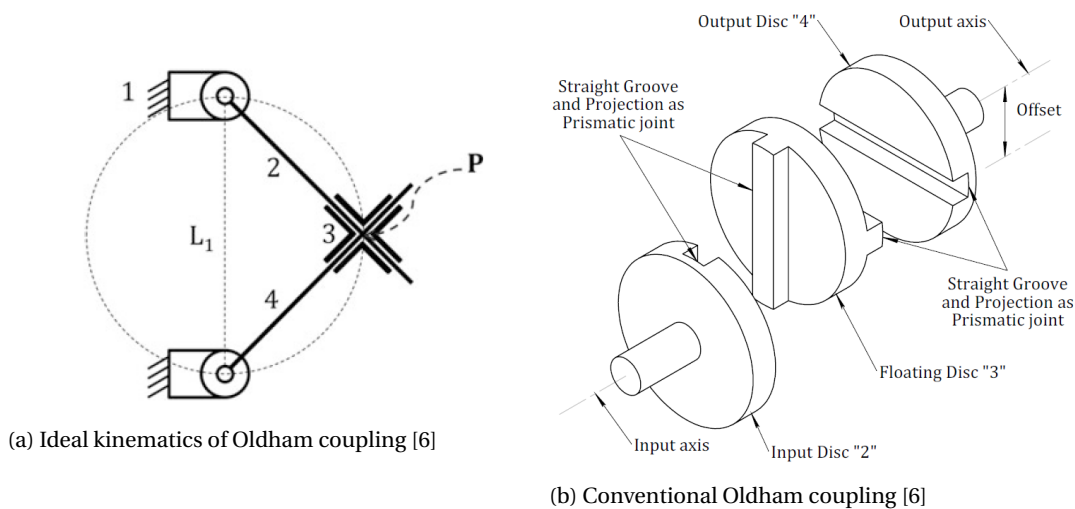


Figure C.1: The conventional Oldham coupling

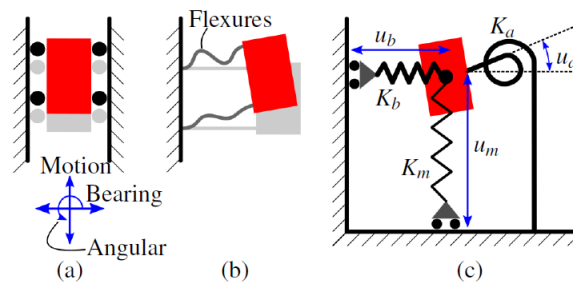


Figure C.2: Planar schematic of (a) a conventional rigid-body prismatic joint, (b) its compliant counterpart, (c) a PRBM of a compliant prismatic joint, indicating the decoupled stiffnesses K and displacements u in motion, bearing and angular direction, indexed with m , b and a respectively.

C.1.1. Conversion to a compliant design

The two conventional prismatic joints have certain disadvantages, such as backlash, friction and wear [4], which do not benefit the precision of the rotational transmission. One way to overcome these disadvantages, is to replace the two conventional prismatic joints by compliant counterparts. The difference between these two types of joints is discussed first. Then, a general description of a compliant Oldham coupling will be given.

A prismatic joint, also known as a slider or translational stage, is a one degree of freedom (1DOF) kinematic pair. The DOF is a linear translation. All other five directions should be constrained, creating five degrees of constraint (5DOC). In the conventional rigid-body version, these rigid bodies can translate with respect to each other. Neglecting friction, the translation motion direction is normally modelled as having zero stiffness. Assuming the two bodies are rigid, the 5DOC, also known as the bearing directions, can be seen as having infinite stiffness.

In a compliant prismatic joints, these assumptions are not valid anymore. Compliant mechanisms transfer motion, force or energy by using elastic deformation of its flexure joints [3]. This results in finite stiffnesses in all directions. The motion stiffness however should be order of magnitude smaller than the bearing stiffnesses. Especially for flexure based joints, non-linear bearing stiffness are common and can depend on the motion direction displacement.

Thus, in the spatial domain, a compliant prismatic joint can be described with six stiffness values of functions. In the following sections, the coupling will be modelled in the planar domain. In figure C.2 a planar schematic of both a conventional and a compliant prismatic joint are given, indicating the different directions. The stiffness of the compliant joint can be described by three decoupled stiffnesses (one motion, two bearing), as depicted.

Two perpendicular compliant prismatic joints can form an Oldham coupling, as will be studied in this work. The full cycle revolute joints of the input and output axes remain as conventional rigid-body revolute joints. The prismatic joints will be connected to these input and output shafts. .

C.1.2. Specific design used in the case study

In the design used for the case study, two double paired parallelogram flexure mechanisms (DP-DP) are used, of which one is shown in figure C.3a. Let's first have a look at one of these prismatic joints:

The three stiffnesses of one DP-DP mechanism are given in equation C.1, C.2 and C.3 [27].

In this mechanism the motion stage can move easily in motion direction Y with respect to the ground. The mechanism is stiff in the so called bearing directions X and rotation θ .

$$K_y = \frac{2EI_1}{L_1^3} k_{11}^0 \quad (C.1)$$

$$K_x = \frac{2EI_1}{L_1^3} \frac{k_{33}}{\left(1 + k_{33} \left(g_{11}^{(1)} + \frac{(k_{11}^{(1)})^2}{k_{11}^{(0)}} \right) \left(\frac{Y}{2L_1} \right)^2 \right)} \quad (C.2)$$

$$K_\theta = \frac{2EI_1}{L_1^3} \frac{4W_1^2 W_2^2}{(W_1^2 + W_2^2)} \frac{k_{33}}{\left(1 + k_{33} g_{11}^{(1)} \left(\frac{Y}{2L_1} \right)^2 \right)} \quad (C.3)$$

where:

$$k_{11}^{(0)} = \frac{6}{(3 - 6a_0 + 4a_0^2)a_0} \quad (C.4)$$

$$k_{11}^{(1)} = \frac{3(15 - 50a_0 + 60a_0^2 - 24a_0^3)}{(3 - 6a_0 + 4a_0^2)a_0} \quad (C.5)$$

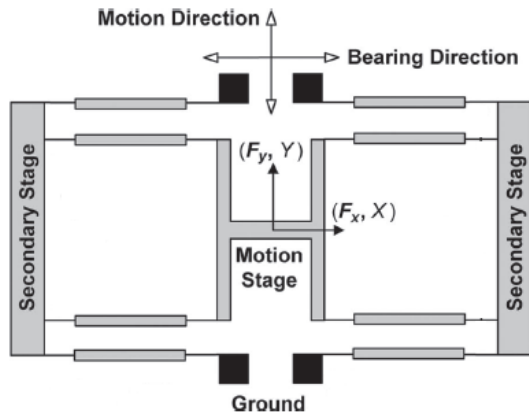
$$g_{11}^{(1)} = \frac{2a_0^3(105 - 630a_0 + 1440a_0^2 - 1480a_0^3 + 576a_0^4)}{175(3 - 6a_0 + 4a_0^2)} \quad (C.6)$$

$$k_{33} = \frac{6l^2}{a_0 t^2} \quad (C.7)$$

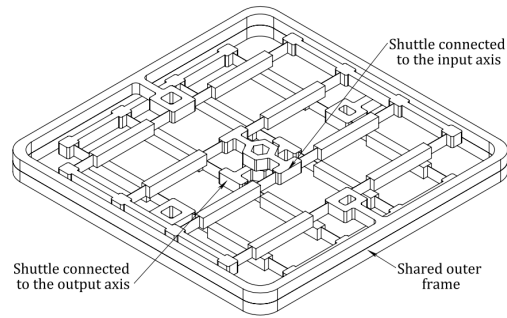
$$I = \frac{ht^3}{12} \quad (C.8)$$

In the above equations $k_{11}^{(0)}$, $k_{11}^{(1)}$, $g_{11}^{(1)}$ and k_{33} are geometrical constants. E is the Young's modulus of the flexure material and I_1 the second moment of inertia of the flexures. L_1 , W_1 and W_2 are again geometrical constants, depicted in figure C.3a.

The motion stiffness is constant, and depends on the flexure material and the mechanisms geometry. The bearing stiffnesses however are non-linearly dependent on the displacement in motion direction. The bearing stiffnesses decrease quadratically with the displacement, and thus have a maximum at zero displacement.



(a) The double paired parallelogram flexure mechanism (DP-DP) [27]



(b) Compliant Oldham coupling consisting of two DP-DP flexure mechanisms [6]

Figure C.3: The compliant Oldham design used for the case study

To implement the DP-DP flexure, the input axis actually is coupled on the motion stage. The 'ground' in figure C.3a becomes the coupler link 3. This forms the first prismatic joint. A second DP-DP flexure then is rotated 90 degrees with respect to the first one, with its 'ground' connected to this coupler link and the output shaft to its motion stage.

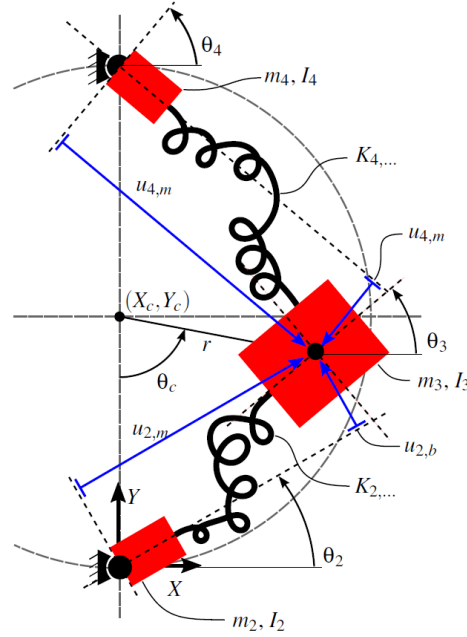


Figure C.4: Dynamic multibody model of a compliant Oldham coupling. The stiffnesses of both prismatic joints are symbolised by two randomly formed coil springs. Each of these consist of three decoupled stiffness directions as depicted in figure C.2c. Translational deformations of these stiffnesses are depicted in blue. Rotational deformations are not depicted, but are simply the difference in body rotation. The three rigid bodies are depicted in red, with their COM represented as a black dot. The dashed circle represents the path a rigid-body Oldham coupling will describe.

C.2. Finding the equations of motion

To study the dynamic behaviour of the compliant Oldham coupling, a planar dynamic multibody model based on the PRBM (C.4) can be build. In the model, three moving rigid bodies can be distinguished, being the input crank (input, body 2), the coupler link (coupler, body 3) and the output crank (output, body 4). The input intersects the origin of a fixed (inertial) reference frame X, Y , resulting in the body coordinates:

$$\mathbf{X} = [X_2, Y_2, \Theta_2, X_3, Y_3, \Theta_3, X_4, Y_4, \Theta_4]^T \quad (\text{C.9})$$

A schematic of the coupling is given in figure C.4.

Angles are measured counter clockwise from the positive X -axis. Two conventional zero stiffness revolute joints connect the input and output to the fixed world, body 1. The parallel offset between input and output axis is defined as $Y_4 - Y_1 = l_1$. The two revolute joints thus give the (holonomic) constraints $X_2 = Y_2 = X_4 = 0$ and $Y_4 = l_1$. In between input and output axis lies the centre point X_c, Y_c of the circular path described by the coupler in the case of a rigid-body Oldham coupling.

Five degrees of freedom remain. Input (2), coupler (3) and output (4) can rotate with respectively angles $\Theta_2, \Theta_3, \Theta_4$. The coupler (3) can also translate in plane with coordinates X_3, Y_3 .

The coupler is only connected to input and output by the two compliant prismatic joints. These joints are described by two sets of three decoupled stiffnesses. Each set consists of two perpendicular translational stiffnesses and one rotational stiffness, as described in the previous section about compliant prismatic joints. To each body, a reference frame x_n, y_n can be connected, rotated with Θ_n . These rotating reference frames will be used to express the elastic deformations between the rigid bodies, which will be given in the next section.

As the compliant prismatic joints have a finite stiffness in bearing directions, the coupler does not describe a perfect circle any more.

C.2.1. Elastic deformations

To calculate the elastic deformation of each prismatic stage, the input and output are defined as the 'ground' for respectively the first and second prismatic stage. The coupler functions as the 'motion stage'. The defor-

mations are then defined as in figure C.2. As input and output rotate, all deformations are functions of the body angles.

To clearly distinguish the different stiffness directions, the two translations will be called 'motion' and 'bearing'. The input (2) is connected to the coupler (3) by the stiffnesses $K_{2,motion}$, $K_{2,bearing}$ and $K_{2,angular}$. Similarly, the coupler is connected to the (4) by $K_{4,motion}$, $K_{4,bearing}$ and $K_{4,angular}$.

The six elastic deformations are given below. As input and output are defined as the ground of both prismatic stages, the deformations are expressed in the moving reference frames connected to input and output. The angular deformation simply is the difference between the body rotations. A graphical representation of the translational deformations is given in figure C.5.

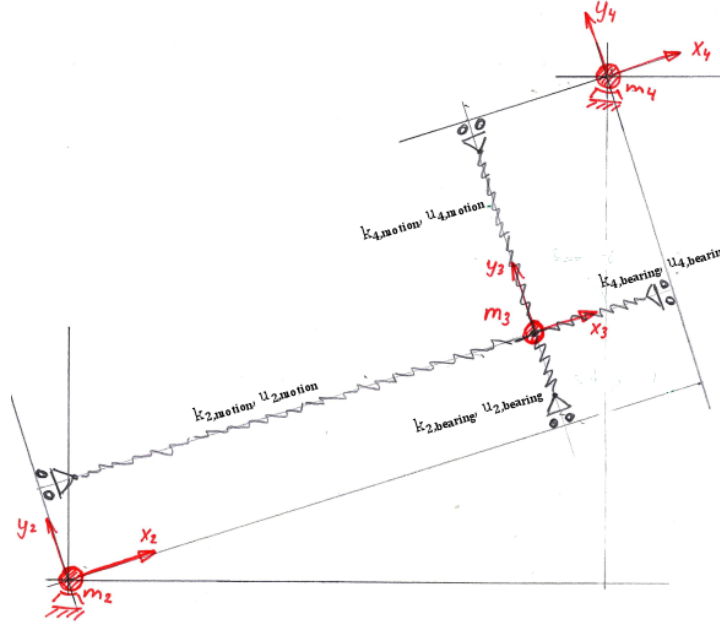


Figure C.5: Translational elastic deformations. The bearing and motion direction are perpendicular and decoupled.

$$u_{2,motion} = (X_3 - X_2) \cos(\Theta_2) + (Y_3 - Y_2) \sin(\Theta_2) \quad (C.10)$$

$$u_{2,bearing} = -(X_3 - X_2) \sin(\Theta_2) + (Y_3 - Y_2) \cos(\Theta_2) \quad (C.11)$$

$$u_{2,angular} = \Theta_3 - \Theta_2 \quad (C.12)$$

$$u_{4,bearing} = -(X_4 - X_3) \cos(\Theta_4) - (Y_4 - Y_3) \sin(\Theta_4) \quad (C.13)$$

$$u_{4,motion} = (X_4 - X_3) \sin(\Theta_4) - (Y_4 - Y_3) \cos(\Theta_4) \quad (C.14)$$

$$u_{4,angular} = \Theta_4 - \Theta_3 \quad (C.15)$$

C.2.2. Kinetic and potential energy

The kinetic energy of the joint can be broken down into three parts, being the transport, mutual and relative kinetic energy. The transport energy is the part that remains when all \mathbf{q} are zero. The relative energy however only consists of the relative motion of \mathbf{q} .

The three kinetic energies:

$$T_0 = \frac{1}{2} \left(\frac{\partial \mathbf{X}}{\partial t} \right)^T \mathbf{M} \left(\frac{\partial \mathbf{X}}{\partial t} \right) \quad (\text{transport}) \quad (\text{C.16})$$

$$T_1 = \left(\frac{\partial \mathbf{X}}{\partial t} \right)^T \mathbf{M} \left(\frac{\partial \mathbf{X}}{\partial \mathbf{q}} \dot{\mathbf{q}} \right) \quad (\text{mutual}) \quad (\text{C.17})$$

$$T_2 = \frac{1}{2} \left(\dot{\mathbf{q}} \frac{\partial \mathbf{X}}{\partial \mathbf{q}} \right) \mathbf{M} \left(\frac{\partial \mathbf{X}}{\partial \mathbf{q}} \dot{\mathbf{q}} \right) \quad (\text{relative}) \quad (\text{C.18})$$

$$T = T_0 + T_1 + T_2 \quad (\text{C.19})$$

$$\mathbf{M} = \text{diag} [m_2, m_2, I_2, m_3, m_3, I_3, m_4, m_4, I_4] \quad (\text{C.20})$$

Here, m_i are the masses of the individual bodies, and I_i their second moment of inertia.

The potential energies can be computed using the deformations and stiffness profiles given in the previous part:

$$V = \frac{\mathbf{u}^T \mathbf{K} \mathbf{u}}{2} \quad \text{with:} \quad (\text{C.21})$$

$$\mathbf{u} = [u_{2,motion}, u_{2,bearing}, u_{2,angular}, u_{4,bearing}, u_{4,motion}, u_{4,angular}]^T \quad (\text{C.22})$$

$$\mathbf{K} = \text{diag} [K_{2,motion}, K_{2,bearing}, K_{2,angular}, K_{4,motion}, K_{4,bearing}, K_{4,angular}] \quad (\text{C.23})$$

C.2.3. Lagrange

Using the Lagrange equation, the equations of motion can be formulated using the system's energies. For this, first a set of generalised coordinates \mathbf{q} has to be chosen, in which the motion of the mechanism will be represented. In the next sections several sets of generalised coordinates will be discussed. For now, let's keep them general as the row vector \mathbf{q} . Without damping the Lagrange equation is defined as:

$$\frac{d}{dt} \frac{\partial T}{\partial \dot{\mathbf{q}}} - \frac{\partial T}{\partial \mathbf{q}} + \frac{\partial V}{\partial \mathbf{q}} - \mathbf{Q}_s = \mathbf{0} \quad (\text{C.24})$$

Here, \mathbf{Q}_s is a forcing vector, which will consist of an input and output torque on the shafts of the coupling:

$$\mathbf{Q}_s = [T_{\text{input}}, 0, 0, 0, -T_{\text{output}}]^T \quad (\text{C.25})$$

C.2.4. Choice of generalised coordinates

For the generalised coordinates \mathbf{q} the five free body coordinates in the inertial reference frame could be used, resulting in $\mathbf{q} = [\Theta_2, X_3, Y_3, \Theta_3, \Theta_4]^T$.

However, as the coupler describes a close-to-circular path around $[X_c, Y_c]$, the inertial reference frame is not the most suited coordinate system to study the behaviour. Different sets of generalised coordinates \mathbf{q} can be chosen to represent the motion of the coupling, which will now be discussed.

Polar coordinate system The close-to-circular path of the coupler could be described using polar coordinates, using the path radius r and angle θ_c with origin $[X_c, Y_c]$. The remaining freedoms of the model would be the original body rotations. The body coordinates can be written as a function of these new generalised coordinates \mathbf{q} , and can be seen in figure C.6a:

$$\mathbf{q} = [\theta_2, \theta_c, r, \theta_3, \theta_4]^T \quad (\text{C.26})$$

$$\Theta_2 = \theta_2 \quad (\text{C.27})$$

$$X_3 = X_c + r \sin(\theta_c) \quad (\text{C.28})$$

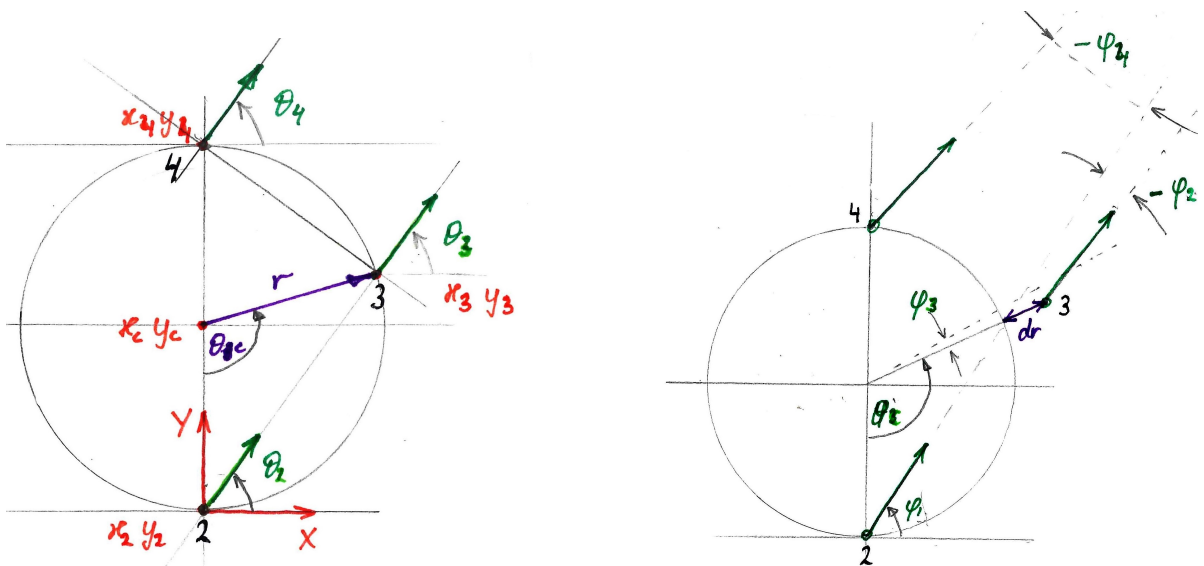
$$Y_3 = Y_c - r \cos(\theta_c) \quad (\text{C.29})$$

$$\Theta_3 = \theta_3 \quad (\text{C.30})$$

$$\Theta_4 = \theta_4 \quad (\text{C.31})$$

Forces in the r and θ_c direction represent the centrifugal and Coriolis force. Interpretation of these forces is more natural than the rectilinear inertial forces which would arise of the translation of the coupler would be analysed in the inertial reference frame $[X, Y]$.

If a specific compliant design leads to a non-linear set of equations, linearisation can be needed. The linearisation then is done around an equilibrium point. In this set of generalised coordinates, a steady motion equilibrium can be expressed with constant values. In the global coordinate system this is impossible as X_3 and Y_3 are constantly changing.



(a) Global body coordinates and generalised (polar) coordinates describing circular-like path.

(b) Generalised coordinates as deviation from quasi-static path.

Figure C.6: Two different sets of generalised coordinates describing the five degrees of freedom of the coupling.

'Steady motion' coordinate system With the set of coordinates given below, a suitable steady motion linearisation point can be described by one coordinate only, being the input rotation and its velocity. For steady motion, all other generalised coordinates and their time derivatives are zero. This eases the linearisation process. The coordinates can be seen as the deviation from the circular path of the coupler described earlier (see figure C.6b).

The body coordinates can be written as a function of the new generalised coordinates \mathbf{q} . The translation of the coupler again is described in some sort of polar coordinate system, for which the radius r is composed of a equilibrium radius r_{eq} and a deviation dr . Similarly, the polar angle consists of an equilibrium part $2\phi_1$ (as the polar angle of the coupler is twice the input body angle in case of steady motion), and a deviation ϕ_3 .

$$\mathbf{q} = [\phi_1, \phi_2, \phi_3, \phi_4, dr]^T \tag{C.32}$$

$$\Theta_2 = \phi_1 \tag{C.33}$$

$$X_3 = X_c + (r_{eq} + dr) \sin(\phi_3 + 2\phi_1) \tag{C.34}$$

$$Y_3 = Y_c - (r_{eq} + dr) \cos(\phi_3 + 2\phi_1) \tag{C.35}$$

$$\Theta_3 = \phi_1 + \phi_2 \tag{C.36}$$

$$\Theta_4 = \phi_1 + \phi_4 \tag{C.37}$$

Prescribed motion or torque To study the dynamic behaviour of the Oldham coupling, some forcing must be applied on the mechanisms. An input axis motion can be prescribed in time, resulting in one less DOF. Prescribing the input motion, for example the behaviour of the coupling can be studied at a constant input velocity:

$$\Theta_2 = \Theta_{2,0} + \omega t \quad (\text{C.38})$$

$$\dot{\Theta}_2 = \omega \quad (\text{C.39})$$

$$\ddot{\Theta}_2 = 0 \quad (\text{C.40})$$

By doing this, the input inertia is neglected, or is assumed infinite. However, this input inertia can influence the dynamic behaviour of the system. Furthermore, the effect of input acceleration is also neglected.

Applying a torque on the input body is a closer resemblance to a real application of the coupling. By doing this, no DOF is removed. Eventually, the model will be compared with data from an experimental setup. As in this setup the input also has a finite inertia to which a torque is applied, torque prescription is chosen.

17DOF model As was already described in the main body of this thesis, an extended version of the 5DOF model was made for comparison. In this model, the four intermediate shuttles are modelled as well, having three degrees of freedom in plane. This results in a total of 17DOF. A short explanation of this model is given in the paper in chapter 2, including the stiffness and inertia values used. All methods discussed in this appendix can be applied on this model in a similar way. In section C.7 the used Matlab code is given. In the following result sections, results for this model will be shown as well.

C.3. Analysis of the equations of motion

In this section, the equations of motion are studied in the polar coordinate system, for prescribed torque.

Using the Lagrange equation, the five equations of motion (EoM) for the system in the directions \mathbf{q} can be formed as a function of the system energies. As the expressions of the elastic forces $\frac{\partial V}{\partial \mathbf{q}}$ are lengthy, they are represented as these partial derivatives for now.

$$I_2 \ddot{\theta}_2 + \frac{\partial V}{\partial \theta_2} - T_{in} = 0 \quad (\text{C.41})$$

$$m_3 r^2 \ddot{\theta}_c + 2m_3 r \dot{r} \dot{\theta}_c + \frac{\partial V}{\partial \theta_c} = 0 \quad (\text{C.42})$$

$$m_3 \ddot{r} - m_3 \dot{\theta}_c^2 r + \frac{\partial V}{\partial r} = 0 \quad (\text{C.43})$$

$$I_3 \ddot{\theta}_3 + \frac{\partial V}{\partial \theta_3} = 0 \quad (\text{C.44})$$

$$I_4 \ddot{\theta}_4 + \frac{\partial V}{\partial \theta_4} - T_{out} = 0 \quad (\text{C.45})$$

The individual terms of the EoM can now be studied. As the COM of body 3 is described in the polar coordinate system around (X_c, Y_c) , inertial forces are present in these directions due to the rotation, which will be further clarified.

The first equation gives the input axle rotation, in which the inertial force, elastic force and applied torque equilibrate each other.

The second equation represents coupler motion in tangential direction as seen from the origin of the circular path at (X_c, Y_c) . The first term is the torque generated by the acceleration $m_3 \ddot{\theta}_c r$. This is a function of the acceleration in tangential direction of the body $\ddot{\theta}_c r$, resulting in a moment $m_3 \ddot{\theta}_c r^2$. The second term represents the moment caused by the Coriolis force $2m_3 \dot{r} \dot{\theta}_c$, which only exists if the radius r changes in time. The third term represents the tangential component of the elastic forces.

The third equation represents coupler motion in radial direction. The first term is the force $m_3 \ddot{r}$ originating from rectilinear acceleration in radial direction. The second term is the centrifugal force, $m_3 r \dot{\theta}_c^2$. The third term represents the radial component of the elastic forces.

The fourth and fifth equation represent the body rotation of body 3 and 4 respectively. The acceleration torque balances the elastic torque (and the output torque for the output shaft).

An example of the elastic forces $\frac{\partial V}{\partial \mathbf{q}}$ is given below for the two polar coordinates. As the bearing and angular stiffness depend on the motion displacement, also partial derivatives of the stiffness to the generalised coordinates \mathbf{q} are present.

$$\frac{\partial V}{\partial \theta_2} = \dots \text{ (terms with all three } K_{2,\dots}) \quad (\text{C.46})$$

$$\frac{\partial V}{\partial \theta_c} = \frac{1}{2} \left(K_{2,m} \frac{\partial u_{2,m}^2}{\partial \theta_c} + K_{2,b} \frac{\partial u_{2,b}^2}{\partial \theta_c} + \frac{\partial K_{2,b}}{\partial \theta_c} u_{2,b}^2 + K_{4,m} \frac{\partial u_{4,m}^2}{\partial \theta_c} + K_{4,b} \frac{\partial u_{4,b}^2}{\partial \theta_c} + \frac{\partial K_{4,b}}{\partial \theta_c} u_{4,b}^2 \right) \quad (\text{C.47})$$

$$\frac{\partial V}{\partial r} = \frac{1}{2} \left(K_{2,m} \frac{\partial u_{2,m}^2}{\partial r} + K_{2,b} \frac{\partial u_{2,b}^2}{\partial r} + \frac{\partial K_{2,b}}{\partial r} u_{2,b}^2 + K_{4,m} \frac{\partial u_{4,m}^2}{\partial r} + K_{4,b} \frac{\partial u_{4,b}^2}{\partial r} + \frac{\partial K_{4,b}}{\partial r} u_{4,b}^2 \right) \quad (\text{C.48})$$

$$\frac{\partial V}{\partial \theta_3} = \dots \text{ (terms with all six } K_{\dots}) \quad (\text{C.49})$$

$$\frac{\partial V}{\partial \theta_4} = \dots \text{ (terms with all three } K_{4,\dots}) \quad (\text{C.50})$$

C.3.1. Radial balance

As the COM of body 3 describes a circular path, problems are expected in radial direction for higher velocities, as the centrifugal force rises with θ_c^2 . The elastic forces $\frac{\partial V}{\partial r}$ have to counteract these centrifugal forces. In figure C.7a the radial component of the elastic forces are plotted for varying r and θ_c , at an axis offset l_1 of 20 mm. The rotations are for now taken as in the rigid-body Oldham coupling: $\dot{\theta}_2 = \dot{\theta}_3 = \dot{\theta}_4 = \dot{\theta}_c/2$. At static equilibrium (or quasi static rotation) the elastic forces are close to zero, which will occur at a radius r of around 10 mm. When velocity and centrifugal force rise, the radius r and with it the elastic force will increase until the balance is restored.

Looking at angle θ_c in figure C.7a, the radial component of elastic force is minimal at every $(90 + n \cdot 180)^\circ$. These points are of interest to study the balance with the centrifugal force. In figure C.7b both forces in radial direction are plotted as a function of rotational velocity $\dot{\theta}_2$ and radius r at $\theta_c = 2\theta_2 = 90^\circ$. At the intersection of the two planes, the elastic force balances the centrifugal force, and no radial acceleration is present, resulting in steady motion (for this coordinate at least). It can be seen that the centrifugal force linearly rises with r and quadratically with $\dot{\theta}_c$. The elastic force depends on r . It can be seen that for velocities above $\dot{\theta}_2 \approx 10.4 \text{ Hz}$, there exists no radius for which the forces are in balance. Thus, for higher velocities an unbounded positive radial acceleration occurs, causing instability.

The effective radial stiffness thus consists of an elastic and a centrifugal contribution:

$$K_{\text{radial}} = K_{\text{radial,el}} - K_{\text{radial,cent}} \quad (\text{C.51})$$

$$= \underbrace{\frac{\partial^2 V}{\partial r^2}}_{\text{elastic}} - \underbrace{m_3 \dot{\theta}_c^2}_{\text{centrifugal}} \quad (\text{C.52})$$

A positive definite radial stiffness is needed for stability. Some more formulations for the effective radial stiffness were already given in the paper in the main body of this thesis.

The rise and fall of the radial component of elastic force can be explained by looking at the stiffness and deflection of the flexure mechanisms. In figure C.8, again the radial forces are plotted, at $\theta_c = 90^\circ$. In the same graph, the elastic deflections and stiffness values of the DP-DP flexures are given. It can be seen that the radial displacement of body 3 results in translational deflections in both motion and bearing direction of both DP-DP flexures. As the deflections in motion direction $u_{\dots,y}$ increase (absolutely) with the radius, the bearing stiffnesses $K_{\dots,x}$ drop (note the logarithmic scale). Motion stiffnesses $K_{\dots,y}$ remain constant. This drop results in a maximum radial elastic force at $r \approx 22 \text{ mm}$ after which the drop in stiffness has a larger influence than the rise in deformation.

C.4. Modal analysis

In order to gain insight in the resonance frequencies and stability of the system at certain rotational velocities, a modal analysis can be done at several steady motion equilibrium configurations. The input axis angle θ_2 and velocity $\dot{\theta}_2$ are prescribed resulting in a 4DOF system, in order to remove the else arising rigid body mode. For simplicity, the external forcing \mathbf{Q}_s is neglected, and no damping is applied.

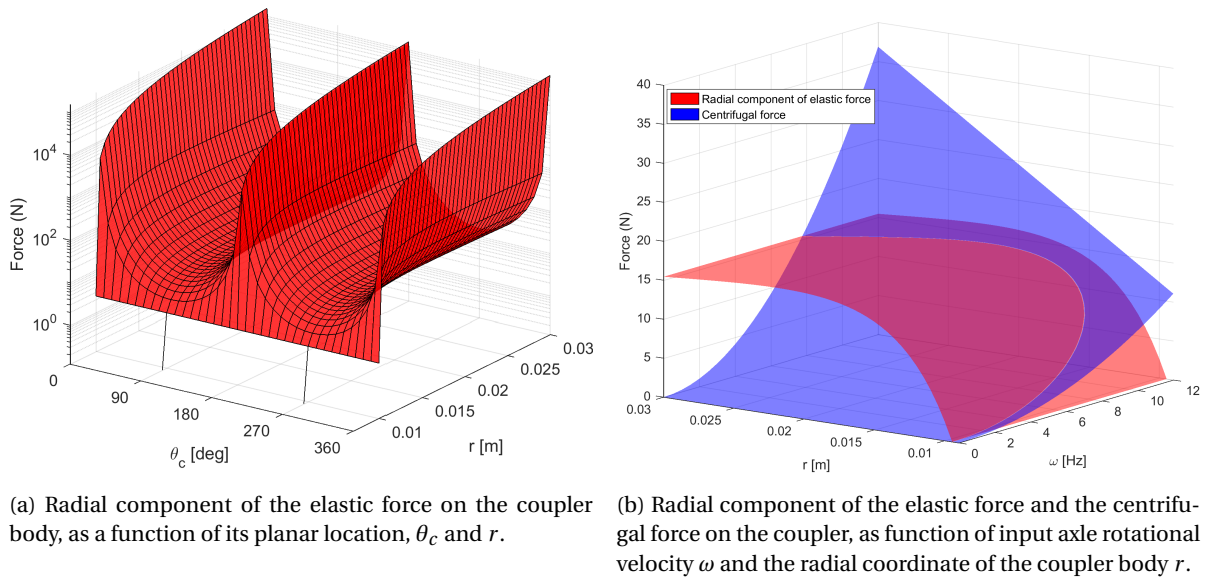
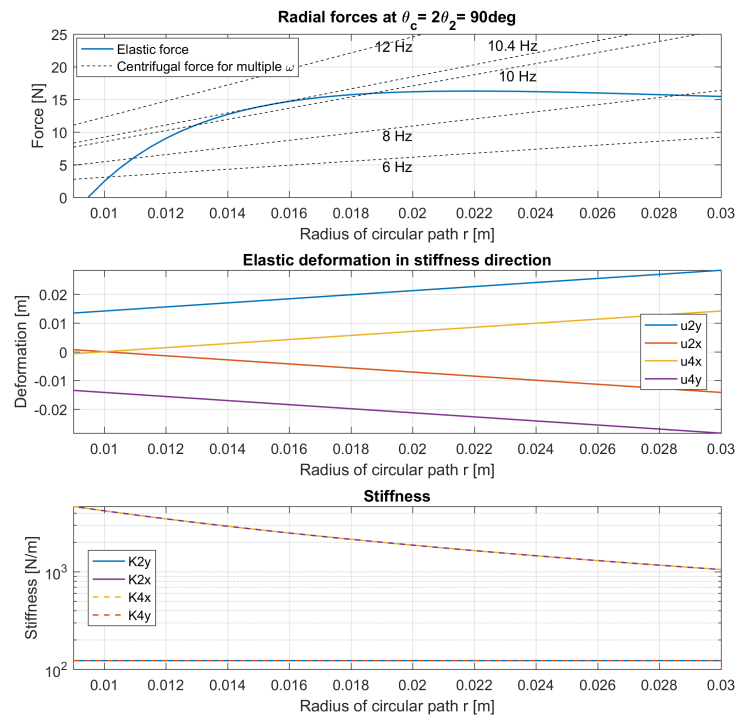


Figure C.7: Radial force balance of the coupler body

Figure C.8: Radial forces, elastic deformation and stiffness for increasing polar path radius r of the coupler body.

At the prescribed conditions for θ_2 and $\dot{\theta}_2$, a numerical approximation of the equilibrium configuration is found using a Newton-Raphson scheme starting from an initial guess and iterating to a steady motion point. As initial guess the motion a conventional Oldham coupling would make is used:

$$\mathbf{q} = [\theta_2, 2\theta_2, L_1/2, \theta_2, \theta_2]^T \quad (\text{C.53})$$

$$\dot{\mathbf{q}} = [\dot{\theta}_2, 2\dot{\theta}_2, 0, \dot{\theta}_2, \dot{\theta}_2]^T \quad (\text{C.54})$$

The steady motion point has the form $\ddot{\mathbf{q}} = \mathbf{0}$, $\dot{\mathbf{q}} = \dot{\mathbf{q}}_{\text{eq}}$, $\mathbf{q} = \mathbf{q}_{\text{eq}}$. Notice that in the case of non-constant stiffness this equilibrium is only valid at this specific point, and will change with changing stiffness.

For nonzero axle misalignment L_1 the stiffness of the coupling both depends on its orientation or angle and on its rotational velocity. Eigenfrequencies will thus change accordingly. Therefore, the modal analysis will be executed at multiple linearisation points for varying angles θ_2 and increasing rotational velocity $\dot{\theta}_2$.

Around such an equilibrium configuration, the linearised system matrices can be built:

$$\mathbf{K} = \frac{\partial(\mathbf{f}_\gamma + \mathbf{f}_{\mathcal{I}})}{\partial \mathbf{q}} \quad (\text{C.55})$$

Here, $\mathbf{f}_{\mathcal{I}}$ represent the inertial forces forces, the first two terms of the Lagrange equation. \mathbf{f}_γ represent the elastic forces, the third term within Lagrange. This now results in the linearised EoM with respect to the linearisation point:

$$\mathbf{M}\ddot{\tilde{\mathbf{q}}} + \mathbf{C}\dot{\tilde{\mathbf{q}}} + \mathbf{K}\tilde{\mathbf{q}} = \mathbf{0} \quad (\text{C.56})$$

$$\mathbf{q} = \mathbf{q}_{\text{eq}} + \tilde{\mathbf{q}}, \quad \dot{\mathbf{q}} = \dot{\mathbf{q}}_{\text{eq}} + \dot{\tilde{\mathbf{q}}} \quad (\text{C.57})$$

The four second order differential equations of equation C.56 can be written as a set of eight first order equations C.58 as given by [28], using state vector \mathbf{z} and system matrices \mathbf{A} and \mathbf{B} .

$$\tilde{\mathbf{A}}\dot{\mathbf{z}} + \tilde{\mathbf{B}}\mathbf{z} = \mathbf{0} \quad \text{with:} \quad (\text{C.58})$$

$$\tilde{\mathbf{A}} = \begin{bmatrix} \mathbf{M} & \mathbf{0} \\ \mathbf{0} & \mathbf{K} \end{bmatrix}, \quad \tilde{\mathbf{B}} = \begin{bmatrix} \mathbf{C} & \mathbf{K} \\ -\mathbf{K} & \mathbf{0} \end{bmatrix} \quad (\text{C.59})$$

The eigen value problem C.60 can then be formed with λ being the roots and \mathbf{V} the matrix of eigen vectors, which could be solved numerically:

$$\lambda \tilde{\mathbf{A}}\mathbf{V} = -\tilde{\mathbf{B}}\mathbf{V} \quad (\text{C.60})$$

The mode shapes can then be represented in the original generalised coordinates \mathbf{q} , being the sum of the found modes and the linearisation point:

$$\mathbf{z} = \begin{bmatrix} \Delta \dot{\mathbf{q}} \\ \Delta \mathbf{q} \end{bmatrix} = \mathbf{V}e^{\lambda t} = \mathbf{V} \left(e^{\Re(\lambda)t} \cdot e^{\Im(\lambda)i t} \right) \quad (\text{C.61})$$

$$= \mathbf{V} \left(e^{\Re(\lambda)t} (\cos \Im(\lambda)t + i \sin \Im(\lambda)t) \right) \quad (\text{C.62})$$

$$\begin{bmatrix} \dot{\mathbf{q}} \\ \mathbf{q} \end{bmatrix} = \begin{bmatrix} \Delta \dot{\mathbf{q}} \\ \Delta \mathbf{q} \end{bmatrix} + \begin{bmatrix} \dot{\mathbf{q}}_{\text{eq}} \\ \mathbf{q}_{\text{eq}} \end{bmatrix} \quad (\text{C.63})$$

For the conservative system without damping, the imaginary part of a λ at a certain linearisation point gives the resonance frequencies of the system. A positive real part of λ indicates instability of the coupling and results in an exponentially growing (unbounded) motion, as for example at the point of zero effective radial stiffness.

C.4.1. Description of the results

In this section, results will be shown for both 5DOF and 17DOF model, as well as for different axle misalignments L_1 . First, all eigenfrequencies will be given for varying angle and velocity. Also, the real part of the roots

λ of the eigenvalue problem will be shown for increasing velocity, giving an indication of the stability of the system.

Secondly, a representation of the eigenvectors or mode shapes is given as bar plots for the different generalised coordinates. Again, these are given for several angles and velocities.

Finally, the behaviour of the first eigenfrequency, which will become zero at instability, is given in a colormap for varying angle and velocity.

At the point of instability, the effective radial stiffness becomes zero as discussed earlier. At this point, the eigenfrequency or the imaginary part of the first root λ drops to zero. The mode shape no longer contains oscillating motion, $e^{\Im(\lambda)t} = 1$. The root λ changes from purely imaginary to purely real and positive. The mode shape thus changes from oscillatory to exponentially increasing. In practice, this results in an unbounded outward radial motion of the coupler body.

Beyond the instability point, no longer a steady motion equilibrium exist, due to the exponential growth of radial motion. The Newton-Raphson scheme thus no longer converges. This results in incorrect results beyond this point, as can be seen in the noise values.

For the eigenvectors, the magnitude is given. This as there can arise a phase difference between the different coordinates for rising velocities. In practice, this means that different coordinates move asynchronously and reach their extremes at different points in time. Damping can also introduce such phase differences. As an example the complex representation of the eigenvectors is given for a few scenarios.

The bar plots of the eigenvectors are furthermore scaled, so that angles are given in radians and translations (radial for example) in centimetres. This because of the dimensions of the mechanism.

C.4.2. Results

Results of the modal analysis. Some notes can be found in the previous section.

5DOF model, 20mm axle misalignment The modal analysis of the 5DOF model for which the input axle angle and velocity are prescribed. 4DOF remain.

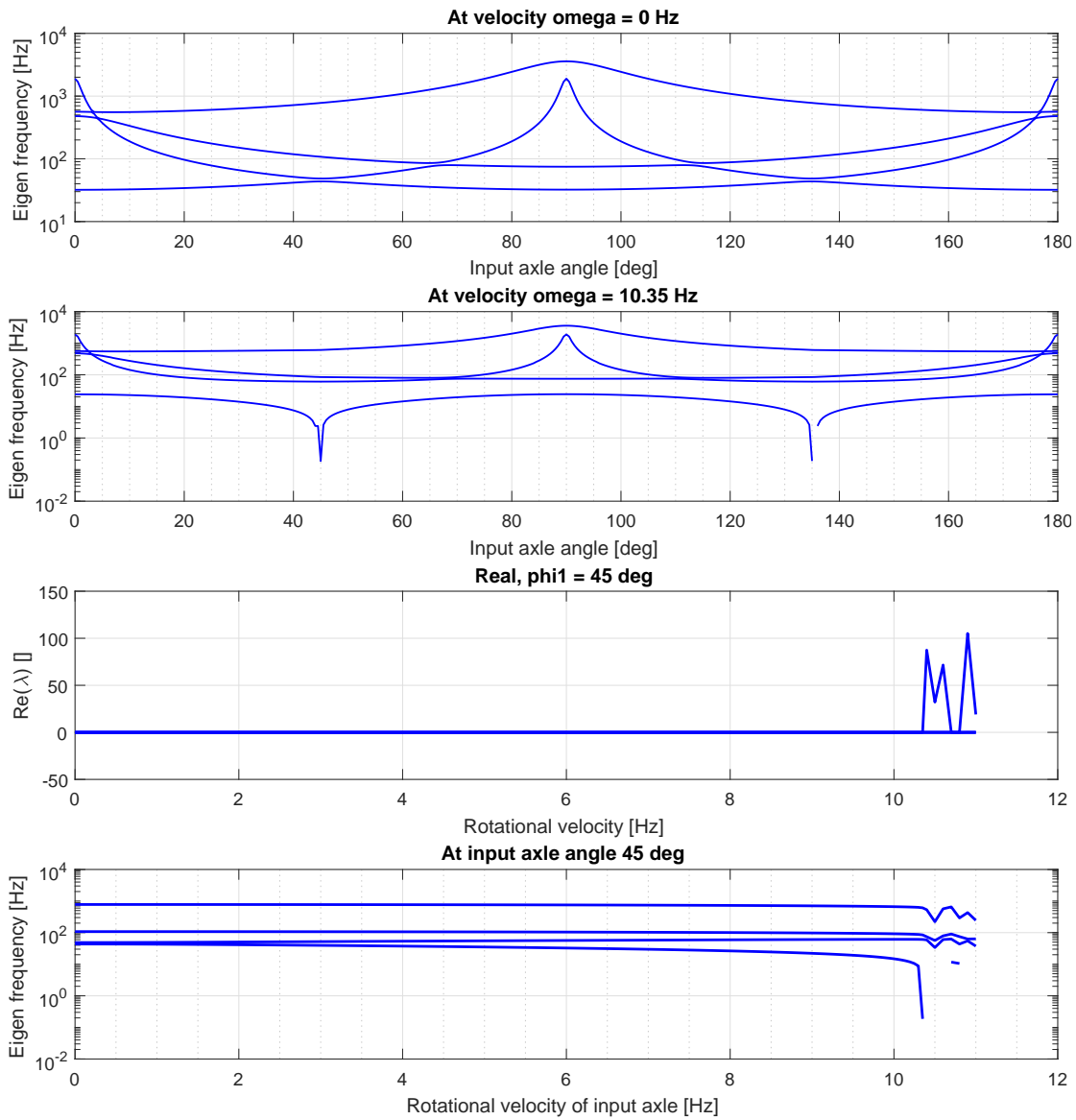


Figure C.9: Eigenfrequencies and real part of eigenproblem roots λ for varying input axle angles θ_2 and input axle velocities $\dot{\theta}_2$.

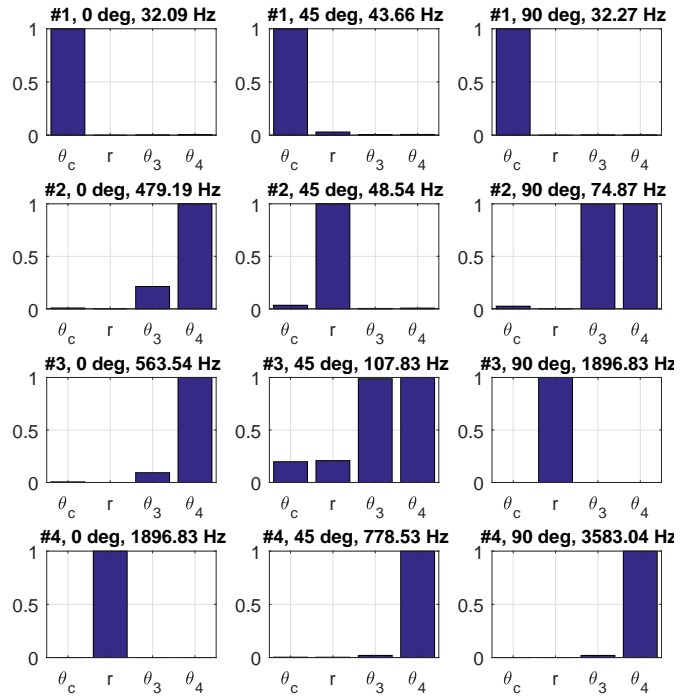


Figure C.10: Magnitude of the eigenvectors of the coupling at standstill, for three different input axle angles θ_2 .

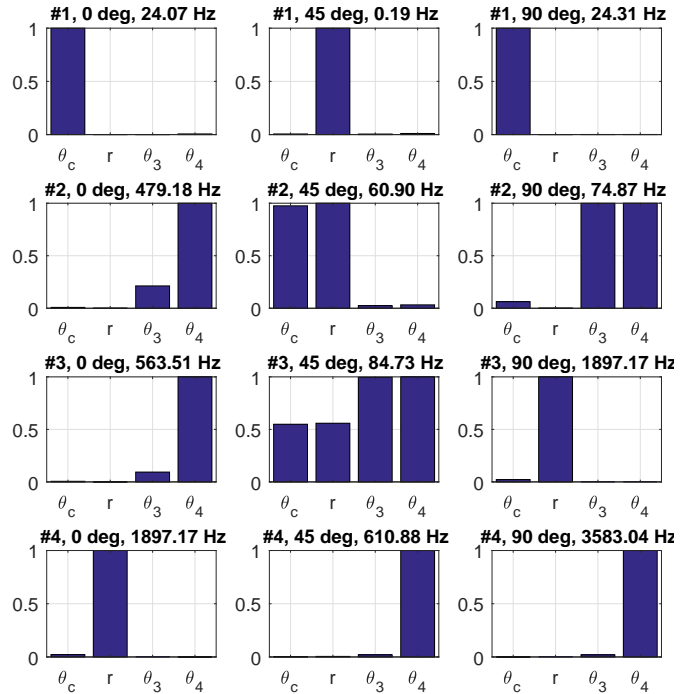


Figure C.11: Magnitude of the eigenvectors of the coupling near the instability point at a rotational velocity of 10.35 Hz, for three different input axle angles θ_2 .

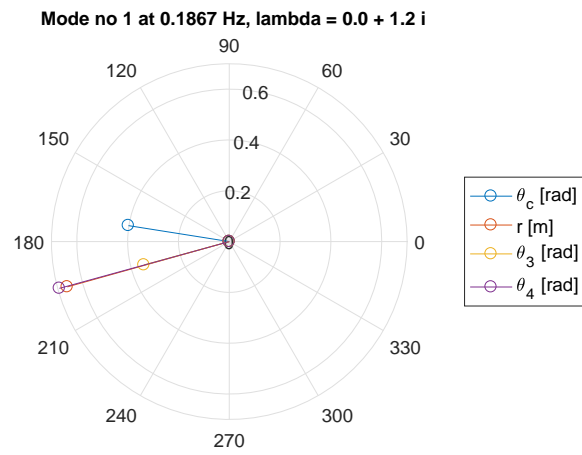


Figure C.12: Representation of the first eigenvector near the instability point, in the complex plane, indicating the phase differences. Note the different units for different coordinates.

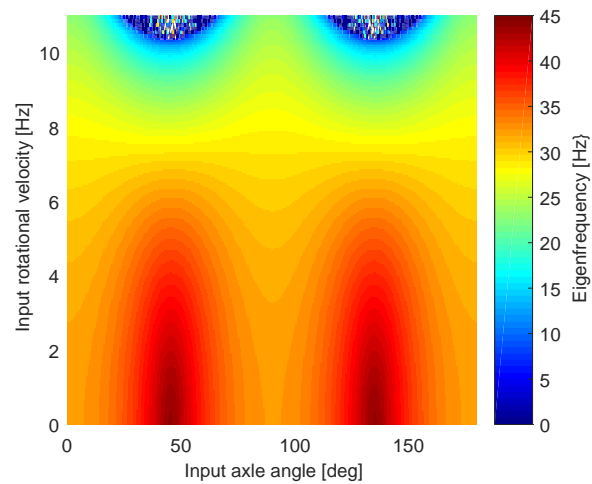


Figure C.13: Colormap of the first eigenfrequency for varying input axle angles θ_2 and input axle velocities $\dot{\theta}_2$. Zero frequency indicates instability.

17DOF model, 20mm axle misalignment The modal analysis of the 17DOF model for which the input axle angle and velocity are prescribed. 16DOF remain.

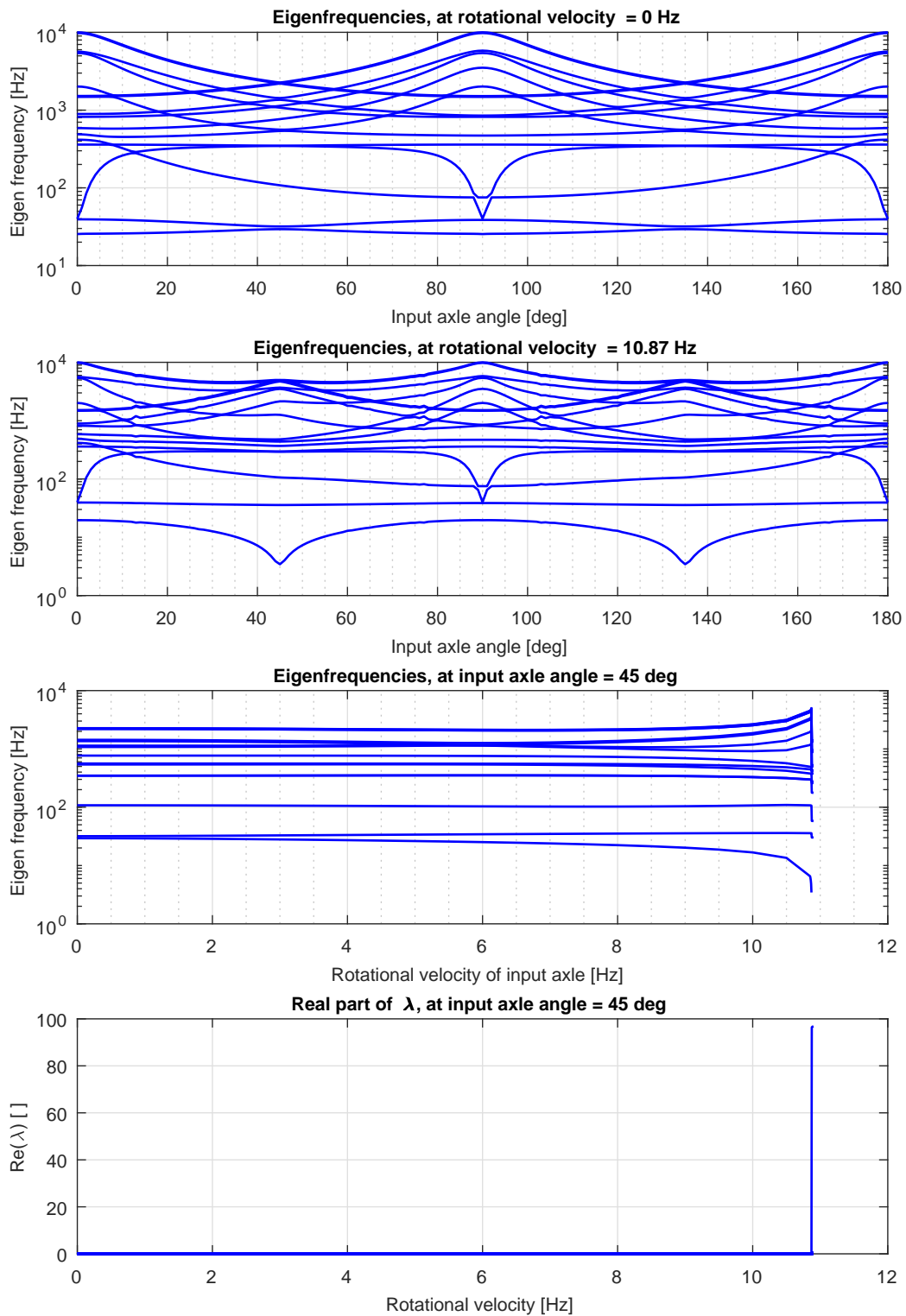


Figure C.14: Eigenfrequencies and real part of eigenproblem roots λ for varying input axle angles θ_2 and input axle velocities $\dot{\theta}_2$.

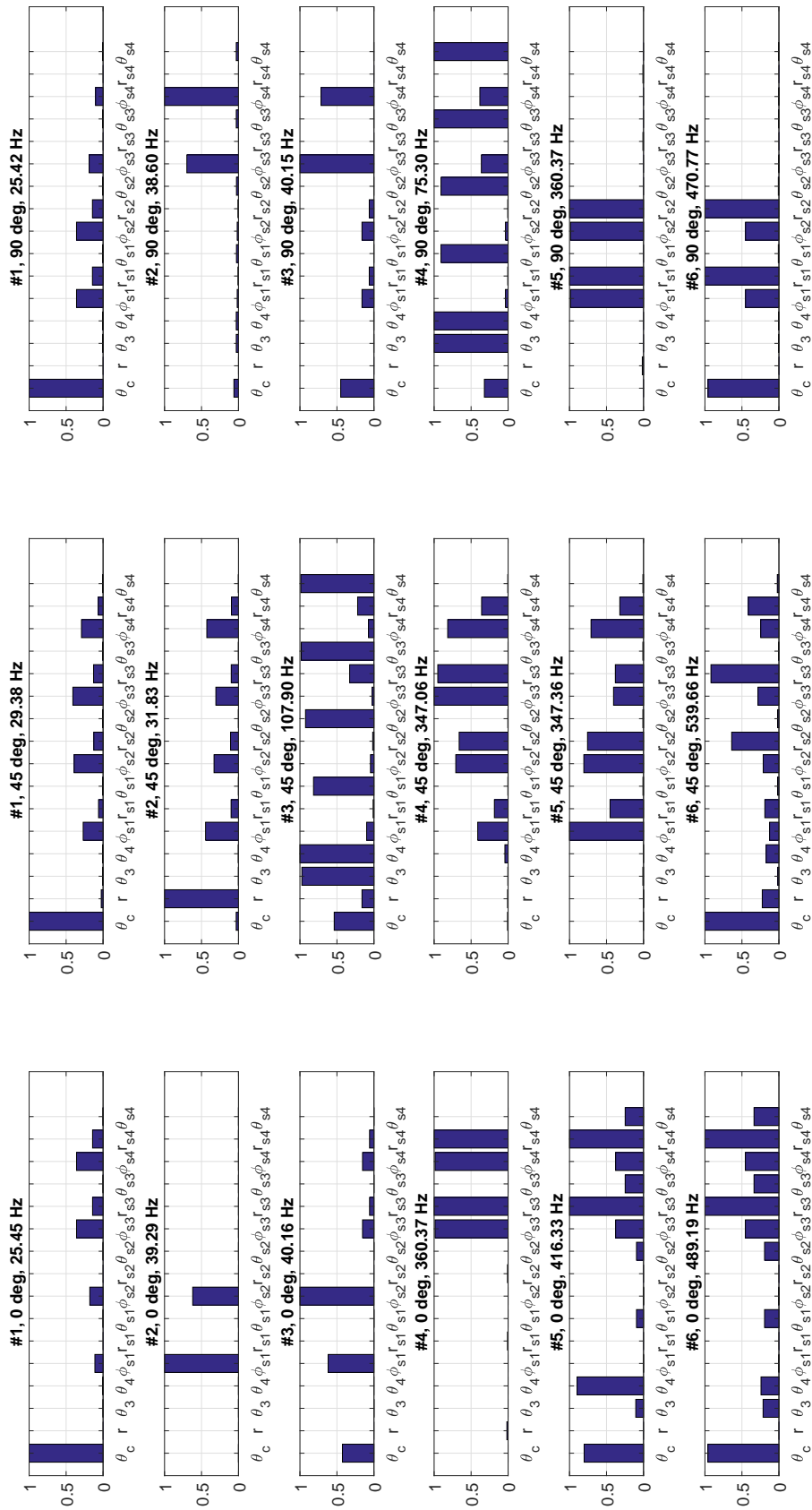


Figure C.15: Magnitude of the eigenvectors of the coupling at standstill, for three different input axle angles θ_2 .

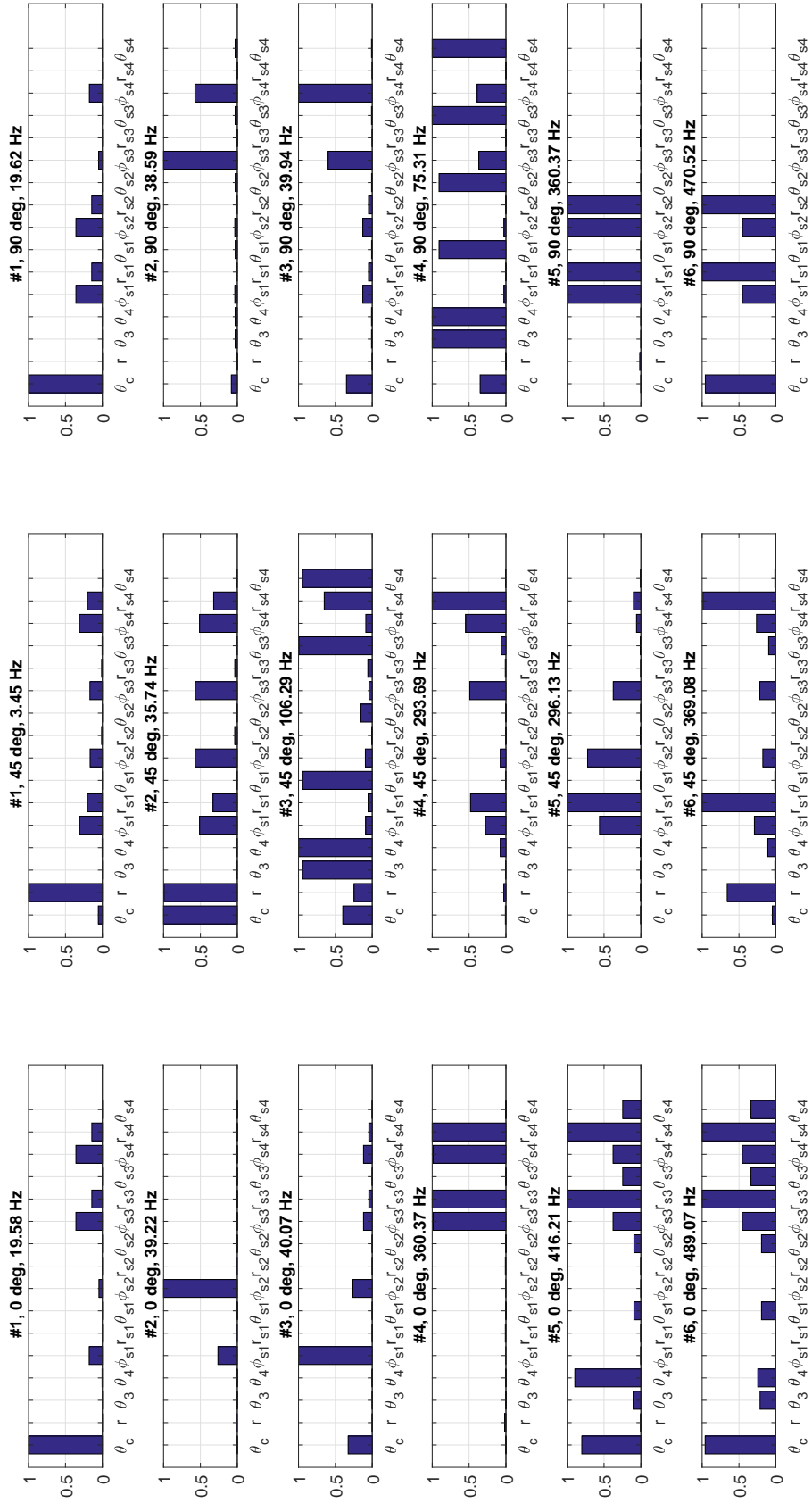


Figure C.16: Magnitude of the eigenvectors of the coupling near the instability point at a rotational velocity of 10.87 Hz, for three different input axle angles θ_2 .

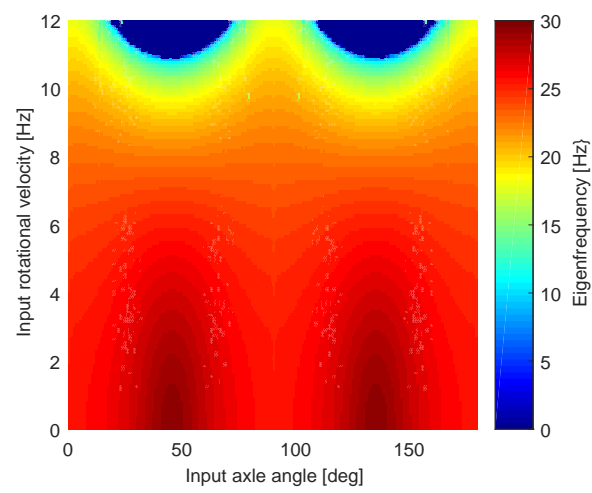


Figure C.17: Colormap of the first eigenfrequency for varying input axle angles θ_2 and input axle velocities $\dot{\theta}_2$. Zero frequency indicates instability.

C.5. Time integration

To get insight in the motion of the different bodies during rotation, the found equations of motion can be integrated in time numerically. This way, scenario's for different velocities, accelerations, loads, damping, bearing friction etcetera can be analysed. In this section, the method for and results of the time integration are discussed.

C.5.1. Method

To be able to compare the results with the experimental data, several terms have to be added to the EoM:

$$\frac{d}{dt} \left(\frac{\partial T}{\partial \dot{\mathbf{q}}} \right) - \frac{\partial T}{\partial \mathbf{q}} + \frac{\partial V}{\partial \mathbf{q}} + \mathbf{C}_{\text{internal}} \dot{\mathbf{q}} + \mathbf{C}_{\text{friction}} \dot{\mathbf{q}} - \mathbf{Q}_s = \mathbf{0} \quad (\text{C.64})$$

The added terms, being the internal damping $\mathbf{C}_{\text{internal}} \dot{\mathbf{q}}$, the damping coming from the setup's bearings $\mathbf{C}_{\text{friction}} \dot{\mathbf{q}}$ and the forcing vector \mathbf{Q}_s will be discussed individually now.

To prevent numerical integration instability, proportional or Rayleigh damping is added to the system. In this damping model, the damping matrix is a linear combination of the mass and stiffness matrix. It thus is assumed that damping is proportional to these. Mass and stiffness matrices are multiplied by the proportionality constants α and β respectively:

$$\mathbf{C}_{\text{int}} = \alpha \mathbf{M} + \beta \mathbf{K} \quad (\text{C.65})$$

This results in modal damping ratios ζ which depend on their eigenfrequency in the following manner:

$$\zeta = \frac{1}{2} \left(\frac{\alpha}{\omega_n} + \beta \omega_n \right) \quad (\text{C.66})$$

The mass proportional term dampens the low resonance frequencies and the stiffness proportional term the high frequencies. The scalar proportionality constants are normally determined empirically. As a starting point, a damping ratio of 0.1 % can be taken for flexure mechanisms [23], which then can be tuned. In figure C.18 a random example of the resulting damping ratio as function of the resonance frequency is given.

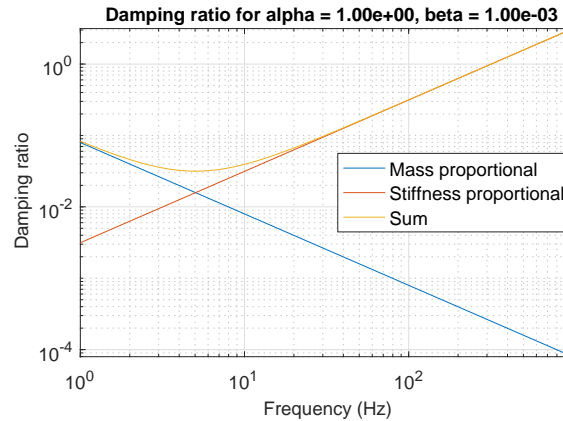


Figure C.18: Damping ratio's for mass and stiffness proportional damping for two random proportionality constants.

As for the coupling at the EoM are non-linear, first a proper linearisation point has to be chosen, at which the mass and stiffness matrices can be computed. Linearisation is done in a similar way as for the modal analysis. For now, as a linearisation point static equilibrium at $\theta_2 = 45^\circ$ is chosen. Looking at the results from the modal analysis, it can be seen that at that point most eigenfrequencies are at the middle of their range. Therefore, this point is considered to be an average representation of the systems stiffnesses. However, the result is that at configurations with a higher stiffness, the resulting mode shape will experience a lower damping ratio, and vice versa. The damping matrix at linearisation point:

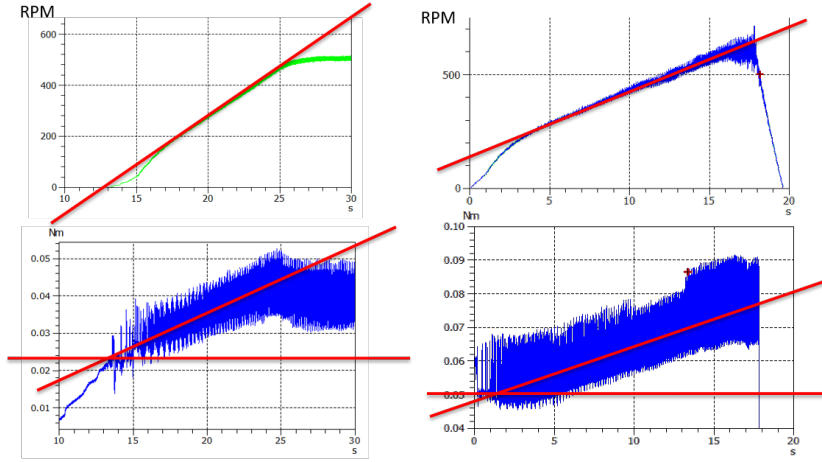


Figure C.19: Rotational velocity (upper figures) and applied motor torque (lower figures) as measured with the experimental setup. The left two figures show a measurement with only the input axle connected to the motor. The right two figures show a 'normal' measurement, in which a compliant coupling at maximum misalignment connects input and output axles.

$$\text{Linearization point: } \mathbf{q}_0 = \text{static equilibrium at } 45\text{deg}, \dot{\mathbf{q}}_0 = \ddot{\mathbf{q}}_0 = \mathbf{0} \quad (\text{C.67})$$

$$\mathbf{C}_{\text{internal}} = \alpha \mathbf{M}|_{\mathbf{q}_0, \dot{\mathbf{q}}_0} + \beta \mathbf{K}|_{\mathbf{q}_0, \dot{\mathbf{q}}_0} \quad (\text{C.68})$$

$$\text{Damping force: } = \mathbf{C}_{\text{internal}} \Delta \dot{\mathbf{q}} = \mathbf{C}_{\text{int}} (\dot{\mathbf{q}} - \dot{\mathbf{q}}_0) = \mathbf{C}_{\text{int}} \dot{\mathbf{q}} \quad (\text{C.69})$$

Furthermore, to prevent coupling between the coordinates, only the diagonal terms of the resulting damping matrix are used, setting all off diagonal terms to zero. This as coupling between the coordinates can sometimes lead to unexpected results.

The friction torque resulting from the bearings and encoders in the experimental setup is modelled as being linearly depended on the rotational velocity. The torque at input and output axle can then be written as:

$$T_{\text{input axle}} = T_{\text{motor}} - T_{\text{bearing, in}} - c_{\text{bearing, in}} \omega_{\text{in}} \quad (\text{C.70})$$

$$T_{\text{output axle}} = -T_{\text{bearing, out}} - c_{\text{bearing, out}} \omega_{\text{out}} \quad (\text{C.71})$$

$$(\text{C.72})$$

Or, using the vectors as given in the EoM:

$$\mathbf{C}_{\text{friction}} = [c_{\text{friction, in}} \ 0 \ 0 \ 0 \ c_{\text{friction, out}}]^T \quad (\text{C.73})$$

$$\mathbf{Q}_s = [T_{\text{motor}} - T_{\text{friction, in}} \ 0 \ 0 \ 0 \ -T_{\text{friction, out}}]^T \quad (\text{C.74})$$

The friction parameters $T_{\text{friction, in}}$, $T_{\text{friction, out}}$, $c_{\text{friction, in}}$ and $c_{\text{friction, out}}$ can then be determined using the experimentally measured torque. A simple schematic is given in figure C.19 in which the applied motor torque is given for a scenario with only a disconnected input axle, and a normal measuring scenario with the compliant coupling between input and output axle at maximum misalignment. In the figure, the constant and velocity depended friction torque can be indicated. A line can be fitted through the torque data, from which in combination with the rotational velocity from the upper figures the needed parameters can be computed. The left figure gives input axle values. If these values are then subtracted from the values from the right figures, the output axle parameters result.

In this method it thus is assumed that all motor torque is absorbed by the friction of bearing and encoders and acts at the input and output axle. In reality also some energy will be dissipated in the coupling itself due to internal material damping, and by air friction on the rotating bodies of the coupling.

For executing the numeric time integration, the ODE solvers from MATLAB are used. For this, the EoM has to be written as a first order ODE $\dot{y} = f(y, t)$. This is done in the following manner:

$$M = \frac{\partial f_{\mathcal{F}}}{\partial \ddot{q}} \quad (C.75)$$

$$F_v = - \left(\frac{d}{dt} \left(\frac{\partial T}{\partial \dot{q}} \right) - \frac{\partial T}{\partial q} + \frac{\partial V}{\partial q} + C_{\text{internal}} \dot{q} + C_{\text{friction}} \dot{q} - Q_s \right) - M \ddot{q} \quad (C.76)$$

$$\ddot{q} = M^{-1} F_v \quad (C.77)$$

$$y = \begin{bmatrix} q \\ \dot{q} \end{bmatrix} \quad (C.78)$$

$$\dot{y} = f(y, t) = \begin{bmatrix} \dot{q} \\ M^{-1} F_v \end{bmatrix} \quad (C.79)$$

Furthermore, some initial conditions are needed for the time integration. For this, an equilibrium as found by a Newton-Raphson scheme is used. A static equilibrium as well as a steady motion equilibrium at some velocity can be used. Furthermore, a driving motor torque T_{motor} has to be chosen. These can be based on the measured torques in the experiments.

C.6. Time integration results

Using the described method for time integration, multiple simulations were executed, of which the results were analysed in multiple ways. As indicated earlier, the time integration as performed did not give trustworthy results. However, some results will be given to show the behaviour of the models. At the end of the section, some recommendations will be given for possible improvement of the time integration results.

Especially at higher velocities, results often give a build up of oscillations, which sometimes leads to excessive unbounded displacements. It is expected that these problems have a numerical origin. Within the explicit ODE solvers used, numerical error can cumulate, resulting in incorrect results. Implementation of proportional damping is used in an attempt to overcome this problem. However, by doing this elements are added to the model which do not resemble reality.

C.6.1. 5DOF model

At velocities up to circa 300 min^{-1} , no damping is needed to maintain integration stability for the 5DOF model. Therefore, the results shown will be at a rotational velocity of circa 300 min^{-1} , without any damping. The introduction of non realistic behaviour caused by damping implementation then is prevented.

5DOF model, 300 RPM, no internal damping The parameters for this set of results are:

- Maximum axle misalignment of $L_1 = 20 \text{ mm}$
- No internal damping: $\alpha = 0, \beta = 0$
- Motor torque T_{motor} of $4.660 \times 10^{-2} \text{ Nm}$, based on experimental values
- Input friction torque $T_{\text{friction,in}}$ of $3.4713 \times 10^{-2} \text{ Nm}$, based on experimental values
- Input friction damping $c_{\text{friction,in}}$ of 0 Nm rad^{-1}
- Output friction torque $T_{\text{friction,out}}$ of 0 Nm
- Output friction damping $c_{\text{friction,out}}$ of $3.7837 \times 10^{-4} \text{ Nm rad}^{-1}$, which equilibrates the effective input torque at 300 min^{-1}
- Matlab ODE15s solver used with a maximum time step of $1 \times 10^{-5} \text{ s}$

Here, all experimentally determined input axle friction at this velocity is subtracted from the motor torque. On the output axle, only the velocity depended friction term is used, and set to equilibrate the resultant input torque at the desired velocity of 300 min^{-1} .

5DOF model, multiple velocities, no internal damping Below, the velocity error for two other velocities is given.

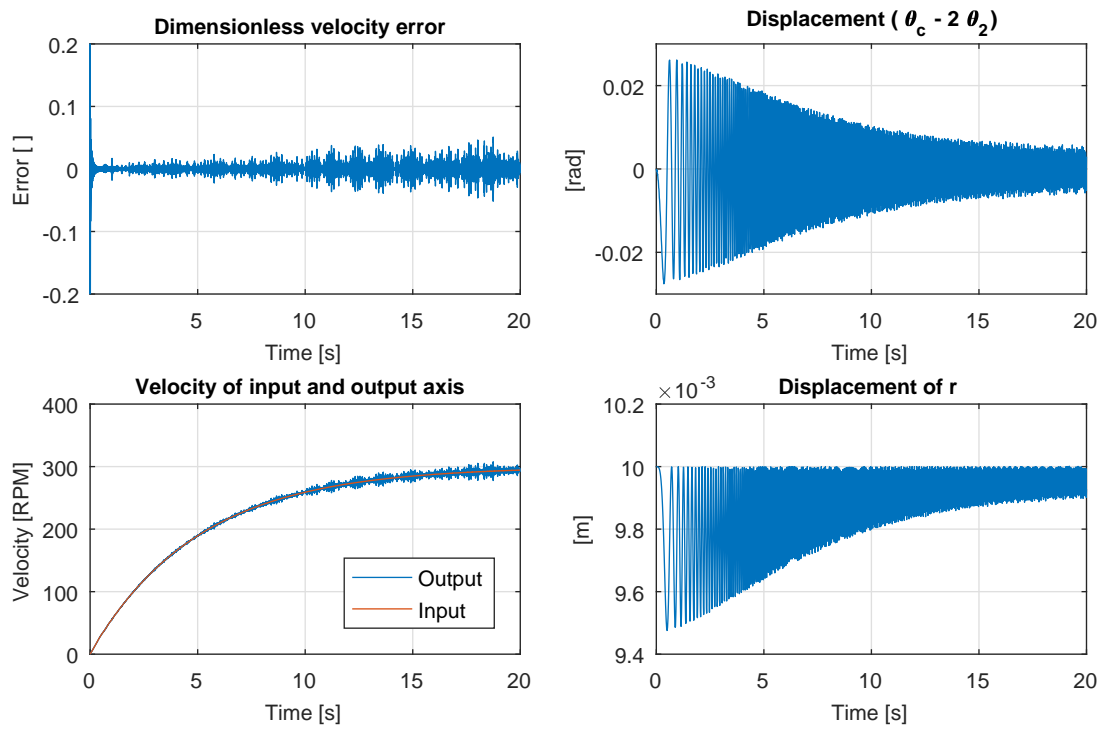


Figure C.20: Velocity error, velocity, and polar coordinates of coupler body. As the polar coupler body angle θ_c is continuously increasing, $2\theta_2$ is subtracted to show only the deviation from its 'conventional Oldham kinematics' path.

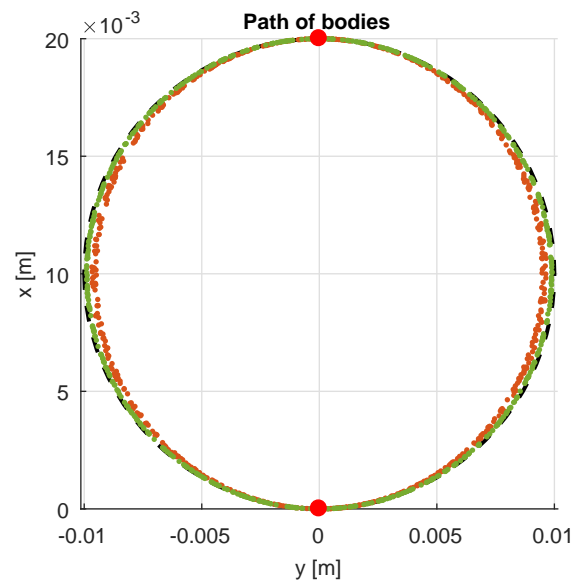


Figure C.21: Path of the coupler body in time. In green, some points at the start of the simulation are given, at which the radius still is low. In red, the path at the end of the simulation is shown, when the maximum speed is reached, in when the radius is larger. The black dashed line gives a circle through input and output.

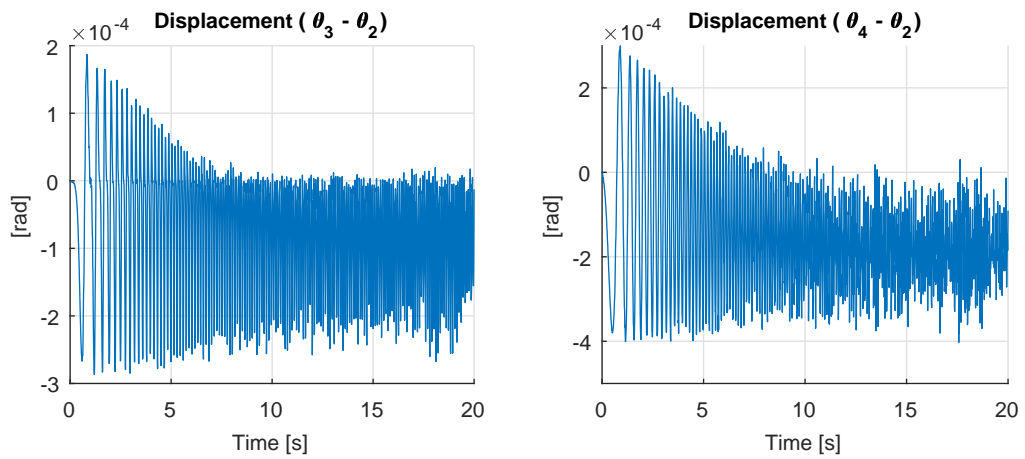


Figure C.22: Body angles of the coupler body and output axle, again given as a deviation from the input axle angle. For both the negative values indicate that they lag the input axle angle

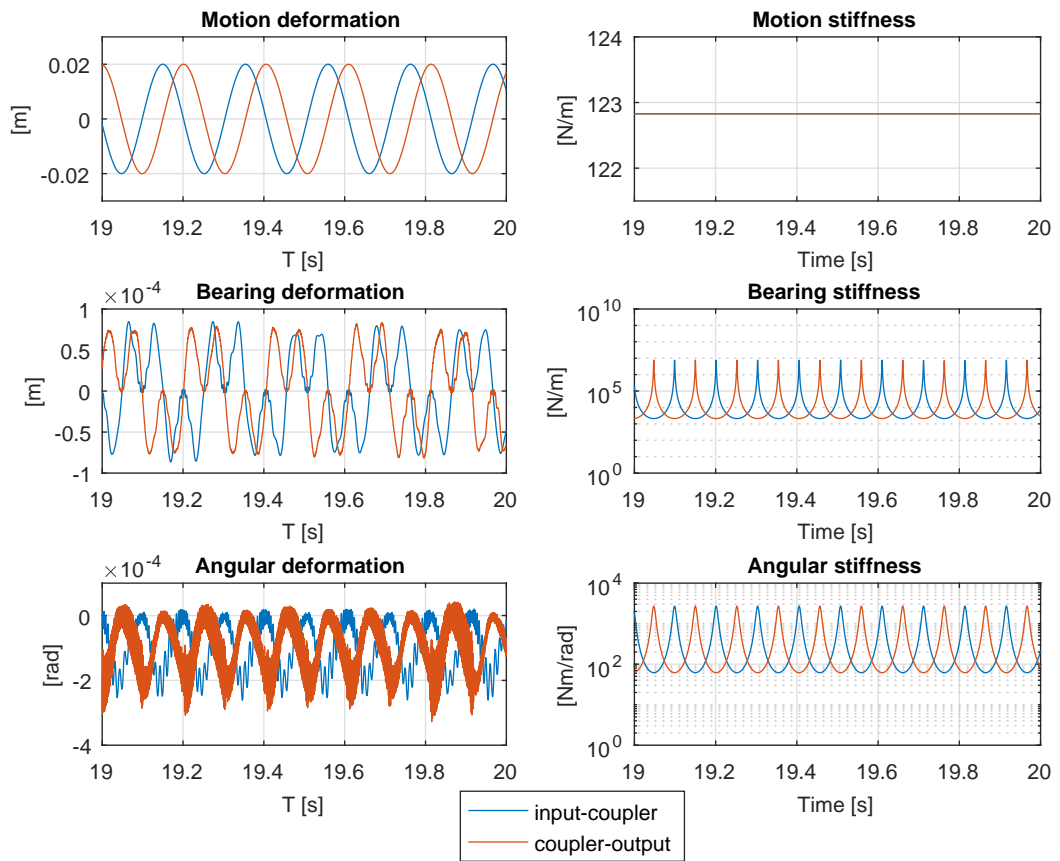


Figure C.23: Elastic deformation and stiffness of the two sets of DP-DP flexures (from input to the coupler body, and from coupler body to output). Given in the three decoupled stiffness directions, being motion, bearing and angular. To show more detail, only the last part of the simulation time is shown.

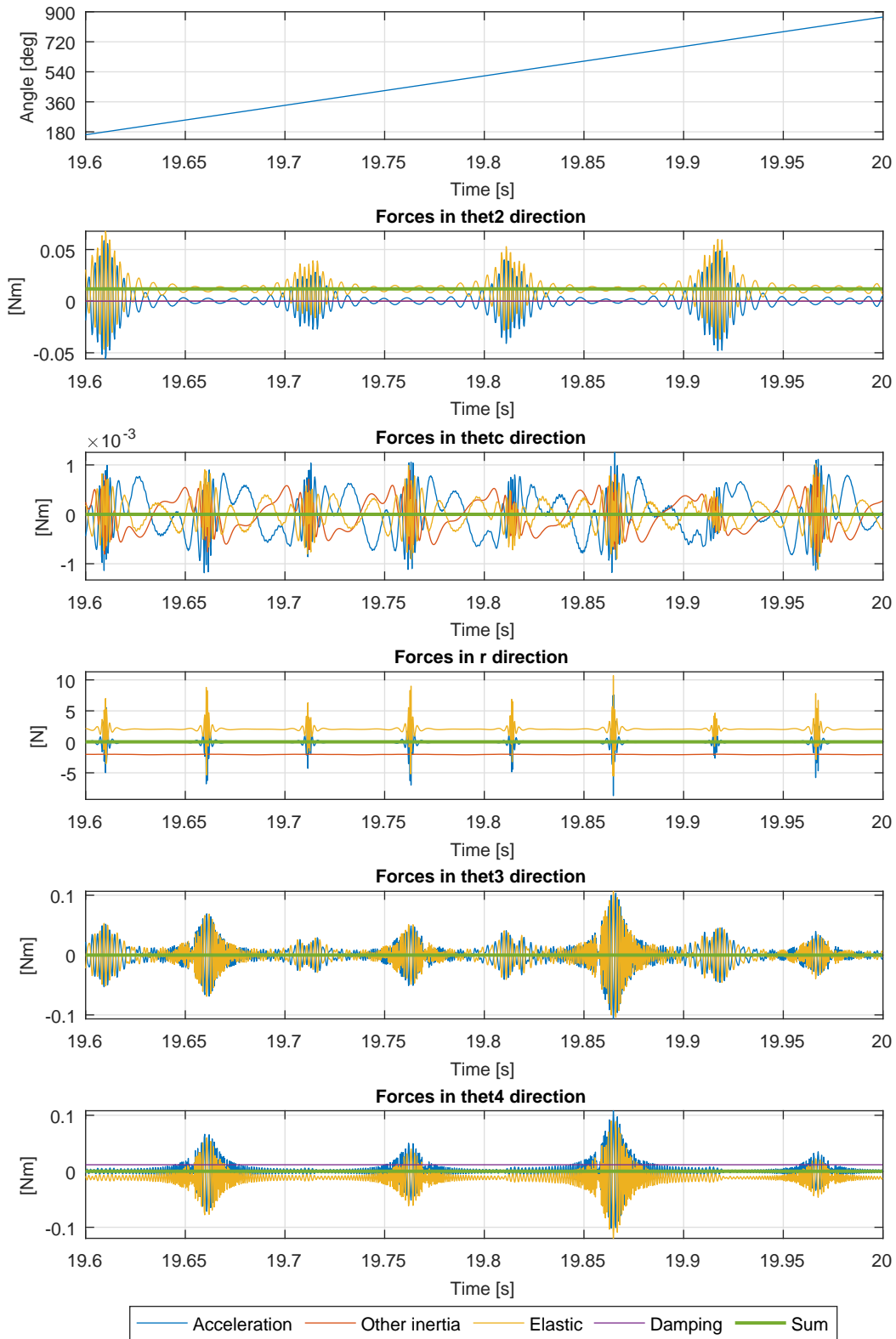


Figure C.24: All forces acting on the different bodies in the directions of the five generalised coordinates. From the upper graph, in which the input axle angle is given, the orientation of the coupling can be derived. Note that in the input axle rotational direction θ_2 the sum of the forces is non-zero. This resultant gives the motor torque, which is not shown in this graph. Furthermore, the friction torque at output is represented by the damping force (as it was modelled to be proportional to rotational velocity) in the output axle angle direction θ_4 . To show more detail, only the last part of the simulation time is shown.

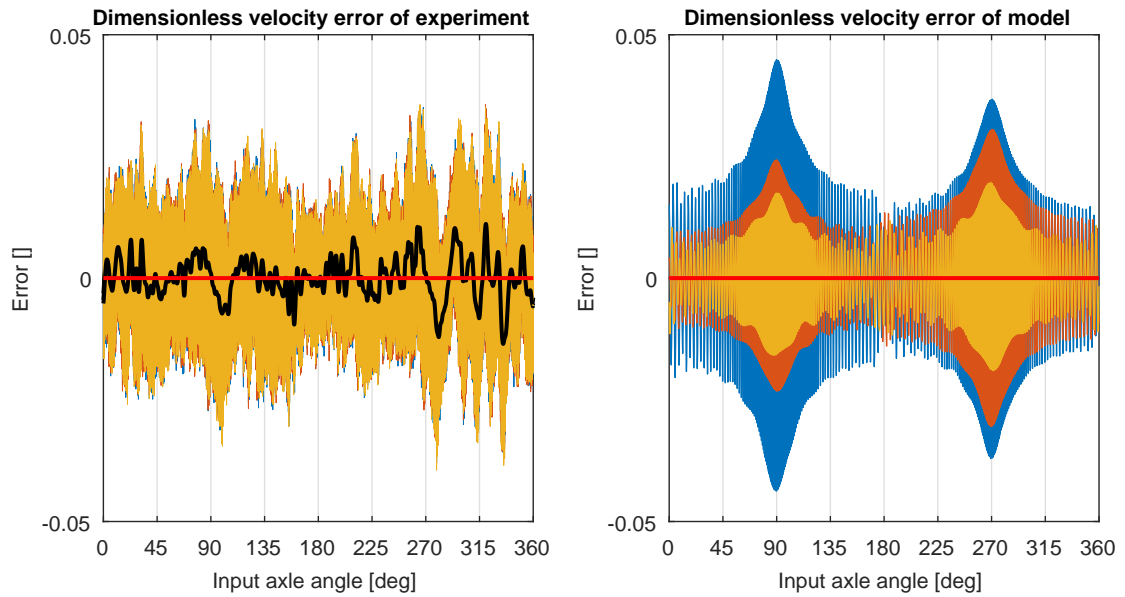


Figure C.25: Comparison of the dimensionless velocity error as resulting from an experiment, and the results from time integration. The error is given as function of the input axle angle. Both for a rotational velocity of circa 300 RPM. In both graphs, three non adjacent duty cycles are shown, in the different colors. In the experimental data, it can be seen that all three duty cycles are similar. The black line in the experimental data shows the 1000Hz low-pass filtered data. For the time integration data however, there is quite some difference between each duty cycle, as is also visible in figure C.20. Furthermore, in the experimental data clearly a repeatable pattern is visible, with peaks at 90 and 270 degree. In the experimental data this can not be seen.

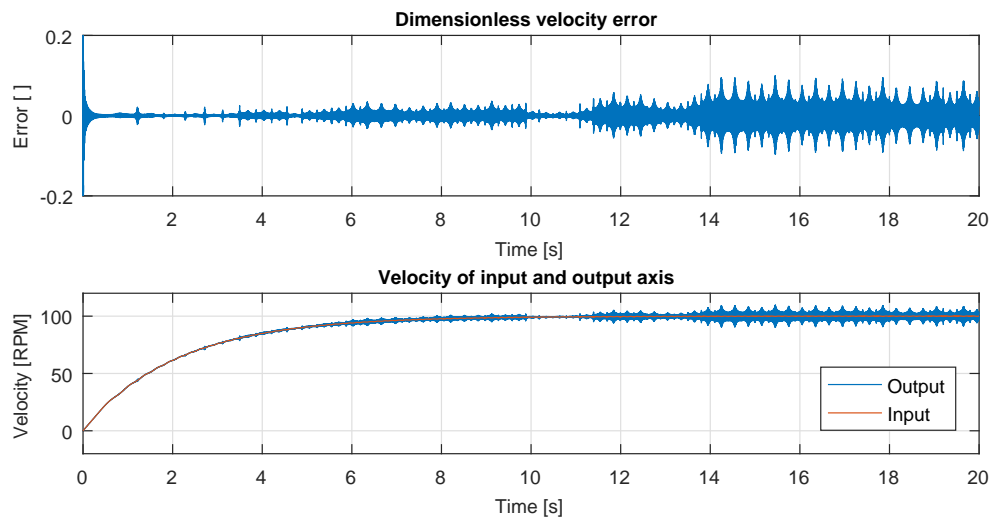


Figure C.26: Dimensionless velocity error and input and output axle velocity at circa 100 rpm. The error is larger than at 300 rpm.

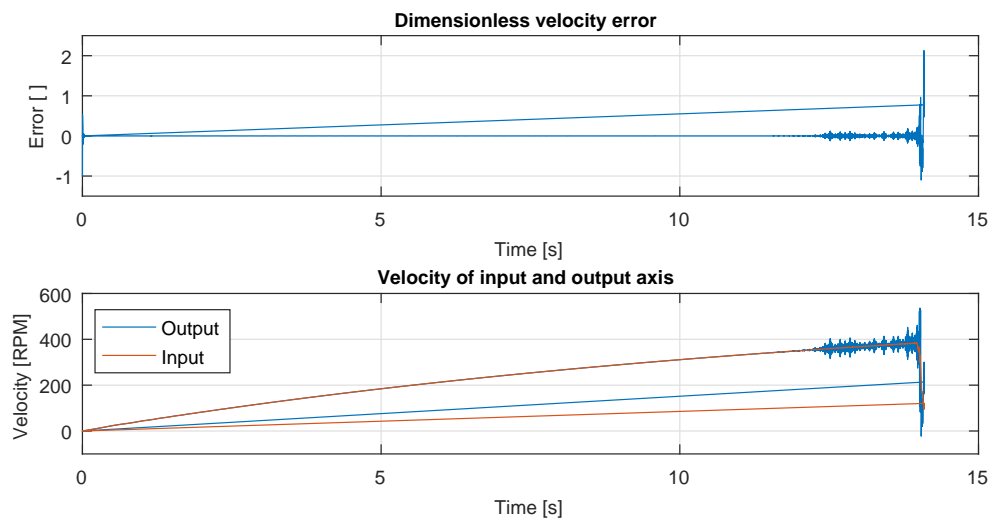


Figure C.27: Dimensionless velocity error and input and output axle velocity at circa 500 rpm. It can be seen that the integration becomes unstable around 400 rpm. No trustworthy results were found for the 5DOF modal above this velocity.

C.6.2. 17DOF model

For the 17DOF model, no stable results were achieved without the implementation of proportional damping. Some results including proportional damping are given below.

17DOF model, multiple velocities, sensitivity to damping In the next figures, the influence of the stiffness proportional damping is shown. An integration is executed, starting from standstill, accelerating to respectively 100, 300 and 500 rpm. For each velocity, the results for six different values of the stiffness proportional damping parameter β are shown. The parameters β are varied within the region that yielded the best results. However, the results at 500 rpm are still far from realistic.

The other parameters used are:

- Maximum axle misalignment of $L_1 = 20$ mm
- Varied stiffness proportional damping: $\alpha = 0$, $\beta = 6 \times 10^{-7} \dots 6.5 \times 10^{-7}$
- Input axle torque T_{in} : (set to yield the desired velocity) 6.2152×10^{-2} N m for 100 rpm 1.5017×10^{-1} N m for 300 rpm 2.4220×10^{-1} N m for 500 rpm

Input friction damping $c_{friction,in}$ of 1.6237×10^{-4} N m rad $^{-1}$ (based on experimental values)

- Output friction torque $T_{friction,out}$ of -1.8114×10^{-2} N m (based on experimental values)
- Output friction damping $c_{friction,out}$ of 3.5801×10^{-4} N m rad $^{-1}$ (based on experimental values)
- Matlab ODE45 solver used with a maximum time step of 1×10^{-5} s

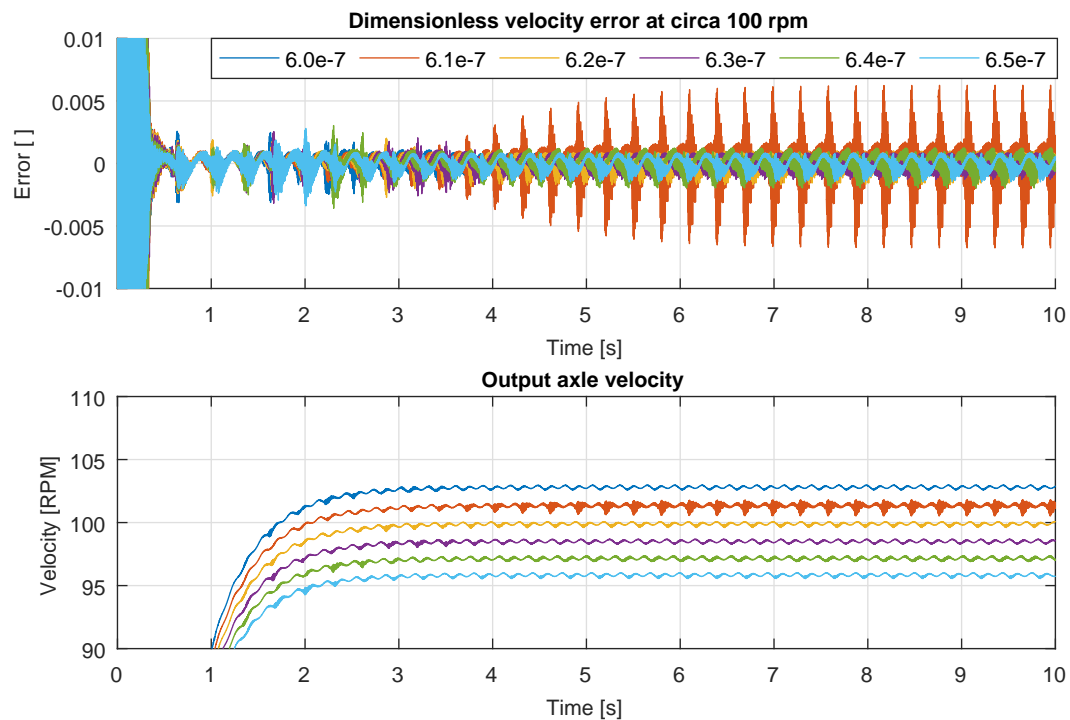


Figure C.28: Dimensionless velocity error and output axle velocity for varying values of β as shown in the legend.

17DOF model, multiple velocities, sensitivity to input torque In the next figures, the influence of a slight change in input torque is shown. All other parameters are kept constant.

The other parameters used are:

- Maximum axle misalignment of $L_1 = 20$ mm
- Stiffness proportional damping: $\alpha = 0$, $\beta = 6.5 \times 10^{-7}$
- Input axle torque T_{in} as given in the legend of the figures
- Input friction damping $c_{friction,in}$ of 1.6237×10^{-4} N m rad $^{-1}$ (based on experimental values)
- Output friction torque $T_{friction,out}$ of -1.8114×10^{-2} N m (based on experimental values)

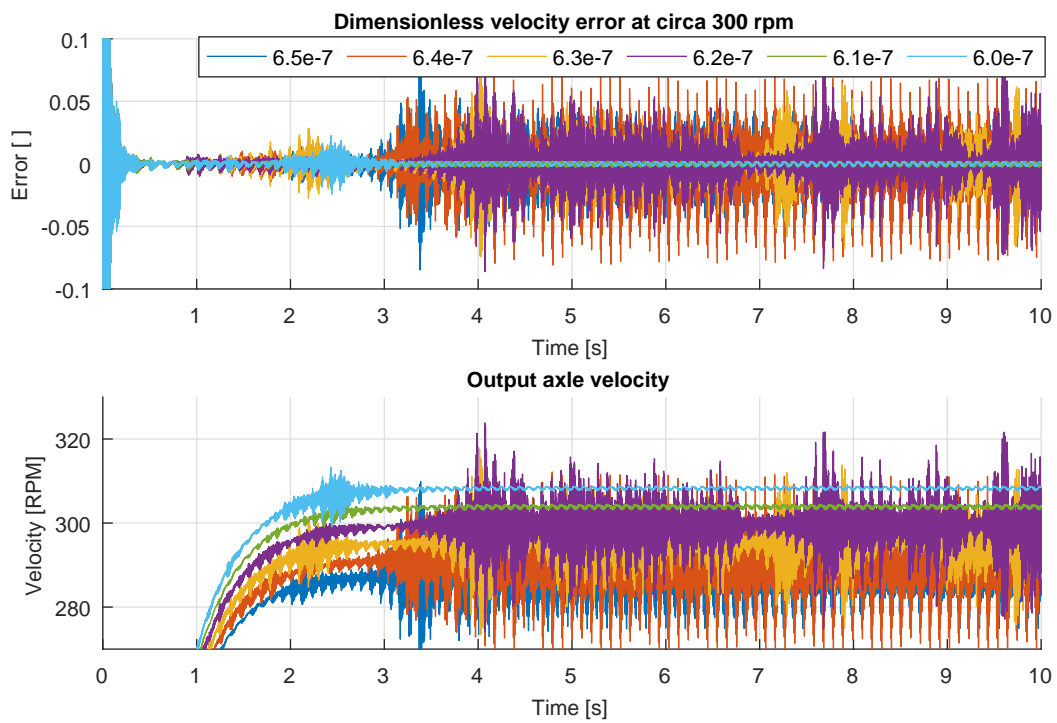


Figure C.29: Dimensionless velocity error and output axle velocity for varying values of β as shown in the legend.

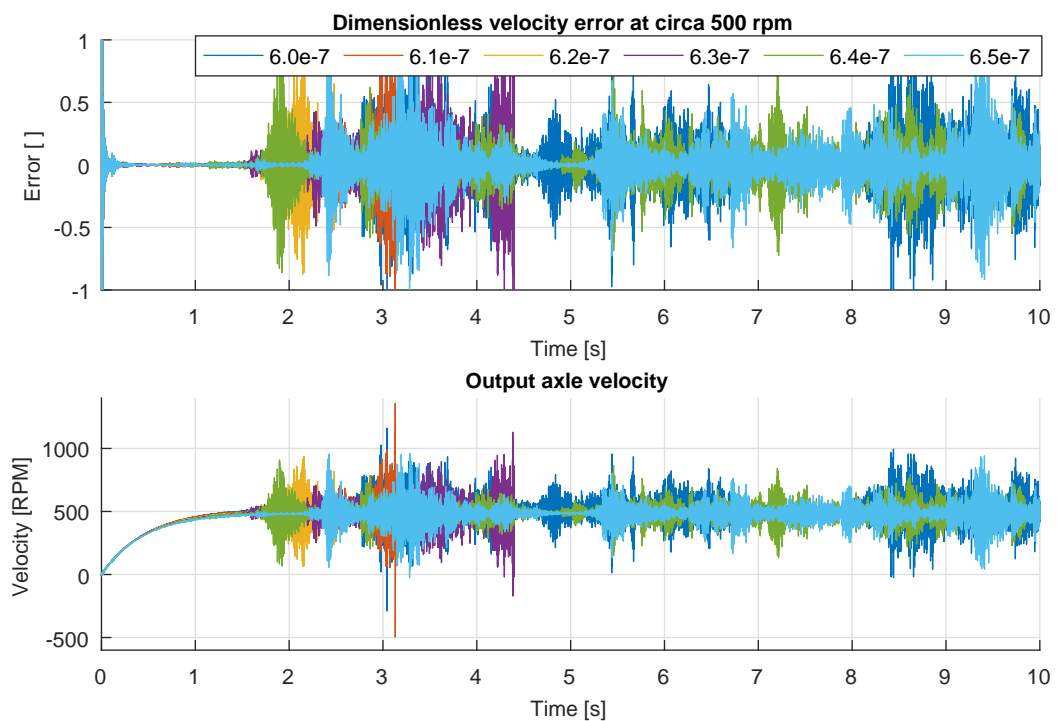


Figure C.30: Dimensionless velocity error and output axle velocity for varying values of β as shown in the legend.

- Output friction damping $c_{\text{friction,out}}$ of $3.5801 \times 10^{-4} \text{ Nmrad}^{-1}$ (based on experimental values)
- Matlab ODE45 solver used with a maximum time step of $1 \times 10^{-5} \text{ s}$

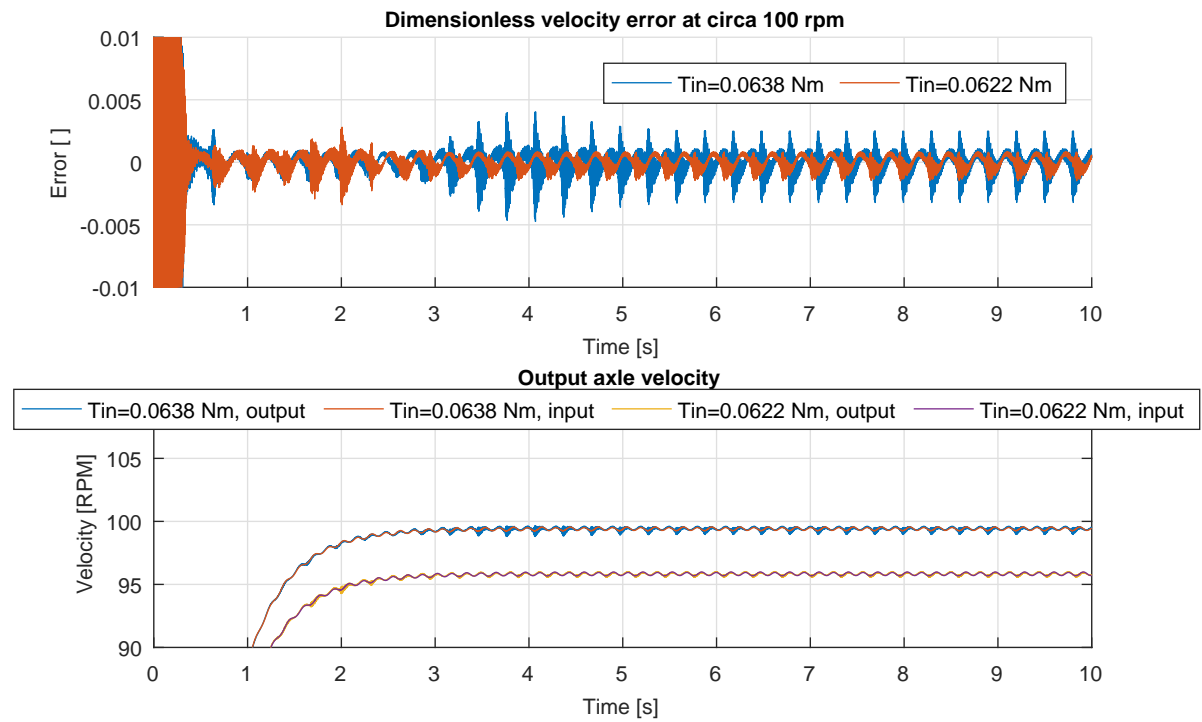


Figure C.31: Dimensionless velocity error and input and output axle velocity for two slightly different input torques as shown in the legend.

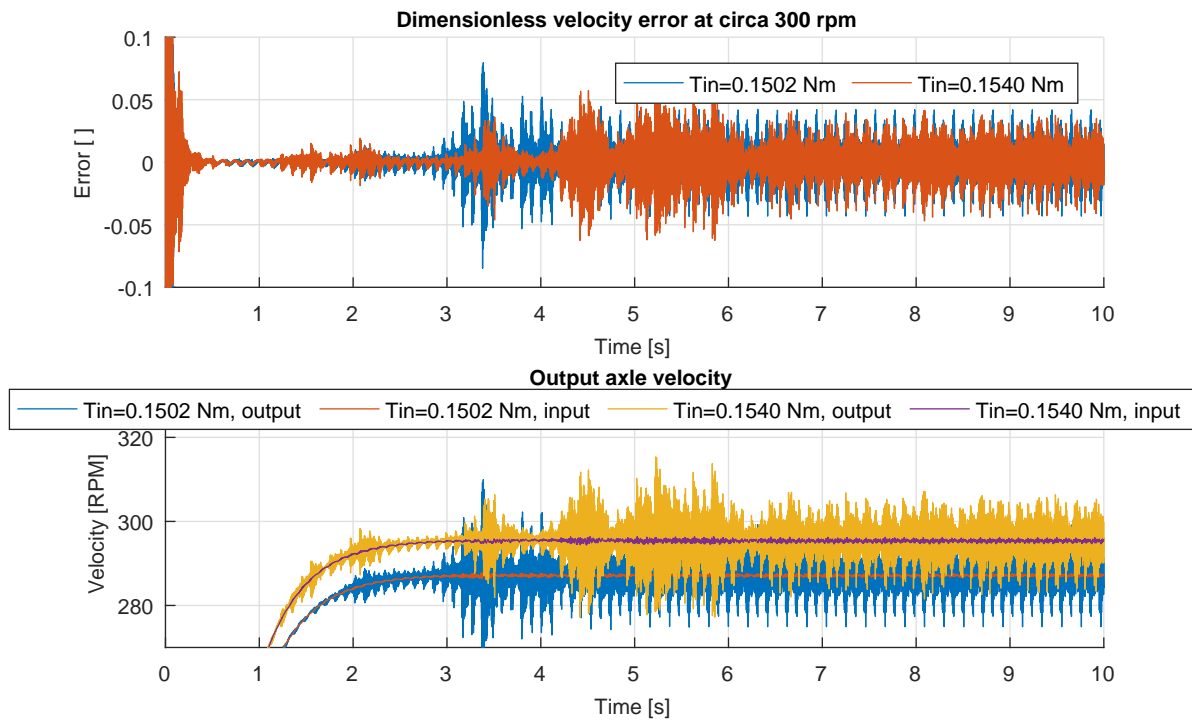


Figure C.32: Dimensionless velocity error and input and output axle velocity for two slightly different input torques as shown in the legend.

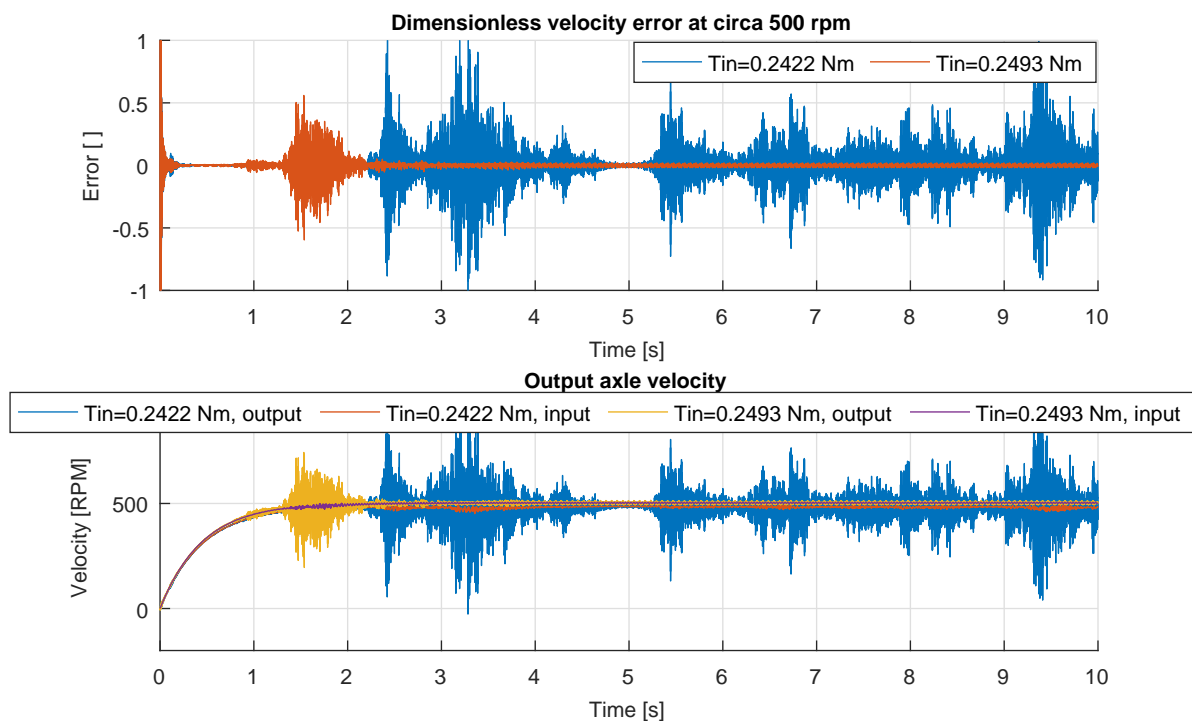


Figure C.33: Dimensionless velocity error and input and output axle velocity for two slightly different input torques as shown in the legend.

In the next figures, the time integration results for the velocity error will be compared with the experimentally measured velocity error. The applied friction parameters in the model are based on the same series of measurements.

- Maximum axle misalignment of $L_1 = 20$ mm
- Stiffness proportional damping: $\alpha = 0$, $\beta = 6.5 \times 10^{-7}$
- Input axle torque T_{in} : (set to yield the desired velocity) 6.38×10^{-2} N m for 100 rpm 1.540×10^{-1} N m for 300 rpm 2.493×10^{-1} N m for 500 rpm

Input friction damping $c_{friction,in}$ of 1.6237×10^{-4} N m rad $^{-1}$ (based on experimental values)

- Output friction torque $T_{friction,out}$ of -1.8114×10^{-2} N m (based on experimental values)
- Output friction damping $c_{friction,out}$ of 3.5801×10^{-4} N m rad $^{-1}$ (based on experimental values)
- Matlab ODE45 solver used with a maximum time step of 1×10^{-5} s

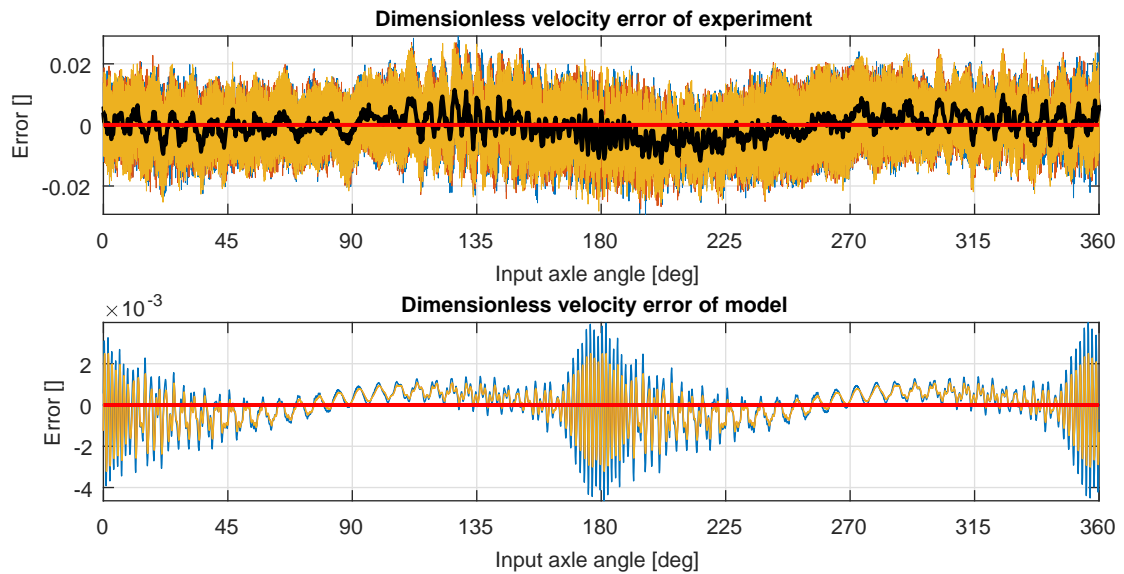


Figure C.34: Comparison of the dimensionless velocity error as resulting from an experiment, and the results from time integration. The error is given as function of the input axle angle. Both for a rotational velocity of circa 100 RPM. In both graphs, three non adjacent duty cycles are shown, in the different colors. The black line in the experimental data shows the 1000Hz low-pass filtered data.

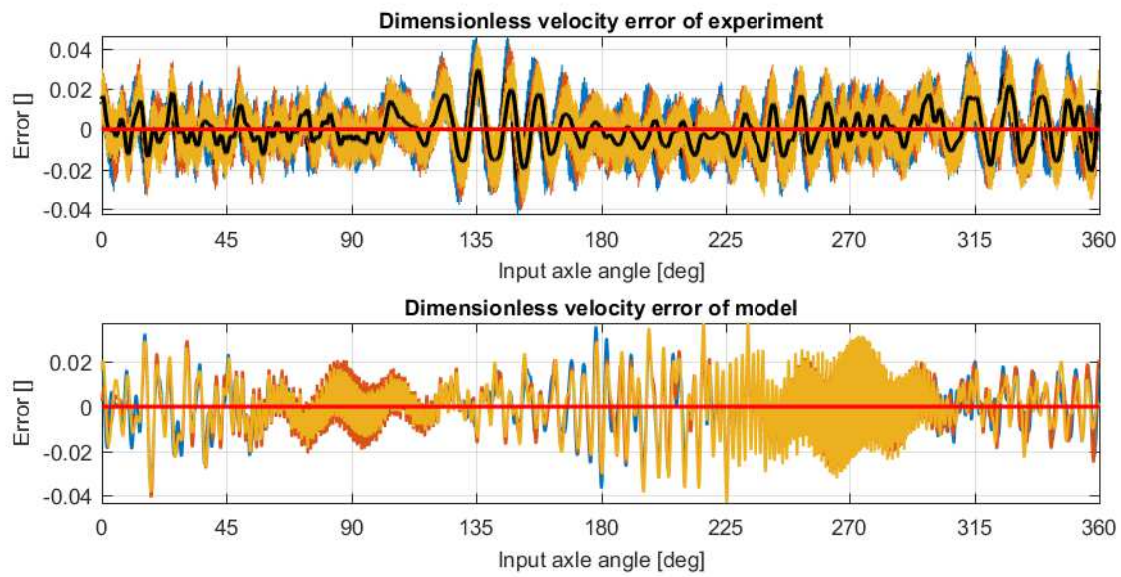


Figure C.35: Comparison of the dimensionless velocity error as resulting from an experiment, and the results from time integration. The error is given as function of the input axle angle. Both for a rotational velocity of circa 300 RPM. In both graphs, three non adjacent duty cycles are shown, in the different colors. The black line in the experimental data shows the 1000Hz low-pass filtered data.

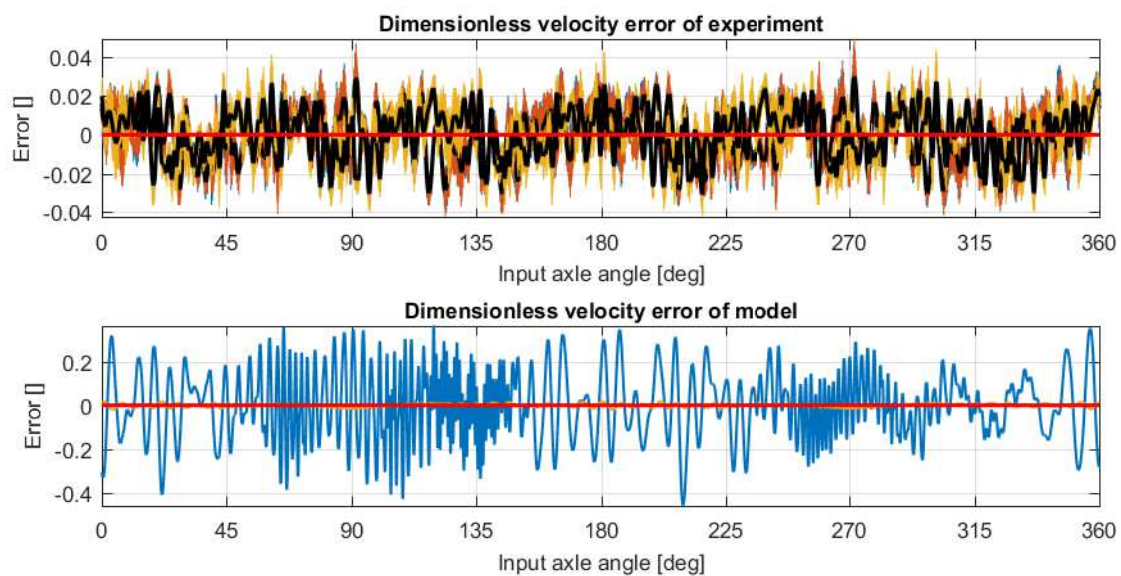


Figure C.36: Comparison of the dimensionless velocity error as resulting from an experiment, and the results from time integration. The error is given as function of the input axle angle. Both for a rotational velocity of circa 500 RPM. In both graphs, three non adjacent duty cycles are shown, in the different colors. The black line in the experimental data shows the 1000Hz low-pass filtered data.

C.6.3. Suggested improvements

It is obvious that the current time integration results are not trustworthy. It is shown that among other things the results depend heavily on the amount of damping applied, the initial conditions and on the applied torque. Some recommendations for future improvement are given:

- Currently, explicit Matlab ODE solvers are used. All available explicit solvers within Matlab are tested on the unstable scenarios, without success. In explicit solvers, numerical errors can build up, which can be the cause of the instability. Use of an implicit solver can potentially give an improvement. For this, the EoM have to be rewritten in another format however.
- For the explicit solvers, it is important to use the proper step size. For most simulations, a step size of 1×10^{-5} s was used, which should represent the highest eigenfrequencies of 1×10^4 Hz well. Smaller step sizes are tried and did not lead to significant improvement.
- For the Matlab ODE solvers, a relative tolerance of 1×10^{-3} was set. The absolute tolerance was set to the maximum expected output values, multiplied by 1×10^{-3} . Smaller tolerances were tried as well, but the enforced maximum step size seemed to be dominant already in the reached accuracy.
- The applied friction conditions are based on experimental data, via the measurement of the motor current. As discussed in other parts of this thesis, this method is inaccurate. This can contribute to the mismatch between model and experiment. Furthermore, the method in which the friction torque is modelled might not be the most realistic representation.
- More attention should be paid to the cause of the excessive motions and instability within the integration results. When the cause is understood better, the search for improvements will be more focussed. Several properties of the model which might contribute to the excessive motions are already indicated:
 - First of all, the EoM are heavily non-linear. Not only the stiffnesses can vary more than an order of magnitude, also geometrical relations introduce non-linearities.
 - A quasi-static rotation, the path radius r of the coupler body is equal to $L_1/2$ when it intersects both axles. Away from these points, the radius decreases. The radius then thus $r \leq L_1/2$. At higher velocities, the centrifugal force pulls the coupler body outwards, and the radius increases. At some point the sign of the radial deflection changes and $r \geq L_1/2$. At this sign inversion, often instabilities were found in the integration results. What exactly causes this problem remains unknown however.
 - Furthermore, toward the point that the coupler COM crosses one of the axles, one of the bearing stiffnesses increases tremendously. This forces the radius r towards $L_1/2$, what often causes high frequency oscillations of the coupler body towards this point. Moreover, in some occasions, the intersection points is not even reached, and the path direction is reversed (the sign of $\dot{\theta}_c$ changes), which off course is unrealistic. It seems to be that the integration finds 'a path of lower potential energy' away from the intersection point and the high stiffness.
 - Finally, as discussed in the method section of this appendix, a linearisation point had to be chosen for the construction of the proportional damping. For this, static equilibrium at 45° input axle angle was chosen, at which most stiffness values are midway their range. However, when stiffness increases from this point onward, less damping is experienced. Therefore, the stiffness maxima experience relatively little damping, which can explain the high frequency oscillations. This effect can be quite significant, as stiffness values vary more than an order of magnitude. Improvements can be made by making the damping matrix state depended as well. Some attempts have been done to implement this, but it did not result in improvement right away. Alternatively, other damping models can be tried and implemented.

C.7. Matlab code

The following Matlab scripts are used to generate the results. Furthermore, multiple scripts are used to plot the results, which are not given here.

- Building the equations of motion:
 - eom_runner.m: Runs all the subfiles, and saves the resulting functions
 - eom_constants.m: Loads constants, formulates inertia and stiffness values
 - eom_coordsys.m: Builds the chosen coordinate system
 - eom_deformation.m: Formulates the elastic deformations
 - eom_eom.m: Finally formulates the equations of motion using Lagrange
 - f_DP_stiffness.m: Function for determination of DP-DP flexure stiffness characteristics (5DOF model)
 - f_DP_stiffness.m: Function for determination of P-flexure stiffness characteristics (17DOF model)
- findequilibrium.m: Function containing Newton-Raphson scheme to find steady motion equilibrium. Is used in multiple files.
- modal.m: Modal analysis, can be executed when the EoM function files are available after running eom_runner.m.
- integration.m: Time integration, can be executed when the EoM function files are available after running eom_runner.m.

eom_runner.m

```
% Runner

% With this file, the time integration can be run for different scenario's
% (can be chosen via the 'para' (parameter) variable)

% For efficiency, equations for all scenarios are saved in the library file
% 'functions.mat'

% If the EoM functions then are generated:
% - a modal analysis can be executed with modal.m
% - time integration can be executed with integration.m

% close all
if exist('f','var')
    clearvars -except f
    save('functionsbackup.mat','f')
else
    clear all
    try
        load functions.mat
        save('functionsbackup.mat','f')
    catch
        end
end

% Parameter choice:
para = {2; % Prescription of: 1 = motion, 2 = torque
        1; % Deformation calculation: 1 = torsion:input/output, 3 = symbolic, 4 = multidof,
        % 6 = multidof + PRBM constraint
        1; % Inertia: 1 = SolidWorks, 3 = symbolic, 4 = multidof
        3; % Damping: 1 = none, 3 = proportional damping
        1; % Stiffness: 1 = nonlinear, 2 = linear, 3 = symbolic, 4 = multidof
        2}; % Coord sys: 1 = q_equi=0, 2 = polar, 3 = global, 4 = multidof global, 5 = multidof polar

eom_constants % load needed constants

eom_coordsys % build chosen coordinate system

eom_deformation % formulate elastic deformations

writefun =1; % 1 = build functions, 0 = dont
eom_eom % compute EoM with Lagrange

disp('Saving')
save('functions.mat','f')
disp('Finished')
```

eom_constants.m

```
% File containing geometrical constants, inertia and stiffness
disp('Loading constants')

%% Parameters
% input axis location:
x1 = 0;
y1 = 0;

% output axis location:
x3 = 0.00;
y3 = 0.02;

l1 = sqrt( (x3-x1)^2 + (y3-y1)^2 ); % parallel axle offset

cent = [(x3-x1)/2; (y3-y1)/2]; % centre between axles

%% Physical constants [m]
% input
d2=20e-3; % diameter
lz2=5e-3; % layer height in z
% output
d4=d2;
lz4=lz2;
% main frame
lx3=134e-3; %length of outer body 3 in local x, [m]
ly3=lx3; %length of outer body 3 in local y, [m]
tx3=4e-3; %thickness of outer body 3 in local x, [m]
ty3=tx3;
lz3=5e-3; %thickness of outer body 3 in local z, [m]

% shuttles
lxs = 90e-3; % shuttle length in local x, [m]
lys = 6e-3; % shuttle height in local y, [m]

% Input Output inertia properties:
daxle = 12e-3;
laxle = 220e-3;
m.axlein = 0.17102552;
m.axleout = 0.07455692;
m.flywheel = 0.92707883;
m.clamp = pi*(28e-3^2-12e-3^2)/4*11e-3*7800;
m.axleshuttle = 0.00220218;
m.hub = 0.00626699;

I.axlein = 2.98E-06;
I.axleout = 1.42e-006;
I.flywheel = 0.0015816;
I.clamp = 1/2*m.clamp*((28e-3/2)^2-(12e-3/2)^2); % huco clamps
I.motorclamp = 4.12E-06; % flexible beam coupling
I.motor = 1.05e-5; % motor inertia
I.axleshuttle = 0.00000030;
I.hub = 2.80E-07;

% Default setup axle inertia
m.in = m.axleshuttle + m.hub + m.axlein + m.clamp + m.flywheel;
m.out = m.axleshuttle + m.hub + m.axleout + m.clamp;

I.in = I.axleshuttle + I.hub + I.axlein + I.clamp + I.flywheel...
+ I.motorclamp + I.motor; % all default input axle inertia
I.out = I.axleshuttle + I.hub + I.axleout + I.clamp;

switch cell2mat(para(3))
case 1
    % Inertia SolidWorks
    % Main frame: 2x main frame + 0.5 of all intermediate shuttles and
    % 0.5 of all flexures
    m.mainframe = 0.01848074;
    m.alusheet = 0.00720046;
    m.intershuttle = 0.00622449; % 2 shuttles
    m.flexure = 0.00366031; % 8 flexures

    I.mainframe = 0.00009612;
    I.alusheet = 0.00004453;
    I.intershuttle = 0.00002585;
    I.flexureinner = 0.00000261;
    I.flexureouter = 0.00000548;

    m3 = 2*m.mainframe + m.alusheet + 0.5*2*m.flexure...
    + 0.5*2*m.intershuttle;
    I3 = 2*I.mainframe + I.alusheet + 2*I.flexureouter...
    + 0.5*2*I.intershuttle;
```



```

m2 = m.in + 2/8*m.flexure;
m4 = m.out + 2/8*m.flexure;

I2 = I.in;
I4 = I.out;

M=diag([m2 m2 I2 m3 m3 I3 m4 m4 I4]);

case 3 % symbolic
syms m2 m2 I2 m3 m3 I3 m4 m4 I4
M=diag([m2 m2 I2 m3 m3 I3 m4 m4 I4]);

case 4 % multidof
% Inertia SolidWorks
% Main frame: 2x main frame + 0.5 of all intermediate shuttles and
% 0.5 of all flexures
m.mainframe = 0.01848074;
m.alusheet = 0.00720046;
m.intershuttle = 0.00622449; % 2 shuttles
m.flexure = 0.00366031; % 8 flexures

I.mainframe = 0.00009612;
I.alusheet = 0.00004453;
I.intershuttle = 0.00002585; % 2 shuttles????
I.flexureinner = 0.00000261; % 4 flexures
I.flexureouter = 0.00000548; % 4 flexures

m3 = 2*m.mainframe + m.alusheet + 1/8*4*m.flexure;
% mass of 4 half flexures = 2/8, x two layers
I3 = 2*I.mainframe + I.alusheet; % no flexure inertia!!

m2 = m.in + 1/8*2*m.flexure;
m4 = m.out + 1/8*2*m.flexure;

I2 = I.in;%moment of inertia , output shuttle + axle [kg m2]
I4 = I.out; % no flexure inertia !!!!

ms = 1/2* m.intershuttle + 1/8*2*m.flexure;
Is = 1/2* I.intershuttle;

M=diag([m2 m2 I2 m3 m3 I3 m4 m4 I4 ...
ms ms Is ms ms Is ms ms Is ms ms Is ]);

end

%% Stiffness
switch cell2mat(para(5))
case {1, 2, 3} % DP-DP flexures
syms f2y f4y% flexure mechanism motion direction
% flexure mechanism connected to input axle , body 2
f2.l = 50e-3; % flexure length
f2.t = 0.2e-3; % flexure thickness
f2.w = 4.972e-3; % flexure height
f2.a = 0.5; % lumped / distributed parameter (flexure has length a*1)
f2.p1 = 28e-3; %=2*W1, distance between inner flexures
f2.p2 = 84e-3; %=2*W2, distance between outer flexures
f2.E = 193e9; % Youngs modulus

[k2.y,k2.x,k2.thet] = f_DP_stiffness(f2y,f2.l,f2.t,f2.w,f2.a,f2.p1,f2.p2,f2.E);

k2.x0=double(subs(k2.x,f2y,0));
k2.xmax=double(subs(k2.x,f2y,1));
k2.thet0=double(subs(k2.thet,f2y,0));
k2.thetmax=double(subs(k2.thet,f2y,1));

% flexure mechanism connected to input axle , body 2
f4.l = 50e-3; % flexure length
f4.t = 0.2e-3; % flexure thickness
f4.w = f2.w; % flexure height
f4.a = 0.5; % lumped / distributed parameter (flexure has length a*1)
f4.p1 = 28e-3; %=2*W1, distance between inner flexures
f4.p2 = 84e-3; %=2*W2, distance between outer flexures
f4.E = f2.E; % Youngs modulus

[k4.y,k4.x,k4.thet] = f_DP_stiffness(f4y,f4.l,f4.t,f4.w,f4.a,f4.p1,f4.p2,f4.E);
k4.x0=subs(k4.x,f4y,0);
case 4 % P flexures
syms fy2s1 fy2s2 fy3s1 fy3s2 % layer 1
syms fy4s3 fy4s4 fy3s3 fy3s4 % layer 2

f1.l = 50e-3; % flexure length
f1.t = 0.2e-3; % flexure thickness
f1.w = 4.972e-3; % flexure height
f1.a = 0.5; % distribution parameter (flexure has length a*1)
f1.p1 = 28e-3; %=2*W1, distance between inner flexures

```

```

fl.p2 = 84e-3; %=2*W2, distance between outer flexures
fl.E = 193e9; % Youngs modulus

% f_P_stiffness: output order: motion, bearing, rotation
% layer 1
[k2s1.x,k2s1.y,k2s1.thet] = f_P_stiffness(fy2s1,fl.l,fl.t,fl.w,fl.a,fl.p1,fl.E);
[k2s2.x,k2s2.y,k2s2.thet] = f_P_stiffness(fy2s2,fl.l,fl.t,fl.w,fl.a,fl.p1,fl.E);
[k3s1.x,k3s1.y,k3s1.thet] = f_P_stiffness(fy3s1,fl.l,fl.t,fl.w,fl.a,fl.p2,fl.E);
[k3s2.x,k3s2.y,k3s2.thet] = f_P_stiffness(fy3s2,fl.l,fl.t,fl.w,fl.a,fl.p2,fl.E);
% layer 2
[k4s3.x,k4s3.y,k4s3.thet] = f_P_stiffness(fy4s3,fl.l,fl.t,fl.w,fl.a,fl.p1,fl.E);
[k4s4.x,k4s4.y,k4s4.thet] = f_P_stiffness(fy4s4,fl.l,fl.t,fl.w,fl.a,fl.p1,fl.E);
[k3s3.x,k3s3.y,k3s3.thet] = f_P_stiffness(fy3s3,fl.l,fl.t,fl.w,fl.a,fl.p2,fl.E);
[k3s4.x,k3s4.y,k3s4.thet] = f_P_stiffness(fy3s4,fl.l,fl.t,fl.w,fl.a,fl.p2,fl.E);

k2.thet0=double(subs(k2s1.thet,fy2s1,0));
k2.thetmax=double(subs(k2s1.thet,fy2s1,l1/2));
k3.thet0=double(subs(k3s1.thet,fy3s1,0));
k3.thetmax=double(subs(k3s1.thet,fy3s1,l1/2));
end

%% Stiffness matrix
switch cell2mat(para(5))
case 1
% non linear stiffness:
K=diag([k2.y k2.x k2.thet k4.x k4.y k4.thet]); % stiffness matrix
% absolute Y axis equilibrium position of main frame:
eqy = double((2*l1*k2.x0) / (2*(k4.y + k2.x0)));

case 2
% linear stiffness:
ky = k2.y;
kx = 1e3;
kthet = 1e3;
K=diag([ky kx kthet kx ky kthet]); % stiffness matrix
% absolute Y axis equilibrium position of main frame:
eqy = double((2*l1*kx) / (2*(ky + kx)));

case 3
% symbolic
syms k2y k2x k2thet k4x k4y k4thet req kx ky kthet
%
K=diag([k2x k2y k2thet k4x k4y k4thet]); % stiffness matrix
K=diag([ky kx kthet kx ky kthet]); % stiffness matrix

case 4
% multidof: single P-flexure
K=diag([ k2s1.x k2s1.y k2s1.thet ... % layer 1
        k2s2.x k2s2.y k2s2.thet ...
        k3s1.x k3s1.y k3s1.thet ...
        k3s2.x k3s2.y k3s2.thet ...
        k4s3.y k4s3.x k4s3.thet ... % layer 2
        k4s4.y k4s4.x k4s4.thet ...
        k3s3.y k3s3.x k3s3.thet ...
        k3s4.y k3s4.x k3s4.thet ]); % stiffness matrix
end

% finding equilibrium radius of main frame path:
try
req = eqy - l1/2;
catch
end

clearvars -except f para M K x1 y1 x3 y3 l1 cent req fl f2y f4y fy* m*

```

eom_coordsys.m

```

% File building body coordinates and coordinate system
disp('Building coordinate system')

%% Coord sys
syms Q
switch cell2mat(para(6))

case 1 % Zero displacement equilibrium config
% Generalized coordinates
syms t omega phi1_0
syms phi2 phi3 phi4 dr
syms phi2d phi3d phi4d drd
syms phi2dd phi3dd phi4dd drdd

q = [phi2 phi3 phi4 dr ].';
qd = [phi2d phi3d phi4d drd ].';
qdd = [phi2dd phi3dd phi4dd drdd ].';
input = [phi1_0 omega Q].';

```

```

% Prescirbed input
phi1 = phi1_0 + omega*t;
phild = omega;

% Body coordinates X(q)
X = [x1;
     y1;
     phi1;
     cent(1) + (dr+req)*sin(phi3+2*phi1); % BODY2
     cent(2) - (dr+req)*cos(phi3+2*phi1);
     phi2 + phi1;
     x3; % BODY3
     y3;
     phi4 + phi1];

case 2 % polar + body rotations
% Generalized coordinates
syms t omega phi1_0
syms thetc r thet3 thet4
syms thetcd rd thet3d thet4d
syms thetccd rdd thet3dd thet4dd

q = [ thetc r thet3 thet4 ].';
qd = [ thetcd rd thet3d thet4d ].';
qdd = [ thetccd rdd thet3dd thet4dd ].';
input = [phi1_0 omega Q].';

% Prescirbed input
phi1 = phi1_0 + omega*t;
phild = omega;
syms phi1

% Body coordinates X(q)
X = [x1;
     y1;
     phi1;
     cent(1) + r*sin(thetc); % BODY2
     cent(2) - r*cos(thetc);
     thet3;
     x3; % BODY3
     y3;
     thet4];

case 3 % global coordinates
% Generalized coordinates
syms t omega phi1_0
syms x y thet3 thet4
syms xd yd thet3d thet4d
syms xdd ydd thet3dd thet4dd

% work in progresssss

q = [ x y thet3 thet4 ].';
qd = [ xd yd thet3d thet4d ].';
qdd = [ xdd ydd thet3dd thet4dd ].';

input = [phi1_0 omega Q].';

% Prescirbed input
phi1 = phi1_0 + omega*t;
phild = omega;

% Body coordinates X(q)
X = [x1;
     y1;
     phi1;
     x; % BODY2
     y;
     thet3;
     x3; % BODY3
     y3;
     thet4];

case 4 % multidof
% Generalized coordinates
syms t omega phi1_0
syms thetc r thet3 thet4
syms thetcd rd thet3d thet4d
syms thetccd rdd thet3dd thet4dd

syms xs1 xs2 xs3 xs4 xs1d xs2d xs3d xs4d xs1dd xs2dd xs3dd xs4dd
syms ys1 ys2 ys3 ys4 ys1d ys2d ys3d ys4d ys1dd ys2dd ys3dd ys4dd
syms thets1 thets2 thets3 thets4 thets1d thets2d thets3d thets4d

```

```

syms thets1dd thets2dd thets3dd thets4dd

q = [ thetc r thet3 thet4 ...
      xs1 ys1 thets1 ...
      xs2 ys2 thets2 ...
      xs3 ys3 thets3 ...
      xs4 ys4 thets4].';

qd = [ thetcd rd thet3d thet4d ...
       xs1d ys1d thets1d ...
       xs2d ys2d thets2d ...
       xs3d ys3d thets3d ...
       xs4d ys4d thets4d].';

qdd = [ thetcdd rdd thet3dd thet4dd ...
        xs1dd ys1dd thets1dd ...
        xs2dd ys2dd thets2dd ...
        xs3dd ys3dd thets3dd ...
        xs4dd ys4dd thets4dd].';

input = [phi1_0 omega Q].';

% Prescirbed input
phi1 = phi1_0 + omega*t;
phi1d = omega;
syms phi1

% Body coordinates X(q)
X = [x1;
      y1;
      phi1;
      cent(1) + r*sin(thetc); % BODY2
      cent(2) - r*cos(thetc);
      thet3;
      x3; % BODY3
      y3;
      thet4;
      q(5:end)];

case 5 % multidof, shuttles polar
% Generalized coordinates
syms t omega phi1_0
syms phi3 r3 thet3 thet4
syms phi3d r3d thet3d thet4d
syms phi3dd r3dd thet3dd thet4dd

syms rs1 rs2 rs3 rs4 rs1d rs2d rs3d rs4d rs1dd rs2dd rs3dd rs4dd
syms phis1 phis2 phis3 phis4 phis1d phis2d phis3d phis4d
syms phis1dd phis2dd phis3dd phis4dd
syms thets1 thets2 thets3 thets4 thets1d thets2d thets3d thets4d
syms thets1dd thets2dd thets3dd thets4dd

q = [ phi3 r3 thet3 thet4 ...
      phis1 rs1 thets1 ...
      phis2 rs2 thets2 ...
      phis3 rs3 thets3 ...
      phis4 rs4 thets4].';

qd = [ phi3d r3d thet3d thet4d ...
       phis1d rs1d thets1d ...
       phis2d rs2d thets2d ...
       phis3d rs3d thets3d ...
       phis4d rs4d thets4d].';

qdd = [ phi3dd r3dd thet3dd thet4dd ...
        phis1dd rs1dd thets1dd ...
        phis2dd rs2dd thets2dd ...
        phis3dd rs3dd thets3dd ...
        phis4dd rs4dd thets4dd].';

input = [phi1_0 omega Q].';

% Prescirbed input
phi1 = phi1_0 + omega*t;
phi1d = omega;
syms phi1

% Body coordinates X(q)
X = [x1;
      y1;
      phi1;
      cent(1) + r3*sin(phi3); % BODY2
      cent(2) - r3*cos(phi3);
      thet3;

```

```

        x3; % BODY3
        y3;
        thet4;
        x1 - rs1*sin(phis1); % shuttle 1
        y1 + rs1*cos(phis1);
        thets1;
        x1 + rs2*sin(phis2); % shuttle 2
        y1 - rs2*cos(phis2);
        thets2;
        x3 + rs3*cos(phis3); % shuttle 3
        y3 + rs3*sin(phis3);
        thets3;
        x3 - rs4*cos(phis4); % shuttle 4
        y3 - rs4*sin(phis4);
        thets4 ];
end

%% Parameter vector
% The input vector contains all parameters that can be changed without recomputing the functions
% Ergo, these parameters remain symbolic in the functions
syms Tout Tin
syms alfa beta Cin Cout
input = [phi1_0 omega Q Tin Tout Cin Cout alfa beta].';
Torque = sym(zeros(length(q),1));
Torque(4) = Tout; % output axis torque

%% Input axis + torque
switch cell2mat(para(1))
case 2
    % Input axis as DOF, prescribed torque
    syms thet2 thet2d thet2dd

    q = [thet2; q]; % add DOF at
    qd = [thet2d; qd];
    qdd = [thet2dd; qdd];
    X(3) = thet2; % instead of prescribed phil

    Torque = [Tin; Torque];
end

%% compute body velocities
dXdT = jacobian(X, t);
dXdq = jacobian(X, q);
Xd = dXdT + dXdq * qd; %time derivatives of x in terms of q, qd, qdd

% write to library:
try
f(para{:}).X = matlabFunction([X], 'Vars', {[q; qd; input; t]});
f(para{:}).Xd = matlabFunction([Xd], 'Vars', {[q; qd; input; t]});

f(para{:}).q = q;
f(para{:}).qd = qd;
f(para{:}).qdd = qdd;
f(para{:}).input = input;
catch
disp(' Generalised displacements cannot be written')
end

clear dXdT dXdq Xd

```

eom_deformation.m

```

% File computing strain u(x)
disp('Building elastic deformation relations')
% Strains as function of X, which is function of q, --> u(q)

switch cell2mat(para(2)) % deformation calculation

case 1 % torsional strain: rotation of input and output used
    u = [ (X(4)-X(1))*cos(X(3)) + (X(5)-X(2))*sin(X(3));
          -(X(4)-X(1))*sin(X(3)) + (X(5)-X(2))*cos(X(3));
          X(6)-X(3); %is this direction correct????
          -(X(7)-X(4))*cos(X(9)) - (X(8)-X(5))*sin(X(9));
          (X(7)-X(4))*sin(X(9)) - (X(8)-X(5))*cos(X(9));
          X(9)-X(6)]; %is this direction correct????

case 3 % symbolic
    syms u2y u2x u2thet u4x u4y u4thet
    u = [u2x u2y u2thet u4x u4y u4thet].';

case {4,5,6} % multidof
    ls0 = 0.0592; % absolute initial hight in Y of shuttles

    u = [ (X(10)-X(1))*cos(X(3)) + (X(11)-X(2))*sin(X(3)); % layer 1

```

```

-(X(10)-X(1))*sin(X(3)) + (X(11)-X(2))*cos(X(3))-ls0;
X(12)-X(3);
(X(13)-X(1))*cos(X(3)) + (X(14)-X(2))*sin(X(3));
-(X(13)-X(1))*sin(X(3)) + (X(14)-X(2))*cos(X(3))+ls0;
X(15)-X(3);
(X(10)-X(4))*cos(X(6)) + (X(11)-X(5))*sin(X(6));
-(X(10)-X(4))*sin(X(6)) + (X(11)-X(5))*cos(X(6))-ls0;
X(12)-X(6);
(X(13)-X(4))*cos(X(6)) + (X(14)-X(5))*sin(X(6));
-(X(13)-X(4))*sin(X(6)) + (X(14)-X(5))*cos(X(6))+ls0;
X(15)-X(6);
(X(16)-X(7))*cos(X(9)) + (X(17)-X(8))*sin(X(9))-ls0; % layer 2: output - shuttle
-(X(16)-X(7))*sin(X(9)) + (X(17)-X(8))*cos(X(9));
X(18)-X(9);
(X(19)-X(7))*cos(X(9)) + (X(20)-X(8))*sin(X(9))+ls0;
-(X(19)-X(7))*sin(X(9)) + (X(20)-X(8))*cos(X(9));
X(21)-X(9);
(X(16)-X(4))*cos(X(6)) + (X(17)-X(5))*sin(X(6))-ls0; % layer 2: ring - shuttle
-(X(16)-X(4))*sin(X(6)) + (X(17)-X(5))*cos(X(6));
X(18)-X(6);
(X(19)-X(4))*cos(X(6)) + (X(20)-X(5))*sin(X(6))+ls0;
-(X(19)-X(4))*sin(X(6)) + (X(20)-X(5))*cos(X(6));
X(21)-X(6);
];
end
switch cell2mat(para(2)) % incorporate beam arc length conservation
case 6
    %PRBM
    gamma = 0.8517; % n=0, pure transverse loading
    u(2) = u(2)+((gamma*fl.1)-sqrt(((gamma*fl.1)^2-u(1)^2)));
    u(5) = u(5)-((gamma*fl.1)-sqrt(((gamma*fl.1)^2-u(4)^2)));
    u(8) = u(8)+((gamma*fl.1)-sqrt(((gamma*fl.1)^2-u(7)^2)));
    u(11) = u(11)-((gamma*fl.1)-sqrt(((gamma*fl.1)^2-u(10)^2)));

    u(13) = u(13)+((gamma*fl.1)-sqrt(((gamma*fl.1)^2-u(14)^2)));
    u(16) = u(16)-((gamma*fl.1)-sqrt(((gamma*fl.1)^2-u(17)^2)));
    u(19) = u(19)+((gamma*fl.1)-sqrt(((gamma*fl.1)^2-u(20)^2)));
    u(22) = u(22)-((gamma*fl.1)-sqrt(((gamma*fl.1)^2-u(23)^2)));
end
clear fl

% write to library:
f(para{:}).u = u;
try
f(para{:}).u = matlabFunction([u, 'Vars' ,{[q; qd; input; t]}]);
catch
disp('Cannot write deformations')
end

```

eom_eom.m

```

% Building the EoM
disp('Building EoM')

%% Energies
disp(' Computing energies')

%% Potential
switch cell2mat(para(5))
case {1, 2, 3}
    K = subs(K,[f2y f4y],[u(1) u(5)]); % motions of flexure mechanisms for non-lin stiffness
case 4
    K = subs(K,[fy2s1 fy2s2 fy3s1 fy3s2 fy4s3 fy4s4 fy3s3 fy3s4].',[u(1:3:12); u(14:3:end)]);
end

V=( 1/2* (u.' * K * u)); %potential energy of the system

%% Kinetic
% computing velocities
dXdT = jacobian(X, t);
dXdq = jacobian(X, q);
Xd = dXdT + dXdq * qd;

T0 = simplify( 1/2* (dXdT.' * M * dXdT)); % transport
T1 = simplify(dXdT.' * M * (dXdq*qd) ); % mutual / coupling,
T2 = simplify( 1/2* ((qd.'*dXdq.') * M * (dXdq*qd) )); % relative
T = T0 + T1 + T2;

%% Lagrange equation, finding all the needed terms
disp(' Building Lagrange equations')

dT_dqd = (jacobian(T,qd)).';

```

```

DdT_Dtdqd = (jacobian(dT_dqd,q)) * qd ...
            + (jacobian(dT_dqd,qd)) * qdd;

dT_dq      = (jacobian(T,q)).' ;
dV_dq      = (jacobian(V,q)).' ;

Equations = (DdT_Dtdqd - dT_dq + dV_dq - Torque); %assembling the Lagrange
fv = dV_dq;
ft = DdT_Dtdqd - dT_dq;

% Linearization
MM = jacobian(ft ,qdd);
KM = jacobian(ft ,q) + jacobian(fv ,q);
KM = subs(KM,qdd,zeros(size(qdd))); %substitutie qdd=0; linearization around steady motion

%% Proportional Damping
switch cell2mat(para(4))
    case 3 % proportional damping

        %% Linearisation point for proportional damping
        philrange = [45]/180*pi; % substitution angle at which to compute proportional damping
        omega_ = 0*2*pi; t_ = 0;

        % formulate q and qd at linearisation point :
        clear vars_eq
        for i=1:length(philrange)
            phil_ = philrange(i);
            switch cell2mat(para(6)) % Coord sys: 1 = q_equi=0
                case 2 % 5DOF
                    vars_eq(:,i) = [2*(phil_+omega_*t_), 0.009999680005120,...
                                    (phil_+omega_*t_), (phil_+omega_*t_), 2*omega_, 0, omega_, omega_ ].';
                case 5 % multidof, shuttles polar
                    ls0 = 0.0592; % absolute initial height in Y of shuttles
                    theta2_0 = phil_+omega_*t_;
                    phidef1 = asin(-0.5*11*sin(theta2_0)/ls0);
                    phidef2 = asin(-0.5*11*cos(theta2_0)/ls0);
                    % only correct for purely vertical (y) offset between axis!
                    vars_eq(:,i) = [ 2*(theta2_0), 0.009999680005120, (theta2_0), (theta2_0) ,...
                                    (theta2_0)+phidef1, ls0, theta2_0,...
                                    (theta2_0)-phidef1, ls0, theta2_0,...
                                    (theta2_0)+phidef2, ls0, theta2_0,...
                                    (theta2_0)-phidef2, ls0, theta2_0,...
                                    2*omega_, 0, omega_, omega_,...
                                    -ls0*cos(theta2_0)*omega_, 0, omega_,...
                                    ls0*cos(theta2_0)*omega_, 0, omega_,...
                                    -ls0*sin(theta2_0)*omega_, 0, omega_,...
                                    ls0*sin(theta2_0)*omega_, 0, omega_ ].';
                    clear ls0 theta2_0 phidef1 phidef2
            end
        end
        clear phil_ i

        % OR, more accurate: import linearisation point from Newton Raphson scheme manually:
        % vars_eq = ...

        %% Bearing friction
        CMbearing = sym(zeros(length(q))); % matrix for bearing friction
        switch cell2mat(para(1))
            case 1 % prescribed motion
                CMbearing(4) = Cout;
            case 2 % prescribed torque; add extra coordinate
                vars_eq = [philrange+omega_*t_; vars_eq(1:end/2,:); ones(size(philrange))*omega_; vars_eq(end/2+1:end,:)];
                CMbearing(1) = Cin;
                CMbearing(5) = Cout;
            end

        %% Adding all damping terms
        % Proportional damping, only diagonal terms, with respect to lineatisation point
        CMprop = diag( alfa.* diag( double(subs(MM,q,vars_eq(1:end/2))) ) + beta.* diag( double(subs(KM,[q; qd],vars_eq)
            ) ) );

        C = CMprop + CMbearing;

        % Recomputing the EoM including damping
        clear Equations;
        Equations = (DdT_Dtdqd - dT_dq + dV_dq + CMprop*(qd-vars_eq(end/2+1:end)) + CMbearing*qd - Torque);
        otherwise
            C = zeros(length(q)); % empty damping matrix
        end
end

CM = jacobian(ft ,qd) + C ; % overall damping matrix, including inertial terms

```

```

%% Solving
disp(' Solving Lagrange equations')

Fv = -(Equations - MM*qdd);
qddsol = inv(MM)*Fv;

%% Dynamic equilibrium
dynequilibrium = qddsol;
dyntangstiff = jacobian(dynequilibrium,[q; qd]); % tangent stiffness matrix for Newton-Raphson

%% Formulation of separate forces of postprocessing
Feuler = MM*qdd;
Finertia = DdT_Dtdqd - dT_dq - Feuler;
Felastic = dV_dq;
switch cell2mat(para(4))
    case 3 % proportional damping
        Fdamper = CMprop*qd + CMbearing*qd;
    otherwise
        Fdamper = C*qd;
end

forces = [Feuler, Finertia, Felastic, Fdamper];

%% Writing to library
% Write function file for EoM (faster integration)
matlabFunction([qd; qddsol], 'Vars', {t, [q; qd; input]}, 'File', 'f_eom');

if writefun
    disp(' Writing functions to library')
    %% Needed for modal analysis
    f(para{:}) .MM = matlabFunction([MM], 'Vars', {[q; qd; input; t]});
    f(para{:}) .CM = matlabFunction([CM], 'Vars', {[q; qd; input; t]});
    f(para{:}) .KM = matlabFunction([KM], 'Vars', {[q; qd; input; t]});

    f(para{:}) .dynequilibrium = matlabFunction([dynequilibrium], 'Vars', {[q; qd; input; t]});
    f(para{:}) .dyntangstiff = matlabFunction([dyntangstiff], 'Vars', {[q; qd; input; t]});

    %% Needed for time integration
    f(para{:}) .eom = matlabFunction([qd; qddsol], 'Vars', {t, [q; qd; input]});

    try
        f(para{:}) .CMprop = matlabFunction([CMprop], 'Vars', {[q; qd; input; t]});
    catch
    end
    f(para{:}) .K = matlabFunction([K], 'Vars', {[q; qd; input; t]});
    f(para{:}) .M = matlabFunction([M], 'Vars', [q; qd; input; t]); % why not as cell?? gives error
    f(para{:}) .offset = 11;

    f(para{:}) .forces = matlabFunction([forces], 'Vars', {[q; qd; qdd; input; t]});
end

clear writefun

```

f_DP_stiffness.m

```

function [ky,kx,kthet] = f_stiffness(y,l,t,w,a,p1,p2,E)
%% Stiffnesses of paired double parallelogram flexure (DP-DP)
I = w*t^3/12; % second moment of inertia of flexure beam

k110 = 6 / ( ( 3 -6*a +4*a^2 ) *a );
k111 = ( 3*(15 -50*a +60*a^2 -24*a^3) ) / ( 5*(3 -6*a +4*a^2)^2 );
g11 = (2*a^3 * (105 -630*a +1440*a^2 -1480*a^3 +576*a^4) ) / ( 175* (3 -6*a +4*a^2)^3 );
k33 = 6 / ( a* (t/l)^2 );

%% DP-DP flexure
% motion direction
ky = 2*E*I*k110/l^3;
% constraint direction
kx = (2*E*I/l^3) * k33 / ( 1 + (k33* (g11+ (k111^2/k110) ) * (y/(2*l))^2) );
% angular direction
kthet = (E*I/l^3) * ( (4* (p2/2)^2 *(p1/2)^2) / ((p2/2)^2 +(p1/2)^2) ) * ( k33 / ( 1 + k33* g11* (y/(2*l))^2) );

```

f_P_stiffness.m

```

function [ky,kx,kthet] = f_P_stiffness(y,l,t,w,a,p,E)
%% Stiffnesses of paired double parallelogram flexure
I = w*t^3/12; % second moment of inertia of flexure beam

k110 = 6 / ( ( 3 -6*a +4*a^2 ) *a );
k111 = ( 3*(15 -50*a +60*a^2 -24*a^3) ) / ( 5*(3 -6*a +4*a^2)^2 );
g11 = (2*a^3 * (105 -630*a +1440*a^2 -1480*a^3 +576*a^4) ) / ( 175* (3 -6*a +4*a^2)^3 );
k33 = 6 / ( a* (t/l)^2 );

```



```

%% P flexure
% motion direction
ky = 2*E*I*k110/1^3;
% constraint direction
kx = (2*E*I/1^3) * k33 / (1 + k33*g11* (y/1)^2 );
% angular direction
kthet = (2*E*I/1^3) * (p/2)^2 * ( k33 / (1 + k33* g11* (y/1)^2 ) );

```

findequilibrium.m

```

function [vars_eq, error, iterations] = findequilibrium(f,para,settings,input,t_,init)
% Function to iterate to a steady motion equilibrium configuration
% Starting from an initial guess 'init'
% 'f' contains all needed functions, 'para' contains the scenario parameters
% 'settings' contain max no. of steps and tolerance
% 'input' contains the model parameters

%%
phil_ = input(1);
omega_ = input(2);
l1 = f(para{:}).offset;

% Newton raphson parameters:
tol = settings(1); % tolerance at which to stop iterations
nmax = settings(2); % maximum number of N-R iterations DEFINED BY FUNCTION INPUT
display = 0; % display iterations in command screen?

%% Model parameters
% Check existence of data for current parameters
try
    if isempty(f(para{:}).MM)==1;
        disp('No data for these model parameters')
        return; end
catch
    disp('No data for these model parameters')
    return
end

%% Equilibrium conditions
equilibrium = f(para{:}).dynequilibrium;
tangstiff = f(para{:}).dyntangstiff;

%% Load variables for current model parameters
q = f(para{:}).q;
qd = f(para{:}).qd;

%% Maximum iteration step
switch cell2mat(para(2)) % deformation
    case {1,2,3,4}
        maxcorr = 5e-2; % maximum iteration step size
    case {5,6}
        maxcorr = 1e-2; % maximum iteration step size
end

%% Initial guess for equilibrium
if isempty(init)
switch cell2mat(para(6)) % Coord sys: 1 = q_equi=0
    case 1
        vars_eq = zeros(2*length(f(para{:}).q),1);
    case 2
        vars_eq = [2*(phil_+omega_*t_), 0.009999680005120*11/20e-3, (phil_+omega_*t_), (phil_+omega_*t_), ...
            2*omega_, 0, omega_, omega_ ].';
    case 3 % 4 dof, global coordinates
        vars_eq = [l1/2,l1/2, (phil_+omega_*t_), (phil_+omega_*t_), 0.1,l1*2*omega_, omega_, omega_ ].';
        % 20mm misalignment, 45deg
    case 4 % multidof
        ls0 = 0.0592; % absolute initial hight in Y of shuttles
        theta2_0 = phil_+omega_*t_;
        % only correct for purely vertical (y) offset between axis!
        vars_eq = [2*(theta2_0), 0.009999680005120*11/20e-3, (theta2_0), (theta2_0), ...
            -ls0*sin(theta2_0), ls0*cos(theta2_0), theta2_0, ...
            ls0*sin(theta2_0), -ls0*cos(theta2_0), theta2_0, ...
            ls0*cos(theta2_0), ls0*sin(theta2_0)+l1, theta2_0, ...
            -ls0*cos(theta2_0), -ls0*sin(theta2_0)+l1, theta2_0, ...
            2*omega_, 0, omega_, omega_ ,...
            -ls0*cos(theta2_0)*omega_, -ls0*sin(theta2_0)*omega_, omega_ ,...
            ls0*cos(theta2_0)*omega_, ls0*sin(theta2_0)*omega_, omega_ ,...
            -ls0*sin(theta2_0)*omega_, ls0*cos(theta2_0)*omega_+l1, omega_ ,...
            ls0*sin(theta2_0)*omega_, -ls0*cos(theta2_0)*omega_+l1, omega_ ].';
    case 5 % multidof, shuttles polar
        ls0 = 0.0592; % absolute initial hight in Y of shuttles

```

```

theta2_0 = phi1+omega_*t_; % input axis angle
phidef1 = asin(-0.5*l1*sin(theta2_0)/ls0);
phidef2 = asin(-0.5*l1*cos(theta2_0)/ls0);
% only correct for purely vertical (y) offset between axis!
vars_eq = [ 2*(theta2_0), 0.009999680005120*l1/20e-3, (theta2_0), (theta2_0), ...
            (theta2_0)+phidef1, ls0, theta2_0, ...
            (theta2_0)-phidef1, ls0, theta2_0, ...
            (theta2_0)+phidef2, ls0, theta2_0, ...
            (theta2_0)-phidef2, ls0, theta2_0, ...
            2*omega_, 0, omega_, omega_, ...
            -ls0*cos(theta2_0)*omega_, 0, omega_, ...
            ls0*cos(theta2_0)*omega_, 0, omega_, ...
            -ls0*sin(theta2_0)*omega_, 0, omega_, ...
            ls0*sin(theta2_0)*omega_, 0, omega_ ].';
end

switch cell2mat(para(1))
case 2 %prescribed torque
    vars_eq = [phi1+omega_*t_; vars_eq(1:end/2); omega_; vars_eq(end/2+1:end)];
end

else
    vars_eq = init;
end

vars = [q;qd];
vars_eq0 = vars_eq;
dof = length(q); %degrees of freedom

% In case of prescribed torque starting from standstill, abort Newton
% Raphson and only use initial conditions as above
if cell2mat(para(1))==2 && omega_==0 && input(4)>0
    iterations = 0; error = 0;
    disp(' Starting from standstill: Newton Raphson aborted')
    return
end

%% Linearization
reference = 1;

%% Find equilibrium point: Newton Raphson:
% Newton Raphson iteration
eqerror = equilibrium([vars_eq; input; t_]);

n=0; % iteration counter
if display
    disp(['Equilibrium for omega = ', num2str(omega_/(2*pi)), ' Hz, phi1_0 = ', num2str(phi1_/pi*180), ' deg'])
    disp([' Initial relative error norm = ', num2str(norm(eqerror)/reference) ]) %norm()=vector length
    disp([' Starting Newton-Raphson iterations (nmax=' int2str(nmax) ', tol=' num2str(tol) ')'])
end
while (norm(eqerror) > tol*reference) & (n<nmax),
    n = n+1;

    % evaluate tangent stiffness matrix at current solution
    K_fix_eq = tangstiff([vars_eq; input; t_]);

    dvars_eq = (-K_fix_eq \ eqerror); % evaluate correction
    if norm(dvars_eq)>maxcorr % maximum correction
        dvars_eq = dvars_eq*maxcorr/norm(dvars_eq);
        if display
            disp(' Maximum correction')
        end
    end

    vars_eq = vars_eq + dvars_eq; % update equilibrium position

    % re-evaluate error
    eqerror = (equilibrium([vars_eq; input; t_]));

    if display
        disp([' Error norm = ', num2str(norm(eqerror)/reference), ', after ' num2str(n), ' steps'])
    end
end

%% End of loop
iterations = n; % number of iteration steps used
error = norm(eqerror)/reference; % number of iteration steps used

if n==nmax
    disp([' Error tolerance not reached at ', num2str(omega_/(2*pi)), ' Hz and ', ...
        num2str(phi1_/pi*180), ' deg!, para(2)=??'])
end

if display % display iterations

```

```

try
    disp('      Last correction :')
    disp(['      ',num2str(dvars_eq')])
catch
end
disp('      Equilibrium found at :')
disp(['      ',num2str(vars_eq')])
disp('      Acceleration: ')
disp(['      ',num2str(eqerror')])
end

disp(['Equilibrium for omega = ', num2str(omega_/(2*pi)), ' Hz, phi1_ = ',num2str(phi1_/pi*180),' deg, in ',...
num2str(n),' steps, with error ',num2str(norm(eqerror)/reference)])

```

modal.m

```

% Modal analysis

%% Initialize
%% Time integration file
if exist('f','var')
    clearvars -except f
else
    clear all
    load functions.mat
end

%% Model parameters
% Parameter choice:
para =      {1; % Prescription of: 1 = motion, 2 = torque
             1; % Deformation calculation: 1 = torsion:input/output, 3 = symbolic, 4 = multidof,
             % 6 = multidof + PRBM constraint
             1; % Inertia: 1 = SolidWorks, 3 = symbolic, 4 = multidof
             1; % Damping: 1 = none, 3 = proportional damping
             1; % Stiffness: 1 = nonlinear, 2 = linear, 3 = symbolic, 4 = multidof
             2}; % Coord sys: 1 = q_equi=0, 2 = polar, 3 = global, 4 = multidof global, 5 = multidof polar

% Check existence of data for current parameters
try
    if isempty(f(para{:}).eom)==1;
        disp('No data for these model parameters')
        return; end
catch
    disp('No data for these model parameters')
    return
end

%% Range and initial guess for equilibrium
t_ = 0;
Q = 0;
range.omega = [0:2:10]*2*pi; % range for input axle velocity
range.phil = [0:45:180]/180*pi; % range for input axle angle
omega_ = range.omega(1);
phil_ = range.phil(1);

% model parameters
Tin = 0; % input axle torque
Tout = 0; % output axle torque
Cin = 0; % output axle damping
Cout = 0; % output axle damping
alfa = 0; % modal damping, mass proportionality constant
beta = 0; % modal damping, stiffness proportionality constant

% Newton raphson parameters:
tol = 1e-7;

%% Load variables for current model parameters
l1 = f(para{:}).offset;
q = f(para{:}).q;
qd = f(para{:}).qd;
qdd = f(para{:}).qdd;
dof = length(q); %degrees of freedom
input = f(para{:}).input;
syms t phil
phil = input(1) + input(2)*t;

% input axis location:
x1 = 0;
y1 = 0;

% output axis location:
x3 = 0.00;
y3 = f(para{:}).offset;

```

```

cent = [(x3-x1)/2; (y3-y1)/2];

%% Linearization
for iomega = 1:length(range.omega)
    disp(['Current freq: ', num2str(range.omega(iomega)/(2*pi))])
for iphi = 1:length(range.phil)
    omega_ = range.omega(iomega);
    phil_ = range.phil(iphi);

    %% Find equilibrium point: Newton Raphson:
    input_eq = [phil_, omega_, Q, Tin, Tout, Cin, Cout, alfa, beta].';

    switch cell2mat(para(6)) % Coordinate sys
    case {6,7} % fixed axles and frame
        ls0 = 0.0592; % absolute initial high in Y of shuttles
        l1 = f(para{:}).offset;
        [vars_eq, itrerror, itrsteps] = findequilibrium(f, para, [1e-14;80], input_eq, t_, []);
    case 8 % simple parallelogram, shuttle 1 with only stiffness to fixed input axle
        ls0 = 0.0592; % absolute initial high in Y of shuttles
        vars_eq = [0, ls0, 0, 0, 0, 0]';
        itrsteps = 0; itrerror = 0;
    otherwise
        switch cell2mat(para(2)) % Deformation
        case {1,2} % 4/5 DOF
            l1 = f(para{:}).offset;
            [vars_eq, itrerror, itrsteps] = findequilibrium(f, para, [1e-8;50], input_eq, t_, []);
        case {4,5,6} % multidof
            ls0 = 0.0592; % absolute initial high in Y of shuttles
            l1 = f(para{:}).offset;
            paratemp = para; paratemp(2)={4};
            [vars_eq, itrerror, itrsteps] = findequilibrium(f, {1;4;4;1;4;5}, [5e-7;50], input_eq, t_, []);
            [vars_eq, itrerror, itrsteps2] = findequilibrium(f, para, [1e-7;100], input_eq, t_, vars_eq);
            itrsteps = itrsteps + itrsteps2; clear itrsteps2 paratemp
        end
    end

    % save equilibrium point
    data_eq(iomega, iphi, :) = [vars_eq; input_eq; t_]; % generalized coordinates
    data_eqx(iomega, iphi, :) = f(para{:}).X([vars_eq; input_eq; t_]); % absolute coordinates
    data_itrsteps(iomega, iphi) = itrsteps; % number of iteration steps used
    data_itrerror(iomega, iphi) = itrerror; % final iteration error

    %% Linearize system matrices
    % Build EoM for four generalized coordinates, with phil as parameter:
    MSub = f(para{:}).MM([vars_eq; input_eq; t_]);
    CSub = f(para{:}).CM([vars_eq; input_eq; t_]);
    KSub = f(para{:}).KM([vars_eq; input_eq; t_]);

    %% Solving Eigen value problem
    A = [MSub zeros(dof); zeros(dof) KSub];
    B = [CSub KSub; -KSub zeros(dof)];

    [eigvec, lambda] = eig(-B, A); % det(A*lambda+B)=0 --> -B*V = A*V*lambda

    data_eigvec(iomega, iphi, :, :) = eigvec;
    data_lambda(iomega, iphi, :) = diag(lambda);
    data_Lre(iomega, iphi, :) = (real(diag(lambda))); % saves im and re part of lambda for every step, in ascending order
    data_Lim(iomega, iphi, :) = (imag(diag(lambda)));

    data_Lre_sort(iomega, iphi, :) = sort(real(diag(lambda))); % saves im and re part of lambda for every step, ascending
    data_Lim_sort(iomega, iphi, :) = sort(imag(diag(lambda)));

    % Stiffnesses and strain for eq point
    data_Ksub(iomega, iphi, :) = double(diag(f(para{:}).K([vars_eq; input_eq; t_])));
    data_usub(iomega, iphi, :) = double(f(para{:}).u([vars_eq; input_eq; t_]));

    clear lambda eigvec MSub CSub KSub A B input_eq itrsteps itrerror
end
% vars_eq = vars_eq0; % resetting starting point of iterations
% disp(['Step omega = ', num2str(range.omega(i)/(2*pi))])
end
clear vars_eq eigvec omega_phil_

% static eigen frequencies:
disp('Static eigen frequencies found at [Hz]:')
disp(num2str(squeeze(data_Lim_sort(1,1,end/2+1:end)) / (2*pi)));
disp(['Maximum equilibrium relative error norm = ', num2str(max(max(data_itrerror)))])

```

integration.m

```

%% Time integration file
disp('Time integration')
if exist('f', 'var')

```

```

clearvars -except f
else
clear all
load functions.mat
end

%% Model parameters
% Parameter choice:
para = {2; % Prescription of: 1 = motion, 2 = torque
        1; % Deformation calculation: 1 = torsion:input/output, 3 = symbolic, 4 = multidof,
        % 6 = multidof + PRBM constraint
        1; % Inertia: 1 = SolidWorks, 3 = symbolic, 4 = multidof
        3; % Damping: 1 = none, 3 = proportional damping
        1; % Stiffness: 1 = nonlinear, 2 = linear, 3 = symbolic, 4 = multidof
        2}; % Coord sys: 1 = q_equi=0, 2 = polar, 3 = global, 4 = multidof global, 5 = multidof polar

% Check existence of data for current parameters
try
if isempty(f(para{:}) .eom)==1;
disp('No data for these model parameters in library')
return; end
catch
disp('No data for these model parameters in library')
return
end

%% Integration conditions
tsim = [0 1]; % time span of integration

phil_0 = 0/180*pi; % initial angle of input axle
omega = 100/60*2*pi; % initial velocity of input axle
Q = 0;

Tin = .045; % input axle torque
Tout = -.045; % output axle torque
Cin = 0; % output axle damping
Cout = 0; % output axle damping
alfa = 0; % modal damping, mass proportionality constant
beta = 0; % modal damping, stiffness proportionality constant

input = [phil_0 omega Q Tin Tout Cin Cout alfa beta].';

%% Initial conditions for different scenarios
disp('Initial conditions')

% Computing the initial conditions using Newton-Raphson
switch cell2mat(para(2)) % Deformation
case {1,2,4} % simple
ls0 = 0.0592; % absolute initial hight in Y of shuttles
l1 = f(para{:}).offset;
[init, itrerror, itrsteps] = findequilibrium(f,para,[1e-12;100],input,tsim(1),[]);
case {5,6} % including PRBM kinematics
ls0 = 0.0592; % absolute initial hight in Y of shuttles
l1 = f(para{:}).offset;
[init, itrerror, itrsteps] = findequilibrium(f,{2;4;4;3;4;5},[1e-10;500],input,tsim(1),[]);
[init, itrerror, itrsteps2] = findequilibrium(f,para,[1e-9;500],input,tsim(1),init);
end

%% ODE Solver parameters:
% ODE23 introduces 'damping', vibrations die out
disp('Integration')
AbsTol = [300 600 0.02 300 300,... % 5dof
          100 200 1 100 100]';
% AbsTol = [300 600 0.02 300 300, 600 0.02 300, 600 0.02 300, 600 0.02 300,... % 17 dof
%          100 200 1 100 100, 200 1 100, 200 1 100, 200 1 100, 200 1 100]';

opts = odeset('AbsTol',AbsTol*1e-3,'RelTol',1e-3,'MaxStep',1e-5);

%% ODE
% multiple ODE solvers can be used; ODE45 and ODE15s gave good results
[T,Y] = ode15s(@(t,y) f(para{:}) .eom(t,[y;input]),tsim,init,opts);

%% Post processing
disp('Post processing')
% calculation of body coordinates from gen coord
Tshort = []; j=1;

poststep = round(length(T)/2e3);
poststep(poststep<1)=1;

clear t y yd Tshort x xd u K F forces
disp(' Forces not computable yet!')

plotindex = round(0*length(T)+1):poststep:length(T);

```

```

dofq = length(f(para{:}) .q);
dofX = dofq+5;

for i=plotindex
    t = T(i);
    y = Y(i,:);
    yd = f(para{:}) .eom(t,[y.'; input]).';
    Tshort(j) = T(i);
    x(j,:) = f(para{:}) .X( [y.'; input; t]);
    xd(j,:) = f(para{:}) .Xd( [y.'; input; t]);

    % spring elongations:
    u(j,:) = f(para{:}) .u([y.'; input; t]);
    Ktemp = f(para{:}) .K([y.'; input; t]);
    K(j,:) = diag(Ktemp);
    F(j,:) = K(j,:) .*u(j,:);

    forces(j,,:) = f(para{:}) .forces([y.'; yd(end/2+1:end)'; input; t]); % postproc step no, q no, force no (Feuler,
    Finertia, Felastic, Fdamper)

    j=j+1;
end
clear i j t y

% matrix to subtract prescribed angle from angular generalised coordinates
switch cell2mat(para(6)) % Coord sys: 1 = q_equi=0
    case 1
        ifangle = [0 0 0 0];
    case 2
        ifangle = [2 0 1 1];
    case 3
        ifangle = [0 0 1 1];
    case {4}
        ifangle = [2 0 1 1, ...
                  0 0 1 0 0 1 0 0 1 0 0 1];
    case {5}
        ifangle = [2 0 1 1, ...
                  1 0 1 1 0 1 1 0 1 1 0 1];
    case {6}
        ifangle = [0 0 1 0 0 1 0 0 1 0 0 1];
    case {7}
        ifangle = [1 0 1 1 0 1 1 0 1 1 0 1];
    case 8
        ifangle = [1 0 1];
end

switch cell2mat(para(1))
    case 2 %prescribed torque
        ifangle = [1, ifangle];
        phil = Y(:,1)*ifangle;

        % velocity difference between input and output:
        thetadiff = Y(:,1) - Y(:,4); % lag of output axis wrt input
        vdiff = (Y(:,end/2+5)-Y(:,end/2+1) ) ./Y(:,end/2+1); % using general coordinates
    otherwise % prescribed motion
        phil = (phil_0 + omega*T)*ifangle;

        thetadiff = phil(:,4) - Y(:,4); % lag of output axis wrt input
        vdiff = (Y(:,end/2+4)-omega ) ./omega; % using general coordinates
end

disp(sprintf('Max energy difference: %0.3e J ', abs(max(Etot)-min(Etot))))
disp('Post processing done')
disp('Finished')

```

D

Experimental setup

D.1. Description of mechanical setup

In this section, a short overview of the experimental setup and all the used components is given. This will be done by the means of figure D.1, indicating the components. The setup and all used prototypes were build from scratch by the author.

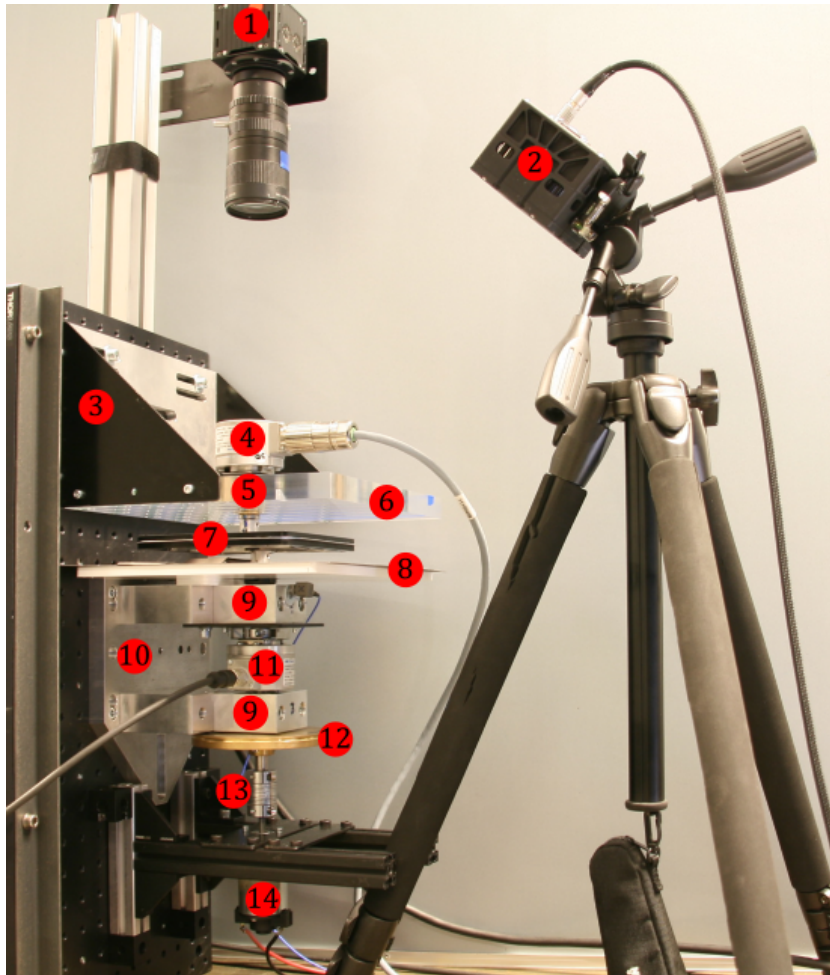


Figure D.1: Experimental setup indicating the different parts.

1. IDT NX4S1 high speed camera, recording at 1000 fps with a resolution of 1024×1024 .
2. IDT strobe light, coupling to the IDT camera controller, flashing in sync with the camera. Care must be taken that in the camera image no reflections of the strobe light are visible, as these appear as bright spots on the images. These disrupt the motion tracking software, as the used marker points are white as well.
3. Output axle support structure. This structure can be displaced horizontally to set the parallel axle misalignment.
4. Output axle encoder. Baumer EIL580P. The number of pulse per rotation given can be programmed between 1 and 65536. The experiments are executed using 2048 pulses per rotation. Furthermore, a reference pulse at a programmed zero angle point is given.
5. Output axle plain/journal bearing. The axial play of the bearing can be adjusted manually. Some axial pre-stress can be added using a disc spring. This way, bearing friction can be changed, which then will be the output load for the compliant coupling. The bearing is lubricated using some sewing machine oil.
6. Transparent cast PMMA plate in which the output axle bearing is fixed. This way the camera has a clear perpendicular sight upon the compliant coupling.
7. Prototype of the compliant coupling. The coupling is pinned to both axles and secured for further vibrations with a drop of Loctite. On the black PMMA bodies of the coupling, round with marker points are stuck which are used as reference points by the motion tracking software.
8. Background for the high speed camera images. It was determined that a matte grey paper background gave the best results for the motion tracking.
9. Input axle deep groove ball bearings, one at each end of the axle. Axial play is removed by applying some axial pre-stress between both bearings using a disk spring.
10. Input axle support structure. In the current setup for parallel misalignment couplings, this structure is fixed to the base plate. For angular misalignment couplings, this structure can be placed under an angle.
11. Input axle encoder, similar to the output axle encoder, but with a hollow shaft so that it can be placed at the middle of the axle.
12. Brass flywheel to even out the rotational velocity of the input axle driven by the DC motor. A groove is machined in the outer surface of the flywheel. When some transmission ratio between the driving DC motor and the setup, the direct coupling between motor and input axle can be removed, and this groove can be used for a belt drive to the motor (using a belt with round cross section).
13. Coupling between DC motor and input axle. Ruland Aluminium Flexible Beam Coupling, FCMR25-6-6-A.
14. Crouzet Brushed DC Motor, 15.7 W, 12 V DC, 75 mNm, 2000 rpm, 6mm Shaft Diameter.

To study the velocity error, the optical encoders are used. For the data acquisition and analysis a Müller-BBM PAK system is used, measuring the 2048 pulses with dedicated tacho channels with a sampling frequency of 50 MHz and the reference pulses with 50 kHz. Furthermore, motor current and voltage is measured. Data analysis is done using the PAK software. For velocity ramp up measurements the DC motor power supply voltage is controlled by an Agilent function generator creating a linear ramp up in motor voltage.

To get insight in the planar motion during rotation, a IDT NX4S1 high speed camera system is used, shooting 1000 frames per second and placed perpendicularly above the coupling, for which the upper axle support structure is made of transparent PMMA cast plate. White marker points on the different bodies of the coupling, also visible in the close up of figure ??, are tracked during motion using IDT Motion Studio. At every frame a pulse is send to the PAK system to be able to sync the two measuring systems.

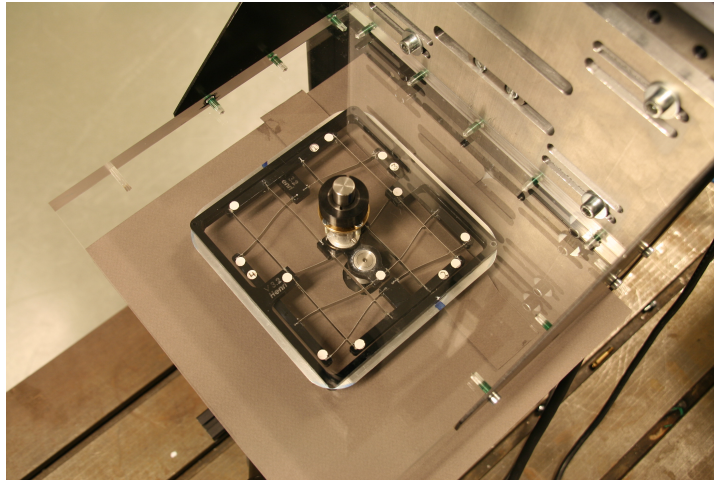


Figure D.2: The prototype placed in the setup.

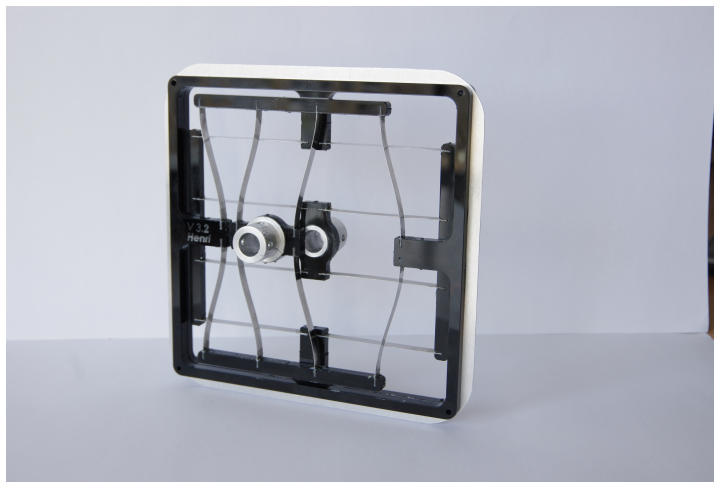


Figure D.3: Detailed picture of the prototype used.

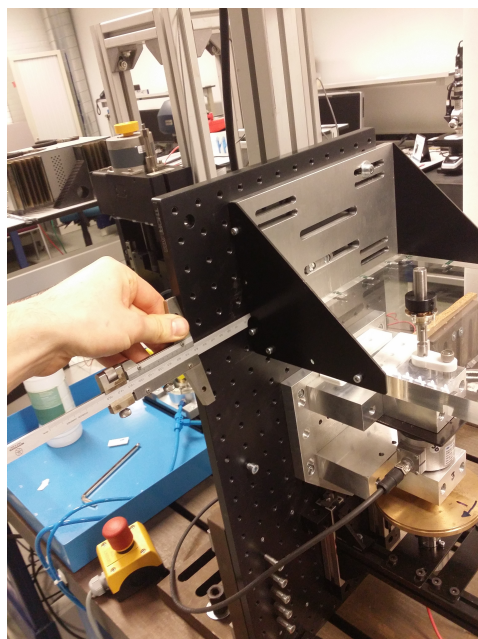


Figure D.4: Setting the amount of misalignment using a depth gauge.

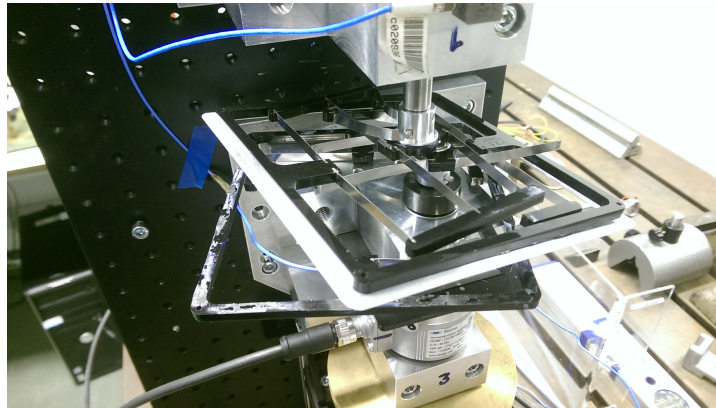


Figure D.5: The effect of dynamics on a compliant coupling.

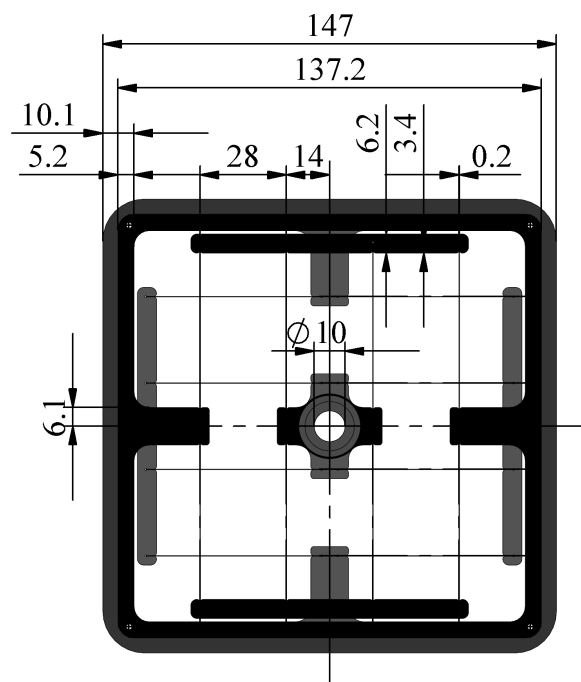


Figure D.6: Dimensions of the used prototypes. The thickness of each PMMA layer is 5 mm

D.2. Measurement of torsional vibration

In this section, some results from the torsional vibration measurements showing the velocity error are given.

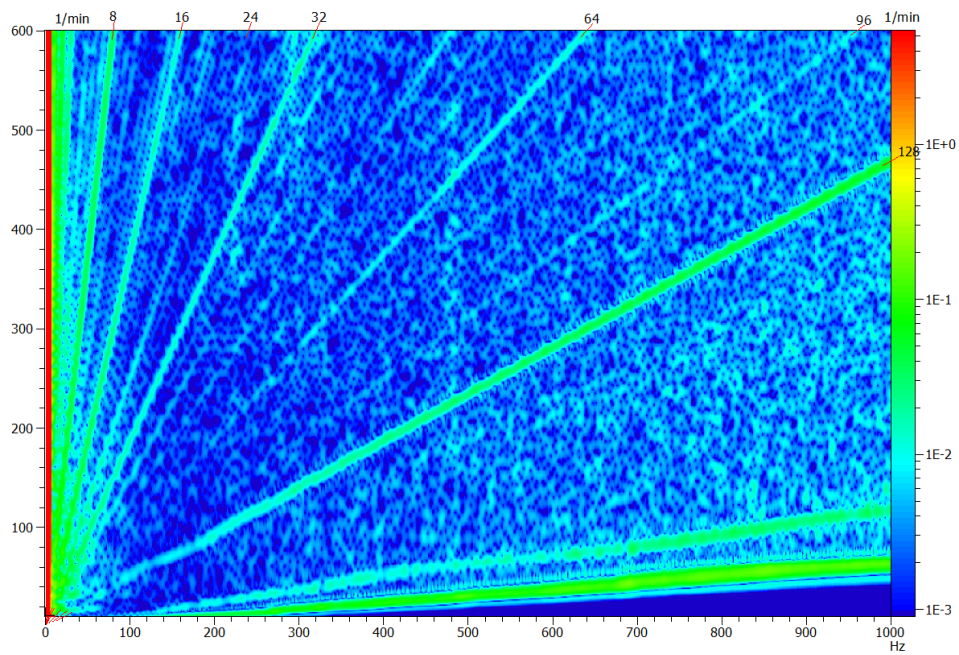


Figure D.7: Campbell diagram showing the torsional vibration of the input axle, without anything connected to it. The color scale has unit RPM.

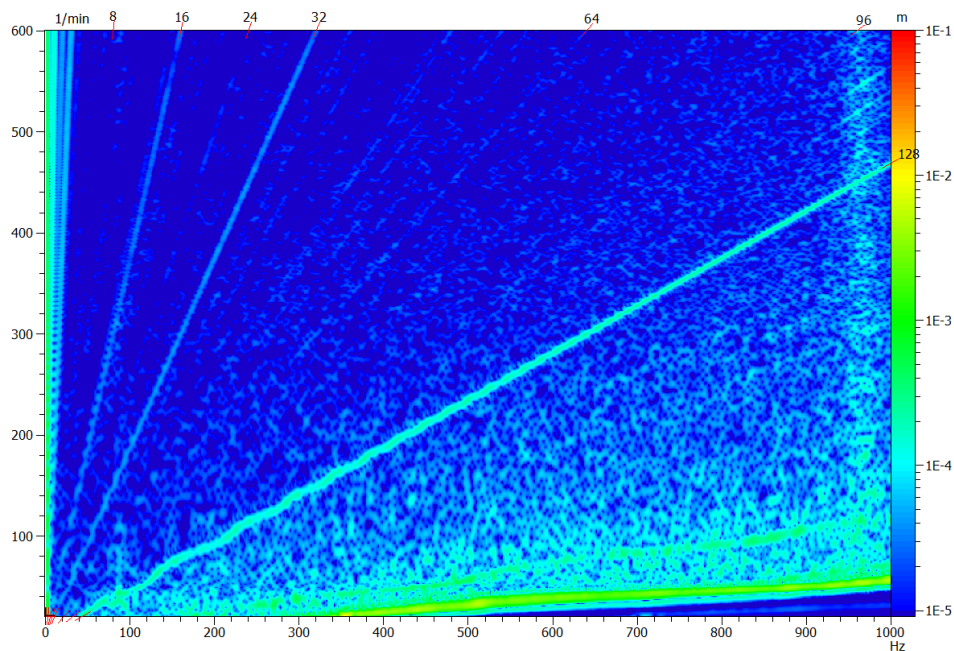


Figure D.8: Campbell diagram showing the dimensionless velocity error (colour scale) between input and output axle, for a the reference measurement using the commercial compliant bellow coupling. Zero axle misalignment.

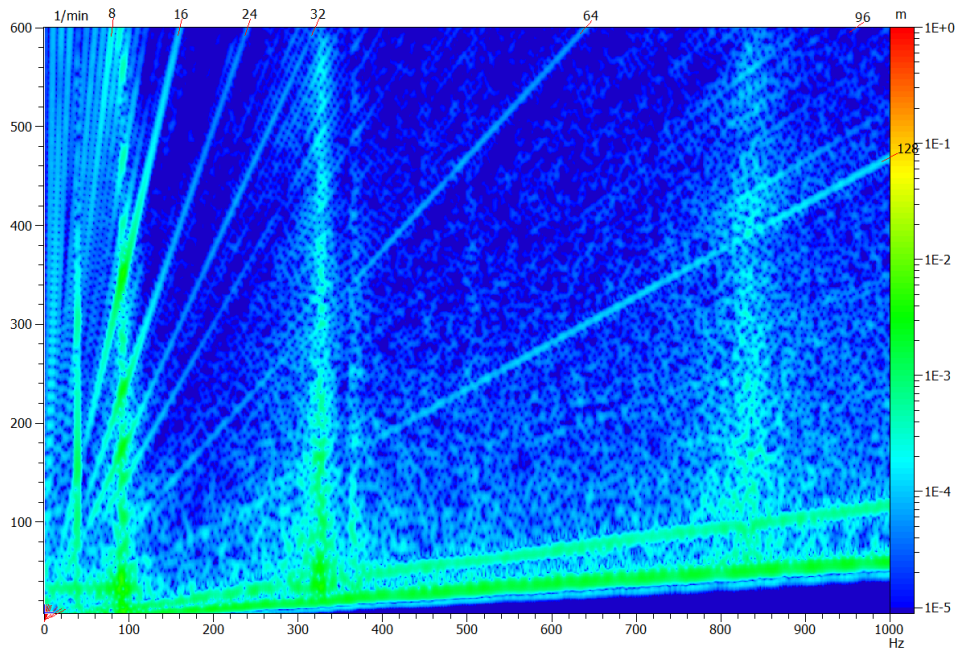


Figure D.9: ampbell diagram showing the dimensionless velocity error (colour scale) between input and output axle. Measurement with the compliant Oldham coupling, at zero axle misalignment.

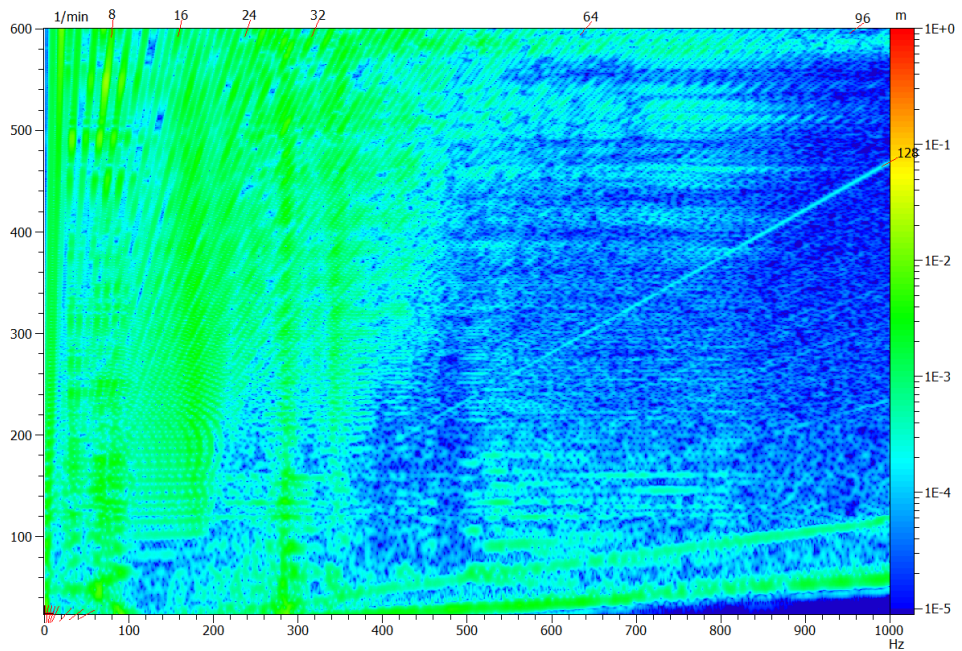


Figure D.10: ampbell diagram showing the dimensionless velocity error (colour scale) between input and output axle. Measurement with the compliant Oldham coupling, at zero axle misalignment.

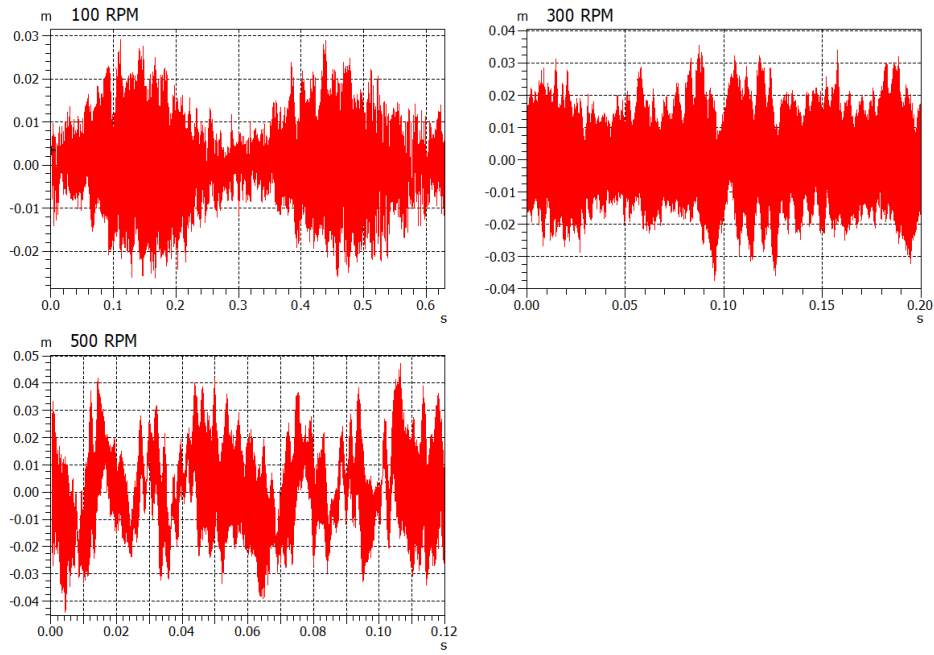


Figure D.11: Dimensionless velocity error for three measurements at constant rotational velocity. Measurement with the compliant Oldham coupling, at zero axle misalignment.

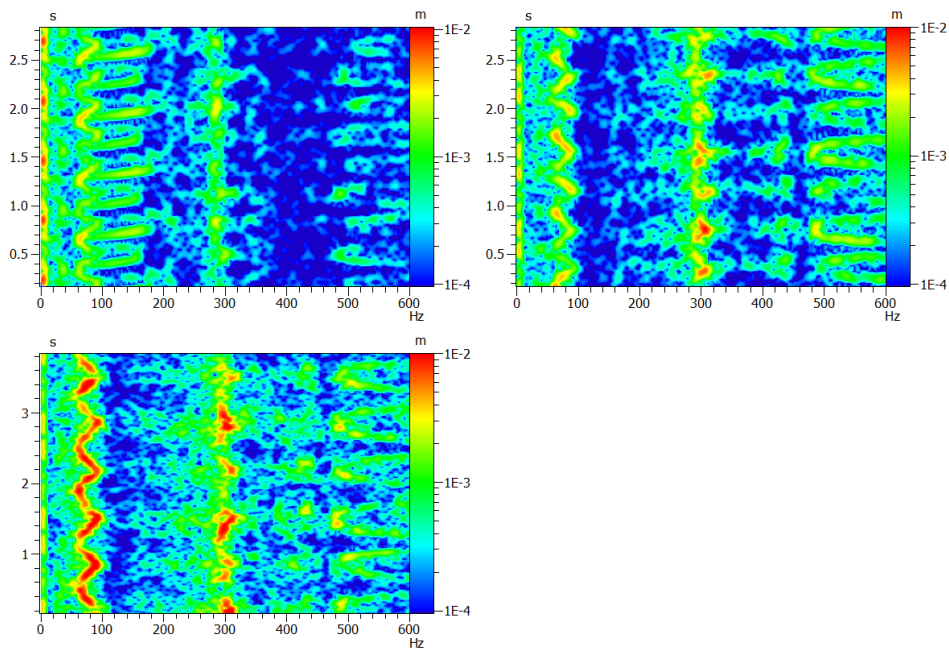


Figure D.12: Waterfall diagram showing the dimensionless velocity error between input and output axle. Three measurements at a constant rotational velocity. Compliant Oldham coupling, at zero axle misalignment.

D.3. Measurement of planar motion

In this section, the result of the motion tracking using the high speed camera is shown. Furthermore, high speed footage is available in which the break down of the prototypes can be observed and analysed.

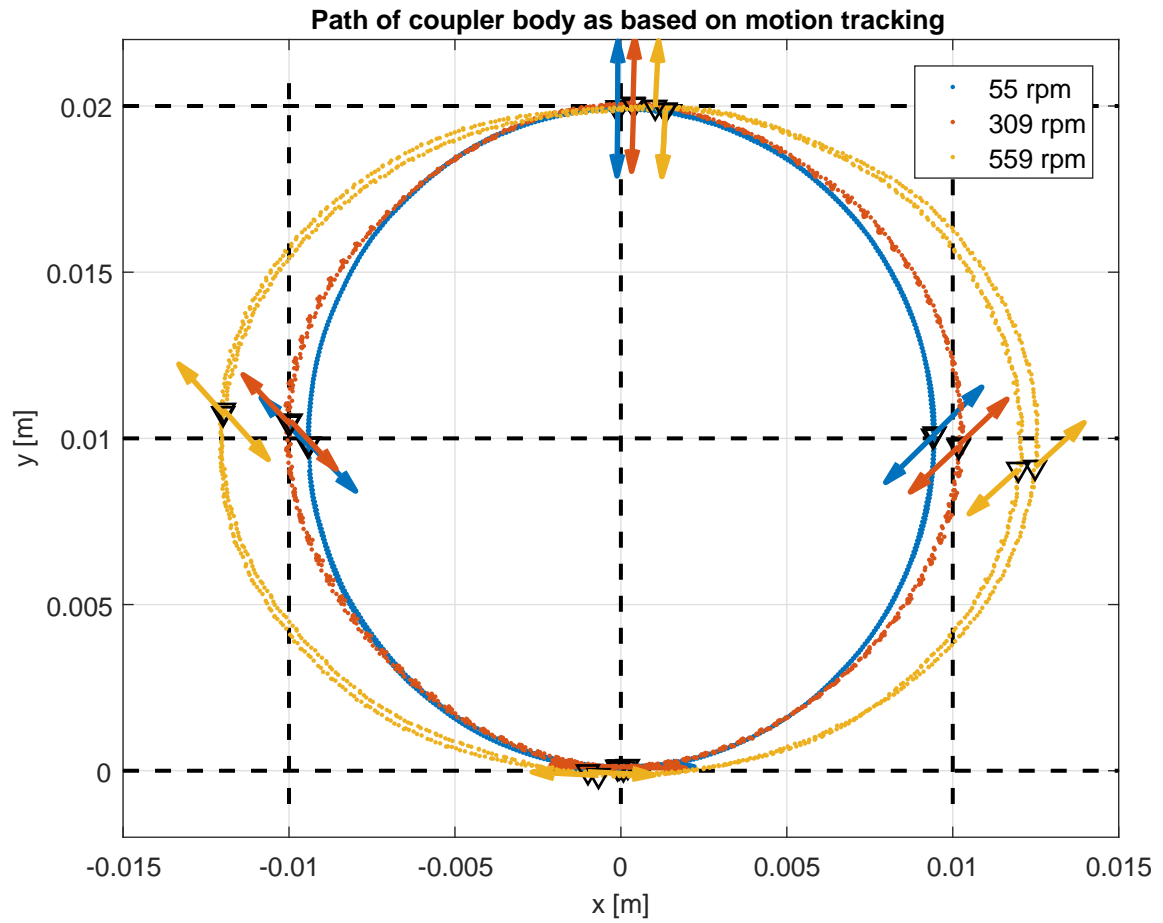
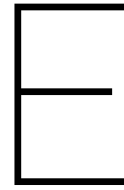


Figure D.13: Path of the COM of the coupler body, based on the motion tracking. Results for three different constant velocities are shown. The black triangular markers indicate the points of $\theta_2 = n \cdot 45 \text{ deg}$. The arrows indicate the body angle of the coupler body at those points



Orientation into Redesign

E.1. Introduction

The goal of this work is to design a compliant rotational power transmission mechanism for dynamic applications. For now, the scope is restricted to the Oldham rigid body kinematics. Within these kinematics, a compliant transmission mechanisms will be designed.

E.2. Design requirements

The current compliant Oldham design is used as a benchmark. The redesign for dynamic purposes should have the same capabilities, apart from the dynamic performance, which should be improved. Based on this benchmark, the following requirements and wishes can be formulated.

Requirements:

- 20 mm parallel misalignment
- $\omega_{max} > 600 \text{ min}^{-1}$
- $\dot{\omega}_{max} > \dots$
- Maximum velocity error $< 4\%$
- Transmission stiffness $> \dots \text{Nm rad}^{-1}$
- Statically balanced?

Wishes:

- Minimize footprint
- Minimize energy dissipation
- Minimize rotational inertia

E.3. Transmission between parallel axis: functional analysis

In this section the functions of the parallel transmission are defined. In figure E.1 a schematic of the transmission is given. The mechanism should transmit the motion and torque of the input axis to the output axis, which has a parallel offset from the former. Both the input and output axes are constrained in all directions but the rotational along their length by conventional bearings. When the rotation of the input axis is prescribed, the mechanism should transmit this rotation and torque to the output axis, and the mechanism thus has no degree of freedom in this configuration. The functions of the mechanism in this case are given below.

When the input axis would be fixed in all directions, and the output axis being free, the latter would have two translational DOF

1. Transmit torque

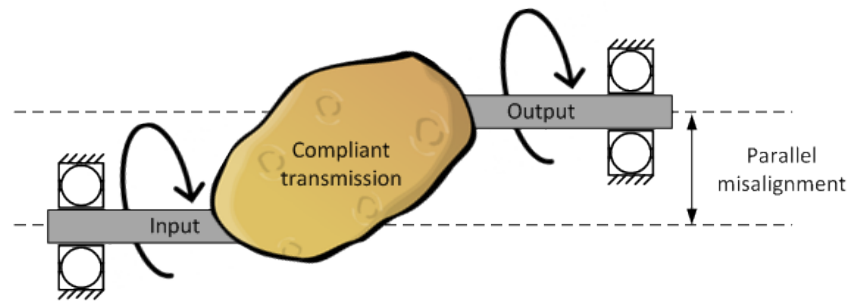


Figure E.1: Schematic of transmission

2. Transmit motion

(a) ... with a constant velocity transfer

As mentioned earlier, the Oldham rigid body kinematics are chosen as a basis. Looking at the system's functions, the motion transmission is done using a mechanism of the linkage type, more specifically, the Oldham linkage. Within the Oldham kinematics, several parameters can be tuned to reach the design requirements, as given below and in the appended table.

1. Kinematic variations within the Oldham kinematics. For example, balancing could be a way to improve the dynamic behaviour.
2. Mass. Distribution of mass, number of 'point masses', location of these masses, ...
3. Stiffness. The way the DOF and DOC are created.
4. Damping. Material damping properties, additional damping material, ...

This categorisation of parameters might not be conclusive. For example, if the system should be dynamically balanced (first parameter), this could be done by placing a counter mass at some location, influencing the second parameter.

E.4. Stiffness: prismatic compliant joints

The current benchmark design is build up of two compliant prismatic joints, placed in series, designed in the planar domain. In this section, this family of mechanisms is elaborated on. First, the most common building block of planar compliant designs, the beam flexure, is discussed. Secondly, some characteristics of beam based flexure modules are given. Finally, a functional analysis of the compliant prismatic joint intended for the Oldham kinematics is performed.

E.4.1. Beam flexures

The beam flexure is the building block for many (planar) flexure mechanisms. Some characteristics of a beam flexure will be given. First of all the possible loading modes of a single long and thin beam are given in figure ... For planar mechanisms, the focus lies on the first three 2D modes. Out of plane loads and deformations are assumed zero and neglected. The transverse and rotational direction are seen as degrees of freedom (DOF) as they possess the lowest stiffness for long thin beams. The axial direction, as well as all other 3D modes, are seen as degrees of constraint (DOC) with a significant higher stiffness.

As in planar designs primarily loads and deformations in-plane are investigated, the only possible way to generate stiffness is to load the flexures axially. This can be done in tension and compression. In the latter case, the beam will buckle at a threshold value, the critical load. This load depends on the way of constraint of the flexure end tip, as seen in figure E.3.

E.4.2. Flexure modules

A flexure module is a compliant mechanism build up out of multiple elastic beam flexures. The mechanism is designed to have certain DOF allowing the primary motion, and DOC in all other directions. Ultimately,

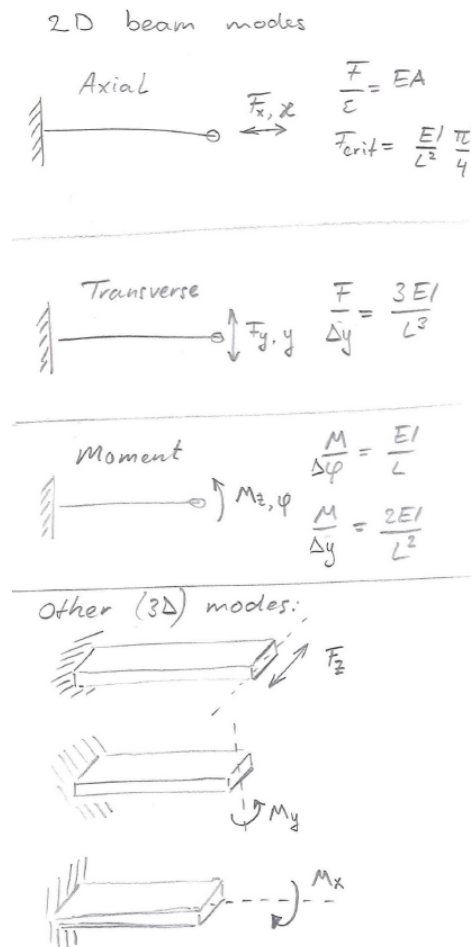


Figure E.2: Possible loading modes of a simple beam

infinite motion in DOF direction is allowed with zero stiffness, and no motion and infinite stiffness along the DOC. Flexures deviate from this ultimatum in several ways, having limited motion and non-zero stiffness along the DOF and non-infinite stiffness along the DOC.

Undesired motions along other DOF are defined as cross-axis error motion, whereas motions in DOC direction are called parasitic error motions. These errors can be force dependent, kinematic, elastokinematic, or a combination.

Increasing displacements lead to error motions and decrease of the DOC stiffness values. These non-linearities in the force-displacement characteristics originate from three sources, being the material constitutive properties, geometric compatibility and force equilibrium conditions.

As long as the flexure material can be seen as linear-elastic, this first part vanishes.

The geometric compatibility however becomes an important source of non-linearity for transverse displacements in the order of one tenth of the beam length. Parametric approximations such as the pseudo rigid body method capture this non-linearity.

The non-linearities resulting from the force equilibrium become significant for much smaller deflections, as small as the beam thickness. The effect largely determines the beam's constraint behaviour, capturing the load stiffening and elastokinematic effects.

E.4.3. Planar prismatic compliant joints using beam flexures

This functional analysis describes the category of compliant prismatic joints in the planar domain. Beam flexures provide the needed elastic deformations. Analysis will be in 2D. The joints will be investigated separately in this part, without integration in the Oldham coupling. Part of the joint is connected to the fixed world. The end effector of the joint, the shuttle, provides compliance in the motion direction y , and stiffness

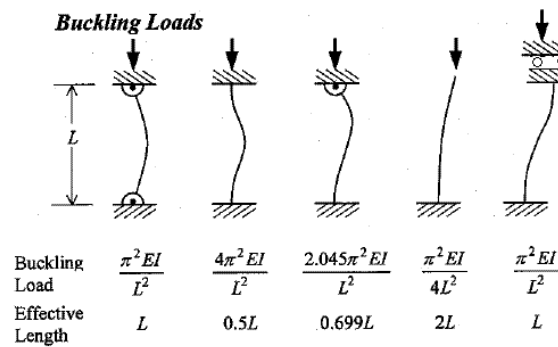


Figure E.3: Critical buckling loads

in the bearing directions x , θ and out of plane with respect to this fixed world. The mechanism thus has one DOF.

The mechanism can possess certain internal DOF, apart from the desired motion DOF. As all deformations in the mechanism originate from the elastic deformation of the flexures, there is no clear distinction between DOF and DOC, apart from that the DOF possesses a significant lower stiffness than the DOC. Looking at the eigen frequencies of the mechanism, the motion direction mode shape is expected to have the lowest eigen frequency. Other mode shapes with an eigen frequency having the same order of magnitude as the motion mode, can be seen as (undesired) internal DOF. Ultimately, the desire is to have $\omega_{2,3,\dots} \gg \omega_1$.

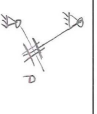
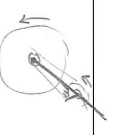
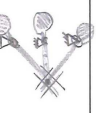
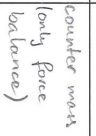





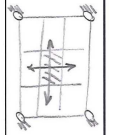
1. **Provide straight line kinematics.** When the shuttle load is applied in pure motion direction, without creating a moment on the shuttle, the shuttle should move in a straight line along y . A simple beam loaded in the traverse direction will not only move in the y direction, but also in x and θ . This behaviour thus has to be compensated for when using flexures, leading to the following subfunctions.
 - (a) **Eliminate parasitic x -motion.** When not constrained, the tip of the beam will move in x -direction when displacement in y occurs due to the fixed arc length of a beam.
 - (b) **Eliminate parasitic θ -motion.** When the tip of a clamped-free beam displaced in y , the tip rotates.
2. **Provide motion compliance.** In this categorisation, the flexures generate the needed elastic deformation. However, as discussed above, different mode shapes of elastic deformation can be used.
3. **Provide bearing stiffness.** The flexure mechanisms should provide stiffness in all bearing directions. Again, different loading modes of the flexure can be used. Several subfunctions can be indicated.
 - (a) **Prevent stiffness drop due to buckling.** Flexures loaded in axial compression will buckle at a certain threshold value, what can lead to drop in bearing stiffness.
 - (b) **Prevent stiffness drop due to bending.** In certain cases displacement of internal DOF can allow for flexure bending resulting in deformation in bearing direction, and thus in drop of bearing stiffness.
 - i. **Eliminate internal DOF.** Quasi-statically, internal DOF can lead to undesired bending modes in the flexure mechanism. Dynamically, internal DOF are also undesired, as these DOF can freely resonate at 'low' frequencies, which are likely to be excited during operation. Certain strategies to eliminate these DOF exist.
 - A. **Coupling internal DOF.** One of the strategies to eliminate the internal DOF is to couple them to other motions within the mechanisms. Different 'coupling methods' exist.
 - (c) **Prevent stiffness drop in rotational direction.** In the above function 'Eliminate parasitic θ -motion' rotation of the shuttle is prevented when loaded in motion direction. The current function is to prevent this same rotation, but then as a function of moments applied on the shuttle.

The functions, including several possible solutions, are given schematically in the appended table.

In the functional analysis, a distinction is made between the case of the shuttle being loaded in pure motion direction (function 1) and loading in other directions (bearing stiffness, function 3). The first one should result in straight line motion of the shuttle. The latter one, assuming that infinite bearing stiffness

can not be reached, inherently results in error motions in the bearing directions, and thus deviation from the desired straight line motion.

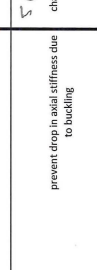
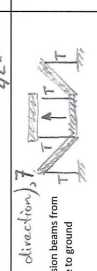
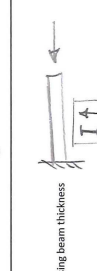
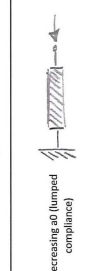
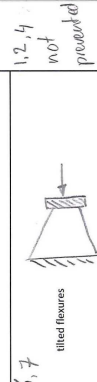
In certain designs, not all functions are fulfilled, and can for example possess internal DOE

functions parallel rotational transmission using Oldham rigid body kinematics	subfunctions	solution strategies			
improving rigid body kinematics 	static balancing	constant potential energy $\frac{1}{2} k u^2 = C$ 	counter mass + separate counter relations 	idler loop	duplicate mechanisms
dynamic balancing (force and/or moment balance)	counter-rotary countermasses	counter mass (only force balance) 			
mass	lumped 	distributed 	no intermediate mass		
mass distribution					
damping	influence damping	change elastic material 	additional damping layer on elastic material 		
stiffness	global compliant strategy for 2DOF Oldham kinematics	two perpendicular prismatic joints (stiffness in series) 2DOF 	'XY stage' (stiffness in parallel) 		
compliant domain		planar	spatial		

→ see other table

Planar designs + leaf springs
 T = tension C = compression
 "Dynamic wish": all w but w₁ → ∞

functions prismatic compliant joint	subfunctions	solution strategies	rotational	axial load, tension	transverse + rotational (clamped bending)	axial load, compression	prevent drop in axial stiffness due to buckling	prevent drop in axial stiffness due to bending	eliminate internal DOF	eliminate internal DOF	coupling method
straight line kinematics (geometric nonlin) (pure motion load) in y -direction	minimize axis drift / (parasitic) error motion	1, 2, 3, 4, 5, 6, 7 overconstraint (symmetric) designs (elastic averaging)									
eliminate parasitic x motion	eliminate parasitic x motion	1, 2, 3, 4, 5, 6, 7 two in series in opposite direction: cancelling by equal deformation or multiple									
eliminate parasitic rotation	eliminate parasitic rotation	1, 2, 3, 4, 5, 6, 7 two in parallel in same direction: creating moment or multiple									
provide motion compliance (y)	provide motion compliance (y)	transverse load (bending)	rotational	axial load, tension $F = EA$	transverse + rotational (clamped bending)	axial load, compression	prevent drop in axial stiffness due to buckling	prevent drop in axial stiffness due to bending			
provide bearing stiffness (force nonlin) (bearing load)	provide bearing stiffness (force nonlin) (bearing load)	axial load, compression $F_{pre,x} = \frac{EIT^2}{4L^3}$	1, 2, 3, 4, 5, 6, 7 axial load, tension	5 (one direction)	1, 2, 3, 4, 5, 6, 7 tension + compression in series	axial load, compression	prevent drop in axial stiffness due to buckling	prevent drop in axial stiffness due to bending			
(x)	(x)	chain of tension beams from shuttle to ground	3	increasing beam thickness	3	axial load, compression	prevent drop in axial stiffness due to buckling	prevent drop in axial stiffness due to bending			
(theta)	(theta)	prevent: bending modes resulting in axial deflection → eliminate internal DOF	7	4, 1, 5, 6 two in parallel to shuttle creating moment	7	axial load, compression	prevent drop in axial stiffness due to buckling	prevent drop in axial stiffness due to bending			
eliminate internal DOF	eliminate internal DOF	reducing: coupling to other internal DOF $y_2 = y_3$	7	4, 1, 5, 6 two in parallel to shuttle creating moment	7	axial load, compression	prevent drop in axial stiffness due to buckling	prevent drop in axial stiffness due to bending			
coupling method	coupling method	internal lever with tilted flexures creating CK	3	external lever	3	axial load, compression	prevent drop in axial stiffness due to buckling	prevent drop in axial stiffness due to bending			



1, 2, 4 not provided

Improved designs from literature Two designs from literature are given.

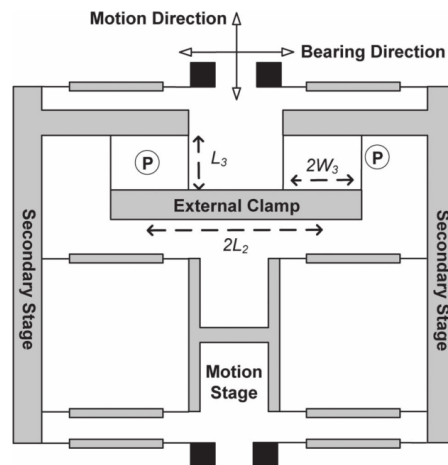


Figure E.4: C-DP joint [27] in which the two free intermediate shuttles are coupled reducing the number of underconstraints from two to one.

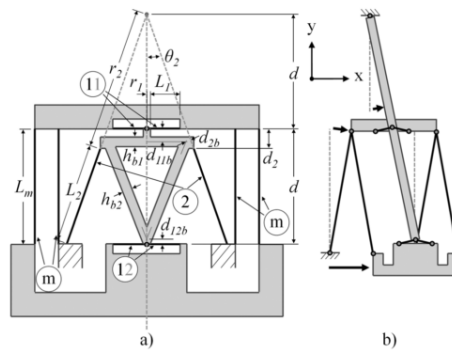
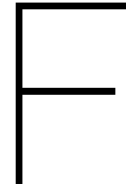


Figure E.5: DP-NL joint [29] in which the intermediate shuttle is coupled to the output shuttle via an internal (nested) linkage, eliminating the underconstraint.



Reflection

In this section, I will shortly reflect on the process of graduating. During this project, I (again) discovered my strengths and weaknesses. I will discuss some of these shortly. First of all, I do not like to seek help when I find myself in a problem. Silly as it might be, I often feel ashamed to ask help from someone about a topic which I did not first fully researched myself. For example, at the beginning of the project, I should have looked for someone within the department who could guide me in the dynamic modelling, as this is not Davood's his speciality. However, I did the first modelling steps primarily on my own. Only later in the project, I contacted Dennis, Arend and Paul van Woerkom, for specific feedback on the dynamic analysis. I think that frequent feedback from the start of the project, from someone of the dynamics department for example, would have eased and accelerated the project.

Furthermore, I am a bad finisher. When I do not fully understand something, I can be stuck in little details and lose track of the bigger picture. This might also be visible in this thesis. Focusing on the details resulted in work stress at the end of the project, when all those details had to be combined to one complete story. I did not had the time to incorporate all those little details.

I also discovered that I like team work above individual work. Although it is nice to focus on some details individually, I really missed the collaboration and discussion with other people. In a team, the responsibility is shared, and everyone is problem owner. In this thesis project, I was 100% problem owner myself. Furthermore, other team members can motivate me to carry on especially when problems arise.

In the search for a thesis topic a year and a half ago, I was looking for a multidisciplinary project. Looking back, that goal is fulfilled for sure. I enjoyed the diversity. A lot of time was spend on the modelling work, but there was also the opportunity to look into the redesign of the coupling. Furthermore, during the building of the experimental setup, I spend quite some time in the workshops behind lathes and milling machines, which is a hobby of mine. Also, when the setup was ready, I really enjoyed the experimental lab work. During this phase, I concluded that I might want to pursuit a job in the field of experimental dynamics.

Bibliography

- [1] D. Farhadi Machekposhti, N. Tolou, and J. Herder, "A Fully Compliant Homokinetic Coupling," *Journal of Mechanical Design, Transactions of the ASME*, vol. 140, p. 012301, nov 2018.
- [2] "ABSSAC, Custom shaft couplings." Available at <https://www.abssac.co.uk/p/Shaft+Couplings/>.
- [3] D. Farhadi Machekposhti, N. Tolou, and J. L. Herder, "A Review on Compliant Joints and Rigid-Body Constant Velocity Universal Joints Toward the Design of Compliant Homokinetic Couplings," *Journal of Mechanical Design*, vol. 137, no. 3, p. 032301, 2015.
- [4] L. L. Howell, *Compliant mechanisms*. Wiley, 2001.
- [5] "Couplings - Flexible Couplings, Bellows, Helical, Junior Flex, Oldham and Multijawed from SDP-SI." Available at <http://www.sdp-si.com/products/Couplings/index.php>.
- [6] D. Farhadi Machekposhti, N. Tolou, and J. L. Herder, "A statically balanced fully compliant power transmission mechanism between parallel rotational axes," *Mechanism and Machine Theory*, vol. 119, pp. 51–60, jan 2018.
- [7] K. Hunt, "Constant Velocity Shaft Couplings: A General Theory," *Journal of Engineering for Industry*, vol. 95, no. 72, pp. 455–464, 1973.
- [8] L.-W. Tsai, "Oldham-Coupling Second-Harmonic Balancer," *Journal of Mechanisms Transmissions and Automation in Design*, vol. 106, no. 3, p. 285, 1984.
- [9] F. Freudenstein, L. W. Tsai, and E. R. Maki, "The Generalized Oldham Coupling," *Journal of Mechanisms Transmissions and Automation in Design*, vol. 106, no. 4, p. 475, 1984.
- [10] R. C. Hibbeler and S. C. Fan, *Engineering mechanics. Dynamics*. Prentice Hall, 2010.
- [11] S. Rao, *Mechanical vibrations*. Prentice Hall, 4th ed., 2005.
- [12] C.-K. Chen and F. Freudenstein, "Dynamic Analysis of a Universal Joint With Manufacturing Tolerances," *ASME J. Mechanisms, Transmissions, and Automation in Design*, vol. 108, no. 86, pp. 524–532, 1986.
- [13] H. Ota and M. Kato, "Lateral Vibrations of a Rotating Shaft Driven by a Universal Joint, 1st report," *Bulletin of JSME*, vol. 27, no. 231, pp. 2002–2007, 1984.
- [14] H. Ota and M. Kato, "Lateral Vibrations of a Rotating Shaft Driven by a Universal Joint, 2nd report," *Bulletin of JSME*, vol. 29, no. 254, pp. 2633–2639, 1986.
- [15] M. Kato, H. Ota, J.-R. Kim, and R. Kato, "Unstable vibrations of a rotating shaft driven through a universal joint," in *Asia-Pacific Vibration Conference*, pp. 236–237, 1997.
- [16] A. J. Mazzei, A. Argento, and R. Scott, "Dynamic Stability of a Rotating Shaft driven through a Universal Joint," *Journal of Sound and Vibration*, vol. 222, no. 1, pp. 19–47, 1999.
- [17] T. Liu and T. W. Lee, "Dynamics of an Overconstrained Shaft Coupling," *Journal of Mechanisms, Transmissions, and Automation in Design*, vol. 108, no. 4, pp. 497–505, 1986.
- [18] W. B. Case, "The pumping of a swing from the standing position," *American Journal of Physics*, vol. 64, pp. 215–220, mar 1996.
- [19] J. Tian, *Self-Excited Vibrations of Rotating Discs and Shafts*. PhD thesis, The University Of British Columbia, 1998.

- [20] M. Xu and R. D. Marangoni, "Vibration Analysis of a Motor-Flexible Coupling-Rotor System Subject To Misalignment and Unbalance, Part I: Theoretical Model and Analysis," *Journal of Sound and Vibration*, vol. 176, no. 5, pp. 663–679, 1994.
- [21] M. Xu and R. Marangoni, "Vibration analysis of a motor-flexible couplingrotor system subjected to misalignment and unbalance Part II: Experimental validation," *Journal of Sound and Vibration* 176 681-691., 1994.
- [22] K. M. Al-Hussain, "Dynamic stability of two rigid rotors connected by a flexible coupling with angular misalignment," *Journal of Sound and Vibration*, vol. 266, no. 2, pp. 217–234, 2003.
- [23] S. M. Lyon, P. A. Erickson, M. S. Evans, and L. L. Howell, "Prediction of the First Modal Frequency of Compliant Mechanisms Using the Pseudo-Rigid-Body Model," *Journal of Mechanical Design*, vol. 121, no. 2, p. 309, 1999.
- [24] C. Boyle, L. L. Howell, S. P. Magleby, and M. S. Evans, "Dynamic modeling of compliant constant-force compression mechanisms," *Mechanism and Machine Theory*, vol. 38, pp. 1469–1487, dec 2003.
- [25] Y.-Q. Yu, L. L. Howell, C. Lusk, Y. Yue, and M.-G. He, "Dynamic Modeling of Compliant Mechanisms Based on the Pseudo-Rigid-Body Model," *Journal of Mechanical Design*, vol. 127, no. 4, p. 760, 2005.
- [26] Z. Li and S. Kota, "Dynamic Analysis of Compliant Mechanisms," in *Volume 5: 27th Biennial Mechanisms and Robotics Conference*, pp. 43–50, ASME, jan 2002.
- [27] M. Olfatnia, S. Sood, J. J. Gorman, and S. Awtar, "Large stroke electrostatic comb-drive actuators enabled by a novel flexure mechanism," *Journal of Microelectromechanical Systems*, vol. 22, no. 2, pp. 483–494, 2013.
- [28] M. Géradin and D. J. Rixen, *Mechanical Vibrations: Theory and Application to Structural Dynamics*. John Wiley, 2015.
- [29] R. M. Panas and J. B. Hopkins, "Eliminating Underconstraint in Double Parallelogram Flexure Mechanisms," *Journal of Mechanical Design*, vol. 137, p. 092301, sep 2015.